# Dynamics of Mooring System for Floating Offshore Wind Turbine (FOWT)

Iman Ramzanpoor

Submitted in fulfilment of the requirements for the
Degree of Doctor of Philosophy

Department of Naval Architecture
Ocean and Marine Engineering
University of Strathclyde


August 2024

# Acknowledgement

First and foremost, I would like to express my gratitude to my supervisor and mentor, Prof. Longbin Tao, for his unwavering support throughout this project. I am particularly thankful for his patience and understanding, which proved invaluable during the course of this research.

I am also grateful to the faculty members of the University of Strathclyde Naval Architecture, Ocean & Marine Engineering School, and UKRI for providing EPSRC funding for this work.

I extend my sincere appreciation to all my colleagues at the University of Strathclyde and friends for their support and encouragement in overcoming the challenges encountered. Special thanks to Doctor Martin Nuernberg for his valuable advice and guidance during the dynamic analysis of the floater wind turbines.

Lastly, I would like to convey my heartfelt thanks to my family for their encouragement, support, and trust. I am especially grateful to my wife, Firouzeh Heydari Kaydan, for her unwavering understanding, support, and love during my PhD. Her steadfast support and inspiration were instrumental in the completion of this work.

# List of Publications

**Ramzanpoor,** Iman, Martin Nuernberg, and Longbin Tao. (2019). **"Coupled Numerical Analysis of a Concept TLB Type Floating Offshore Wind Turbine."** In ASME 2019 38th International Conference on Ocean, Offshore and Arctic Engineering. American Society of Mechanical Engineers Digital Collection.

Xiudi Ren, Longbin Tao, Martin Nuernberg, **Iman Ramzanpoor,** (2022) **"Interaction of offshore support vessel with adjacent offshore wind turbine during maintenance operation".** in International Conference on Offshore Mechanics and Arctic Engineering. 2022. American Society of Mechanical Engineers.

**Ramzanpoor,** Iman, Martin Nuernberg, and Longbin Tao. (2023). **'Coupled aero-hydro-servo-elastic analysis of 10MW TLB floating offshore wind turbine',** Journal of Ocean Engineering and Science.

**Ramzanpoor,** Iman, Martin Nuernberg, and Longbin Tao. (2023). **'Benchmarking Study of 10MW TLB Floating Offshore Wind Turbine',** Journal of Ocean Engineering and Marine Energy.

# Abstract

This study introduces a novel concept for a Tension Leg Buoy (TLB) floating offshore wind turbine (FOWT) system intended to support a 10 MW wind turbine and anchored by an innovative taut mooring system for deployment in water depths of 110 meters in the challenging environmental conditions of the Northern North Sea. The unique design of this system underwent a thorough iterative development process to attain an optimal configuration, followed by a detailed analysis that adheres to the recognized principles and criteria for the design of floating wind turbines.

Frequency domain and hydro-aero-servo-elastic time domain analysis carried out by considering wave drift and second order effect. The performance of the 10 MW TLB FOWT utilizing synthetic fibre materials was evaluated in comparison to that using steel wire rope. Furthermore, a benchmarking study was conducted by scaling the current leading technology types FOWT platforms to verify an innovative TLB design. Finally, an examination was conducted to assess the practicality of anchor sharing in the suggested TLB system by analysing the system dynamics within a wind farm.

The results of the study indicate that the integration of second-order effects plays a significant role in influencing outcomes. It is imperative to consider second-order effects in order to enhance conceptual design and attain more accurate predictions of forces and responses during the early phases of a project, thus preventing unnecessary overdesign.

The optimal design utilizing steel, polyester, and nylon mooring materials effectively demonstrated stability with limited motion responses and satisfied the rule-based limitations including the design criterion for ultimate limit state (ULS) and accidental limit state (ALS). Increased motion responses were found to be associated with decreased dynamic tension in mooring lines that have higher elasticity, while higher dynamic tension was observed in mooring lines made of more rigid materials. This highlights the significance of high stress on steel mooring line. The effect of the wind turbulence on the system responses utilized higher elasticity mooring material was significant. TLB systems with steel and polyester are suitable for applications requiring consistent behaviour due to minimal variability, while TLB systems with nylon may be less reliable for applications necessitating consistent performance.

Platforms utilizing catenary mooring systems exhibit more responses when contrasted with those utilizing tensioned mooring systems and show different low-frequency motion behaviour compared to the high-frequency motions experienced by the stiff-mooring stabilised platforms. The environmental forces exerted on motion responses, particularly pitch motion, are more pronounced on the Semi-Submersible platform, leading to decreased power production.

Analysing the motion and tension responses that apply loads on common anchors, while considering specific assumptions, can offer valuable insights into the feasibility of anchor sharing for a designed TLB utilizing semi-taut mooring lines.

# List of Symbols

| | |
|---|---|
| $EA$ | Mooring line axial stiffness |
| $\epsilon$ | Mooring line strain |
| $f_s, g_s$ | Constants parameters estimated from full-scale mooring line testing |
| $\frac{E}{\rho}$ | Specific modulus |
| $L_m$ | Mean load (% of MBL) |
| $L_a$ | Load amplitude (% of MBL) |
| $T_o$ | Period of loading |
| $\alpha, \beta, \gamma, \delta$ | Empirical coefficients |
| $K_{rs}$ | Non-dimensional axial stiffness |
| $K_{rd}$ | Dynamic stiffness |
| $\Omega_0$ | Fluid domain |
| $n$ | Normal vector |
| $S_{FS}$ | Water level free surface |
| $S_{SB}$ | Seabed surface |
| $S_B$ | Mean body wetted surface |
| $V_B$ | Body velocity |
| $\vec{n}$ | Unit vector |
| $(x, y, z)$ | Position vector on body surface |
| $\Phi(x, y, z, t)$ | Total velocity potential |
| $\Phi^{(1)}(x, y, z, t)$ | Total first-order velocity potential |
| $\Phi^{(2)}(x, y, z, t)$ | Total second-order velocity potential |
| $\emptyset^{(1)}(x, y, z)$ | Complex first-order time-independent total velocity potential |
| $\emptyset_D{}^{(1)}$ | Complex first-order time-independent diffraction wave potential |
| $\emptyset_I{}^{(1)}$ | Complex first-order time-independent incident wave potential |
| $\emptyset_R{}^{(1)}$ | Complex first-order time-independent radiation wave potential |
| $\Psi$ | Wake amplification factor |
| $N_i$ | $i-th$ body in the multi-body system |
| $\xi_m^{(1)N_i}$ | First-order complex amplitude of the oscillatory motion of body $N_i$ in $m-th$ mode |
| $\xi_m^{(2)N_i}$ | Second-order complex amplitude of the oscillatory motion of body $N_i$ in $m-th$ mode |
| $\phi_m^{(1)N_i}$ | First-order unit-amplitude radiation potential for body $N_i$ in $m-th$ mode |
| $\phi_m^{(2)N_i}$ | Second-order unit-amplitude radiation potential for body $N_i$ in $m-th$ mode |
| $m, k$ | Modes referred to as surge, sway, heave, roll, pitch, and yaw |
| $\Phi_{ij}^{+}$ | Sum-frequency time-independent velocity potential |
| $\Phi_{ij}^{-}$ | Difference-frequency time-independent velocity potential |
| $\phi_I^{(\pm)}$ | Second-order time-independent incident wave potential |
| $\phi_D^{(\pm)}$ | Second-order time-independent diffraction wave potential |
| $\phi_R^{(\pm)}$ | Second-order time-independent radiation wave potential |
| $\phi_F^{(\pm)}$ | Inhomogeneous terms of second-order free surface condition |
| $\phi_B^{(\pm)}$ | Inhomogeneous terms of second-order boundary condition |

| | |
|---|---|
| $G(\zeta; x)$ | Green function which is referred to as wave source potential |
| $\varepsilon$ | Non-dimensional perturbation parameter |
| $\sigma$ | Source strength |
| $X_p$ | The coordinate of the centre of the $p-th$ panel |
| $\omega$ | Circular frequency of incident wave |
| $\xi$ | Amplitude of motion |
| $\mu$ | Added mass |
| $\lambda$ | Damping coefficient |
| $C$ | Linear restoring coefficient |
| $M$ | Mass |
| $i, j$ | Degree of freedom |
| $\xi(\omega)$ | The frequency-domain motion amplitude |
| $I_{44}, I_{55}, I_{66}$ | Roll, pitch, and yaw moments of inertia |
| $I_{46}$ | Roll-yaw moment of inertia |
| $x_G, y_G, z_G$ | Centre of gravity |
| $\delta_{i3}$ | $(i, 3)$ component of the Kronecker-Delta function |
| $z_B$ | Centre of buoyancy |
| $\varsigma^{(1)}(t)$ | First-order time-dependent surface elevation |
| $\varsigma^{(2)}(t)$ | Second-order time-dependent surface elevation |
| $\eta^{(1)}$ | First-order time-independent surface elevation |
| $\eta^{(2)}$ | Second-order time-independent surface elevation |
| $\bar{\eta}$ | Constant term time-independent surface elevation |
| $F^{(1)}$ | Total first-order force |
| $F^{(2)}$ | Total second-order force |
| $F_I^{(1)}$ | First-order incident wave force (Froude–Krylov force) |
| $F_I^{(2)}$ | Second-order incident wave force |
| $F_D^{(1)}$ | First-order diffraction wave force |
| $F_D^{(2)}$ | Second-order diffraction wave force |
| $F_R^{(1)}$ | First-order radiation wave force |
| $F_R^{(2)}$ | Second-order radiation wave force |
| $F_{HS}^{(1)}$ | First-order hydrostatic force |
| $F_{HS}^{(2)}$ | Second-order hydrostatic force |
| $F_{ex}^{(1)}$ | First-order exciting force |
| $F_{ex}^{(2)}$ | Second-order exciting force |
| $F_q^{(2)}$ | Second-order force caused by quadratic first-order quantities |
| $f_{ji}^{\pm}$ | Quadratic transfer function of second-order exciting force |
| $\eta_{ji}^{\pm}$ | Quadratic transfer function of second-order surface elevation |
| $A_w, A_c$ | Shadow area |
| $V_w$ | Displaced volume of fluid |
| $k(t)$ | Wave radiation retardation kernel |
| $F_{Wind}$ | Wind force on the structure |
| $F_{Current}$ | Current force on the structure |
| $C_W$ | Wind coefficient |
| $C_C$ | Current coefficient |
| $\rho_w$ | Fluid density |

| | |
|---|---|
| $\rho_\alpha$ | Air density |
| $U$ | relative wind speed on the platform |
| $V$ | Current speed |
| $F_M$ | total mooring system force |
| $R^I$ | Inertia force vector of slender system |
| $R^D$ | Damping force vector of slender system |
| $R^S$ | Internal structural reaction force vector of slender system |
| $R^E$ | External force vector of slender system |
| $r, \dot{r}, \ddot{r}$ | Structural displacement, velocity, and acceleration vectors |
| $M^S$ | Structural mass matrix of slender system |
| $M^F(r)$ | Mass matrix accounting for internal fluid flow |
| $M^H(r)$ | Displacement-dependent hydrodynamic mass matrix |
| $C^S(r)$ | Internal structural damping |
| $C^H(r)$ | Hydrodynamic damping matrix |
| $\Delta t$ | Time interval |
| $M_t$ | Tangential mass matrix |
| $C_t$ | Damping matrix |
| $K_t$ | Stiffness matrix |
| $\widehat{K}_t$ | Effective stiffness |
| $\Delta\widehat{R}_t$ | Effective incremental load vector |
| $\gamma, \beta$ | Time integration parameters of Newmark β-family method |
| $x(t)$ | Imposed tangential motion of the upper line end |
| $k_G, k_E$ | Geometric catenary stiffness and the axial line stiffness of the line |
| $C^*$ | Generalised line damping |
| $a$ | Axial induction factor |
| $L$ | Tether chord |
| $K^P$ | Stiffness matrix of the cable in the plane of the cable profile |
| $K_I$ | Stiffness of the tether |
| $\alpha$ | Angle of mooring line attached to fairlead |
| $n$ | Number of mooring lines |
| $T$ | Tension per mooring line |
| $D$ | Fairlead distance to SWL |
| $R$ | Floater radius |
| $K_m$ | Total hydrostatic stiffness matrix |
| $R_C$ | Anchor radius |
| $d_w$ | Water depth |
| $d_u, d_L$ | Depth to attachment points of the fairleads for upper and lower mooring lines |
| $H_s$ | Significant wave height |
| $H_{s,50yr}$ | Significant wave height, 3-h reference period, with a return period of 50 year |
| $H_{s,1yr}$ | Significant wave height, 3-h reference period, with a return period of 1 year |
| $T$ | Wave period |
| $T_P$ | Peak spectral period |
| $T_R$ | Return period |
| $T_s$ | Reference period of duration |
| $U_0$ | 1-hour mean wind speed at 10 m height |
| $U_{10}$ | 10-minute mean wind speed |

| | |
|---|---|
| $U_{10,50yr}$ | Reference 10-min average wind speed with a recurrence period of 50 year |
| $U_{10,1yr}$ | Reference 10-min average wind speed with a recurrence period of 1 year |
| $U_{10,Hub}$ | 10-minute mean wind speed at hub height |
| $U_{tide0}$ | Tidal current at still water level |
| $U_{wind0}$ | Wind-driven current at still water level |
| $V_{in}$ | Cut-in wind speed |
| $V_{out}$ | Cut-out wind speed |
| $V_r$ | Rated wind speed |
| $V_{50yr}$ | Current speed in 50 years |
| $V_{1yr}$ | Current speed in 1 year |
| $\beta$ | Weibull parameters |
| $\gamma$ | Peakedness parameter |
| $T_d$ | Mooring line design tension |
| $\gamma_{mean}, \gamma_{dyn}$ | Load factors |
| $T_{c,mean}$ | Characteristic mean tension |
| $T_{c,dyn}$ | Characteristic dynamic tension |
| $S_C$ | Characteristic capacity of the mooring lines |
| $S_{mbs}$ | Minimum breaking strength |

# List of Abbreviations

| | |
|---|---|
| FOWT | Floating Offshore Wind Turbine |
| LCOE | Levelized Cost of Energy |
| TLB | Tension Leg Buoy |
| ROCs | Renewable Obligation Certificates |
| CfD | Contracts for Difference |
| OEM | Original Equipment Manufacturers |
| TLP | Tension Leg Platform |
| TRL | Technology Readiness Level |
| HMPE | High Modulus Polyethylene Fibre |
| MBL | Minimum breaking load |
| CAPEX | Capital Expenditure |
| SIMO | Simulation of Marine Operations |
| BEM | Beam Element Method |
| WADAM | Wave Analysis by Diffraction and Morison Theory |
| RAO | Response Amplitude Operator |
| FEM | Finite Element Method |
| NTM | Normal Turbulence Model |
| EWM | Extreme Wind Model |
| B.C. | Boundary Condition |
| DOF | Degree of Freedom |
| WL | Waterline |
| PC | Partition Circle |
| QTF | Quadratic Transfer Function |
| GM | Metacentric Height |
| FFT | Fast Fourier Transform |
| WTG | Wind Turbine Generators |
| ULS | Ultimate Limit State |
| ALS | Accidental Limit State |
| SWR | Steel Wire Rope |
| UX, UY, UZ | Translational Responses |
| ROTX, ROTY, ROTZ | Rotational Response |
| SWL | Still Water Level |
| VIV | Vortex Induced Vibration |
| M | Mooring Line |
| d | Depth |
| D | Draft |
| DLCs | Design Load Cases |
| NSS | Normal Sea State |
| ESS | Extreme Sea State |
| SSS | Severe Sea State |
| RWM | Random Wave Model |
| MBL | Minimum Breaking Load |

# Table of Contents

# Table of Figures

# Table of Tables

# 1. Introduction

## 1.1. Background

The shift away from fossil fuels and towards cleaner, renewable energy sources is driven by growing concerns about climate change. Governmental entities are providing financial aid to support the reduction of emissions in accordance with mandatory targets outlined in both domestic and international agreements. Renewable energy resources are significantly contributing to the ongoing decline in carbon emissions within the global energy sector, with offshore wind technology emerging as a prominent means to achieve this goal [1-3].

Offshore wind energy offers several notable advantages compared to other wind energy sources. Firstly, offshore locations typically experience consistently higher and more reliable wind speeds, with the potential to be up to 90% greater than those observed on land [4]. Additionally, producing offshore wind turbines near the coast can address logistical challenges related to road or rail limitations [5]. Moreover, placing turbines further from the shore can help minimize concerns regarding visual and noise pollution [6]. Furthermore, installing turbines further from shore avoids issues of visual and noise annoyances [7]. Lastly, expansive unobstructed ocean areas offer numerous opportunities for potential utilization, considering maritime transportation routes and fishing zones [8].

## 1.2. Fixed Offshore Wind Turbine

The offshore power generation sector originated in the shallow waters of the North Sea due to the abundance of suitable sites and superior wind resources compared to onshore locations in Europe. In Europe, more than a thousand offshore wind turbines have been connected to the power grid, collectively providing a capacity of 3,294 MW across 49 wind farms in nine countries [1]. The United Kingdom, Denmark, the Netherlands, and Belgium are the leading European nations in terms of offshore installed capacity. Additionally, Japan, China, and the United States have also made substantial investments in wind energy [9]. Fig. 1-1 illustrates various types of marine foundations used for offshore wind turbines installed in shallow waters [9].

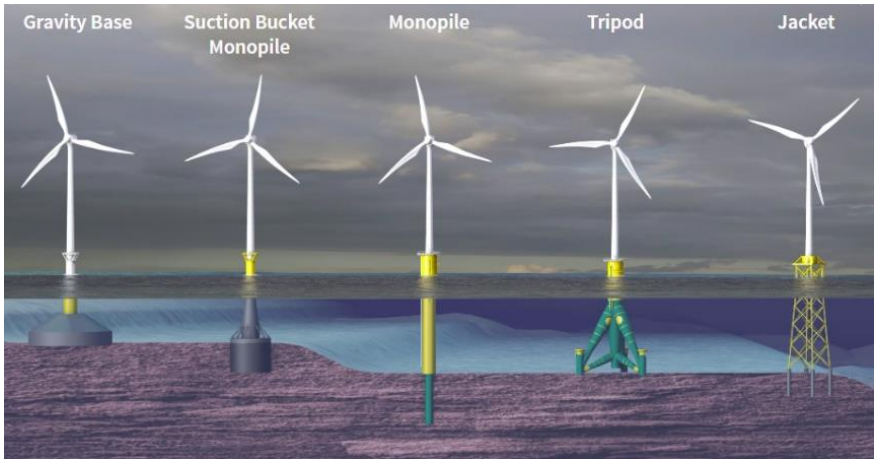


**Fig. 1-1** Different Bottom-Fixed Foundation Types for Offshore Wind Turbines (Source: ACTEON)

In water depths ranging from 10 m to less than 60 m, the most commonly utilized marine foundations consist of gravity-based foundations, monopiles, tripods, and jackets. Offshore wind power projects have gained significant traction, particularly in Europe, due to advancements in technology. Europe has been a frontrunner in offshore wind power technology and played a key role in commercializing offshore wind technologies through the installation of offshore wind turbines on fixed-bottom substructures. These turbines have predominantly been deployed in water shallower than 20 m by either driving monopiles into the seabed or utilizing traditional concrete gravity bases. It is estimated that Europe could potentially generate up to 3400 TWh of offshore wind energy within its waters by 2030 [10].

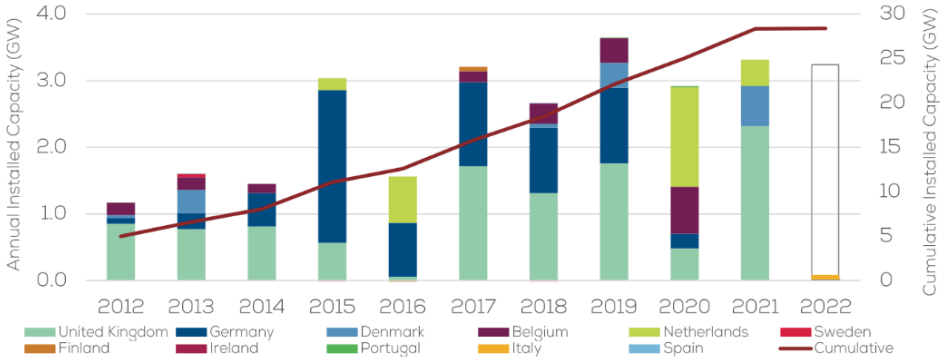


**Fig. 1-2** Cumulative and Annual Offshore Wind Installations 2012-2022 [13]

Fig. 1-2 illustrated a significant increase in the establishment of offshore wind farms in Europe from 2012 to 2019. Initially, the UK led in annual installed capacity until Germany began to increase its capacity. However, the UK regained its lead from 2017

to 2019 and held the largest share of total installed capacity from 2010 to 2020. Germany also demonstrated sustained deployment from 2010 to 2020 but did not add any capacity in 2020, resulting in the UK reclaimed the lead in capacity by 2021 [10]. There is ongoing progress with plans for the extensive deployment of offshore wind farms. Historically, offshore wind farms were typically established near the shore in shallow waters using onshore wind technology. However, exceptions have been observed, such as the installation of the Beatrice wind farm at a water depth of 46 m using jacket substructures, and the use of jacket and tripod foundations for the Alpha Ventus wind farm off the coast of Germany [11]. Currently, the majority of offshore wind projects are situated in waters of moderate depth. However, it is anticipated that future projects will transition towards employing floating foundations for wind turbines in deeper waters. This shift is driven by the industry's rapid expansion in recent decades and influenced by social and economic factors such as noise and visual pollution [1, 12, 13].

As the installed capacity increases and shallow water sites near the U.K. and Europe become depleted, future projects will need to be located farther from the shore and in deeper waters, posing greater technical and economic challenges. Presently, most offshore wind turbines are fixed to the seabed using monopiles or jacket foundations, which limits deployment to specific water depths [14-16]. Approximately 80% of offshore wind resources are believed to be situated at depths of 60 meters or more, where traditional bottom-fixed offshore wind installations are not financially viable [17]. As the distance from the shore increases, the water depth rises rapidly, and the cost of conventional gravity-based or jacket-type foundations also escalates steeply with the water depth. FOWTs [18] are a cost-effective option for offshore wind farms in water depths exceeding 60 m [19]. Accordingly, the offshore wind energy industry must address the challenge of developing affordable support systems for a broader range of installation locations. Consequently, there has been a gradual shift in the design and construction of wind farms situated in more remote offshore areas and deeper waters. The use of floating platforms for wind turbines could be the most economical approach for placing turbines in deeper waters, away from populated areas.

## 1.3. Floating Offshore Wind Turbine

The utilization of floating platforms for wind turbines presents an innovative approach to address the depth limitations in the wind energy sector. Although the concept of large-scale floating offshore wind turbines was initially proposed by Professor William E. Heronemus at the University of Massachusetts in 1972, it was not until the mid-1990s that the commercial wind industry gained momentum and researchers began to reconsider the idea [20]. However, the development of floating offshore wind systems is still in its nascent stages due to the intricate relationships and complexities involved in wind turbines and their floating foundations.

In recent years, the technology for FOWT has progressed sufficiently to overcome the technical barriers in establishing a commercial system [21-23]. While the long-term durability of floating structures has been demonstrated over many years, the economic feasibility of deploying floating wind turbine platforms has not been proven to the extent observed in the offshore oil and gas industry [16]. Although the technical challenges in the oil and gas sector have been effectively addressed, the economic viability of implementing these solutions is not be practical for deploying floating wind turbines in a competitive wind energy market [19]. Different types of floating wind turbines are categorized based on the type of floating support structure they utilize to support the wind turbine. There are four primary concepts for floating foundations: Spar-Buoy, Semi-Submersible, barge, and TLP (refer to Fig. 1-3).

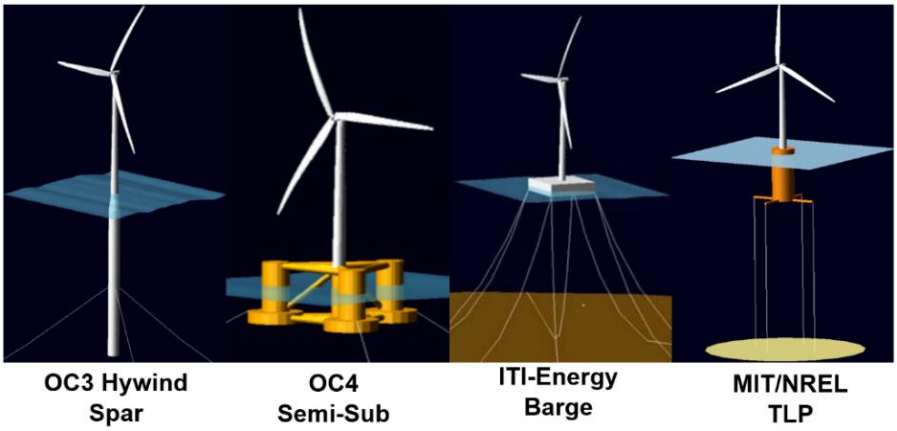


**Fig. 1-3** The FOWT Models Created by the National Renewable Energy Laboratory (NREL) for Compatibility with the 5-MW Reference Wind Turbine [24]

A Spar platform is a cylindrical structure with a small underwater surface area that uses ballast to keep its centre of gravity below the centre of buoyancy. It is primarily held in place by catenary mooring lines with drag or suction anchors. Spar platforms are known for their reduced wave-induced movements, simple design, and lower mooring installation costs. However, they require heavy-lift vessels for offshore operations and can only be deployed in relatively sheltered deep water. Spar platforms also require deeper water compared to other designs, usually exceeding 100 meters [25-28]. The first demonstration of a Spar wind turbine was in Norway in 2009 with a 2.3 MW Hywind, and a 5 MW version was installed in Scotland in 2017 [22]. Additionally, a floating wind farm with a 30 MW power generation capacity at a water depth of over 100 meters was operational [29]. Following the Statoil (Hywind) demonstration in Norway in 2013, Japan Marine United demonstrated an advanced (hybrid) 2 MW Spar, supporting floating substations [30], and later installed a 5 MW capacity Spar in 2016. Other examples of Spar-type FOWT include SeaTwirl [31, 32], which supports vertical wind turbines, and Windcrete [33], a concrete support platform that eliminates the need for costly maintenance and repair operations (low OPEX). The differences of these spar platform designs are related to the wind turbine capacity, water depth, and environmental factors present at the installation locations.

Although Hywind is capable of operating in deep waters, it encounters difficulties such as complex maintenance procedures due to its dynamic nature and exposure to harsh marine environments, higher initial investment costs compared to traditional offshore wind farms, and the need for further advancements and operational experience to thoroughly assess its long-term performance and reliability [34]. SeaTwirl offers several benefits, such as potential simplicity, reliability, and decreased maintenance needs in comparison to conventional horizontal-axis turbines. It also provides improved stability in diverse wind and wave conditions and the potential to create new prospects for offshore wind energy production in specific environmental or logistical limitations [31, 32]. However, the Fukushima Spar also presents several challenges, including technical obstacles related to stability, mooring systems, and dynamic response in diverse environmental conditions. Additionally, its construction and deployment costs are higher compared to other floating or fixed-bottom foundation options [35, 36]. Despite the inherent strength and durability advantages of precast concrete structures, as well as the potential cost savings and environmental

compatibility associated with Windcrete [33], there are several challenges that must be addressed. These include the higher weight of Windcrete compared to alternative materials used in floating foundations, potential barriers to adoption related to market acceptance, regulatory compliance, and industry standards, and the necessity to optimize concrete mix designs for marine environments while simultaneously balancing structural requirements with material efficiency [37].

Semi-Submersible support platforms are constructed using multiple large columns connected by bracings and submerged pontoons, resulting in an increased water plane area compared to Spar platforms. The columns provide hydrostatic stability, while the pontoons offer additional buoyancy. These platforms are typically positioned using catenary or taut spread mooring lines and drag anchors [34]. Fully equipped platforms, including turbines, can be transported with drafts of less than 10 m using conventional tugs. They can operate at water depths of around 40 m but are prone to experiencing higher critical wave-induced motions. These platforms are generally larger and more complex to fabricate compared to other concepts, such as Spar buoys [28, 38, 39]. Examples of this design include the Principle Power (WindFloat) demonstrated in Portugal in 2011 (2 MW) [40] and the Fukushima FORWARD demonstrated in Japan in 2013 (2 MW) [23] and 2015 (7 MW) [41]. The 50 MW Kincardine offshore wind farm in Scotland, operational since October 2021, also utilizes this design [42]. Additionally, the Hexicon 5MW supports two 5MW wind turbines [43], and the Pentland Floating Offshore Wind Farm (PFOWF) considers two characteristic design options: Semi-Submersible and Tension Leg Platform (TLP) [44].

A TLP is a buoyant floating platform with a central column and arms connected to tensioned tendons [45]. These tendons are typically linked to suction pile anchors to secure the platform. TLPs are typically lightweight and exhibit reduced wave-induced motion. They can be utilized at depths of 50 to 60 m, subject to metocean conditions [14, 28]. Compared to other platforms, TLPs may face challenges in maintaining stability during transport and installation, potentially requiring a specialized vessel. There are uncertainties regarding the impact of high-frequency dynamic effects on the turbine when utilizing this support platform design. Additionally, the mooring cost for TLP installation is higher than that of catenary mooring line installation due to the complexity of pre-tensioning the tendons [19, 46]. GICON was the first commercial operator of TLP floating wind technology, demonstrated in Germany in 2016, with a

capacity of 2.3 MW [47]. Another example is PelaStar (capacity 6 MW), developed by Glosten Associates, which involves designing and developing advanced controls for a 12 MW floating wind turbine in 2019 [48].

The floating wind turbine with a barge design features a large pontoon structure and utilizes distributed buoyancy to maintain stability by leveraging the weighted water plane area for the righting moment. Mooring for this type of wind turbine is often carried out using traditional catenary anchor chains [49]. The IDEOL floater concept was created with a ring-shaped surface floater that has a shallow draft and compact dimensions [25, 50]. The four primary principles for floating foundations exhibit different dynamic properties, each with its own pros and cons in terms of performance, cost, and system complexity [19, 51-55], as outlined in Table 2-4.

By the end of 2019, a combined capacity of 73 MW utilizing FOWTs had been installed in Asian and European countries. It was projected to rise to 127.9 MW by 2022 (refer to Fig. 1-4) Nevertheless, the Covid-19 pandemic has caused delays in projects throughout the supply chain and at the installation sites, leading to the postponement of most projects until mid-2021 and early 2022 [56].

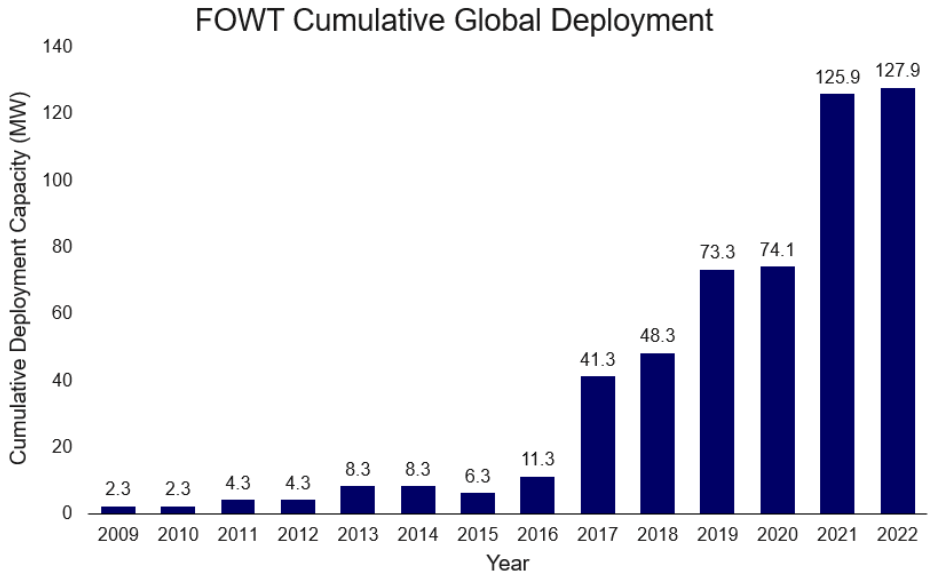


**Fig. 1-4** Cumulative Global FOWT Development (2009-2022) [56]

**Table 1-1** Globally Floating Wind Projects [46]

| Year | Region | Project | Total Capacity (MW) | Turbine Rating (MW) | Concept |
|---|---|---|---|---|---|
| **2009** | Norway | Hywind I | 2.3 | 2.3 | Hywind |
| **2011** | Portugal | WindFloat I | 2 | 2 | WindFloat |
| **2013** | Japan | Kabashima | 2 | 2 | Hybrid Spar |
| **2013** | Japan | Fukushima FORWARD | 2 | 2 | Semi-Sub |
| **2015** | Japan | Fukushima FORWARD | 7 | 7 | Semi-Sub |
| **2016** | Japan | Fukushima FORWARD | 5 | 5 | Advanced Spar |
| **2016** | Japan | Sakiyama | 2 | 2 | Hybrid Spar |
| **2017** | UK | Hywind Pilot Park | 30 | 6 | Hywind |
| **2018** | France | FloatGen | 2 | 2 | Damping Pool |
| **2018** | Japan | IDEOL Kitakyushu | 3 | 3 | Damping Pool |
| **2018** | UK | Kincardine Phase I | 2 | 2 | WindFloat |
| **2019** | Portugal | WindFloat Atlantic II | 25 | 8.3 | WindFloat |
| **2020** | S Korea | Ulsan Demo | 0.75 | 0.75 | Semi-Sub |
| **2021** | Norway | Tetra Spar | 3.6 | 3.6 | Tetra Spar |
| **2021** | Spain | PivotBuoy | 0.22 | 0.22 | Pivot Buoy |
| **2021** | UK | Kincardine Phase II | 48MW | 9.5 | WindFloat |
| **2022** | Spain | SATH | 2MW | 2 | TBC |

Table 1-1 presents a variety of prototype examples that demonstrate the efficacy of FOWT technology in demanding environmental circumstances. Notable technological developments in this field include the WindFloat [57] and Hywind [22] floating offshore wind platforms. Of particular significance is the Hywind Scotland project, which marked the inauguration of the first commercial floating offshore wind farm in October 2017, boasting a capacity of 30 MW (refer to Fig. 1-5) [22, 29, 58].

**Fig. 1-5** Hywind Scotland floating wind farm. (Photo: Øyvind Gravås / Woldcam-Statoil ASA) [29]

The WindFloat Atlantic II initiative, with a capacity of 25 MW capacity, is situated off the coast of Portugal and represents as the second pilot project installed in 2020. It features a distinct floating platform design and incorporates the V164-8.4 MW wind turbine in a floating wind project (refer to Fig. 1-6) [57].

**Fig. 1-6** WindFloat Atlantic II Project (Source: Windplus) [59]

Currently, both platforms are in operation along the eastern coast of Scotland. These platforms have been constructed based on established principles from the oil and gas sector, albeit with modifications in terms of size and system components to accommodate a wind turbine tower and generator assembly. The successful execution of numerous floating wind projects, as detailed in Table 1-1, serves to enhance confidence in these emerging technologies. Consequently, there are additional projects in the pipeline, with a majority of these initiatives concentrated in Europe, alongside several projects in the United States and Japan (refer to Table 1-2). It is anticipated that this trend will lead to an increase in the installed FOWT power generation capacity to a range of 200 to 260 MW by the year 2023 [60].

**Table 1-2** Upcoming FOWT Projects [60]

| Year | Region | Total Capacity (MW) | Turbine Rating (MW) | Concept |
|---|---|---|---|---|
| **2022** | Japan | 22 | 2-5 | Hybrid Spar |
| **2022** | Norway | 88 | 8 | Hywind |
| **2022** | Ireland | 6 | 6 | Hexafloat |
| **2022** | Spain | 8 | 8 | P37 Hybrid |
| **2023** | France | 28.5 | 9.5 | Sea Reed |
| **2023** | France | 30 | 10 | WindFloat |
| **2023** | France | 30 | 10 | Damping Pool |
| **2023** | France | 25.2 | 8.4 | TLP |
| **2023** | USA | 12 | 6 | VolturnUS-S SemiSubmersible |

While Semi-Submersible, Spar, and TLP concepts have been extensively researched in both academic and industrial contexts, there is currently no economically viable platform that is universally considered optimal. A comparison of the primary technology types for floating offshore wind power shows that the current LCOE values are greatly influenced by the design of the support structure, mooring lines, water depth, and distance from shore [61].

The design of offshore wind turbine structures is complex due to the numerous and intricate design parameters, as well as the diverse operational requirements and environmental conditions [19, 62, 63]. These challenges must be addressed to achieve optimized parameters for offshore wind turbine structures, balancing energy generation performance and the lifespan of the floating wind turbine [64]. A comprehensive examination of the challenges of FOWT can be found in the literature review section.

# 2. Literature of Review

## 2.1. Floating Offshore Wind Turbine Market

Roughly 80% of offshore wind resources are situated at water depths exceeding 60 m, necessitating the use of FOWT in these locations as are too deep for current bottom-fixed offshore wind technology [46, 65]. FOWT will facilitate access to sites further from the shore, which are not visible and have more favourable wind conditions. The United Kingdom has been a frontrunner in Europe for installing floating offshore wind power [66]. A recent report from the World Forum Offshore Wind (WFO) [67], disclosed that in 2022, a global offshore wind capacity of 9.4 GW was installed, with China alone contributing 6.8 GW. Last year, 42 new offshore wind farms became operational, with 29 of them being installed in China [68].

Fig. 2-1 illustrates that the deployment of FOWT is expected to increase with upcoming projects in the forthcoming years. It is projected that Asia will emerge as the primary global hub for FOWT installation over the next 30 years, with a combined capacity of over 100 GW by 2030 and 600 GW by 2050 [69].


**Fig. 2-1** Installed Capacities (GW) of FOWT Prediction for 2050 [69]

In spite of the effects of the COVID-19 pandemic, the global offshore wind capacity expanded by 5.2 GW in 2020, resulting in a cumulative capacity of 32.5 GW [70]. This study investigated a comparative perspective on the FOWT markets in Europe, Asia, and the United States.

### 2.1.1. European Market Overview

The advancement of FOWT offers a significant industrial opportunity for both domestic and international markets. Progress has been made in harnessing the country's full potential for floating offshore wind resources, especially in regions with water depths exceeding 60 m [15]. It is estimated that approximately 80% of global wind energy resources are situated in offshore areas with water depths of 60 m or more [71, 72]. The UK has substantial potential for electricity generation from FOWT due to the abundant wind resources in the region with more than half of the North Sea offers water depths ranging from 50 meters to 220 meters, making it suitable for the deployment of FOWTs [61]. Projections suggest that developments in offshore wind energy up to 2030 will primarily concentrate on the North Sea and Baltic Sea, with an increase in average water depth and distance to shore for offshore wind farms [73, 74]. Scotland has emerged as a global leader in floating offshore wind technology, boasting the world's first commercial floating offshore wind farm and the ongoing construction of the Kincardine wind farm. The Scottish Government has also invested in establishing the DeepWind supply chain cluster to bolster the industry [75]. The UK government is investing £17.5 million floating offshore wind demonstration program to support the deployment of floating wind innovations by 2030 [76]. The UK government aims to achieve a 5GW power generation capacity from FOWTs by 2030, while the French and Italian FOWT industries have set targets of 3GW and 5GW for 2030 and 2040, respectively [77, 78].

Fig. 2-2 illustrates the deployment projects for floating offshore wind turbines in European countries. The UK aims to achieve a power generation capacity of 5GW from FOWTs by 2030, while the French and Italian FOWT industries have set targets of 3GW by 2030 and 5GW by 2040, respectively [56].

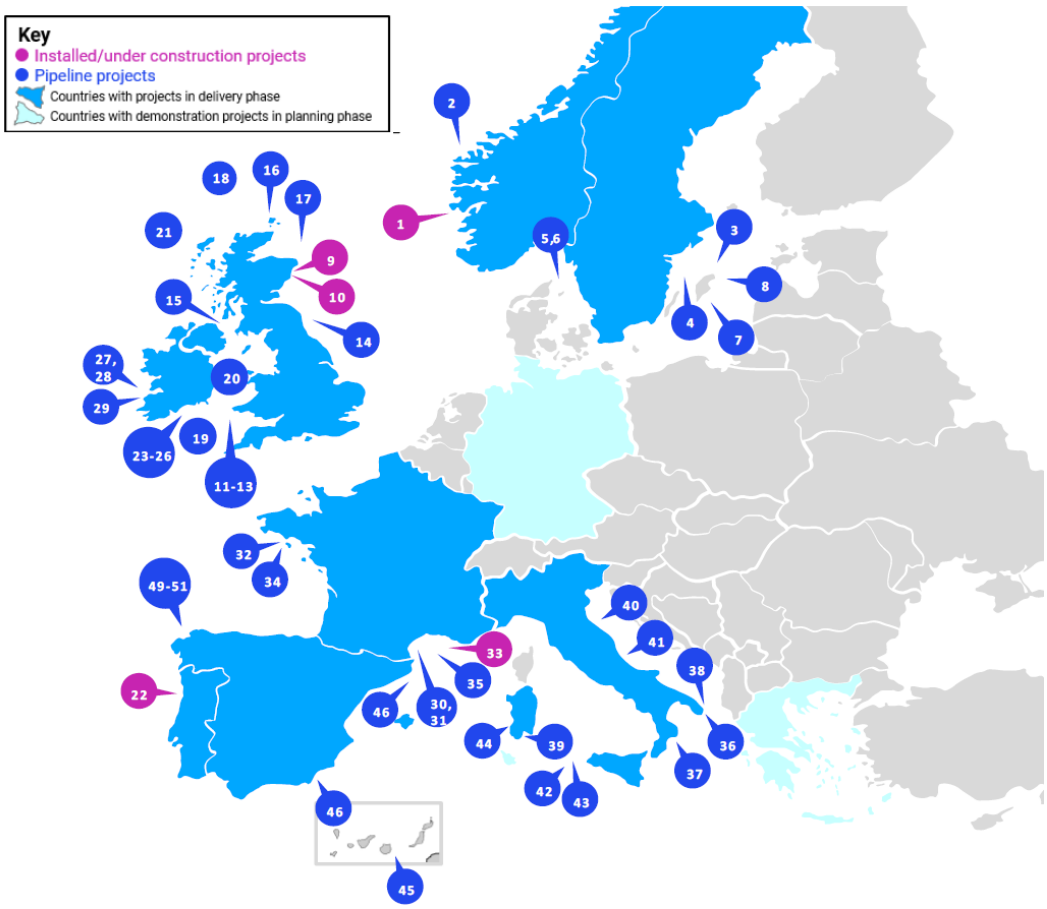


| Project | MW |
|---|---|
| **Norway** | |
| 1. Hywind Tampen | 88 |
| 2. Frøyabanken | 500-1500 |
| **Sweden** | |
| 3. Dyning | 2000 |
| 4. Kultje | 2150 |
| 5. Mareld | 2300 |
| 6. Poseidon Nord | 1000 |
| 7. Skidbladner | 2000 |
| 8. Herkules | 2750 |
| **United Kingdom – floating target 5 GW by 2030 *** | |
| 9. Hywind pilot park | 30 |
| 10. Kincardine | 50 |
| 11. Erebus (commercial) | 600 |
| 12. Petroc | 300 |
| 13. Celtic Deep | 398 |
| 14. Blyth | 58.4 |
| 15. North Channel Wind | 400 |
| 16. Dolphyn project | 2000 |
| 17. Green Volt | 480 |
| 18. Cerulean North Sea | 3000 |
| 19. Crown Estate Test & Demonstration | 400 |
| 20. Celtic Sea Floating | 4000 |
| 21. Scotwind | 15,000 |
| **Portugal** | |
| 22. WindFloat Atlantic | 25 |

| Project | MW |
|---|---|
| **Ireland** | |
| 23. Emerald | 1300 |
| 24. Inis Ealga | 1000 |
| 25. Blackwater | 1500 |
| 26. SSE Celtic Sea | 800 |
| 27. Clarus | 1000 |
| 28. Western Star | 1350 |
| 29. Moneypoint | 1000-1500 |
| **France – floating target 3 GW by 2030 **** | |
| 30. EOLMed | 30 |
| 31. Gulf du Lion | 30 |
| 32. Groix & Belleîle | 28.5 |
| 33. Provence Grand Large | 25.2 |
| 34. Triskéol | 250 |
| 35. Méditerranée I-IV | 1500 |
| **Italy – floating target 5 GW by 2040 **** | |
| 36. Odra Energia | 1500 |
| 37. Minervia Energia | 675 |
| 38. KailiaEnergia | 1200 |
| 39. Nora Energia | 1395 |
| 40. Marche | 840 |
| 41. Abruzzi | 1760 |
| 42. MedWind | 2800 |
| 43. Marsala | 750 |
| 44. Sardegna Sud Occidentale | 504 |

| Project | MW |
|---|---|
| **Spain – floating target of 1-3 GW by 2030 *** | |
| 45. Canarray I & II | 180 |
| 46. Mar de Agata | 300 |
| 47. Parque Tramuntana I | 500 |
| 49. Parque Nordes I | 525 |
| 50. San Brandan | 490 |
| 51. San Cibrao | 490 |

* target government set
** target set by industry

**Fig. 2-2** Map of European FOWTs Deployment (Data source: 4COffshore)

## 2.1.2. Asian Market Overview

The Asia region is anticipated to emerge as the predominant market for floating offshore wind technology in the future due to its deep waters, abundant wind resources, extensive coastline, and significant energy demand from coastal urban centres. The region's proven ability to enhance and reduce the costs of current technologies increases its economic appeal. Consequently, innovation will play a pivotal role in the widespread adoption of floating wind technology in this market, as evidenced by the planning of numerous demonstration projects. This trend has positioned China as the global frontrunner in offshore wind power installation (refer to Fig. 2-3) [2, 56].

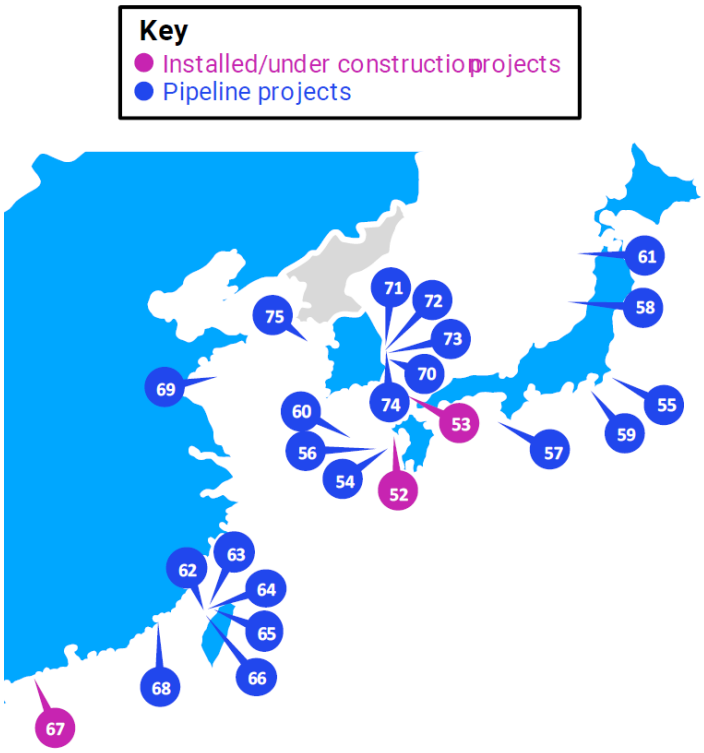


| Project | MW |
|---|---|
| Japan | |
| 52. Sakiyama | 2 |
| 53. IDEOL Kitakyshu demo | 3 |
| 54. Goto City | 17 |
| 55. Sakura | 520 |
| 56. Kyushu | 1000 |
| 57. Kishuu | 450 |
| 58. Toki I & II | 1100 |
| 59. Progression Energy Floating | 800 |
| 60. Goto Sakiyama Oki Oki | 500 |
| 61. Seihoku-ouki | 600 |
| Taiwan | |
| 62. Eolfi Taiwan | 500-2000 |
| 63. Chu Tin I & II | 1300 |
| 64. Huan Ya | 1400 |
| 65. Laifeng | 950 |
| 66. Hai Shuo | 1350 |
| China | |
| 67. CTGNE Yangjiang Shapa | 5.5 |
| 68. Longyuan Nanri Island | 4 |
| 69. Qingdao | 2000 |
| South Korea | |
| 70. Ulsan Prototype | 5 |
| 71. Donghae Sites | 500-4500 |
| 72. Firefly | 804 |
| 73. Munmu Baram | 420-1500 |
| 74. Ulsan Floating | 1000-2500 |
| 75. Incheon | 1600 |

**Fig. 2-3** Map of Asian FOWTs Deployment (Data source: 4COffshore)

In 2011, Japan launched the first floating offshore wind demonstrator in Asia as part of the Fukushima FORWARD project. Subsequently, additional floating turbine demonstrators were established in Goto Island and Kitakyushu [23]. In 2018, the Japanese government enacted legislation to develop offshore wind in deeper waters,

including areas outside ports and harbours [39], which has opened up opportunities for Floating Offshore Wind Turbine (FOWT) technology and could strengthen Japan's position as a market leader in Asia. South Korea has set a goal of 12GW of offshore wind power by 2030, emphasizing the significance of floating wind technology in its offshore wind market [13]. In May 2021, the Korean Development Institute approved the 200MW Donghae 1 floating wind farm following a feasibility study, marking South Korea's first floating wind farm (see 27 in Fig. 2-3) [79]. President Moon Jae-in also announced plans for a 6GW floating complex offshore from Ulsan, at the same site as the Donghae 1 gas field, which is set to cease production in 2022 [56]. Vietnam has significant potential for offshore wind power, with floating wind turbines being well-suited due to water depths ranging from about 60 to 500 meters and distances from the land of up to 100 kilometres [80].

### 2.1.3. US Market Overview

The United States has historically underappreciated the potential of offshore wind energy, largely due to the abundance of onshore wind resources. However, challenges in transmitting electricity to major load centres have posed limitations on the integration of land-based turbines into the grid. Consequently, the reduced transmission constraints, more reliable and potent winds, and successful European advancements have heightened the attractiveness of offshore wind energy for the United States [81].

As indicated in Fig. 2-4, there is a notable focus on floating offshore wind in specific regions, particularly the West Coast, where the seabed is deeper. The U.S. government has committed to accelerating the development and deployment of offshore wind in areas off the northern and central coasts of California, necessitating the utilization of floating turbine technology due to the deep waters near the Pacific coast [13, 56].

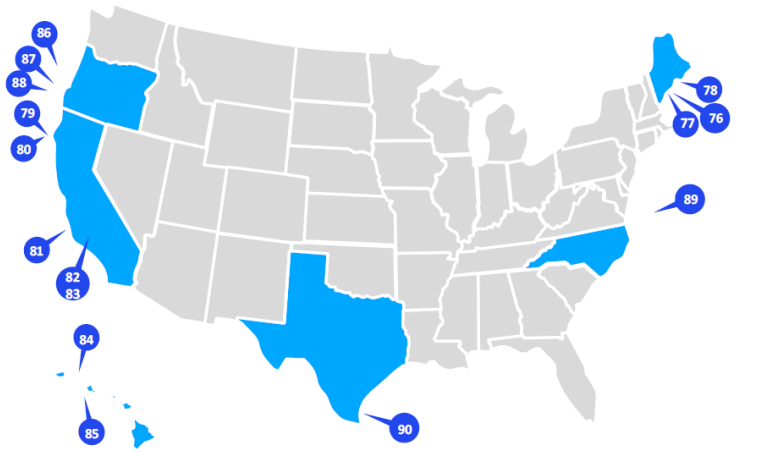


| Project | MW |
|---|---|
| Maine | |
| 76. Aqua Ventus I | 12 |
| 77. Maine Research Array | 144 |
| 78. Future Floating * | 450 - 1500 |
| California | |
| 79. Redwood | 150 |
| 80. Humboldt WEA * | 1600 |
| 81. Morro Bay * | 700-1000 |
| 82. Lompoc/CADEMO | 60 |
| 83. Castle Wind * | 1000 |
| Hawaii | |
| 84. Oahu Northwest * | 400 |
| 85. Oahu South * | 400 |
| Oregon | |
| 86. Coos Bay * | 10,000 |
| 87. Bandon * | 2,800 |
| 88. Brookings * | 3,400 |
| North Carolina | |
| 89. Central Atlantic E * | 1000 |
| Texas | |
| 90. Gulf of Mexico * | 2000 |

** = call areas*

**Fig. 2-4** Map of US FOWTs Deployment (Data source: 4COffshore)

The United States has set a challenging goal of establishing 15 GW of floating wind capacity by 2035 and intends to allocate substantial financial resources toward the development of FOWT projects. Nevertheless, it is imperative to confront substantial market obstacles, including elevated expenses, risks, limitations in transmission and supply chain infrastructure, and the engagement of stakeholders, in order to influence the trajectory of the floating wind market [82].

### 2.1.4. Market Growth to 2040

The Carbon Trust has projected a potential floating wind capacity of 10.7 GW by 2030 and 70 GW by 2040 [2]. The anticipated growth of FOWT in Asia, Europe, and North America is depicted in Fig. 2-5. However, the 2030 forecast has been revised due to a significant development in 2029 [2]. It is expected that the build-out rate will surpass 3 GW per year starting in 2030, with an anticipated increase to over 12 GW in 2031 [56]. Table 2-1 presents the installed capacity of FOWT and the projected deployment from 2025 to 2040 in Europe, Asia, and the US. In 2020, the UK had 85% more installed capacity than all of Asia. Deployment in Europe was sluggish in 2020, with 255 MW, while Asia only reached 25 MW. This slow progress may be attributed to the impact of Covid-19, causing delays in projects throughout the supply chain and on-site [70]. However, with substantial policy support and technology commercialization, Asia is projected to deploy 14% more power generation capacity than Europe by 2025, and 19% more by 2040. In contrast, the US lags significantly behind Europe and Asia in installed capacity, with expected projects to be installed in 2022 [83].

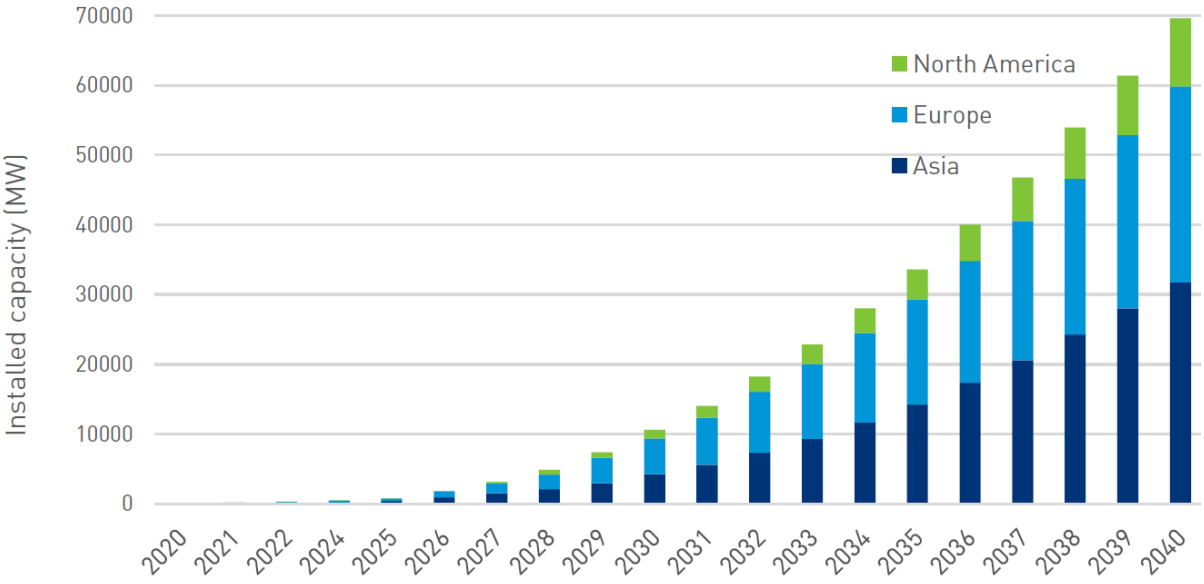


**Fig. 2-5** Global FOWT Deployment Prediction for 2040 (Source: Carbon Trust, Phase II Summary report [8])

**Table 2-1** Industry Deployment Ambitions Until 2040 (Source: Carbon Trust, Phase II Summary report [8])

| Region | Country | Installed (MW) | Expected (MW) | Estimated Deployment (MW) | | | |
|---|---|---|---|---|---|---|---|
| | | 2020 | 2022 | 2025 | 2030 | 2035 | 2040 |
| Europe | UK | 80 | 80 | 142 | 1100 | 3800 | 7400 |
| | France | 2 | 116 | 116 | 1550 | 5100 | 8900 |
| | Other Europe | 31 | 125 | 160 | 2450 | 6200 | 11900 |
| | Europe (slow) | - | 255 | 296 | 2300 | 6300 | 11000 |
| | Europe (expected) | 113 | 320 | 420 | 5100 | 15100 | 28200 |
| | Europe (accelerated) | - | 355 | 449 | 5950 | 21900 | 45600 |
| Aisa | Japan | 12 | 30 | 80 | 930 | 4200 | 11000 |
| | China | 0 | 0 | 20 | 495 | 2500 | 7000 |
| | South Korea | 0 | 3 | 320 | 1600 | 5000 | 10000 |
| | Asia (slow) | - | 25 | 210 | 1800 | 5900 | 12900 |
| | Asia (expected) | 12 | 33 | 420 | 4300 | 14300 | 31800 |
| | Asia (accelerated) | - | 40 | 520 | 5300 | 21200 | 56200 |
| US | US (slow) | - | 0 | 0 | 370 | 1500 | 3700 |
| | US (expected) | 0 | 12 | 12 | 1270 | 4300 | 9800 |
| | US (accelerated) | - | 12 | 12 | 1800 | 6600 | 17500 |

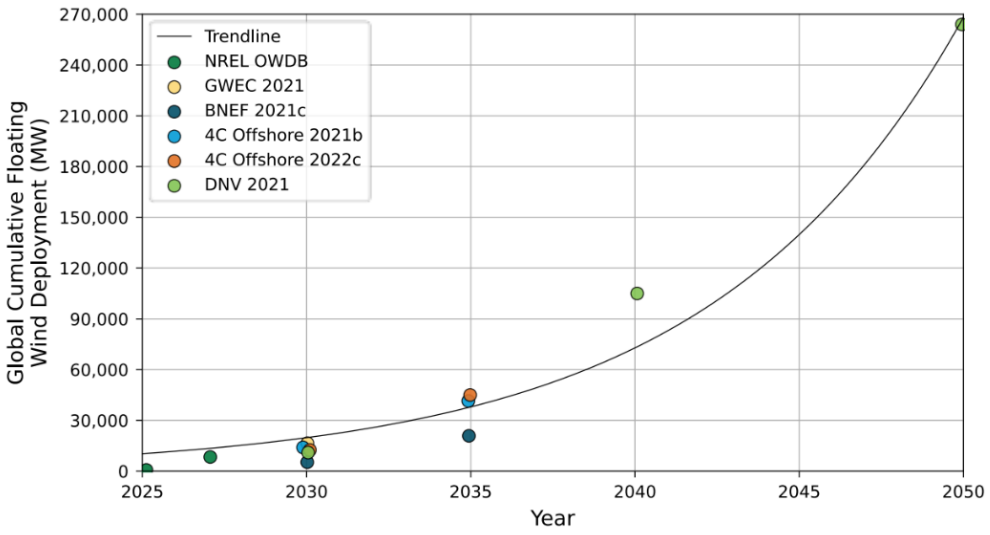


**Fig. 2-6** Long-term Cumulative Floating Offshore Wind Deployment Projections [84]

The United Kingdom has played a pivotal role in supporting the initial development of floating wind technology, with the Energy Technologies Institute securing £25 million

in funding for an offshore wind floating system demonstrator from both public and private sources [1]. While there is a recognized potential demand for floating offshore wind technology in the market, the transition from pilot projects to large-scale commercial developments necessitates a supportive policy and regulatory framework.

Projections depicted in Fig. 2-6 indicate a substantial increase in floating offshore wind deployment from 2025 to 2050, with forecasts ranging from approximately 10 GW by 2030 to as much as 264 GW by 2050, as reported by various groups [3]. The trendline indicates an exponential growth trajectory for the global cumulative deployment of floating wind by 2050. This growth is anticipated to be driven by factors such as declining costs, industry commercialization, supply chain maturity, scarcity of shallow, fixed-bottom sites, technical innovation specific to floating wind, and interest from new markets [85].

### 2.1.5. Overview of Key UK Market

Since 2018, Scotland has implemented policy measures to support the development of FOWT technology through the Renewable Obligation Certificates (ROCs) program, with the aim of promoting the advancement of floating offshore wind devices and innovative turbines [86, 87]. It is projected that the United Kingdom will represent nearly half of the worldwide installed capacity by 2020, with 108 MW in the development phase, all of which is situated in Scotland. The future development beyond 2018 is contingent upon the success of initial demonstrations and political considerations [1, 76, 88, 89]. In 2019, there was a total of 268 MW in the development phase for floating wind projects that have at least applied for consent. An additional 24 projects are in the early stages of planning (i.e., have not applied for consent) and could potentially deliver an additional 5.9 GW of installed capacity, possibly before 2030 [76]. It is estimated that by 2030, the global capacity of floating wind could reach as high as 4.3 GW [89]. Subsequently, the UK government introduced Contracts for Difference (CfDs) for floating wind as the primary mechanism for supporting low-carbon electricity generation, resulting in significant cost reductions in the offshore wind sector [13, 90]. The announcement of new leasing for FOWTs by Crown Estate Scotland has attracted interest and investment from developers. According to Simon Hodge, Chief Executive of Crown Estate Scotland, the new leasing represents a

significant investment in the Scottish economy, with approximately £700 million going into public finances and billions of pounds in supply chain commitments. This indicates significant progress in the offshore wind sector and suggests that Scotland is positioned to become a major hub for the further development of this technology in the future [91]. However, the scale of the project and visibility of a route to the market are crucial for the development of these opportunities [92]. The Carbon Trust's market outlook assumes that floating wind will be considered in future CfD rounds, providing a route to market for future commercial projects [13].

The summary report of The Carbon Trust's Floating Wind Joint Industry Project Phase I [2], underscores the necessity of addressing key requirements to expedite the development of FOWT. These requirements include enhancing market visibility, establishing support mechanisms, reducing project risks, fostering technology innovation, and developing the supply chain.

The most suitable locations for FOWT deployment in the UK are found off the coast of Scotland, particularly in near-shore deep-water sites [93, 94]. The Northern North Sea also offers suitable areas for floating wind technology [95]. For example, the Buchan Deep, located 25 km offshore of Peterhead, is a prime instance of a far-offshore FOWT location, where Statoil has installed a 30 MW wind turbine farm on floating structures (Hywind Spar) to harness Scottish wind resources. The water depth in these locations ranges from 95 m to 120 m [96]. Another example is the Magnora Offshore wind farm located in the northwestern part of Scotland, 40 km offshore the Western Isles. The planned wind farm will cover an area of approximately 100 square kilometres, with water depths ranging from 106 m to 125 m [97].

Scotland has experienced significant success in the floating wind market, with a combined capacity of 15,071 MW from all floating wind projects and eleven more wind farms planning to incorporate floating wind turbines. Consequently, FOWTs now constitute nearly 65% of the total number of planned projects in Scotland [98].

## 2.2. Technology Status

In the advancement of technology for FOWT, it is imperative to comprehend the structural behaviour under considered conditions in order to establish a sustainable, dependable, and economically efficient design for support platforms, as well as mooring and anchor systems [99]. There are multiple floating wind concepts in various stages of development, including four primary foundation types (see section 1.3).

Although the concept of floating platforms for wind turbines has been around for a considerable period, recent technological advancements have helped overcome technical challenges in designing a commercial system. The long-term survivability of floating structures has been successfully demonstrated, but the economic feasibility enabled mass production deployment of offshore oil rigs has yet to be proven in the renewable energy sector [19].

A timeline illustrating the evolution of floating offshore wind turbines highlights the most promising and advanced platform concepts that complement traditional horizontal axis turbines (see Fig. 2-7). Several platform designs have been implemented at the pilot farm stage, while others are in various stages of development [100]. Although many concepts have undergone tank testing, transitioning to full-scale demonstration requires a substantial increase in investment.

Four types of FOWTs have successfully demonstrated proof-of-concept, indicating the industry's capability to design support platforms for turbines of various power ratings. These leading concepts are anticipated to originate from European and US companies, with a deceleration in the advancement of Japanese-designed concepts [1, 2, 101].

The range of designs for FOWTs shown in Fig. 2-7 indicates a lack of standardization in platform design. Consequently, reaching a consensus on engineering designs can lead to cost reductions, which are crucial for the numerous planned future installations of floating offshore wind turbines. Globally, the floating offshore wind energy market is currently in the experimental phase in Europe, Asia, and North America. These experimental and demonstration projects are generally anticipated to begin operations between 2022 and 2024 and are expected to generate data and expertise that will contribute to the development of cost-effective, large-scale projects that could

potentially be deployed as early as 2025 [2, 102]. Table 2-2 provides an overview of platform designs that currently have a demonstration or prototype project or had one that has been decommissioned.

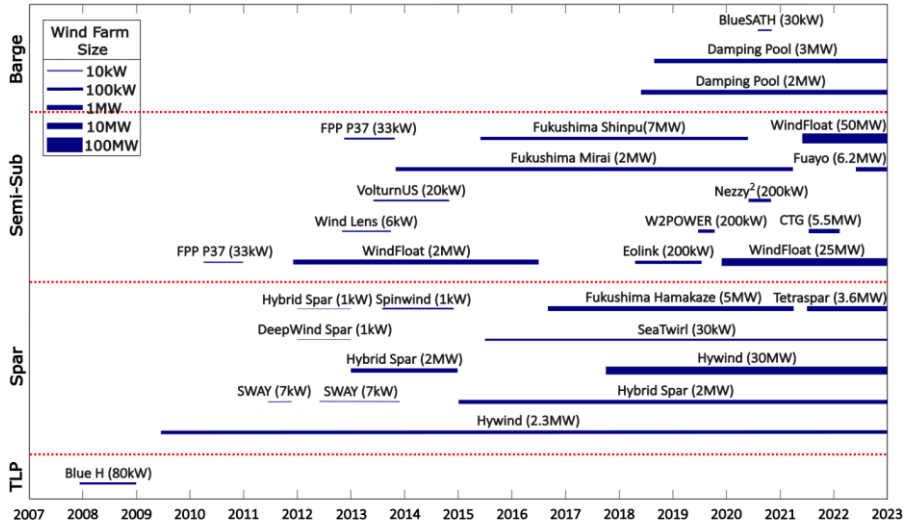


**Fig. 2-7** Floating Offshore Wind Technology Readiness Level (TRL) Status [80] (See Table 2-2 for References for Each Device)

**Table 2-2** Platform Designs with A Live or Decommissioned Prototype

| Platform Name | Years Active | Type | References |
|---|---|---|---|
| Blue H | 2007-2008 | TLP | [103, 104] |
| SWYAY | 2011 | Spar-TLP | [105-107] |
| DeepWind Spar | 2011 | Spar | [99, 108-110] |
| Hybrid Spar | 2012-2013, 2013-2015 | Spar | [105, 111-115] |
| VoltumUS/VolturnUS-S | 2013-2014 | Semi-sub | [116-118] |
| Fukushima Mirai | 2013-2021 | Semi-sub | [23, 100, 119] |
| Spinwind | 2013-2014 | Spar | [109] |
| SeaTwirl S1 | 2015 | Spar | [108, 109, 120] |
| Fukushima Shinpu | 2015-2018 | Semi-sub | [121] |
| Fukushima (Adv. Spar) | 2016-2021 | Spar | [35] |
| Damping Pool | 2018-present | Barge | [50, 122] |
| Eolink | 2018-2019 | Semi-sub | [123, 124] |
| SATH | 2020 | Barge | [125-127] |
| TetraSpar | 2021-present | Spar | [128, 129] |
| China Three Gorges | 2021-2021 | Semi-sub | [68] |
| Fuyao | 2022-present | Semi-sub | [130, 131] |
| W2Power | 2019 | Semi-sub | [132-134] |
| Nezzy2 | 2020 | Semi-sub | [135] |
| FPP | 2010, 2012-2013 | Semi-sub | [136] |
| Hakata Bay | 2012-2013 | Semi-sub | [137] |

### 2.2.1. Wind Turbine Capacity

In recent years, there have been significant advancements in wind power technology, particularly in the areas of structural design, blade design, and generator design for variable-speed operation [138]. The introduction of the NREL 5 MW reference wind turbine in 2009 [139] marked a turning point, leading to the development of larger turbines in the offshore wind industry. Companies such as Siemens Gamesa, GE, Samsung, and Vestas have designed turbines ranging from 6 MW to 10 MW, with a focus on increasing power generation capacity [140]. Siemens Gamesa and GE designed a 6 MW turbine; Samsung and Vestas developed 7 MW and 8 MW models, respectively; Senvion, AMSC, and Siemens Gamesa collaborated on a 10 MW turbine [141]. While scaling up turbines has been effective in reducing costs, it remains uncertain whether this trend can be sustained indefinitely. Odfjell Oceanwind has received approval for a floating wind foundation capable of supporting a 15 MW turbine, which is scheduled to be operational by 2024 [142, 143]. Vestas Wind Systems A/S, the world's largest wind turbine manufacturer, produces onshore turbines with a rated power of 6.8 MW and offshore turbines with a rated power of 15 MW [144]. According to WindEurope [145], the offshore turbine capacity has been increasing by 16% annually since 2014, with the average rated capacity of installed offshore wind turbines in 2019 reaching 7.8 MW. The progression in turbine size from the 19th century to 2025 is illustrated in Fig. 2-8, showing a rise in turbine capacity from a 50kW power rating with a hub height of approximately 25 m to turbines now capable of exceeding 15 MW, utilizing a hub height of 200 m [146].

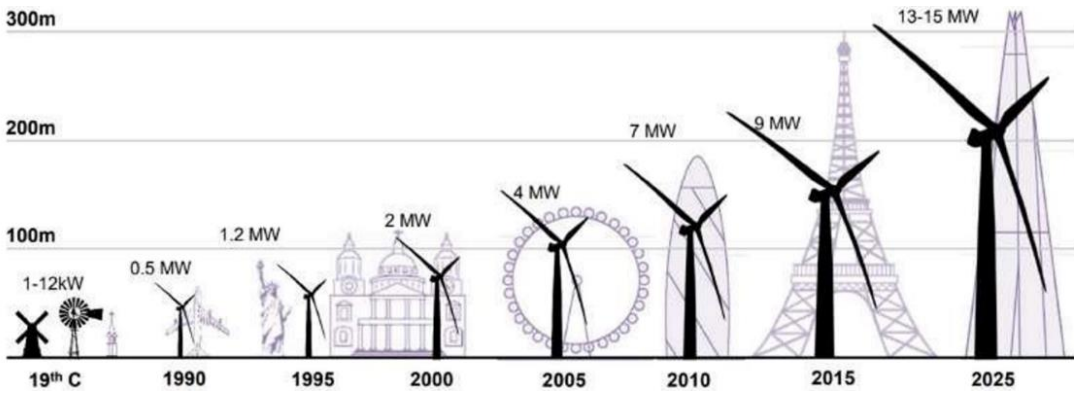


**Fig. 2-8** Evolution of Wind Turbine Heights & Output (Source: Bloomberg New Energy Finance)

**Table 2-3** Summary of the Characteristics for Reference Wind Turbine Models

| Turbine | NREL | LW | DTU | IEA |
|---|---|---|---|---|
| Rating (MW) | 5 | 8 | 10 | 15 |
| Rotor diameter (m) | 126 | 164 | 178.3 | 240 |
| Hub height (m) | 90 | 110 | 119 | 150 |
| Hub mass (kg) | 56.78 | 90 | 105.52 | 190 |
| Nacelle mass (kg) | 240 | 285 | 446 | 630 |
| Blade mass (kg) | 17.74 | 35 | 41.7 | 65 |
| Tower mass (kg) | 347.46 | 558 | 605 | 860 |

As the power capacity of the turbine increases, the dimensions of the rotor and its structural weight also expand, resulting in a significant increase in the thrust force at different wind velocities. This necessitates a larger supporting framework, posing difficulties in the design of the mooring system as the size of the floating structure grows. Furthermore, the development of these larger turbines necessitates adjustments in infrastructure, including ports and vessels, thereby demanding the expansion of installation vessels, fabrication facilities, and operational approaches [147].

The structural properties of four representative reference wind turbine models, including the 5 MW NREL (National Renewable Energy Laboratory) [139], 8 MW LW (LEANWIND) [148], 10 MW DTU (Denmark Technical University) [149] and 15 MW IEA (International Energy Agency) [141] are compared in Table 2-3.

Several research studies have been conducted by scholars at the Norwegian University of Science and Technology (NTNU) focusing on 10 MW wind turbines. These investigations have led to the development of different types of foundations to accommodate the DTU 10 MW reference wind turbines (RWT), such as bottom-fixed foundations, Semi-Submersible type floaters [150, 151], TLP type floater [152, 153], and Spar type floater [154-156]. Son et al. [157] have also proposed a new WindFloat type Semi-Submersible platform to support the DTU 10 MW wind turbine. These investigations assert that the 10 MW DTU reference turbine is currently more reliable, efficient, and cost-effective for FOWTs, which are utilized for academic analysis of TLP, Semi-Submersible, and Spar support platforms [152, 158, 159]. Therefore, in this thesis, the DTU 10 MW reference wind turbine was selected for upscaling, modelling, and analysis due to its extensive research and frequent use as a benchmark.

### 2.2.2. Current Supporting Structure Concept

The FWOT has been engaged in the long-term observation of the offshore oil and gas industry's progress. The knowledge and expertise gained from the oil and gas sector are valuable and should be applied to wind projects [160]. Despite the differences in technology, there are similarities. At times, engineers in the oil and gas industry may caution against certain approaches in offshore wind projects. Ideally, wind platforms should operate reliably for extended periods through a combination of automation, remote monitoring and control. The presence of rotating blades will also affect the stability of FOWT [161, 162].

Four primary platform designs for FOWT, originating from the oil and gas industry, are illustrated in Fig. 2-9 [163]. However, while the typologies are similar, the structures are distinct and must meet different requirements. Nevertheless, the offshore wind industry could potentially replicate the oil and gas industry's transition from fixed to floating foundations [161].

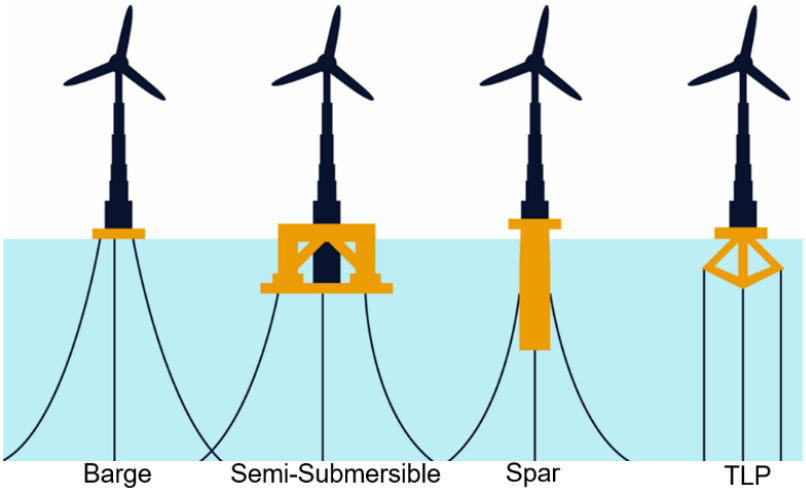


**Fig. 2-9** Floating Offshore Wind Foundation Typologies [141]

Various types of floating support structures are used to meet the requirements for static stability. These structures can be classified into three primary stabilizing mechanisms [19, 55, 164], namely ballast-stabilized, waterplane-stabilized, and mooring-stabilized. The ballast-stabilized mechanism involves the utilization of large ballast tanks positioned at the base of the structure to lower the centre of gravity below the centre of buoyancy, thereby creating a stabilizing righting moment. Waterplane-stabilized

structures rely on the waterplane area to restore stability, while mooring-stabilized structures employ high-tension mooring lines to generate a restoring moment when the structure is inclined.

The classification of the system is based on the primary source of the restoring moment, with waterplane-stabilized systems relying on the waterplane area (e.g. Dutch Trifloater [165], WindFloat [166], NOVA Semi-Submersible [167]), ballast-stabilized systems utilizing buoyancy and gravity positions (e.g. Hywind SPAR by Statoil [22]), and mooring-stabilized systems depending on the mooring system (e.g. MIT TLP [168], BlueH). The overall stiffness of the system is represented by the 'stability triangle', which encompasses the contributions from all three mechanisms [168].

A visual representation of the stability triangle is depicted in Fig. 2-10. Additionally, a modified stability triangle concept is introduced, considering the potential negative contribution of the restoring term due to the position of the centre of gravity [100]. The primary concepts for floating offshore wind turbine structures include the Semi-Submersible Platform, Spar-buoy, TLP, and Barges, each with their unique set of benefits and drawbacks [46]. Each concept has its own set of advantages and disadvantages, as outlined in Table 2-4.

The susceptibility of a floating offshore wind turbine substructure to waves is influenced by factors such as the structure's shape and dimensions at and near the waterline. Spar and TLP designs have a reduced cross-sectional area at the water level, which makes them less vulnerable to waves. Spars are naturally designed to be long and slender, and this can be further optimized by tapering the design to a smaller diameter at the waterline, as demonstrated in the Hywind project. TLPs rely on a high buoyancy force-to-weight ratio, which causes most of the substructure to be positioned well below the waterline. This positioning helps to reduce the impact of buoyancy forces as waves pass. Conversely, Semi-Submersibles derive stability from a large waterplane area, making them more responsive to wave forces [169].

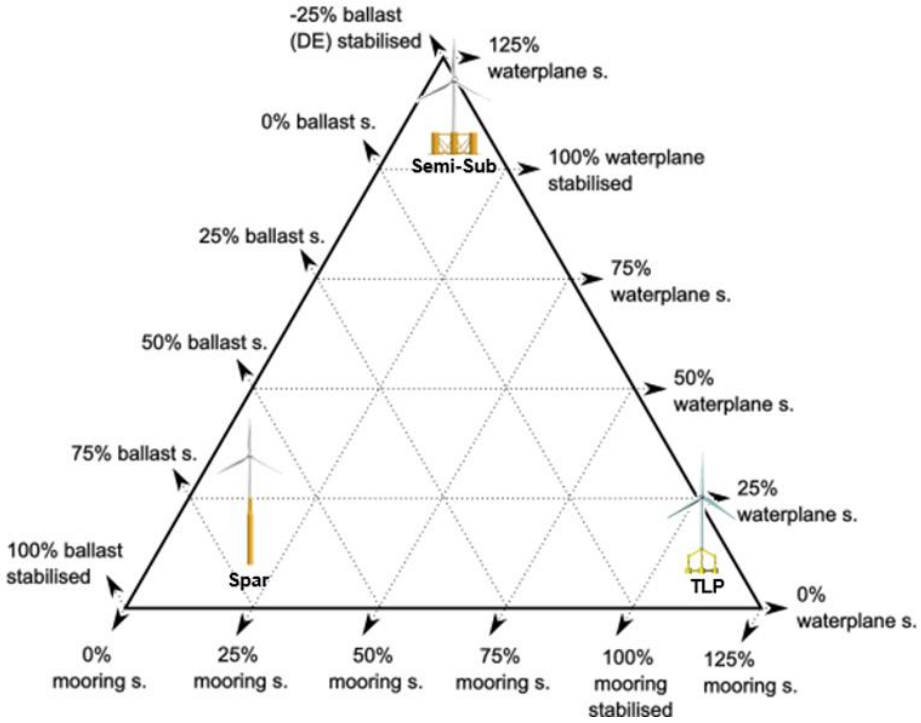


**Fig. 2-10** Floating Support Structure Stability Triangle [100]

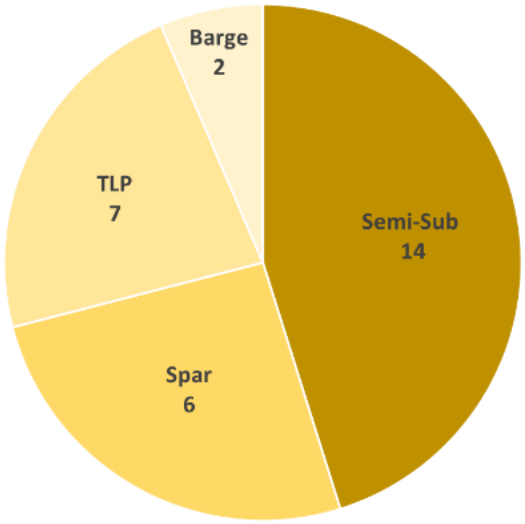


**Fig. 2-11** FOWT Platforms under Development (Source: Carbon trust (2015))

**Table 2-4** Semi-Submersible, Spar, and TLP Support Platforms Strength and Weaknesses

| Platform | Strengths | Weaknesses |
|---|---|---|
| **Semi-Sub**  | • Depth independence (Flexible application)[14, 19, 26, 28, 38, 39, 55]<br>• Simple installation & decommissioning [14, 19, 26, 28, 38, 39, 55]<br>• Onshore turbine assembly[19, 26, 55, 69]<br>• Cheap & simple mooring & anchoring system[19, 46, 55, 69] | • Large ballast to provide stability[14, 19, 26, 55, 93]<br>• Complex steel structures with many welded joints[26, 28, 39, 55]<br>• Lower stability, higher motions, and potentially costly active ballast systems[28, 38, 55]<br>• Larger impact on turbine due to motions<br>• Large seabed footprint and long mooring lines[19] |
| **Spar** 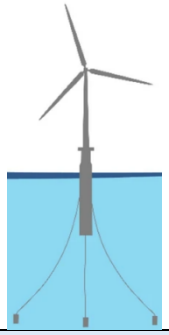 | • Simple design with no active ballast, easy manufacturing & maintenance [19, 25, 26, 28, 55, 93]<br>• Excellent stability [38, 55, 69, 93]<br>• Suitable for even higher sea states [19]<br>• Cheap & simple mooring & anchoring system [19, 46, 55, 69] | • Constrained to deep water locations[14, 38, 55, 93]<br>• Challenging, time-consuming & costly float-out & installation[1, 19, 25, 69]<br>• Long & heavy structure with large draft [55, 164]<br>• Long mooring lines [19] |
| **TLP**  | • High stability, low motions[19, 25, 26, 28, 38, 55, 69, 93]<br>• Little wave sensitivity (in case of submerged platform)[38]<br>• Suitable for intermediate depths[14, 28]<br>• Simple, small & light structure, easy maintenance [14, 19, 26, 55, 93]<br>• Onshore turbine assembly [170, 171]<br>• No active ballast required.<br>• Short mooring lines[19, 26] | • Unsuitable for strong tidal currents or storm surges[19, 25, 26, 28, 55, 172]<br>• Unsuitable for shallow water[14, 38, 55, 93]<br>• High vertical loads on the mooring and anchoring system[25, 55, 93]<br>• Complex & risky installation & disconnection for onshore maintenance[19, 38, 46, 55, 69]<br>• Large stresses in structure[19, 93] |
| **Barge** 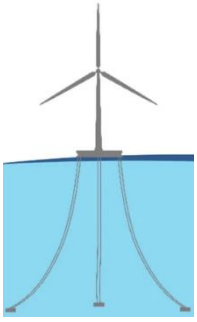 | • Simplicity in design and fabrication [19, 25, 26, 28, 38, 55, 69, 93]<br>• Relatively easy to be installed using conventional mooring lines [69, 173]<br>• Suitable for water depth greater than 50 m [69] | • Poor motion behaviour due to large water plane area. [19, 25, 26, 28, 38, 55, 69, 93]<br>• Large volume close to free surface, resulting large wave forces[25, 55, 93, 174]<br>• Relatively large manufacturing cost [173]<br>• Challenging in natural frequency [69, 173] |

In addition to hybrid wind/wave and multi-turbine platforms, the majority of the considered concepts are Semi-Submersibles, likely due to their adaptability to shallow water depths and lower installation infrastructure requirements. Other concepts such as TLPs and Spars, which are more limited in their site applications, are also represented but in smaller numbers [175, 176]. There has been a recent surge in interest in barge-type foundation concepts [93, 177]. While barge-type FOWT systems are relatively simple to manufacture, they are sensitive to motions, which is why only a few existing systems (see Fig. 2-11).

Despite the complexity of the semi-submersible support platform, it is currently favoured due to fewer depth restrictions and the ability to install the wind turbine onshore. However, there is no clear favourite for the most cost-effective concept likely to be deployed at an industrial scale, as the LCOE for FOWTs is higher than that of bottom-fixed foundations [24].

The Tension Leg Buoy (TLB) concept, also known as the MIT Double Taut Leg, was introduced in 2005 as an alternative floating platform solution [170, 178]. The initial design, named Njord, was developed for a two-bladed downwind turbine with adjustable mooring lines [179]. The TLB features a cylindrical shape to support the tower and wind turbine, offering advantages such as a slim and simple design, low draft potential, reduced material usage, and response characteristics similar to land-based towers due to taut mooring lines [180]. Variations of the TLB, including TLB B, TLB X3, and X4 [181, 182], were developed at the University of Life Science in Norway, based on the original works presented in [183] to explore different approaches for reducing wave loading and anchor loads. The TLB X3 is a hybrid tripod that reduces the necessity for bracing and streamlines the manufacturing process. The TLB X4 is a conventional slim spaceframe with four legs, as depicted in Fig. 2-12, and was further explored in a study by Anders Myhr [209] to develop a design methodology. The TLB platform is constructed using standardized steel sections and utilizes high buoyancy and tensioned mooring lines to maintain stability. Compared to a Spar platform, the main cylindrical body of the TLB is shorter, resulting in lower motion ranges than catenary moored floaters. The TLB design is influenced by site optimization, making it challenging to apply available data to other sites with varying depths.

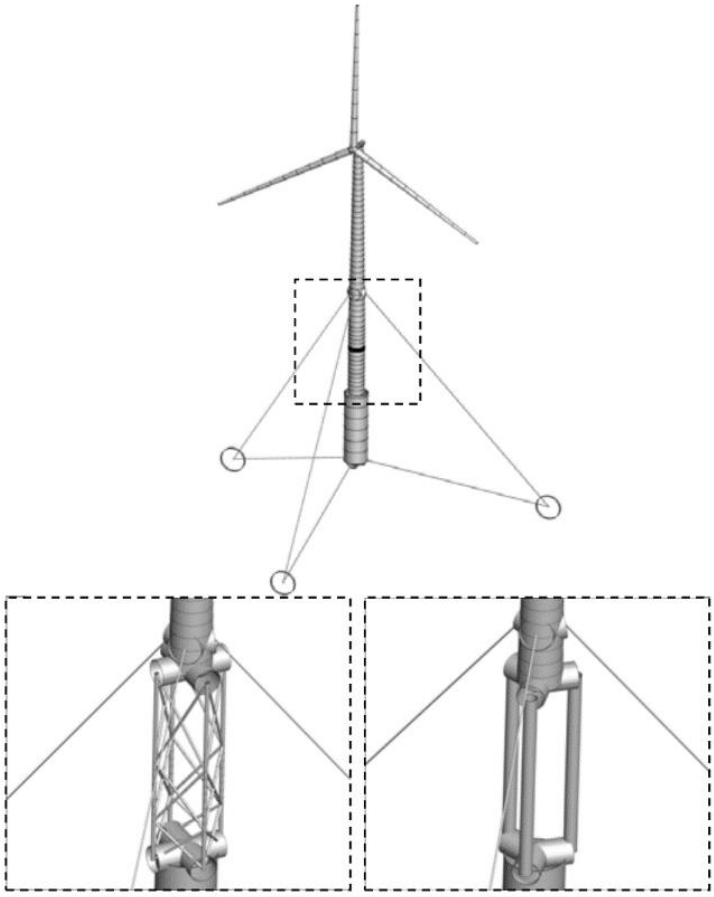

**Fig. 2-12** The baseline TLB B with plain cylinders on the top. Below are the tri-column solution for TLB X3 and the traditional spaceframe on TLB X4 [182]

Various support platforms for floating offshore wind turbines are analysed, each offering unique advantages and disadvantages. The absence of a universally ideal support platform is attributed to various factors, including water depth, port limitations, seabed characteristics, production costs, and the prevailing weather conditions at the installation site [100]. The development of support platforms for floating offshore wind turbines is a multifaceted matter, and it is crucial to identify the most economically efficient designs in relation to the LCOE [184].

### 2.2.2.1. Upscaling Platform

In recent years, wind turbines have significantly increased in size, particularly offshore turbines, which are now twice as large as land-based ones. They have power ratings ranging from 3 to 15 MW and continuing to grow due to technological advancements [185]. This increase in size increase has led to cost reductions in construction, installation, operation, and maintenance, as well as higher capacity factors [85]. To support these larger turbines and ensure system stability, floating platforms will also need to be scaled up. For example, the UpWind project explored the boundaries of increasing in size and determined that a 20 MW wind turbine could be viable [186]. Various methods have been suggested in research papers, such as using geometric scale factors to modify an existing platform design [156, 187-190]. Research has been conducted on increasing the size of wind turbines has been explored using different methods.

Jamieson (2018) explained the 'Square-Cube' law of linear scaling and examined scaling patterns of commercial wind turbines using industry data. Additionally, nonlinear and optimization techniques have been developed [191]. Capponi and colleagues (2011) developed a nonlinear method to scale up wind turbine blades to 20 MW while keeping stress levels constant. They discovered that including the weight of the blade itself would require a heavier blade [192]. Kikuchi & Ishihara (2019) discovered that the maximum overturning moment increases in a manner that closely resembles a square law when transitioning from 2 MW to larger reference turbines such as the NREL 5 MW and DTU 10 MW models. They used this overturning moment scaling as a basis for upscaling a semisubmersible structure based on the 2 MW turbine in the Fukushima FORWARD project. Their research revealed that the maximum overturning moment scaled slightly higher than the square of the scale factor. This observation is also noted in the description of the LEANWIND 8 MW reference wind turbine [188]. Desmond et al, 2016 [148] have calculated that the maximum thrust for the NREL 5 MW and 10 MW turbines is estimated to be 1600 kN and 3200 kN, respectively. Another study by Leimeister et al. (2016) [187] explores the scaling up of semisubmersibles for floating wind turbines. The study utilizes a linear square-cube scaling method to upscale the OC4 semisubmersible from an NREL 5 MW turbine to a Fraunhofer 7.5 MW turbine.

Aina Crozier [153] presented two designs of TLP support structures for the 10 MW reference wind turbine. The TLP is a 5 MW platform designed and developed based on the Massachusetts Institute of Technology (MIT) design. The designs are developed through a series of iterative design processes that take into consideration key design factors, including performance requirements, natural frequencies, and primary cost drivers.

George (2014) employed a similar method but upheld a steady framework to facilitate theoretical advancement in European dry docks. They increased the size of an OC4 semisubmersible from a 5 MW turbine to a 10 MW turbine from DTU, as well as a 7.5 MW turbine created through linear interpolation between the two reference turbines. Their findings indicated that the version with a constant draft showed enhanced stability [189].

According to the Square-Cube law, the linear dimensions of the rotor and the platform increase proportionally for larger turbines. Therefore, the scaling factor (s) for the platform can be calculated as the square ratio of the rated powers of the base model and the scaled one. Consequently, the platform's share of the total mass of the floating wind system will expand, impacting the overall cost [193]. A scaling factor has been suggested to maintain the proportion between the masses of the turbine and platform by applying the square-cube law ($s^{2/3}$). This scaling law aims to preserve the mass characteristics of the platform system while maintaining the draft of the floating support unchanged, constrained by the limitations of the port facilities [156, 159, 188, 189]. As a result, the platform's horizontal ($xy$) and vertical ($z$) linear dimensions scale at different rates.

The methodology of the George study maintained the draft and kept the centre of the mass of 10 MW design at the same position as in the 5 MW design. The spacing between the offset columns is identical to that of the respective scaled platform model. By subtracting the displaced volume of the main column and neglecting the pontoons and crossbars, the total required volume for each of the offset columns is calculated.

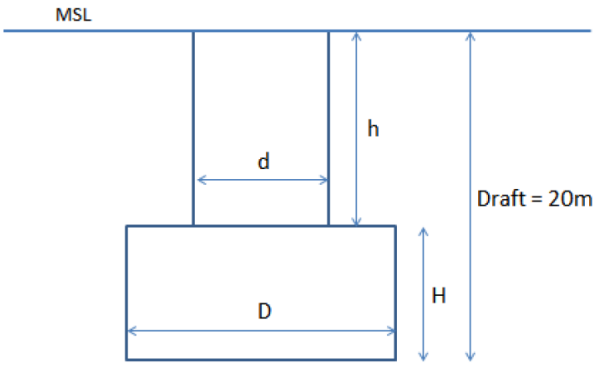


**Fig. 2-13** Cross Sectional View of the Submerged Offset Column [189]

The Fig. 2-13 illustrates the submerged portion of the offset column [189], where the base diameter (D) is twice the diameter of the top column (d), and the base height (H) is a quarter of D. Consequently, the height of the upper column is determined by subtracting the base height (H) from the maximum draft of 20 meters. The key distinction between the scaled and reduced draft designs lies in the configuration of the offset columns. The relative positioning of the offset columns to each other and to the central main column on the platform remains consistent for the corresponding power rating of the system. The main column diameter for both reduced draft and scaled platforms remains constant for a specific turbine size to align with wind turbine tower dimensions. The dimensions of the crossbars and pontoons connecting the main column to the offset columns are determined based on the scaled platform specifications.

Introducing new offset column geometries not only affects the draft but also influences the total steel mass. The revised draft design is slightly lighter, leading to a marginal decrease in material costs. The overall weight is maintained by adjusting the ballast water volume accordingly.

### 2.2.3. Mooring System

Mooring systems play a critical role in restraining the movement of floating wind turbines, thereby controlling their translational and rotational motions within acceptable limits [194]. The specific design of the mooring system is influenced by various factors, including the type of floater, water depth, maximum allowable offset, and environmental conditions [195]. It is imperative for the mooring system to be engineered with a lifespan that aligns with that of the wind turbine, thus minimizing the need for premature replacement. Station-keeping, which involves the mooring system of a floating structure based on either a catenary or taut system, is essential for maintaining the position of the structure. While dynamic positioning systems can achieve station-keeping, they are not considered suitable for floating wind turbines due to their high cost and extended operational duration [196, 197]. An overview of the primary mooring systems is depicted in Fig. 2-14.

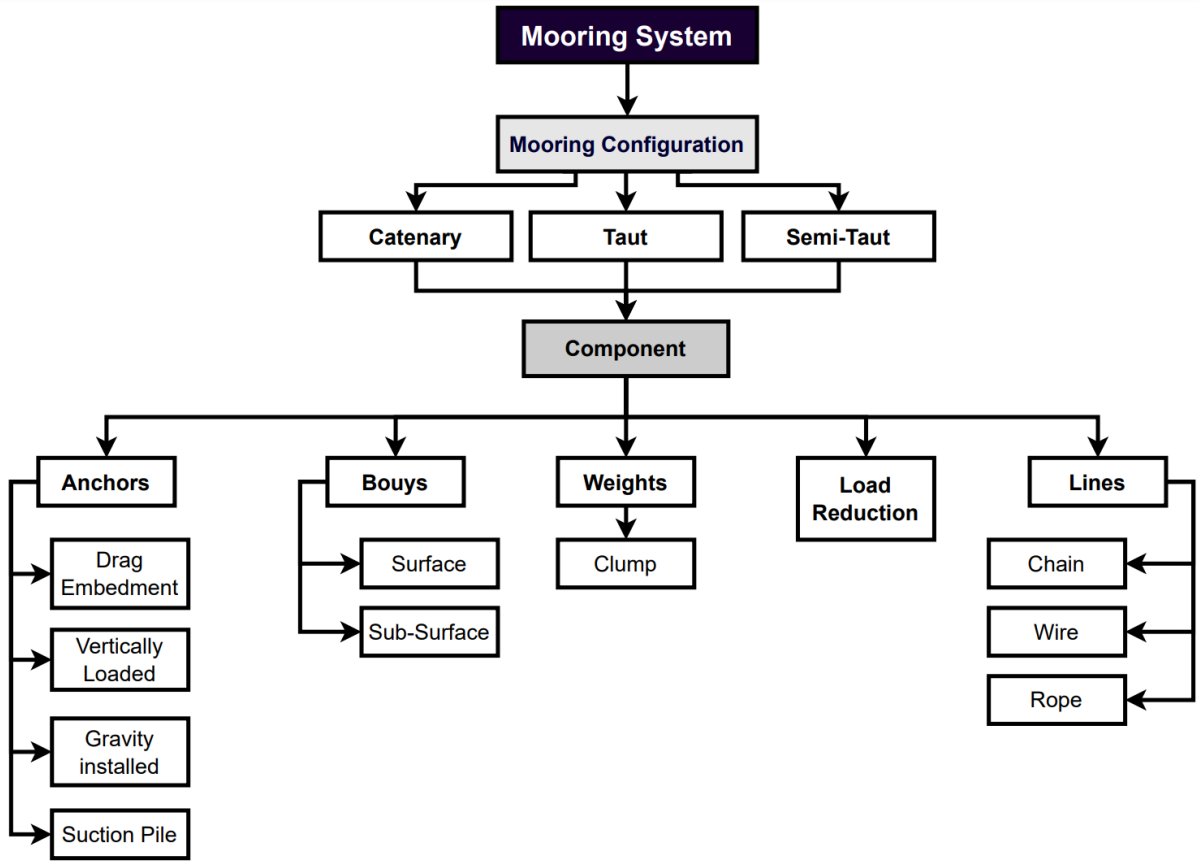


**Fig. 2-14** Overview of Elements of a Mooring System

Several researchers have investigated the design considerations of mooring systems for floating wind turbines in shallow water. Brommundt (2012) [198] developed a computational tool to optimize catenary mooring systems. Benassai (2014) [199] conducted a comparative analysis of the motion control performance of catenary and tensioned line mooring systems for the Dutch tri-floater wind turbine at water depths ranging from 50 m to 200 m under operational and extreme load conditions. Benassai also studied the influence of line number, platform maximum admissible offset, and mooring line pattern. In a subsequent study, Benassai (2015) further explored mooring optimization techniques based on allowable platform offset, line number, and mooring pattern. The findings suggested that reducing mooring weight for traditional configurations could be achieved by designing non-uniform angular distribution mooring patterns [194]. Additionally, Xu (2018) proposed mooring system designs for three different water depths and concluded that the nonlinear mooring line tension increment becomes more pronounced as water depth decreases [200].

Harrold (2020) [201] conducted a study on an innovative mooring system for FOWTs, focusing on the large-scale physical testing of a hydraulic-based mooring component with non-linear stiffness characteristics. The Intelligent Mooring System (IMS) consists of a hollow braided Vectran rope containing a pressurized water-filled bladder and a gas-charged accumulator. When the rope is under tension, the internal bladder compresses, transferring water to the accumulator. This process effectively stores the energy from the loading event, reduces tension in the line, and functions as a shock absorber [202].

The mooring system is considered a significant cost factor in enhancing cost competitiveness for floating offshore wind turbines [201]. As mentioned in Section 2.2.2, FOWT projects have predominantly utilized Semi-Submersible and Spar support platforms with traditional catenary mooring systems. However, the absence of applicable standards requires a more cautious and overly engineered approach in these mooring systems [2], resulting in expensive designs and a preference for heavy steel and wire materials. It has been emphasized that the mooring system may represent more than 10% of the overall FOWT CAPEX [1], highlighting the critical need for improvement in the design of mooring systems for FOWTs.

### 2.2.3.1. Mooring Configuration

Designing a mooring system for a floating energy production system is complex. With floating wind turbines, there are additional elements that need to be considered. Turbine proximity, for instance, to other turbines must be accounted for as it affects energy production efficiency. In addition, the system's interaction with other marine users and marine life must be evaluated. For example, arrays of multiple turbines moored and anchored together can impact marine traffic and local fisheries [203]. Furthermore, the fairlead location is crucial for providing service vessel access for repair and maintenance. Considering these impacts early in the design stage can help mitigate potential concerns [204].

The majority of FOWTs are expected to be installed in shallow waters with depths of less than 200 meters [205]. It has been proposed that the mooring system commonly used in the oil and gas industry could be adapted for use in this context [206]. Additionally, in such shallow water depths, the implementation of a semi-taut or taut mooring design for FOWTs is also feasible, offering potential cost reductions for the overall mooring system [206]. The tension leg mooring concept is associated with the TLP, which uses the buoyancy-induced tension of the vertical tendons to sustain stability and position [170]. The horizontal restoring force of the tension leg system is determined by the combined horizontal components of the tension forces in the tension legs [207]. The mooring system's compliant horizontal offset range and restraining or restoring force are generated by the catenary shape of the mooring line, which is caused by the distributed weight of the steel chain or wire suspended in the water as the floater moves away from its equilibrium position [208, 209]. The taut leg mooring concept relies on the axial elongation of the mooring line to offer offset flexibility for the floater as it moves away from its equilibrium position [210]. The mooring configuration concepts for FOWTs are depicted in Fig. 2-15.

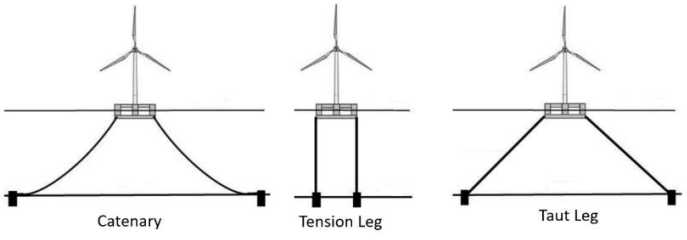


**Fig. 2-15** Mooring Configuration Concepts [210]

Each configuration of the mooring system has unique dynamic characteristics, along with advantages and disadvantages in terms of effectiveness, costs, and system complexity, as detailed in Table 2-5.

**Table 2-5** Mooring System Configuration Characteristics [209, 211-214]

| Configuration | Characteristics |
|---|---|
| **Tension leg** 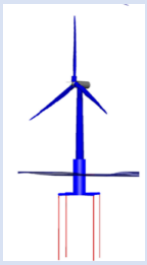 | • Small footprint<br>• Vertical loading at anchoring point<br>• Large loads placed on the anchors which requires anchors which can withstand large vertical forces.<br>• Very limited horizontal movement<br>• High tension limits floater motion (pitch/roll/heave) to maintain excellent stability.<br>• Challenging installation procedure<br>• Minimal disruption to the seabed (small footprint) |
| **Catenary**  | • Large footprint<br>• Horizontal loading at anchoring point<br>• Long mooring lines, partly resting on the seabed, reduce loads on the anchors.<br>• Some degree of horizontal movement<br>• Weight of mooring lines limits floater motion, but greater freedom of movement than taut leg.<br>• Relatively simple installation procedure<br>• Lower section of chain rests on the seabed, resulting in more disruption |
| **Taut Leg** 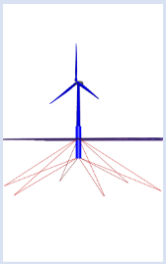 | • Medium footprint<br>• Loading typically at angle to anchoring point<br>• Medium loads on the anchors<br>• Limited horizontal movement, but full structure can swivel around the turret connection.<br>• Single connection point makes the platform susceptible to wave induced motion.<br>• Relatively simple installation procedure<br>• Low level of disruption (medium footprint) |

Several studies have examined various mooring configurations for FOWT. Brommundt (2012) [215] developed an optimization tool to analyse the optimal parameters of a catenary mooring system, including line length, angle, and anchor radius. The study included a case analysis at two different water depths (75 m and 330 m). Benassai et al. [194, 199, 216] compared the performance of motion control in catenary and tensioned line mooring systems for the Dutch tri-floater wind turbine at water depths ranging from 50 m to 200 m. The study investigated the impact of line number, platform maximum admissible offset, and mooring line pattern. Campanile (2018) [195]

proposed various design concepts for catenary mooring systems at water depths ranging from 50 m to 80 m and 200 m to 350 m. Trolle [217] conducted analyses to explore and potentially optimize the TLB concept in the event of a stabilization failure due to a taut mooring line fracture. The taut leg system offers the advantage of a smaller mooring footprint but requires specific anchor types capable of withstanding the uplift force. Additionally, it demonstrates superior station-keeping performance compared to a catenary mooring system [218].

Fig. 2-16 depicts a catenary mooring line, where the line is suspended from point A and anchored to the seabed at point B. As point A moves horizontally through positions A1-A4, the section of the catenary line resting on the seabed decreases. The tension at point A is caused by the combined weight of the submerged line in seawater. As the structure moves through positions A1-A4, the tension in the line at point A increases due to an expanding section of the line being suspended. This, combined with the simultaneous decrease in line angle to the horizontal, results in a non-linearly increasing horizontal restoring force with the structure offset [219]. This non-linear restoring force and geometric shape can be described by the catenary equations. These equations are derived by considering a mooring line in the x-z plane, while neglecting bending stiffness and dynamic effects in the line, which is suitable for chain and wire materials [220].

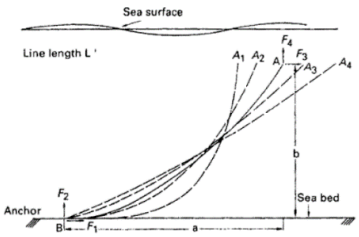


**Fig. 2-16** The Behaviour of a Catenary Mooring Line [162]

In deep-water environments, lightweight multi-segmented lines are considered more suitable for certain applications [221]. Furthermore, the catenary mooring footprint expands in deep water, making taut systems appealing due to their smaller footprint and exposure to only horizontal forces. To prevent the line close to the anchor from being lifted at an angle, the weight of the line must be sufficient to create a restoring force. This can be achieved by increasing the length of the mooring line. However, this can lead to a large footprint of catenary systems, especially in shallow water [222-224].

In contrast to catenary moorings, taut mooring lines have a smaller footprint because they do not rest on the seabed. While taut mooring lines can be angled, tension leg systems represent a specific case where the tendons are vertical. Tension leg floaters typically experience greater horizontal movements compared to floaters moored in an angled taut manner due to a lower horizontal restoring force. To prevent horizontal movements in tension leg systems, additional angled bracing can be employed [225]. However, taut systems face additional challenges compared to other configurations [226]. The mooring stiffness of the catenary system primarily depends on the weight and geometry of the chain system, while the taut mooring is significantly influenced by the material properties [227]. In a taut leg mooring, the anchor point must be able to withstand both horizontal and vertical forces, whereas in a catenary mooring, the anchor point is only exposed to horizontal forces [228]. According to Masuda, Ikoma, and Nagai (1994), "One of the most serious problems of the TLP is the springing phenomenon in the mooring system due to super harmonic resonance of heaving motion in a high-frequency zone" [229].

The semi-taut mooring system consists of both catenary and taut mooring components, with its restoring force derived from line elasticity and weight [230]. Yuan (2014) [231] proposed a hybrid system based on the taut mooring system, utilizing clump weights to create a catenary shape at the bottom of the mooring line, while a buoy is attached at the top section of the mooring line.

The marginal water depth between bottom-fixed and floating wind turbines typically ranges from 60 m to 80 m, posing a challenge for the implementation of floating structures. This is primarily due to the design of the mooring system [200]. Furthermore, the system's interaction with other marine users and marine life must be carefully assessed. For instance, arrays of multiple turbines moored and anchored together can have an impact on marine traffic and local fisheries [203]. Furthermore, the location of the fairlead is crucial for providing service vessel access for repair and maintenance. Considering these impacts at the early stages of the design process can help address potential concerns [204]. With the expansion of the floating wind industry, there is an increasing interest in investigating novel mooring and anchor system solutions [232, 233]. Some of the solutions entail the use of several moored floaters and multiple mooring lines secured with shared anchors. For instance, Wu (2023) [218] introduced a novel mooring design known as the V-Share mooring

system. This system employs two lines connecting from two different floater columns to one anchor. Similarly, Liu (2021) [234] proposed a novel mooring system specifically designed for Spar-type floating offshore wind turbines, featuring six mooring lines divided into three groups, with two mooring lines in the same group connected to the same fairlead. Additionally, Fan (2022) [235] demonstrated a novel design of hybrid mooring systems, known as the Low Tension Hybrid Mooring model (LTHM), which involves arranging buoys and weight at intervals on the mooring line floating structure in shallow water for different floater types, such as floating barge and Semi-Submersible. Furthermore, Pillai (2022) [236] investigated the use of novel and synthetic mooring tethers to enable the tuning of a floating wind turbine's mooring system stiffness behaviours, with the aim of achieving specific desirable response, load characteristics, and potential cost reductions.

The mooring system loads can be decreased by utilizing load reduction devices (LRDs). Load Reduction Devices (LRDs), including Tuned Mass Dampers (TMDs), Active Mass Dampers (AMDs), and Hybrid Systems, are specifically designed to diminish the dynamic loads on the mooring system, thereby enhancing the overall performance and reliability of FOWTs [237, 238]. TMDs, for instance, are passive devices that consist of a mass connected to a structure via springs and dampers. They are designed to reduce the dynamic response of the structure through springs and dampers, aimed at diminishing the structure's response to dynamic loads by absorbing and dissipating energy. They can be strategically positioned within the mooring system to mitigate various types of loads, including wave-induced motions and wind-induced vibrations [239]. In contrast, AMDs are devices utilizing control systems to actively counteract the dynamic forces acting on the structure. By detecting the motion and applying counteracting forces, AMDs effectively reduce the impact of waves and wind on the mooring system [240]. Moreover, hybrid systems combine passive and active technologies to effectively mitigate a wider range of dynamic loading conditions [241]. LRDs provide benefits including enhanced structural integrity, enhanced power production, and increased safety. Nevertheless, the implementation of these systems poses challenges and considerations in implementing these systems include cost, reliability, and integration [237, 242, 243].

### 2.2.3.2. Mooring Materials

The choice of mooring systems can exert a substantial influence on the expenses and effectiveness of a project. Moreover, opting for alternative mooring materials can influence the overall economics of a wind farm [17, 244]. Hence, it is essential to investigate different materials for mooring lines as the floating wind industry expands [198].

Traditionally, conventional steel chains, such as studless and studlink chains, are frequently utilized in marine mooring systems [245]. Studlink chains contain a stud within the link to enhance stability and prevent entanglement, rendering them appropriate for temporary moorings. In contrast, studless chains are used for permanent applications, such as FOWTs. The utilization of studlink chains offers higher restoring forces in catenary mooring configurations [221, 246]. These chains are classified into five grades based on the nominal tensile strength of the steels used for manufacture, including R3, R3S, R4, R4S, and R5. Hence, the selection of mooring line materials is a crucial consideration for achieving the economic objectives of wind farm projects [247].

In comparison to chains, wire ropes are characterized by their reduced weight and increased elasticity. Wire ropes consist of individual wires twisted in a helical arrangement to create a strand, where the flexibility and rigidity are influenced by the pitch of the helix. Wire ropes are frequently favoured over chains for mooring in deep waters because of their reduced weight and increased elasticity, particularly when used in conjunction with chains to create a comprehensive mooring line [248]. When exposed to equivalent tension, wire ropes generally exhibit a higher restoring force in comparison to chains. This is due to the same pretension, wire ropes typically provide greater restoring force compared to chains, as lighter weight mooring lines result in a less pronounced catenary shape. This characteristic renders wire rope suitable for deep-water applications where the use of chains is impractical due to their high weight [248]. Wire ropes can be configured in various configurations, including those with multiple wire strands [249]. DNVGLST0119 [250] provides recommendations regarding the selection of steel wire rope type and sheathing for mooring floating offshore wind turbines, taking into account factors such as required lifetime and replaceability.

Mooring systems often use six-strand or eight-strand wire ropes due to the combination of strength, flexibility, durability, ease of handling, safety, and versatility makes six-strand and eight-strand wire ropes a preferred choice for mooring systems [251]. Lang lay ropes typically exhibit greater axial torque compared to regular lay ropes, particularly under torsion load [252]. Lang lay ropes typically exhibit greater axial torque compared to regular lay ropes, particularly under torsion load [252]. This difference in torque generation can be attributed to the specific construction of lang lay ropes, where the wire strands are wound in the same direction as the rope lay. This means that if the rope lay is right-handed, the wire strands within each strand are also right-handed. Consequently, when lang lay ropes experience torsional loads, the forces produced by the twisting motion are more efficiently transmitted along the rope's axis due to this alignment. This direct transmission of forces prompts the individual wires to tighten further, resulting in increased axial torque [253]. On the other hand, in regular lay ropes, the wire strands are wound in the opposite direction to the rope lay. For instance, if the rope lay is right-handed, the wire strands within each strand are laid left-handed. This opposing alignment causes the forces generated by torsion to be somewhat counteracted as the wire strands resist the twisting motion by moving in opposing directions [254]. Consequently, the transfer of torsional forces along the rope's axis is less direct in regular lay ropes, leading to lower levels of axial torque generation [255, 256].

Permanent mooring systems commonly employ spiral strand wire ropes, which are made up of multiple individual wires that come together to form a single strand. The wires are organized in layers, with each layer being wound in the opposite direction to achieve torque balancing and to avoid twisting under tension. For enduring applications, it is customary to utilize spiral strand wire ropes coated with polyethylene to safeguard against corrosion [221].

As advancements in the marine industry progress, there is an emerging tendency to substitute steel materials with synthetic fibres like polyester or high modulus polyethylene fibre (HMPE) in different mooring lines [257]. Synthetic fibre ropes are regarded as a cost-effective mooring option and are progressively being employed in deep-water mooring applications in the oil and gas sector [258, 259]. Additionally, they are being considered for use in offshore renewable projects [260]. While only a few projects currently employ fibre rope as a mooring solution, such as the CETO wave

energy converter [261] and the Floatgen wind turbine [50, 122], there is ongoing research into its feasibility and performance compared to other mooring materials. Various studies have examined the influence of load history on synthetic rope and provided an overview of its application for marine renewable projects, encompassing classification, model testing, installation, degradation, and maintenance. Johanning and Smith (2009) [262] examined the feasibility of applying fibre rope to a wave energy converter by comparing it with other mooring materials. Weller (2013) [263] conducted a study on the influence of load history on synthetic rope, where different initial bedding levels were used to investigate the rope's immediate quasi-static and dynamic properties. An overview of the utilization of synthetic ropes for marine renewable projects was provided by Weller (2015) [264] including classification, model testing, installation, degradation and maintenance.

Fig. 2-17 depicts a typical configuration of a synthetic rope that is frequently utilized in mooring operations. The rope consists of several sub-ropes organized in a parallel construction [265]. The rope comprises multiple sub-ropes arranged in parallel, with each sub-rope consisting of strands and being constructed in parallel, braided, or laid configurations to attain specific rope properties. The sub-ropes are arranged to create a core that is shielded with a soil filter to prevent soil penetration. Additionally, a braided jacket to protect against external abrasion, although the jacket does not bear any tensile load. Synthetic fibre ropes, particularly high-efficiency polyester fibre ropes, have been successfully used in the oil and gas industry, with Petrobras being the first to integrate them into deepwater mooring systems [258, 266]. The transition to renewable energies presents new challenges, such as increased dynamic loads, which may require adjustments to established design procedures from the oil and gas sector [267].

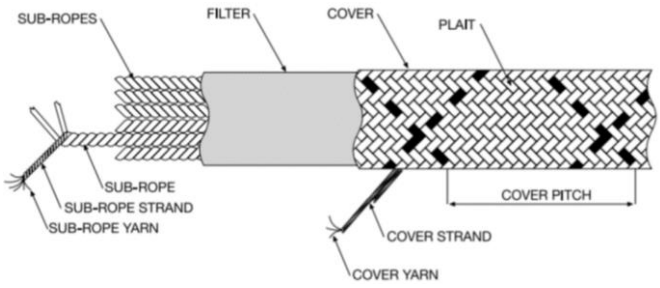


**Fig. 2-17** Illustrates an Example of Polyester Rope Construction [265]

Polyester is presently the most frequently utilized material in synthetic fibre ropes because of its advantageous blend of characteristics, including low weight, cost-effectiveness, low axial stiffness, and high fatigue resistance. Nevertheless, there are several alternative synthetic materials that are appropriate for mooring applications [56], such as nylon, HMPE, aramid, and others. Nylon, for instance, exhibits high elasticity and could be suitable for applications in shallow water locations where polyester ropes might become excessively rigid. In compliant mooring systems, nylon and polyester are both suitable choices because of their low modulus of elasticity. Conversely, materials with high modulus, such as HMPE, LCP, and aramid, are deemed more appropriate for taut applications [264]. In the case of catenary FOWTs, nylon may be preferred over polyester due to its lower stiffness, which can help reduce maximum tensions. However, the design of nylon mooring systems is complicated by the material's nonlinear behaviour, which affects fatigue characteristics and other factors [268]. Pham (2019) [212] explored the integration of this complexity into design modelling. Furthermore, in taut configurations, fibre ropes may experience relaxation over time, resulting in a decrease in the initial tension [250].

#### 2.2.3.3. Mooring Line Static and Dynamic Stiffness

The response of mooring lines can be calculated using either the frequency domain (FD) or time domain (TD), and there are various mathematical modelling options available for mooring lines, depending on the desired level of accuracy and computational costs [269].

The static model is suitable for considering only the static shape and forces of the mooring line. When small motions of the floaters are taken into account, the mooring line stiffness assumed to be constant, and the static approach can be extended to small and slow motions [270]. However, as motions become more extensive, the change in mooring line stiffness must be considered, necessitating the adoption of the quasi-static approach [271]. Furthermore, damping and inertia terms need to be considered for higher frequency loads, while motions remain relatively small, leading to the adoption of the quasi-dynamic approach [272]. Finally, if the entire system dynamics, including nonlinear drag, inertial loads, and nonlinear stiffness, are to be included, the complete dynamic model should be utilized [273].

The static and quasi-static characteristics of a mooring system have a significantly influence on the static stability and dynamic response of a floating structure to environmental loads [274-277]. The quasi-static can be considered in the initial stages of design as it is computationally efficient compared to fully dynamic methods, making it suitable for preliminary design and optimization studies [278-280]. A classic catenary equation is used to determine the quasi-static profile of the mooring line based on fundamental parameters [281], and it is adjusted to assess the quasi-static response of a slack mooring line that hangs freely under its own weight per unit length [228]. According to Hall (2014) [282], quasi-static models can provide a good approximation of the actual system dynamics in low waves, where platform and mooring line velocities are minimal. However, dynamic effects such as hydrodynamic drag, added mass, and mooring line inertia, which are not accounted for in the quasi-static model, may be significant in cases with higher platform and mooring line velocities. In such instances, dynamic mooring line models that incorporate these effects may be necessary. In shallow water depths (≤ 100 m), catenary moorings without buoyancy elements or clump weights are considered to exhibit quasi-static behaviour, allowing tension to be calculated from a static representation of the mooring line [269].

Kallesøe (2011) [283] conducted a study in which a dynamic mooring line model was integrated with a state-of-the-art hydro-aero-elastic wind turbine simulation code and compared it with a quasi-static modelling approach. The findings indicated that the dynamic mooring line model, in certain load cases, have influence on equivalent load and the equivalent lifetime load which were decreased by 5-20% and by 5-10% respectively.

In a study by Faltinsen [220], it was noted that the stiffness of a mooring line consists of two components: axial elongation and geometric changes of the mooring line during a change in position of the floating structure. The total stiffness of a mooring line is the product of axial stiffness and geometric stiffness, as illustrated in Fig. 2-18. For catenary systems consisting of chain and steel wire ropes, the geometric stiffness is the dominant component due to the high weight of the components, while for taut systems, the axial stiffness takes precedence [284, 285].

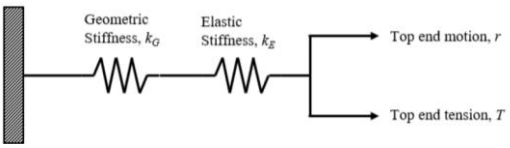


**Fig. 2-18** Stiffness Contributions in a Quasi-Static Analysis [286]

Al-Solihat (2016) [287] conducted an extensive nonlinear investigation into the stiffness characteristics of a mooring system in relation to the displacement and orientation of the floating structure. The study aimed to derive the mooring stiffness matrix, accounting for slack mooring lines resting on the seabed, as well as slack and taut suspended lines. The analysis focused on evaluating the stiffness matrix for symmetric slack catenary and taut-leg mooring systems, as well as TLP at equilibrium. The study made assumptions about the uniformity of line material and cross-section, as well as the application of Hooke's law to govern the structural elongation of the line. Quasi-static cable models were developed to determine mooring line tensions, neglecting cable inertia forces, external fluid loads such as drag and added mass forces, and cable seabed interaction forces.

The use of synthetic fibre ropes in deep water offers several advantages over catenary chain or wire lines. However, the material complexity and mechanical properties, which are not as well understood as those of chain and wire ropes, present challenges for being utilizing in FOWTs [264]. Therefore, it is crucial to comprehend the behaviour of synthetic ropes, especially for mooring systems of the taut leg configuration, where elastic stiffness is the dominant factor [288]. The conventional model for the axial elastic stiffness of a synthetic rope is a linear stiffness model, as represented in Eq. (1), where $T$ denotes the line tension, $EA$ represents the axial stiffness, and $\epsilon$ signifies the line strain.

$$T = EA.\epsilon \tag{1}$$

Ma [221] observed that the industry has traditionally employed simplified models, such as the upper-lower bound model, to estimate the stiffness of synthetic ropes. This model defines lower and upper bound stiffness values to represent static and dynamic stiffness, respectively. However, relying solely on two extreme values to capture the intricate behaviour of synthetic ropes may result in overly cautious or non-cautious

analysis outcomes. To overcome this limitation, a novel conceptual model for synthetic rope behaviour, referred to as the "SyROPE" model, has been recently developed [289, 290], as illustrated in Fig. 2-19. This model is based on tension-strain characteristics observed and measured during full-scale testing.

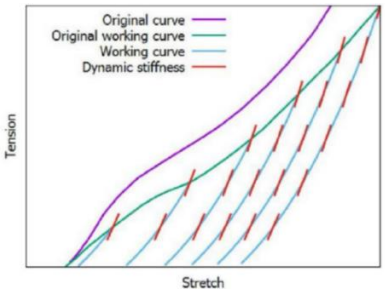


**Fig. 2-19** Principle Tension-Strain Curves Used In The SyROPE Model [289, 290]

The SyROPE model presents several key characteristics, including the working point, original curve, original working curve, and working curve [289]:

- Working point:
  The working point represents the average strain and tension at which dynamic wave frequency and low-frequency responses occur. For polyester ropes, the majority of length change occurs within the first 10-20 minutes after environmental loads change, making it suitable to analyse mooring lines based on their length at the end of a 3-hour sea state [291].
- Original curve:
  The original curve illustrates the tension and strain during the initial loading of a new rope.
- Original working curve:
  The original working curve represents the stationary working point when the rope is at its historically highest tension, and the permanent strain has been removed.
- Working curve:
  The working curve illustrates the working points when the rope is under lower mean tension than the previous maximum tension, and it is determined by the preceding highest mean tension. In a stationary sea state lasting 3 hours, each rope will be represented by a working point on the working curve determined by its highest preceding mean tension.

The diagram in Fig. 2-20 provides an overview of the SyROPE element. Synthetic fibre ropes display viscoelastic changes in length, characterized by nonlinear and load-sequence-dependent responses to variations in tension. The length variation is influenced by the rate and duration of loading, due to elongation and contraction, as well as different unload-reload stiffness. The initial framework for the SyROPE joint industry project was based on the spring-dashpot model depicted in Fig. 2-20, which is derived from a previous source [292]. While this model does not directly represent the actual components of a polyester rope, it serves as a visual aid for understanding changes in length behaviour. The elastic stretch includes both instant-elastic and viscoelastic stretches. The instant-elastic stretch is tension-level dependent and slightly amplitude-dependent, resembling a spring without damping. On the other hand, the viscoelastic stretch is similar to a dampened spring, resulting in additional change in length over time. The non-linear material curve used in static analysis is determined by shifting the working curve and redefining the initial stress-free length. This adjustment ensures that the working and original working curves intersect at maximum tension [293, 294]. On the other hand, the linear material curve utilized in the dynamic analysis is given by dynamic stiffness coefficients using the mean tension of the segment. The initial stress-free length is then redefined so that the tension is identical between static and dynamic analysis given the elongation of static analysis [289, 293].

The permanent stretch includes the effects of polymer stretching and construction stretching. The creep dashpot illustrates the irreversible polymer stretch that occurs when tension is applied to the rope. Additionally, the construction spring with a ratchet is used to demonstrate the compaction, burr formation, and rearrangement of strands, yarns, and fibres in a rope [295]. The parallel arrangement of the ratchet with the construction spring allows the spring to extend in response to tension above the previous highest tension applied to the rope but prevents it from retracting. In the tests conducted as part of the Joint Industry Project (JIP), the construction spring was found to have minimal significance [290].

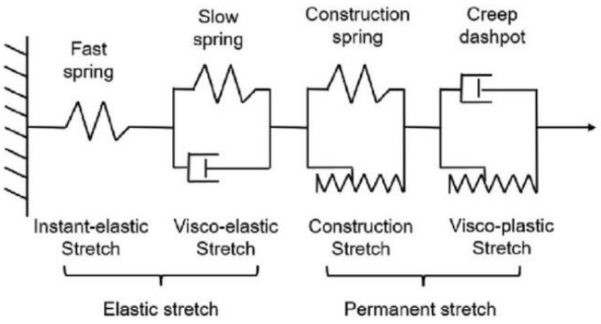


**Fig. 2-20** Overview of The SYROPE Element [286, 290]

The non-linear working curves depict the static elastic stiffness, which remains relatively constant during operation when the tension is below the installation tension. The correlation between the average tension change and average strain is articulated in Eq. (2) where $MBL$ signifies the minimum breaking load of the rope, $EA_s$ represents the static elastic stiffness, and $f_s$ and $g_s$ are constants derived from comprehensive testing.

$$dT_{mean} = EA_s \,.\, d\epsilon_{mean} = (100.\, g_s.\, T_{mean} + f_s \,.\, MBL) d\epsilon_{mean} \tag{2}$$

The equation represented by Eq. (2) can be reformulated as a differential equation, and its complete solution can be expressed as:

$$T_{mean} = C_1 \,.\, exp(100 \,.\, g_s \,.\, \epsilon_{mean}) - \frac{f_s \,.\, MBL}{100 \,.\, g_s} \tag{3}$$

By setting $T_{mean}\,(0)$ equal to zero, the equation $C_1 = \frac{f_s \,.\, MBL}{100 \,.\, g_s}$ is obtained, resulting in the transformation of Eq. (3).

$$\frac{T_{mean}}{MBL} = \frac{f_s}{100 \,.\, g_s} [exp(100 \,.\, g_s \,.\, \epsilon_{mean}) - 1] \tag{4}$$

The values of $f_s$ and $g_s$ are established by K. Larsen [286], in connection with the properties of polyester and nylon ropes, as illustrated in Fig. 2-21.

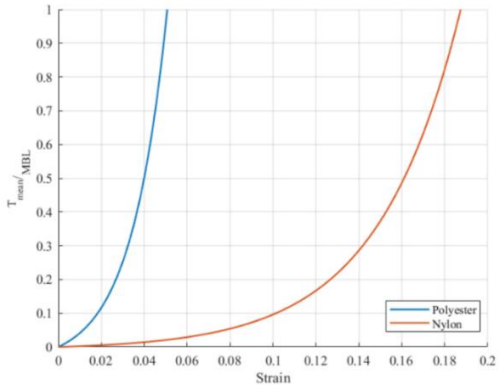


**Fig. 2-21** Static Elastic Stiffness (Working Curves) for Polyester and Nylon Ropes [286]

It is crucial to consider that the dynamic stiffness of polyester ropes can be two to three times higher than the static stiffness. The static stiffness is relevant for the initial part of the loading curve up to the mean load, while the dynamic stiffness is used to predict the cyclic part of the loading, including low frequency and wave frequencies [296, 297]. In a harsh environment, a mooring line typically experiences both a steady mean load and dynamic loads oscillating around the mean load. The typical static stiffness ranges from 10 to 20 times the minimum breaking load (MBL), while the typical dynamic stiffness ranges from 20 to 35 times the MBL [221, 297]. It is advisable to model the load-elongation properties of polyester ropes as nonlinear elastic by expressing the load-elongation relationship [296, 298]. The current industrial practice for modelling fibre rope involves using the upper-bound and lower-bound method [299], which is considered conservative and inconsistent due to the offset being based on a lower-bound stiffness model, while the dynamic tension is estimated through an upper-bound stiffness model. There is a need for more commercially available mooring analysis programs that can simulate the non-linear change-in-length response [209].

In general, the dynamic stiffness of fibre ropes is heavily influenced by the average tension, moderately affected by tension fluctuations, and slightly impacted by the frequency of loading. The effects of loading frequency and tension fluctuations are minimal for polyester ropes [300]. While nylon exhibits similar behaviour to polyester, its responses are more nonlinear. The average tension significantly influences dynamic stiffness, and the effects of strain fluctuations and loading cycles should not be disregarded. Fernandes et al. [301] proposed an empirical expression for the

dynamic stiffness of polyester ropes in Eq. (5), where $\frac{E}{\rho}$ represents specific modulus (N/tex), $L_m$ is mean load (% of MBL), $L_a$ load amplitude (% of MBL), $T_o$ is the period of loading, and $\alpha, \beta, \gamma, \delta$ are empirical coefficients. Eq. (6) presents the expression for the non-dimensional axial stiffness of polyester ropes, where $MBL$ is minimum breaking load, $L_a$ is tension amplitude, $l$ is initial length of the rope, and $\Delta l$ is the stretch.

$$\frac{E}{\rho} = \alpha + \beta L_m - \gamma L_a - \delta log(T_o) \quad (5)$$

$$K_{rs} = \frac{L_a l}{\Delta l . MBL} \quad (6)$$

According to Huntley's dynamic stiffness tests on a 3-strand nylon rope, it was found that the dynamic stiffness of the rope is significantly influenced by the average tension and tension fluctuations [302]. Eq. (7) presents the dynamic stiffness formula for nylon rope, with the coefficients $a$, $b$ and $c$ derived from a multiple linear regression analysis of the dynamic stiffness testing data provided by Huntley [302].

$$K_{rd} = aL_m - bL_a + c \quad (7)$$

This research study utilized the quasi-static and dynamic stiffness test results of post-installation polyester and nylon ropes from Bridon-Bekaert Ropes Group [265, 303] to analyse the dynamic stiffness of these ropes. Fig. 2-22 illustrates the dynamic stiffness curve for (a) polyester and (b) nylon ropes.

Fig. 2-23 showed a comparison of the stiffness curves for polyester and nylon ropes. The solid lines depict the static elastic stiffness (working curves) for polyester and nylon ropes, as reported by Tomren (2022) [286] in Fig. 2-21. Meanwhile, the dotted lines illustrate the quasi-static tension-elongation relationship based on stiffness tests conducted on polyester and nylon ropes by Bridon-Bekaert. The differences observed between the curves are attributed to the variations in the static and quasi-static methods used.

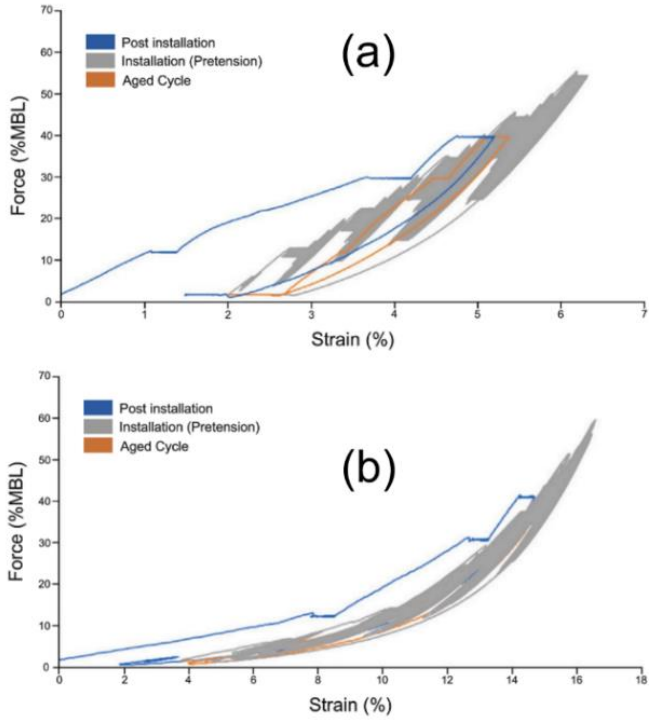


**Fig. 2-22** (a) Polyester and (b) Nylon Dynamic Stiffness Curve (Data Obtained from Bridon-Bekaert - The Ropes Group) [265, 303]

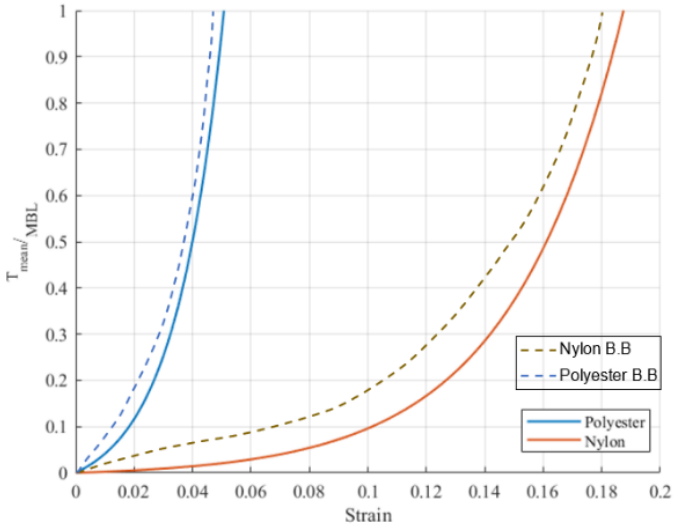


**Fig. 2-23** Comparison of Quasi-static Tension-Elongation Relationship Based on the Stiffness Tests Carried out by Bridon-Bekaert (dotted lines) with Static Elastic Stiffness for Polyester and Nylon Ropes [286] shown in Fig. 2-21

## 2.3. Anchor

Various anchoring solutions are accessible for maintaining the position of FOWTs. The selection of anchor type is contingent upon factors such as mooring configuration, seabed soil conditions, and holding capacity requirements. Appropriate anchoring systems encompass drag embedment, vertically loaded, gravity-installed anchors such as torpedo anchors, and suction pile anchors [221]. A compendium of the principal anchor types is delineated in Table 2-6, demonstrating established concepts extensively employed in the marine and oil and gas sectors [69]. Nonetheless, there exists substantial diversity even within these classifications. For mooring systems with a catenary configuration, drag embedment anchors are generally favoured due to cost-effectiveness. For systems with a taut-leg configuration, the remaining anchors in the inventory may be employed. The suction pile, recognized for its high resistance against vertical loads, is particularly well-suited for farm configurations where multiple mooring lines share the same anchor [304, 305].

**Table 2-6** Anchor Types Summary [1]

| Anchor System | Characteristics |
|---|---|
| **Drag Embedded**  | • Best suited to consistent residues, though not too stiff to obstruct penetration Horizontal loading at anchoring point.<br>• Horizontal loading<br>• Simple installation process<br>• Recoverable during decommissioning |
| **Driven Pile** 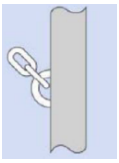 | • Applicable in a wide range of seabed conditions<br>• Vertical or horizontal loading<br>• Noise impact during installation (requires hammer piling)<br>• Difficult to remove upon decommissioning |
| **Gravity anchor**  | • Requires medium to hard soil conditions.<br>• Usually vertical loading, but horizontal also applicable<br>• Large size and weight can increase installation costs.<br>• Difficult to remove upon decommissioning |
| **Suction Pile** 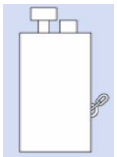 | • Application constrained by appropriate seabed conditions – not suitable in loose sandy soils or stiff soils where penetration is difficult.<br>• Vertical or horizontal loading<br>• Relatively simple installation, less invasive than other methods<br>• Easy removal during decommissioning |

## 2.4. Numerical Approach and Design Tool

The hydrodynamic analysis of offshore structures typically involves determining the sea states at the relevant site depth, selecting appropriate wave theory, choosing the suitable method for computing hydrodynamic loads, and calculating structural response [209]. It is crucial to consider fluid-structure interaction in the design of floating offshore wind turbines. The force on the floating structures and the motion of the platform resulting from these interactions are key aspects of marine hydrodynamics [306]. By considering fluid-structure interaction, the force on the floating structures and the motion of the platform caused by these interactions are one of the main subjects of marine hydrodynamics [307]. The hydrodynamics are mainly divided into two parts: the influence of fluid motions on the structures (diffraction) and the influence of moving structures that lead to wave generation (radiation) [308]. Hydrostatics should also be taken into account to consider the effects of buoyancy and hydrostatic restoring forces. The Morison equation and potential flow theory can be used to estimate hydrodynamic loads [309]. The Morison Equation is used to calculate hydrodynamic loads for slender structures with small diameters compared to the wavelength. For large-volume structures, diffraction and radiation are relatively essential, and potential flow theory is used to calculate the hydrodynamic loads acting on the platform [310].

The potential flow theory [220, 311, 312] is utilized in the design of marine structures to calculate hydrodynamics. This theory considers the flow around a body to be incompressible, inviscid, and irrotational, with negligible surface tension effects. The hydrodynamic loads that typically affect the response of floating wind turbines include first-order wave loads and second-order wave loads. In linear potential theory, the velocity potential and fluid pressure on the submerged surface of a body are solved using the Boundary Element Method (BEM) [313, 314]. The boundary element method is based on the concept of integrating the boundary conditions of a problem to obtain the solution. It works by dividing the boundary of the domain into small segments, known as boundary elements. These elements are then used to represent the solution in terms of the unknown boundary values. By doing this, BEM avoids the need for discretizing the interior of the domain, which is often computationally expensive and time-consuming [315]. Separate solutions are carried out simultaneously for the

diffraction problem, which examines the effects of incident waves on the body, and the radiation problem, which gives the effects of the body's motion for each of the prescribed modes. Each contribution of the first-order solution can be calculated distinctly and independently from the others [316].

Wave kinematics are determined through the application of Linear Airy wave theory [317] with adjustments for the free surface. Airy wave theory utilized a potential flow approach to explain the propagation of gravity waves on a fluid surface. The hydrodynamic loading encompasses contributions from linear hydrostatic restoring, nonlinear viscous drag based on Morison's equation, added mass and damping from linear wave radiation (including free-surface memory effects), and incident wave excitation from linear diffraction [308]. Forces and moments are expressed in terms of transfer functions. Added mass and radiation damping, hydrodynamic coefficients, wave excitation forces, and response operators are computed in WADAM. The calculations are solved by potential theory utilizing the 3D panel method and Green's theorem [318, 319]. Linearized radiation and diffraction problems can be resolved in the frequency domain for a platform using WADAM to calculate wave loads and motions of offshore structures [320]. The module solves the tensions within each mooring line for a given platform displacement by assuming that each cable is in static equilibrium at that moment and uses the resulting tensions to solve the dynamic equations of motion for the rest of the system [321]. The theoretical formulations and methodologies are outlined in detail in appendices A and B.

The comprehensive examination of FOWT in the time domain is essential for understanding the dynamics and effectiveness of FOWT systems. This involves considering factors such as wind, waves, and currents, as well as the interaction between the wind turbine and its immediate environment [322]. The fully coupled analysis in the time domain is crucial for the advancement, enhancement, and regulation of floating offshore wind turbines [323]. This analysis enables engineers and researchers to predict the performance of turbines under various environmental conditions, identify potential challenges and issues, and develop appropriate mitigation strategies [324]. Håland (2022) [325] provides an extensive overview of the existing literature on the time domain fully coupled analysis of floating offshore wind turbines, covering aspects such as modelling, validation, and practical applications. Gao (2022) [306] conducted a research investigation to compare the analysis of a

system that is both coupled and uncoupled. The study involved an OO-Star floater installed with a WINDMOOR 12MW wind turbine, under different environmental conditions. The objective was to examine the disparities between the two approaches. It was noted that the uncoupled method resulted in variations in response, even with the inclusion of second-order wave loads.

Regarding the numerical methodology for hydrodynamic analysis of FOWT, several numerical simulation tools [326-330] have been employed to investigate dynamic performance using first-order radiation and diffraction. However, the offshore oil and gas industry has highlighted the significance of second-order hydrodynamic loads for specific floating platforms [306]. The second-order wave loads primarily consist of mean drift force, sum- and difference-frequency wave loads. The sum-frequency and difference-frequency loads can stimulate the eigenfrequencies of offshore structures and may lead to substantial oscillations that can damage the floating structure [331]. For second-order results, a second-order free surface Finite Element Method (FEM) is necessary [332], which can be created using the HydroMesh meshing tool [333]. Newman's approximation method [334], widely accepted in the offshore industry, is based on the assumption that the natural frequency of slow-drift motion is sufficiently small so that the exact quadratic transfer function (QTF) for difference-frequency forces can be approximated by the mean drift force value, which is a second-order effect depending only on the first-order velocity potential and motions [335]. Second-order hydrodynamic loads are proportional to the square of the wave amplitude and have frequencies equal to both the sum and the difference of pairs of incident wave frequencies [306]. This suggests that, even though the natural frequencies of the structure are designed to be outside the first-order wave energy spectrum, the second-order loads could excite these frequencies. Therefore, despite the typically small second-order hydrodynamic loads, the resonant effect may be significant. Second-order wave exciting forces can be analysed in the frequency domain by decomposing them into three terms [336-338]. Several studies have been conducted to examine the significant impact of second-order hydrodynamics on FOWTs [316, 331, 339-343], as the second-order difference frequency wave diffraction forces are crucial for accurately modelling the overall response of FOWTs [344-346]. In the context of the second-order solution, the diffraction and radiation problems cannot be treated independently. The second-order velocity potential can be fully computed using the WADAM method [320].

Coulling (2013) [331] utilized Newman's approximation method in FAST to assess the influence of second-order wave force on the OC4-DeepCwind semisubmersible FOWT. The findings indicate that the second-order difference-frequency wave-diffraction forcing significantly impacted the global response of the DeepCwind semisubmersible FOWT. Roald (2013) [341] employed a technique to evaluate the effect of second-order hydrodynamics on two distinct floating wind concepts: a Spar and a TLP, both supporting the NREL 5-MW baseline wind turbine. The proposed approach primarily relies on simulation using the frequency-domain tool WADAM. The results reveal that the second-order wave forces are minimal for OC3-Hywind, while they are considerably high for UMaine TLP. Yan (2016) [332] proposed a computational fluid-structure interaction (FSI) framework for simulating the interaction between free-surface flow and FOWT, which investigated full-scale free-surface simulations of the OC3-Hywind floating wind turbine design subjected to wave action. The comparison of the computational results with experimental and simulation data demonstrated good agreement. Zhang (2020) [306] examined the effects of second-order hydrodynamics on the response of three semisubmersible floating offshore wind turbines (the V-shaped semisubmersible floating platform, the Braceless semisubmersible floating platform, and the OC4-DeepCwind), where hydrodynamic analysis included second-order hydrodynamic and viscous effects, indicating that the complete QTF method should be employed to better calculate the second-order wave force for simulating the realistic dynamic response of semisubmersible FOWTs.

Several studies have utilized linear frequency-domain analysis, a method commonly used in the offshore oil and gas industry [341, 347-349]. However, these studies have a notable limitation in that they are unable to capture the nonlinear dynamic characteristics and transient events essential for analysis. In response to this limitation, several studies have attempted to address the need for coupled analysis in the context of offshore floating wind turbines. For instance, Fulton (2006) [350] and Withee (2004) [351] introduced different time-domain aero-elastic wind turbine simulators, demonstrating that platform motions have minimal impact on power capture and rotor loads, which are primarily influenced by rotor aerodynamics. However, they also revealed that platform motions significantly affect nacelle and tower loads, which are predominantly influenced by inertia. Consequently, strengthening the tower is necessary if platform motions cannot be reduced.

In more recent analyses, Nielsen, Hanson, and Skaare [352, 353] and Larsen and Hanson [354] utilized a combined aero-servo-elastic, hydrodynamic, and mooring program to design a deep-drafted Spar buoy, Hywind, to support a 5-MW wind turbine and develop its corresponding control system. This study was particularly important because the computer program simulations were validated by the response of a scaled-down model in a wave tank experiment.

The advancement of floating wind turbines depends on accurately predicting extreme loads on the turbine, its floating substructure, and its mooring system [355]. Such predictions can only be achieved through simulations that simultaneously account for the hydrodynamic loads and response of the floater, as well as the aeroelastic loads and response of the turbine. Furthermore, the limitations of previous time and frequency domain studies on floating offshore wind turbines have spurred the development of simulation capabilities for modelling such systems in a fully coupled aero-hydro-servo-elastic response [356]. A structural model coupled with a hydrodynamic load model is known as a hydro-elastic model, while the relationship between aerodynamic loads and structural response in an elastic structure is called an aero-elastic model. When an aerodynamic model, a hydrodynamic model, a structural model, and a controller theory are combined, a hydro-aero-servo-elastic model considers the dependencies of all these effects [357].

Furthermore, alongside the development of floating concepts, a range of numerical codes and software, including FAST [358], HAWC2 [359], DNV SIMA [360], OrcaFlex, [361], have been tailored to enable thorough analysis of integrated wind and wave loads and responses using a time-domain approach.

FAST (Fatigue, Aerodynamics, Structures, and Turbulence) [358] with AeroDyn [362, 363] developed by the National Renewable Energy Laboratory, which addresses the limitations of previous time- and frequency-domain studies [364]. HydroDyn [365] utilizes a hydrodynamic subroutine package to calculate the applied hydrodynamic forces.

Another simulation tool, the SESAM package [366, 367] is capable of analysing FOWTs. The package includes GeniE [368] , HydroD [369], DeepC, and SIMA. GeniE [368], allows for various modelling strategies, such as concept or high-level modelling of structural components, to create finite element mesh files for the floating wind

turbine support structure [370] which can be used as inputs in HydroD for the hydrodynamical coefficients needed. HydroD [371, 372] is used to calculate the hydrodynamical properties of the substructure, and the Wadam analysis is employed to compute the hydrodynamic outputs. These outputs are then used in a simulation to couple wind, wave, and current effects [373]. HydroD uses the panel model specified in GeniE as the primary FEM model. All the panels on the wet surface must have hydrostatic pressure or wet surface properties [367]. After HydroD has provided the necessary values, they will be imported into DeepC or into an environment where wind, wave, and current can be coupled, such as SIMA. DeepC [374] is an interactive program that models floating configurations attached to the seabed with mooring lines, tension legs, and risers. It provides a comprehensive and accurate analysis of mooring systems in the time domain. This software system is based on the programs RIFLEX [375] and SIMO [376].

The SIMA program is a computer simulation and analysis tool designed for marine operations and floating systems [377]. Several studies have utilized the SIMA workbench to analyse Floating Offshore Wind Turbines (FOWTs) [378-380]. SIMA supports several physics engines that can operate independently or in conjunction with each other [360]. SIMO is used to model marine operations [376, 381]. RIFLEX is Used to model a system consisting of slender elements [375, 382]. RIFLEX Coupled, SIMO and RIFLEX coupled, is used to simulate slender, elastic structures in marine operations.

SIMO, developed by MARINTEK, is a general-purpose time-domain program for modelling offshore structures and marine operations [376, 382]. SIMO has also been coupled with the nonlinear FEM code RIFLEX by Nielsen and Skaare [352, 383]. SIMO is designed for the simulation of the motions of floating structures. It integrates hydrodynamic and aerodynamic forces to analyse the behaviour of offshore structures under various environmental conditions and RIFLEX is specialized for the analysis of slender marine structures such as mooring lines. It focuses on the structural response of these components under dynamic loading [384].

To model a complete FOWT system, an external module can be added to simulate rotor aerodynamic forces, such as TurbSim [385] and implemented in SIMO as an external force. Hansen (2006) [386] and Jonkman (2007) [387] made progress in

integrating of aeroelastic codes with hydrodynamic modules. TurbSim is a stochastic, full-field, turbulent wind simulator that utilizes a statistical model to numerically simulate time series of three-component wind-speed vectors at points specified in a two-dimensional vertical rectangular grid fixed in space [385].

OrcaFlex, developed by Orcina [361], is a software tool utilized for the analysis FOWTs, providing features for conducting hydrodynamic and structural dynamic simulations [388]. While OrcaFlex offers a user-friendly interface, attaining expertise in its comprehensive functionalities and features requires substantial time investment and focused practice [389]. Additionally, conducting complex simulations may necessitate considerable computational resources and advanced hardware specifications [390]. Another program is designed to model and dynamically analyse the floater and mooring lines, and it can be integrated with aerodynamic simulation tools such as FAST via the FASTlink interface [388]. However, this program presents a steep learning curve, especially for users lacking a background in wind turbine dynamics and control systems. Additionally, its interface is less intuitive, as it relies on text-based input files and command-line operations. Consequently, complex simulations may require significant time and computational resources [391].

Furthermore, coupling modules developed by Innosea [392] and Siemens Gamesa Renewable Energy [393] facilitate integration between BHawC software and OrcaFlex software [394]. Atalay (2022) conducted a comparative study between OrcaFlex and SIMA to analyse the FOWT hybrid substructure. The study concluded that discrepancies primarily stem from differences in wind input and the docking cone issue with the current SIMA values [395]. The study carried out by Fabian F. Wendt, Amy N. Robertson, and Jason M. Jonkman as part of the OC5 project reveals that numerical models, including FAST, tend to underpredict loads and motions compared to experimental data. The paper discusses several calibration studies aimed at improving the agreement between simulations and experimental results, highlighting the need for adjustments in wind-field-specific parameters, hydrodynamic and aerodynamic modelling approaches, and rotor and tower models [396].

Consequently, there is a critical need for ongoing calibration and validation efforts to improve the accuracy and dependability of the FAST model. Furthermore, achieving proficiency in the comprehensive functionalities and features of OrcaFlex requires a

significant investment of time and dedicated practice. Additionally, executing complex simulations may demand substantial computational resources and advanced hardware specifications. In contrast, SIMA methodologies have proven effective in the analysis of floating offshore wind turbines within both academic and industrial research settings. Therefore, this thesis employed the SIMA software to conduct analysis of FOWT due to its comprehensive coupled analysis, advanced modelling capabilities, visualization and simulation, integration with other tools, widespread acceptance and application.

## 2.5. Cost

The primary obstacle currently confronting the FOWT industry and research is the need to develop economically efficient floating systems that can effectively compete with fixed-bottom offshore turbines in terms of CAPEX and LCOE [397]. Several studies have conducted LCOE analyses of FOWT farms, considering varying water depths, distances from shore, and FOWT concepts [17, 398].

As illustrated in Fig. 2-24, the main cost driver of a FOWT system is the support platform. Therefore, advancements in platform design and mooring systems offer the greatest potential for reducing the overall cost of FOWT systems [1]. The cost of the platform structure is directly proportional to its mass, encompassing material, fabrication, and installation expenses. The substructure of a FOWT system can account for approximately 29.5% of the system's CAPEX [399]. Additionally, the cost of mooring lines is modelled as a linear function of their combined length and the maximum steady-state tension they must endure [400]. Consequently, simplifying the design of the FOWT support platform is a critical factor in reducing material and fabrication costs, and an innovative platform design that can be constructed and assembled in a port before being towed to the deployment location would significantly decrease installation expenses.

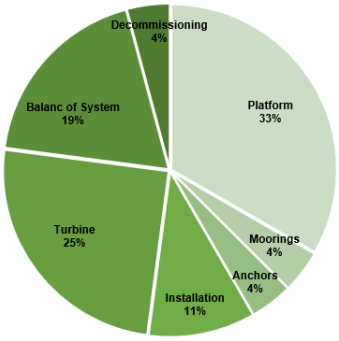


**Fig. 2-24** FOWT System Reduction in Capital Expenditure [1]

In shallow waters, the LCOE for the catenary mooring system experiences a significant increase due to the longer mooring lines. However, alternative mooring solutions have the potential to enhance both the LCOE and CAPEX [209]. A study involving a scaled wave energy converter demonstrated that compliant taut mooring lines of varying stiffness can achieve the desired dynamic response [401] and indicated the possibility of cost reduction [402]. Therefore, it is pertinent to investigate whether similar outcomes can be observed for FOWTs and to identify the essential parameters to be considered in the design process.

Laura (2014) [398] identified water depth and proximity to the shore or shipyard as influential factors affecting the LCOE, emphasizing the need to optimize FOWTs for competitiveness and the necessity for further research to achieve cost-competitiveness.

Myhr (2014) [17] conducted a study to examine the impact of water depths on the LCOE for FOWTs compared to fixed-bottom counterparts. The study found that as water depths increase, the LCOE of FOWTs rises at a slower rate, making more complex mooring systems with lower steel mass economically feasible in shallower waters, and those with larger steel mass more suitable for intermediate water depths. Myhr (2014) suggested potential future improvements, such as exploring different mooring options and soil conditions, and considering the scaling effects through mass production for mooring lines and anchors. Furthermore, Myhr (2016) [180] investigated the LCOE assessment to compare the TLB design with other concepts, highlighting its potential to drive costs down not only during construction but also throughout the lifetime of the structures, particularly when producing them in large quantities. One of the designs proposed by Myhr showed promise in competing with onshore wind

turbines in terms of LCOE. Therefore, the LCOE value of FOWT is significantly influenced by water depth and distance from shore, primarily due to mooring costs and the length of export cables.

An alternative approach to reducing the LCOE and CAPEX for FOWT involves the utilization of lightweight synthetic mooring lines with established long-term durability, high residual strength, and compliance [264]. Research indicates that fibre rope mooring systems for floating wind turbines have the potential to halve mooring costs compared to chain systems [293]. However, challenges persist due to limited data on long-term properties, particularly for nylon, and a lack of detailed finite-element representations of fibre ropes in design software, as well as a lack of experience with fibre ropes among wind energy engineers [196].

A study by Bach-Gansmo (2020) [403] examined the impact of two parameters for a taut-compliant mooring system on a 10 MW floating offshore wind turbine, demonstrating significant potential for the taut-compliant mooring lines in terms of hydrodynamics and maximum line loads, with a potential reduction in footprint and line loads compared to the original catenary station-keeping system. Consequently, a less complex system utilizing synthetic mooring lines has the potential to reduce costs [404], especially in shallow water, due to the lower elastic stiffness and capital cost of synthetic fibre rope mooring systems [198].

Another approach to cost reduction in floating wind farms involves the utilization of shared anchors for mooring lines, resulting in a multi-line anchor configuration [405]. This configuration reduces the quantity of anchors needed for installation and minimizes the amount of geotechnical site investigations required [406]. Goldschmidt (2015) [407] conducted a study on anchor sharing for various wind farm layouts, demonstrating that the number of anchors can be reduced as FOWTs are also moored to each other, leading to potential cost savings of up to 60% in the mooring system and 8% in the overall FOWT system. Hall and Connolly (2018) [408] focused on the interconnected dynamics of shared mooring lines. They discovered that shared mooring lines possess intricate restoring properties and experience significant fluctuations in mooring line tension. Fully coupled simulations of multiple FOWTs with shared moorings are also explored, as demonstrated by Chow (2019) [409]. Connolly and Hall (2019) [410] investigated wind farm layouts with shared moorings between

the FOWTs, revealing that cost reduction is achievable. They also found that appropriate line properties can restrict the tension in the mooring lines for shared mooring farms.

By utilizing shared anchors in offshore wind farms, the quantity of anchors is decreased. Additionally, the anchors may also experience reduced loads in the horizontal direction while facing increased load in the vertical direction [406]. Fontana ( 2018) [304] found that the number of anchors in 100-turbine FOWT farms can be reduced by 60% with the use of 3-line anchors and by 79% with 6-line anchors. However, the use of multiline anchors can lead to susceptibility to rapid load direction reversals due to mooring line connections from multiple directions, and a decrease in multiline reliability if one of the connected mooring lines fails [411]. Diaz (2016) [412] also discusses the suitable anchor types for shared anchor layouts, emphasizing the potential cost reduction of innovative anchor systems/shared anchor points due to the high installation costs of anchors.

When comparing the CAPEX of TLB systems with other concepts, it is recommended to focus on mooring, production, and installation costs specific to a particular site, as there are significant uncertainties and variations among different estimates and LCOE analyses [180]. Since the platform for an FOWT system accounts for approximately one-third of the capital expenditure, optimizing or developing a new FOWT design to improve the substructure of the FOWT system could provide an effective approach to reducing costs [399]. Additionally, considering the complex dynamic behaviour of FOWT systems, an appropriate optimization framework is crucial for balancing the design and optimization of the substructures and managing computational costs [413]. One additional expense associated with FOWT pertains to the adaptation of the control system, which is a costly endeavour due to the requirement for specialized hardware, software, and expertise [414]. Although the precise cost may vary, projections indicate that the overall expense per turbine can fall within the range of $5 million to $10 million [415]. As the floating wind turbine technology and market continue to advance, it is probable that the cost of adapting control systems will diminish as economies of scale and technological progress are achieved [416].

## 2.6. Design Analysis and Optimisation

The importance of reliability and cost-effectiveness in the FOWT system is essential. Economic modelling plays a significant role in assessing the cost advantages of new FOWT configurations [417]. The floating support structures have been specifically engineered to provide a stable and rigid platform for the tower and turbine, drawing from the design principles of bottom-fixed offshore wind turbines. Additionally, an integrated optimization of the floating platform, mooring system, tower, rotor, and controllers enables the development of a comprehensive system with a less rigid and lighter substructure [185]. Due to limited experience in designing, manufacturing, installing, and operating FOWT systems, assumptions and models related to cost components are associated with significant uncertainties [418]. A parameterization that covers the entire design space is essential to establish a global optimization framework for the support structure [400]. Several studies have focused on the design optimization of FOWT using various methods [185, 413, 419, 420]. For instance, Tracy (2001) [421] conducted a parameterization study of a cylindrical platform with variable dimensions and mooring lines, presenting a parametric approach to the design of the support platform for FOWT. This approach draws on relevant design concepts from the offshore oil and gas industry and identifies suitable combinations of structures and mooring systems that meet the requirements for a generic 5MW wind turbine. Leimeister (2021) [420] asserted that reliability-based design optimization (RBDO) methods are a promising approach for optimizing systems when classification and standardization are not fully available. Leimeister selected the OC3 as a reference FOWT system and specified design variables, objective functions, limit states, environmental conditions, stochastic variables, reliability criteria, and optimization constraints.

To develop a FOWT substructure, the essential criteria for a successful support structure design are comprehensively outlined in DNV-OS-J101 (2013) [422] and DNVGL-ST-0119 (2018) [250]. The initial/conceptual design of a FOWT involves an iterative process, commencing with a reference design and progressing to a more detailed design and analysis of the loads and the system's response to ensure that the structural integrity is adequate to withstand the load effects [250]. Various studies on the preliminary design of a floating substructure [164, 423, 424] have indicated that

the preliminary design can be segmented into two stages: the initial sizing of the support structure's concept, followed by the design for further development and refinement.

## 2.7. Technical Challenges

The design and construction complexity of the platform need to be reduced to lower the overall cost of FOWT while also introducing an optimal solution for the mooring system [83]. The critical point for developing concepts within each form of technology is to consider at an early stage in the design process that the design capabilities are as flexible as possible, thus facilitating the adaptation of the platform to a range of installation sites [180]. The technical challenges associated with FOWT designs [15, 16] can be categorized into various areas, including design standards and tools, wind turbines, support structures, moorings and anchors, and installation and maintenance. Each of these categories will be discussed in detail.

### 2.7.1. Design Standard and Tool

The advancement and manufacture of efficient and cost-effective floating wind turbines require dependable and sophisticated design tools that can fully integrate the dynamics and response of floating wind turbine platforms [352, 387]. The computational speeds of these tools are influenced by various factors, such as user-selected discretization, enabled code features, and specific details of the coupling scheme in the case of coupled codes. Without a comprehensive understanding of these variables, a direct comparison of the computational speeds of the presented codes is unfeasible [350]. However, it can be generally stated that codes with more complex coupling schemes will have slower computational speeds.

The offshore oil and gas industry has demonstrated the significance of second-order hydrodynamic load for specific floating platforms [306], as the second-order difference frequency wave-diffraction forces are crucial for accurately simulating the global response of the FOWT [344-346]. Conversely, the use of linear frequency-domain analysis, commonly employed in the offshore oil and gas industry [341, 347-349], has

a limitation in capturing the nonlinear dynamic characteristics and transient events essential for the analysis of FOWT. The development of floating wind turbines relies on accurately predicting extreme loads on the turbine, its floating substructure, and its mooring system [308]. To achieve this, and due to limitations of previous time and frequency domain studies on floating offshore wind turbines, there is a need to develop simulation capability for modelling such systems in fully coupled aero-hydro-servo-elastic response [356].

Due to a lack of installation and operational experience using floating offshore wind turbines, designs may be overly cautious, leading to uneconomical costs. Therefore, it is crucial to focus on enhancing design knowledge early in demonstration projects, including analysis of observed behaviour and feedback to the design process, to avoid overdesign of the system and achieve significant cost savings.

### 2.7.2. Wind Turbines

The existing turbines have been adapted from designs originally intended for land-based wind turbines and fixed-bottom offshore structures. Therefore, it is crucial to understand the design constraints specific to FOWT, particularly in relation to the rotation and acceleration of the rotor nacelle assembly, and to devise appropriate control systems. It is advisable to promote cooperation between wind turbine designers and designers of floating support structures to achieve optimal system design [425]. In terms of aerodynamics, the substantial low-frequency movements of the platform experienced by floating offshore wind turbines result in flow conditions that can be significantly more intricate than those experienced by traditional land-based or fixed-bottom offshore wind turbines, and which are not accounted for by Blade Element Momentum theory (BEM). Notable pitch and surge movements result in a change in the interaction between the rotor and wake [387].

One of the expenses related to FOWT is the construction of the tower, which requires a focus on reducing weight and costs by adjusting the tower's diameter and thickness along its length [426]. This can be accomplished by altering the mass of the tower or reducing its height [189]. Decreasing the height of wind turbine towers can lead to significant cost savings during construction and installation, as well as improving the

overall safety and efficiency of maintenance operations [154]. Additionally, reducing the height of these towers and integrating them into FOWT platforms can help reduce the degradation and overturning bending moments of the wind turbine [166, 427]. Another cost consideration for FOWT is the requirement for a control system customized to the hydrodynamic characteristics of the platform [414]. To mitigate expenses related to the tower, it is feasible to reduce the tower height and allocate the to the support platform, thereby improving system stability, reducing overturning bending moments, and lowering costs [428].

### 2.7.3. Support Structure

As a result of the underdeveloped state of the industry, a thorough examination of the interconnected response of the wind turbine, floating platform, and mooring system is crucial for achieving substantial cost savings and ensuring the safe and reliable performance of the entire system. Support structures for FOWT have not yet been fully refined, and there is a need for cost reduction [19].

While concepts such as Semi-Submersible, Spar, and TLP are widely studied in academic and industrial research, the most cost-effective platform has yet to be developed. The current LCOE values are heavily influenced by the design of the support structure, mooring line, water depth, and distance from shore [61]. To decrease the cost of FOWT, the complexity of platform design and construction must be reduced, while also implementing an optimal solution for the mooring system [83].

Therefore, designers must carefully weigh the advantages and disadvantages of each support platform to achieve the most cost-effective system design, and projects should showcase innovative solutions for cost reduction through optimization, drawing from early projects to enhance next-generation designs. Understanding the essential relationship between turbine rating and platform size and optimizing designs based on demonstrated projects will be advantageous. Therefore, optimizing the substructure system is crucial for minimizing motion responses [429].

### 2.7.4. Mooring System

Several industrial projects have examined the design challenges of mooring systems for floating wind turbines in shallow water. Researchers have also investigated the design considerations of mooring systems for floating wind turbines in shallow water, as discussed in Section 2.2.3 and its subsections. The focus has been on the influence of water depth on design parameters rather than on sophisticated structural design at a specific water depth. More knowledge of the dynamic behaviour of moorings, especially in shallow waters, is necessary for mooring design. Regarding mooring design, there is a need for a deeper understanding of the dynamic behaviour of moorings, particularly in shallow waters. Research conducted by Xu (2021) [198] has shown that the impact of drag resistance and inertial effects of mooring lines is relatively limited in shallow water. Consequently, the primary challenge in design lies in effectively combining elastic and geometric stiffness.

The INNWIND.EU and LIFES50+ [430, 431] projects have introduced the technique of moving the fairlead from underwater to above water level to design floating wind turbines, artificially increasing the adequate water depth from the fairlead to the seabed and improving the mooring line tension characteristics. Moving fairleads below the waterline ensures sufficient draft to allow vessels to approach the platform for service and maintenance operations. One potential disadvantage of this approach is the corrosion and fatigue concerns, especially for chain links and steel wires, which can be overlooked when using fibre mooring materials.

Drawing lessons from the oil and gas industry can be beneficial in understanding how existing techniques can be adapted. However, the experience with synthetic fibre ropes in the oil and gas sector is primarily for deep and ultra-deep water. The material properties and structural behaviour of synthetic fibre ropes are more complex than those of chain cables and steel wire ropes. Current industrial practice utilizes the upper-bound and lower-bound methods [299], which are conservative and inconsistent because the offset is obtained based on a lower-bound stiffness model. At the same time, the dynamic tension is estimated using upper-bound stiffness model. By systematically analysing the mooring system under different conditions and using a combination of static and dynamic analysis, empirical data, and numerical simulations, can establish lower and upper bounds for mooring stiffness.

Innovative anchor systems or shared anchor points can reduce the high costs associated with anchor installation [407].

### 2.7.5. Installation, Operation and Maintenance

The installation procedures vary depending on the floater types. Generally, the installation of floating wind turbines requires a greater number of vessels compared to fixed wind turbines. However, these vessels are cost-effective to hire and readily available [432]. While numerous floating wind concepts have been developed, only a few have been successfully deployed and commissioned for commercial use. For example, the Spar-type substructures used in the Hywind Scotland wind farm have high draft, requiring offshore assembly. The installation process involved tasks such as towing, upending, ballasting, de-ballasting, and mating [433]. During ballasting, a rock installation vessel with a loading arm was employed to load solid ballast into the substructure, while simultaneously de-ballasting water was performed to maintain the draft [434]. The installation spanned nearly eight months [435] (refer to Fig. 2-25), and a challenge arose due to the wave-induced motions of the Spar floater during installation [436]. Notably, the installation of Hywind involved the use of an expensive heavy-lift vessel. Future cost reductions can be achieved through innovative installation methods that eliminate the need for such vessels [434]. Different types of FOWTs have distinct advantages and disadvantages in terms of installation, operation, and maintenance [69, 93, 99], as summarized in Table 2-7.

It is imperative to explore the most effective approach for installing FOWTs and to develop an innovative system design. Identifying knowledge gaps, researching trends, and reviewing innovations at various development stages are crucial for reducing installation costs. Emphasizing a design that can be constructed and assembled in a port and then towed to the deployment location is essential. It is important to note that technological advancements play a significant role in cost reduction, which can be addressed through engineering design and philosophical initiatives [437].

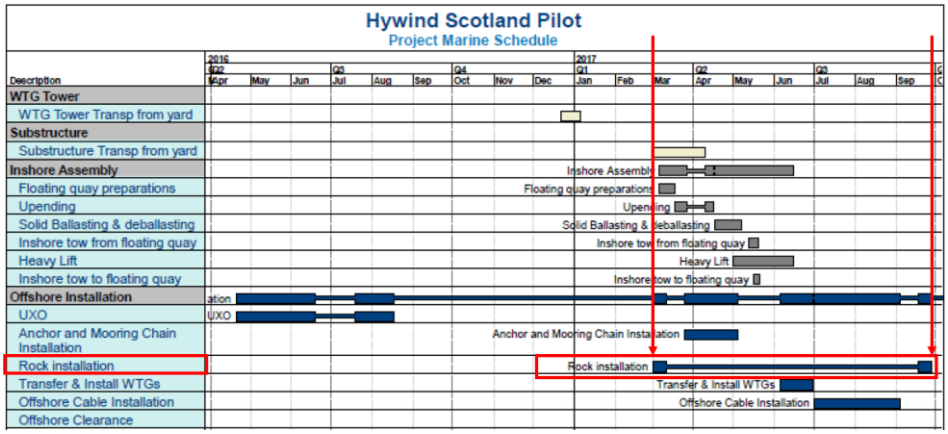


**Fig. 2-25** Hywind Scotland Pilot Park Project Plan for Construction [438]

**Table 2-7** Advantages and Disadvantages Concerning installation, Operational and Maintenance of Different Floater Types of FOWTs [434]

| | Installation | Operation and Maintenance |
|---|---|---|
| **Semi-Submersible** | Simple installation<br>Completely assembled at the quayside<br>Short installation time<br>Low installation cost<br>More sensitive to wave height limits | Simple unhook from mooring system.<br>Can be towed back to quayside for major repairs.<br>No heavy-lift vessels required |
| **Spar** | High draught makes installation difficult.<br>Requires heavy lift vessels.<br>Unstable motion of floater during mating<br>High installation cost<br>Requires deep water ports and sheltered areas. | Heavy-lift vessels might be required for major repairs.<br>Needs deep water ports and sheltered areas for repairs |
| **TLP** | Can be completely constructed onshore.<br>Slow and lengthy installation process<br>High installation cost<br>Bespoke barge required.<br>High environmental impact | Difficult to unhook, more onsite repairs.<br>Mooring system highly susceptible to failure |

## 2.8. Aim and Objectives

As the demand for installed capacity increases and shallow water nearshore sites becomes depleted, projects will need to be developed further from shore and in deeper water. In such cases, the cost of fixed-mounted offshore wind turbines becomes economically inefficient. Therefore, the installation of FOWTs can be the most cost-effective and practical solution in deep-water areas. The literature review section highlights several key issues with current FOWTs:

- The most promising sites for deploying FOWT in the UK are off the coast of Scotland, where near-shore deep-water sites are located [93]. The water depth of these locations ranges from 95 m to 120 m [96].
- The current LCOE value of FOWT is heavily influenced by the design of support structures and mooring lines. Four different types of FOWT support platforms have been widely researched in academic and industrial circles [19, 55, 164]. However, there is no ideal category of support platform, and the optimal cost-effective platform design is yet to be determined [100]. An innovative solution for the FOWT support structure is needed to address constraints in cost complexity, infrastructure, and installation for large-scale deployment [184]. This is essential to achieve significant cost reduction from the prototype to the commercial phases of development by avoiding design complexity and reducing system material and fabrication costs [1].
- The power capacity of wind turbines has significantly increased to reduce the LCOE. This increase in capacity has resulted in the deployment of larger turbines, as well as the use of floating platforms for offshore installations, presenting additional complexities and challenges [146].
- The design of mooring systems for FOWT is a crucial aspect in reducing the overall cost of the FOWT system. This design depends on the characteristics of the support platform and the water depth. Catenary mooring systems offer advantages in terms of installation and response characteristics due to lower tensions. However, they also permit large offsets, potentially limiting the number of turbines that can be installed in a specific area. Given that most FOWTs are expected to be deployed in shallow waters with depths less than 200 meters [206], it becomes feasible to employ a semi-taut (or taut) mooring

design for FOWTs in such water depths, as opposed to catenary mooring. This alternative design also contributes to an improvement in the LCOE [218].

- The knowledge and application of fibre rope in the oil and gas industry have primarily focused on deep and ultra-deepwater operations. Nevertheless, there is significant potential for the utilization of fibre rope in shallow water mooring due to its reduced elastic stiffness and lower capital cost, an aspect that has not been extensively addressed previously. There remains a need for the development of commercially available mooring analysis programs capable of simulating the nonlinear change in length response [209, 258].
- In relation to the benefits and drawbacks of support platforms for FOWT during installation and maintenance, a design that can be fabricated and assembled at the port and subsequently towed to the deployment site would offer substantial cost reduction for installation [434]. To facilitate maintenance, fairleads positioned below the water level could ensure sufficient draft, allowing vessels to reach the platform for servicing and maintenance activities.
- Shared anchors for mooring lines, resulting in a multi-line anchor configuration is an approach to reducing cost in floating wind farms [405] which leads to potential cost savings of up to 60% in the mooring system and 8% in the overall FOWT system [407].

Through a comprehensive review of existing literature on FOWTs, this study aims to address the key issues associated with current FOWTs by employing a reliable numerical analysis to develop an innovative configuration for a FOWT platform and mooring system. The proposed design aims to demonstrate the TLB concept for deploying offshore wind turbines in the shallow waters of the Northern North Sea region. The system was designed to provide structural support for a 10 MW wind turbine, meeting both static and dynamic operational and survival criteria while minimizing motion responses. This approach will facilitate the adaptation of a control system originally designed for onshore wind turbines, thereby eliminating the need to develop a new control system customized specifically for offshore wind turbines. The study has outlined specific objectives to achieve the stated aim.

- Produce a conceptual design for a novel FOWT system, emphasizing an optimal mooring solution that reduces construction complexity and effectively controls motion responses to acceptable levels.

- Develop a mooring system arrangement suitable for shallow waters that can accommodate minor movements while ensuring a stable foundation for offshore wind turbine installations. This configuration should eliminate the need to create platform-specific control systems to facilitate the installation of turbines on floating platforms.
- To examine the dynamic response attributes of the floating system in the environmental conditions of the northern North Sea, with a water depth of 110m, it is necessary to establish design load cases that encompass a range of environmental scenarios, from steady to extreme weather events. These cases should account for various operational conditions, in order to accurately represent real-world design situations.
- Utilize both frequency domain and time domain analyses to precisely predict the extreme tension response in the early phases of the design process, to attain adequate accuracy in forecasting mooring line loads and to enable subsequent design enhancements.
- Conduct a comprehensive analysis of the aero-hydro-servo-elastic behaviour in the time domain, integrating the complete turbine-structure-mooring system to account for dynamic interactions, non-linear effects, and interdependencies among the system components.
- Investigating the feasibility of utilizing mooring lines constructed from polyester and nylon for FOWT platforms.
- Examine the platform's response in the event of a mooring line malfunction.
- Utilize an aero-hydro-servo-elastic software to compare and evaluate different support platforms for floating offshore wind turbines.
- Examine the feasibility of implementing a wind farm using FOWT with an anchor-sharing concept.

## 2.9. Rules and Regulations

According to DNV-ST-0119 (Design of Floating Wind Turbine Structures) [439] to adequately capture effects associated with the natural frequencies of floating support structures during the calculation of loads and responses, it is essential to extend the duration of the simulations being conducted. It is advised to extend the simulation periods beyond the conventional 10-minute default setting. A minimum duration of 3 hours is suggested to effectively capture phenomena such as nonlinearities, secondary effects, gradual responses, and to appropriately determine the design load effects.

The results will be assessed in accordance with the guidelines and regulations set by DNV [440], specifically focusing on the recommended values for motion responses and nacelle acceleration at the serviceability limit state. The prescribed limitations on response motion stipulate that the tilt inclination should not exceed an average value of 5° and a maximum value of 10° during operational conditions, with a permissible maximum of 15° during non-operational conditions. The design against the accidental limit state (ALS) aims to ensure that the mooring can withstand the loads in an intact station keeping system under accidental load conditions and retain adequate capacity if mooring lines fail due to reasons beyond the designer's control. According to DNV-RP-0286 [440], the load pattern of an anchor shared by multiple mooring lines may significantly change if one of the attached lines breaks or fails. In the case of a taut mooring system distributed in multiple clusters, it should be assumed that one mooring line will fail at each cluster. The modified load pattern should be considered when evaluating system stability performance in the ALS post-accidental damaged condition. Furthermore, according to DNVGL-ST-0437 [439], the inclination angle after damage should not exceed 17°.

As per the guidelines outlined in DNV-OS-J103 [441], the determination of the design tension, denoted as $T_d$, is achievable through the utilization of Eq. (8). This equation incorporates load factors, $\gamma_{mean}$ and $\gamma_{dyn}$ , as specified in Table 2-8. Additionally, $T_{c,mean}$ represents the characteristic mean tension, while $T_{c,dyn}$ denotes the characteristic dynamic tension.

$$T_d = \gamma_{mean}.T_{c,mean} + \gamma_{dyn}.T_{c,dyn} \quad (8)$$

**Table 2-8** Mooring Lines Design Load Factor Requirements

| Limit State | Load Factor | Safety Class | |
|---|---|---|---|
| | | Normal | High |
| ULS | $\gamma_{mean}$ | 1.30 | 1.50 |
| ULS | $\gamma_{dyn}$ | 1.75 | 2.2 |
| ALS | $\gamma_{mean}$ | 1.00 | 1.00 |
| ALS | $\gamma_{dyn}$ | 1.10 | 1.25 |

For ultimate limit state (ULS), $T_{c,mean}$ should be taken as the maximum loaded line tension given environmental loads with a 50-year return period. $T_{c,dyn}$ should be taken as the worst dynamic part of the line tension caused by oscillatory LF and WF excitation for a 50-year return period. For accidental limit state, the components are to be found through a similar deduction, but with a 1-year return period. The characteristic capacity of the mooring lines, $S_C$, is given in DNV-OS-J103 [441], and is shown in Eq. (9), where $S_{mbs}$ is the minimum breaking strength (MBL).

$$S_C = 0.95 S_{mbs} \tag{9}$$

The design criterion for ULS and ALS is given in DNV-OS-J103, as expressed in Eq. (10).

$$S_C > T_d \tag{10}$$

As investigating nacelle accelerations in floating wind turbines is essential for ensuring structural integrity, optimizing performance, maintaining safety, understanding environmental interactions, improving design, and enhancing economic viability, DNVGL-RP-0286 [440] provides guidance on limitations, the maximum nacelle acceleration should be 0.3 g (2.943 m/s$^2$) in the time series for the operational load cases, and should have a limit of 0.6 g (5.886 m/s$^2$) in the time series for the survival events.

## 2.10. Approach

The approach employed to accomplish the objectives of this thesis is illustrated in Fig. 2-26, depicting the methodology utilized. The flowchart visually represents the interrelatedness of each chapter, thereby contributing to the overall aim of the research endeavour.

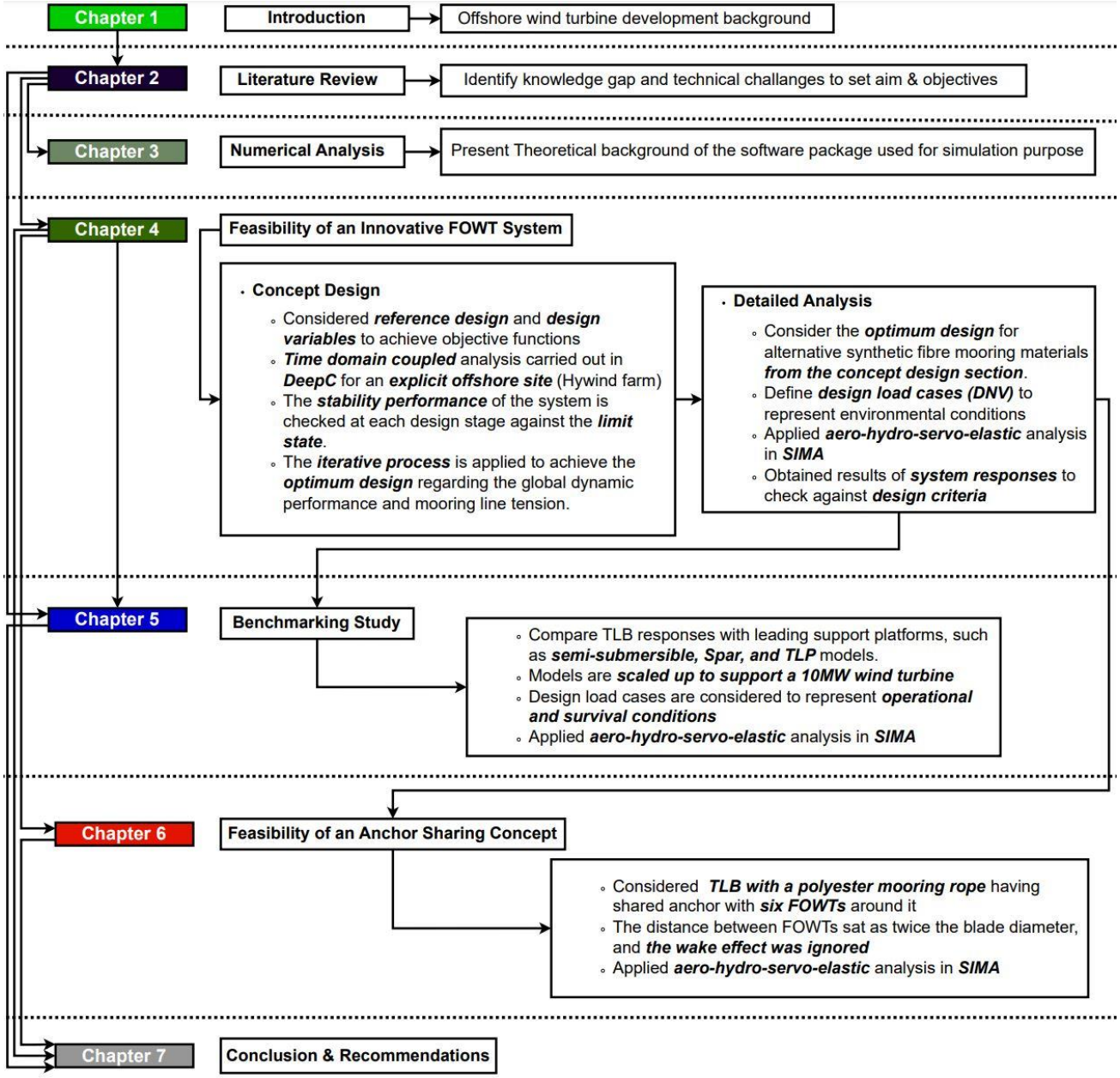


**Fig. 2-26** Methodology Flowchart

Section 3 provided numerical analyses and theoretical foundations briefly followed by providing the software package used for simulation. Comprehensive detail of theoretical formulations and methods provided in the Appendix A and B. Section 4 explores the investigation of optimization and the development of a new FOWT design to enhance the substructure and reduce costs. This involves an initial design process, starting with a reference design and progressing to detailed design and load analysis to ensure structural integrity. Section 5 presents the results of a benchmark study on aero-servo-hydro-elastic codes for dynamic simulation of offshore wind turbines. The responses of the detailed design in Section 5 are compared with three different support platforms to validate an innovative design. These platforms are designed to support a 10 MW wind turbine; however, the results obtained from these platforms may not be representative of all types within these categories. Section 6 discusses the feasibility of a novel FOWT support platform with an innovative mooring layout utilizing shared anchors.

# 3. Numerical Modelling and Analysis Method

## 3.1. Theory

This research conducted analyses in both the frequency domain and the time domain. Frequency domain analysis involves solving responses at various frequencies by applying potential flow theory, which assumes inviscid, incompressible, and irrotational fluid properties. This theory allows the use of potential flow theory to describe flow around floating structure, with linear potential flow theory applied for small amplitude waves and linear structure responses. Boundary Element Method (BEM) is utilized to solve the potential flow equations. In this method, the surface of the structure is discretized into panels, and the boundary conditions are applied to solve for the potential flow around the structure. hydrostatic calculations are done to determine the stability and buoyancy of floating structures. This involves calculating the equilibrium position and righting moments based on the geometry and weight distribution of the structure. The interaction between waves and the structure is modelled using wave theories such as Airy wave theory (linear wave theory) for regular waves, and spectral methods for irregular waves. By integrating these theoretical principles, HydroD SESAM provides hydrodynamic coefficients. This study performs fully coupled time domain analysis, integrating hydrodynamic, aerodynamic, and structural dynamics as it is crucial for accurately predicting the behaviour of FOWTs, as the interaction between the wind, waves, and structural response is highly interdependent. By employing potential flow theory to model the fluid-structure interaction, the boundary value problem solved for the velocity potential around the floating structure. BEM used to discretize the wetted surface of the platform into panels and solve for wave-induced pressures and forces due to incident waves and the waves radiated by the structure's motion. The kinematics of ocean waves are modelled using linear wave theory (Airy wave theory) and higher-order theories for more accuracy in non-linear wave conditions. The dynamics of the mooring lines are modelled using finite element methods (FEM), which account for the elasticity, damping, and dynamic response of the mooring system. integrated advanced aerodynamic models to calculate the forces and moments on the wind turbine rotor blades. This typically involves Blade Element Momentum (BEM) theory, which combines blade element theory with momentum

theory. Dynamic inflow and aeroelastic effects are considered to account for the time-varying nature of the wind load on the rotating blades. using nonlinear finite element methods to model the structural behaviour of slender bodies. It accounts for large deformations, material nonlinearities, and contact problems. For slender structures, Morison's equation is used to calculate hydrodynamic forces. This equation combines inertial and drag forces based on the relative motion between the structure and the fluid. models the interaction between waves, current, and the structure, capturing the dynamic loading on mooring lines. solves the equations of motion for the slender structures, considering the effects of axial, bending, and torsional deformations. It includes damping and dynamic response characteristics.

SIMO is designed for the simulation of the motions of floating structures. It integrates hydrodynamic and aerodynamic forces to analyse the behaviour of offshore structures under various environmental conditions and RIFLEX is specialized for the analysis of slender marine structures such as mooring lines. It focuses on the structural response of these components under dynamic loading.

The combination of SIMO and RIFLEX allows for a comprehensive analysis of offshore structures by integrating hydrodynamic, aerodynamic, and structural dynamics:

- Coupled Dynamic Analysis: The motions of the floating structure simulated in SIMO are used as input for RIFLEX to determine the dynamic response of moorings and risers. This ensures consistency and accuracy in predicting the overall behaviour of the FOWT system.
- Time-Domain Simulations: Both tools perform time-domain simulations, capturing the transient and non-linear interactions between the floating structure and its slender components.
- Environmental and Operational Scenarios: SIMO/RIFLEX simulate environmental and operational scenarios, providing insights into the performance and safety of FOWT system under different conditions.

This study considered frequency domain and time domain analysis using the SESAM package to conduct simulations based on DNV design requirements for offshore floating wind turbines. The theoretical methods and formulations are presented in the appendix A and B.

## 3.2. Simulation Tool

In order to ensure the accuracy of results obtained from a model of a FOWT, it is crucial to consider the interaction between hydrodynamic and aerodynamic loads. To address this issue, the current investigation utilized the SESAM package [367] to conduct a fully coupled analysis. This approach enabled the examination of dynamic responses of the floating structure, including considerations for moorings and the wind turbine. This approach aimed to capture the comprehensive dynamic interactions within the complex system, with particular emphasis on nonlinear effects and the coupling between different components. A visual representation of the SESAM workflow used in this study is presented in Fig. 3-1.

The designs are initially created in GeniE and subsequently exported as FEM files to HydroD for conducting frequency domain hydrodynamic analysis in order to determine the Response Amplitude Operator (RAO) through the hydrodynamic wave-body interaction program. The hydrodynamic coefficients obtained for the platform are then transferred to DeepC for time-domain analysis during the conceptual design phase. Additionally, these coefficients are imported into SIMA for aero-hydro-servo-elastic analysis using SIMO/RIFLEX, which enables the acquisition of integrated response results for the coupled floater and mooring system.

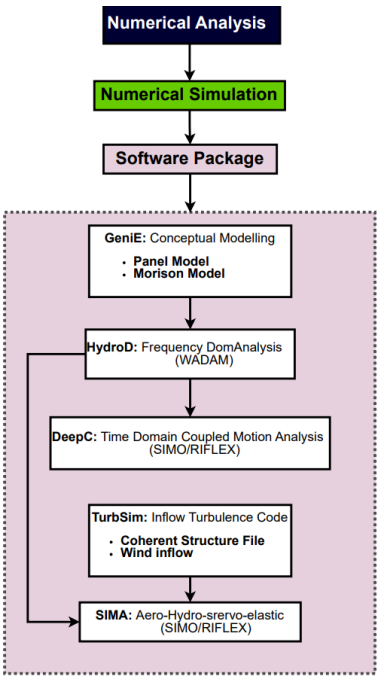


**Fig. 3-1** SESAM Workflow

### 3.2.1. GeniE

DNV's GeniE software [368], a conceptual modelling tool, was used to generate the required models for conducting analyses in Wadam [442] within the HydroD framework [369]. Typically, a *.FEM model serves as a panel model in Wadam, and this model is directly generated and meshed within GeniE. The meshing commands in GeniE were used to mesh the GeniE model, which was then exported as a T*.FEM file. The T*.FEM panel model presented in this section was used as a Green's function-based panel model for HydroD and Wadam. Crucial for conducting motion analysis are the mass and panel models. The mass model determines the mass properties of the structure and, consequently, the mass matrix used in the equation of motion. Conversely, the panel model represents the outer surface of the model and is meshed with panels. In potential flow analysis, panel methods are used to calculate the pressure on each panel in the model, enabling for the computation of the hydrodynamic pressure distribution on the body. Additionally, the pressure distribution is integrated into a frequency domain analysis to derive hydrodynamic coefficients that are utilized in the equation of motion.

### 3.2.2. HydroD

The physical model of the FOWT is imported into HydroD in a three-dimensional (3D) environment using a composite model configuration to apply both the Morison equation and 3D potential theory to the structure. This process yields hydrodynamic coefficients derived from the interaction between the floater body and waves. Within HydroD, the Wadam analysis utilizes the Morison equation and potential theory for wave load calculations. The Morison model intersects with the panel model. The Morison elements are being modelled with minimal diameter and added mass coefficients, as well as substantial drag coefficients. When loads are transferred, pressures on the panel model are applied to a structural FEM, and beam loads to the Morison FEM. Load transfer is also necessary to achieve the required pressure and loads on the panels.

Accurate estimation of the extreme tension response is crucial in the initial stages of the design process to ensure precise prediction of mooring line loads and for further

design optimizations. Hydrodynamic coefficients are computed in WADAM for first-order, first-order + wave drift, and second-order, considering the second-order velocity potential. The frequency domain condition is specified as the input data, and a surface mesh is required to account for the second-order effect. This mesh was generated using the program HydroMesh [333]. The mesh size should be at least one wavelength of the longest radiated or scattered wave [443]. In this project, a radius of 5 times the vessel length was utilized [325]. The second-order analysis considers the interactions between two harmonically oscillating components, resulting in forces and motions at the sum-frequency and difference-frequency of the incident waves. The frequency-domain hydrodynamic analysis is conducted without directly considering the mooring lines, but the static stiffness of the resulting mooring system is applied for static equilibrium position of the system. Forces and moments are expressed in terms of transfer functions, and hydrodynamic coefficients such as added mass and radiation damping, wave excitation forces, and response operators are calculated in WADAM to obtain the response amplitude operator (RAO).

In accordance with DNVGL-ST-0119 [439], it is essential to ensure a sufficient duration of simulations to accurately consider the effects associated with the natural frequencies of floating support structures when determining loads and responses. It is recommended to have a minimum simulation length of three hours to adequately capture nonlinearities, second-order effects, and slowly varying responses, as well as to accurately establish the design load effects. Subsequently, the hydrodynamic coefficients obtained from HydroD can be utilized in DeepC (time domain coupled floater motion analysis) or SIMA (time domain aero-hydro-servo-elastic analysis) for conducting the coupled time domain analysis.

### 3.2.3. DeepC

DeepC [374] is an interactive program that models floating configurations attached to the seabed with mooring lines, tension legs, and risers, providing a comprehensive and accurate analysis of mooring systems in the time domain. This software system is based on the programs RIFLEX [375] and SIMO [376]. Prior to running DeepC the geometry of the large volume floaters must be modelled. These models must be run through HydroD/Wadam to calculate frequency domain added mass, potential

damping and excitation forces, which is input to DeepC. Once HydroD has been run, DeepC takes full control of the analysis.

The DeepC [444] application is utilized for the conceptual design approach, with the actual wind turbine installed on the turbine being disregarded. The wind force acting on the FOWT is directly computed based on the drag on the tower and blade structures for survival conditions. During operational modes, the turbine responds to the incoming wind conditions by incorporating a control system that aims to optimize the generated power output.

### 3.2.4. SIMA

The software tool Sima is designed for simulating marine operations, mooring analyses, and floating offshore wind turbines [377]. It employs coupled aero-hydro-servo-elastic analyses and can incorporate various nonlinear effects such as drag forces, aerodynamic loads, and nonlinear restoring. Calculations are performed in the time domain according to DNV [445].

Sima offers detailed modelling capabilities for physical problems, including environment modelling with features such as current and wind profiles, wave and wind spectra, various seafloor properties, and location-specific data. Floating structures can be represented with added mass, potential damping, 1st and 2nd order wave excitation, and additional viscous force elements to account for Morison forces. The software calculates retardation functions from added mass and damping to consider frequency-dependent effects during time-domain calculations.

Sima integrates the software tools Riflex and Simo. Riflex is a nonlinear finite element software for slender marine structures and Simo is a simulator for marine operations. The aerodynamic model in Riflex is based on the blade element momentum theory [384], incorporating dynamic stall and dynamic wake effects using the Øye models [386] and corrections such as Glauert's correction for high induction factors and Prandtl's correction for hub and tip losses [446].

The hydrodynamics and aerodynamics governing equations are simultaneously solved in a fully coupled approach. The coupled motion response of the floating

platform and mooring lines is computed in the time domain using SIMO-RIFLEX to provide dynamic responses related to motion and mooring forces.

During the detailed design stage, aero-hydro-servo-elastic analysis was conducted in SIMA, an environment capable of simulating coupled wind, wave, and current effects.

### 3.2.5. TurbSim

The TurbSim software is a stochastic simulator designed to model turbulent wind fields. It generates a sequence of discrete two-dimensional grids that represent wind speed vectors in three dimensions [385]. By combining these grids, a time series of fully turbulent wind is produced, as depicted in Fig. 3-2. TurbSim offers various customizable parameters for users to define the characteristics of the turbulent wind, including grid size, number of grid points, reference wind speed and height, turbulence type, turbulence intensity, and turbulence model. TurbSim is able to generate the wind profiles where the analysis duration extended to produce a periodic output file.

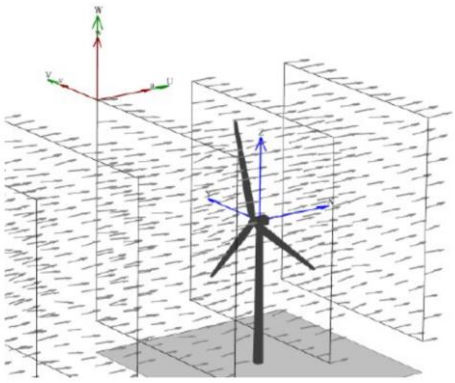

**Fig. 3-2** TurbSim turbulent wind illustration [385]

It is advisable to uphold a minimum analysis duration of 600 seconds. The analysis duration can be extended, and a periodic output file can be created at intervals that align with the analysis duration [385]. TurbSim can generate input files for Sima software. TurbSim generates time series data by applying an inverse Fourier transform that considers velocity components and spatial coherence in the frequency domain. The definition of these velocity components and spatial coherence is based on

spectra. This methodology operates under the assumption of stationarity, leading TurbSim to superimpose coherent turbulent structures onto the resulting stationary time series [385].

The complete aerodynamic effects from the rotating turbine, acting on the entire system, are taken into account by utilizing TurbSim [385] to generate wind fields such as the Normal Turbulence Wind (NTM) model for operational conditions and the Extreme Wind Model (EWM) with turbulence intensity for survival conditions. The aerodynamic calculations are performed using the Blade Element Momentum methos (BEM) method. Further information can be found in Appendix A.

# 4. Tension Leg Buoy Floating Offshore Wind Turbine

As indicated by the literature review, there is currently a lack of consensus on the most cost-effective approach for extensive implementation in the industrial sector, given that the LCOE for FOWTs exceeds that of fixed-bottom foundations. The design challenge of FOWT support platforms is characterized by its high complexity, making it imperative to identify an optimal design in terms of LCOE for use in transitional water depths where bottom-fixed turbines are not economically feasible. A solution is being sought to simplify certain constraints related to manufacturing, construction, installation, and maintenance. This is intended to offer an alternative to the prevailing industry practice of Spar, Semi-Submersible, and TLP platforms.

The TLB, initially introduced by Sclavonous in 2008 [183] and further studied by Myhr in 2016 [180] (refer to Fig. 4-1), shows potential for improvement in all these areas and could serve as a floating support structure for a 10MW offshore wind turbine. The main platform could be constructed using standardized steel sections and rely on excessive buoyancy and tensioned mooring lines for stability. The length of the main cylindrical body is reduced compared to a Spar platform design, and the system allows for much lower motion envelopes than catenary moored floaters.

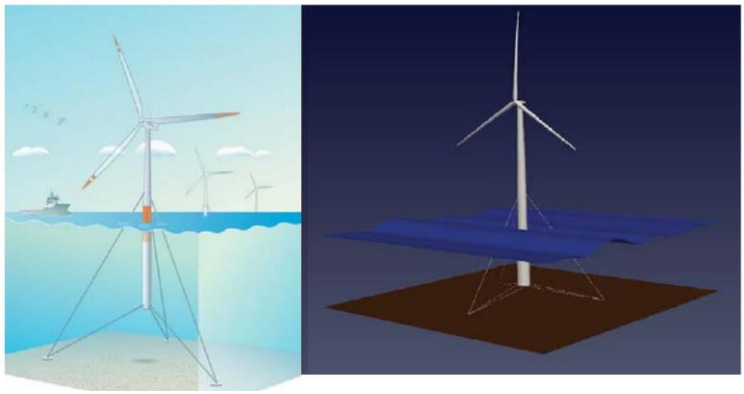

**Fig. 4-1** Previous TLB Design

This section outlines the development of a configuration for a floating platform and mooring system, which serves as a demonstration of the TLB design concept for installing offshore wind turbines in transitional water depths where fixed-bottom

turbines are no longer economically viable. To achieve this, an innovative FOWT system is conceptualized through an iterative process to determine an optimal design that adheres to the regulations outlined in section 2.9. Subsequently, a comprehensive design analysis is carried out using aero-hydro-servo-elastic analysis.

## 4.1. Initial Design

The stability of the TLB concept design heavily relies on the mooring system for both operational and survival conditions. The TLB presented in this study is based on the 5MW TLB system reference design developed by Anders Myhr [180], with the optimized TLB B2 design selected as the reference design.

The initial TLB (TLB I) floating platform was developed to support a 10MW offshore wind turbine generator. A key factor in upscaling the floating platform from Myhr's TLB B2 design [180] was to maintain consistent excess buoyancy levels between the two models to ensure stability. The relevant dimensions were adjusted based on the ratio between excess buoyancy and the total weight of the floating assembly in response to the increased weight of the DTU 10MW reference turbine compared to the previously used 5MW turbine. The floating platform extends 20 meters above the still water level to accommodate the wind turbine model. Mooring line attachments are located 10 meters below the surface and at the bottom of the floating body.

The primary structure of the TLB main body is constructed using circular steel sections with a thickness of approximately 30 mm, and the material density is adjusted to 8.5 tonnes/m$^3$ to accommodate small equipment and structural details. The thickness of the wall of a the floater body can be determined by applying the formula $t = \frac{Outer\ Dimeter\ of\ Floater}{500} + 0.018$, as specified in DNV-RP-C202 [180, 447].

The resulting structural parameters of the scaled-up TLB B2 design and initial design are presented in Table 4-1, indicating that the EB/B ratio is maintained constant between the two designs.

**Table 4-1** Overview of Comparable Reference Design (TLB B2) from Myhr Study to the Scaled Design (Initial Design) (TLB I)

| | TLB B | TLB I |
|---|---|---|
| **Depth to Platform Base Below WL (Total Draft) (m)** | 52 | 52 |
| **Elevation to Platform Top (Tower Base) Above WL (m)** | 10 | 20 |
| **Platform Diameter (m)** | 6 | 9.5 |
| **Floater Mass (ton)** | 355 | 574.8 |
| **Total mass (ton)** | 1068 | 1878.8 |
| **Total buoyancy (ton)** | 2166 | 3649.5 |
| **EB (ton)** | 1110 | 1862.7 |
| **EB/Total Buoyancy** | 0.50 | 0.51 |

The initial design specification is outlined in Table 4-2. It is important to note that the weight of the 10MW DTU turbine (including rotor and nacelle weight of 674 tons and tower weight of 630 tons) is taken into account during the hydrostatic calculations.

**Table 4-2** Initial Design Specifications

| Initial Design of 10MW TLB Platform | |
|---|---|
| **Connection to Tower from WL (m)** | 20 |
| **Draft (m)** | 52 |
| **Diameter above Taper (m)** | 9.5 |
| **Centre of Mass (m)** | 52.32 |
| **Centre of Buoyancy** | -26 |

**Table 4-3** Initial Mooring System Design Principal Properties

| Taut Mooring system Characteristics | |
|---|---|
| **No. of Lines** | 2 sets of 3 lines |
| **Angle between Lines** | 120° |
| **Anchor Radius** | 180 m |
| **Fairlead below SWL** | -10 m & -52 m |
| **Angle of attached at top Fairlead** | 29.7° |
| **Angle of attached at bottom Fairlead** | 18.3° |
| **Axial Stiffness** | 2.39e+6 kN |

**Table 4-4** Initial Mooring Line Model Characteristics

| Spiral Strand Xtreme 1960 Grade | |
|---|---|
| **Diameter (m)** | 0.480 |
| **MBL (kN)** | 61920 |
| **Weight (t/m)** | 0.295 |

A taut mooring system is developed for a TLB I concept model, similar to Trolle and Hornbak [217] to counteract the excess buoyancy of the platform. The system consists of two sets of clusters, each with three mooring lines. This research distinguishes itself apart from previous studies that have examined semi-taut mooring lines by specifically addressing the placement of upper cluster mooring lines below the waterline. This arrangement allows service vessels to safely access the mooring lines for maintenance and inspection activities. The mooring lines are attached at two distinct elevations, with the upper and lower mooring lines linked to an anchor. The upper mooring line connection is submerged at a depth sufficient to ensure a distance from the waterline. The schematic mooring arrangement characteristics for the initial design are summarized in Table 4-3. Initially, steel wire rope is used to simulate the mooring lines, with a single mooring line consisting of 3 strands of the spiral strand, as detailed in Table 4-4. All the provided data is derived from empirical formulas and estimations based on manufacturer information [448].

The mooring system is characterized by the anchor radius ($R_C$), water depth ($d_w$), and the depth to the attachment points of the fairleads for both upper ($d_u$) and lower ($d_L$) mooring lines (see Fig. 4-2). In the initial design, the taut mooring system comprises two clusters of three sets of taut mooring lines, totalling six mooring lines, arranged at 120˚angles (refer to Fig. 4-3 (a)). These mooring lines are connected at two different heights: one at the bottom of the floater with an attachment angle of 18.3˚, and the other 10m below the water level with an attachment angle of 29.7˚. This configuration ensures sufficient clearance with respect to the fairlead location and free surface for the manoeuvring of vessels near the platform (see Fig. 4-3 (b)). The anchor radius is established at 180 m to accommodate the innovative anchor sharing concept for multiple turbines installed in an array.

It is important to highlight that the current study, conducted in 2018, considered2D distance between wind turbine platforms based on existing references [449-451]. Nevertheless, subsequent research has indicated that the ideal distance between neighbouring turbines should surpass 2D, with a preference for distances approaching 5D. Furthermore, turbines arranged in a linear configuration should maintain a separation of more than 10D [452]. Therefore, it is imperative that the design of wind farm systems integrates these updated findings to improve the wake effects encountered by the turbines.

The stiffness matrix for a symmetric taut mooring system can be determined using the Eq. (1-23) to (1-32) provided in the appendix B. While simplified assumptions are often made for mooring lines, providing a more detailed description of the material used in the mooring line may help decrease the occurrence of snap loading. Alternatively, incorporating additional damping would have similar effect. These aspects could reduce the accuracy of the predicted hydrodynamic loads exerted on the platform and mooring lines, especially at low and moderate fluid speeds which may affect the resulting system response. The restoring matrix is computed for a single cluster, and the overall stiffness matrix is formed by aggregating the stiffness matrices of the individual lines, as outlined in the procedure described in reference [287]. The complete hydrostatic stiffness matrix, denoted as $K_m$, for the initial design featuring three mooring lines at each cluster, is calculated and presented in Eq. (11) for the system when moored with steel mooring ropes.

$$K_m = \begin{bmatrix} 4.97\text{E}+08 & 0 & 0 & 0 & -1.58\text{E}+13 & 0 \\ 0 & 4.97\text{E}+08 & 0 & 1.58\text{E}+13 & 0 & 0 \\ 0 & 0 & 2.02\text{E}+08 & 0 & 0 & 0 \\ 0 & 1.58\text{E}+13 & 0 & 2.98\text{E}+20 & 0 & 0 \\ -1.58\text{E}+13 & 0 & 0 & 0 & 2.98\text{E}+20 & 0 \\ 0 & 0 & 0 & 0 & 0 & 2.00\text{E}+14 \end{bmatrix} \quad (11)$$

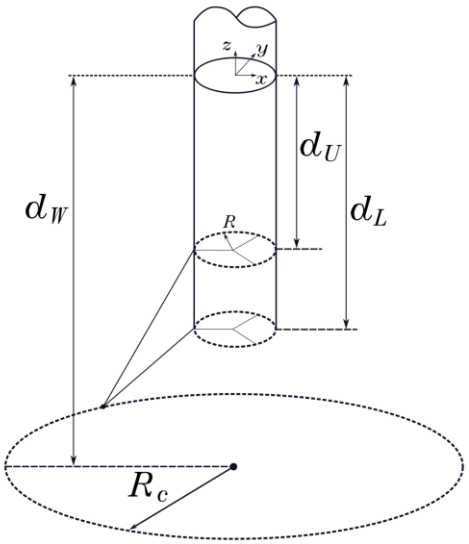


**Fig. 4-2** Taut-Leg Mooring System Configurations

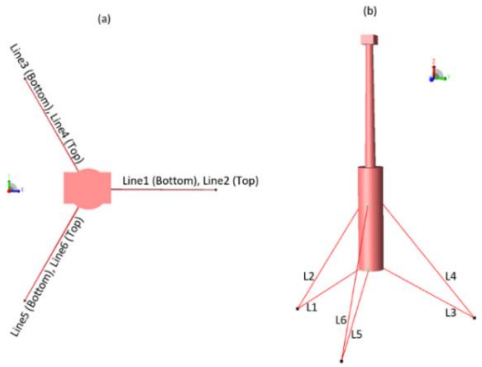


**Fig. 4-3** (a) Mooring Lines Top View & (b) 3M-9.5d-52D TLB Taut-Leg Mooring Layout (M is the number of mooring line at each cluster, d is the floater diameter, and D is the draft)

Hence, the characteristics of the design can be succinctly outlined as follows:

- The design requires a significant amount of buoyancy to guarantee stability in water depths of 110 meters.
- The upper mooring line connection is submerged at a significant distance from the waterline.
- The design facilitates the potential sharing of anchors between lines and multiple platforms.
- It is assumed that the design will accommodate a 10MW wind turbine generator.

As outlined in the literature review section 2.6, multiple studies have examined the initial design of a floating substructure [164, 423, 424] and have suggested that this process can be divided into two stages: the initial conceptual sizing of the support structure, followed by subsequent development and refinement. This current study adheres to such a methodology. Additionally, several research works have concentrated on optimizing the design of FOWT using diverse methodologies [185, 413, 419, 420]. One of these methods involved a parameterization study of a cylindrical platform with variable dimensions and mooring lines, presenting a parametric approach to the design of the support platform for FOWT [421]. This approach draws on relevant design principles from the offshore oil and gas industry and identifies suitable combinations of structures and mooring systems that fulfil the requirements for a generic 5MW wind turbine [421]. Consequently, this study follows a similar approach and employs iterative processes by establishing specific design variables.

## 4.2. Concept Design Development

The study employed an approach that involved independent optimization in both the frequency and time domains. This approach led to a reduction in the number of design variables in each optimization phase, resulting in a significant decrease in simulation time compared to integrated optimization with environmental loads necessary to characterize the system's dynamic responses.

During the concept design development stage, it is advantageous to optimize the system for a site intended for an offshore wind farm, rather than the harsh conditions of the North Sea. The concept design approach was implemented at the Hywind site in the North Sea [453] to enhance and refine the concept. The environmental variables were fixed for each part of the concept design stage, with a 100-year return period event based on design data from the Hywind Scotland wind farm being illustrated in Table 4-5. It is assumed that the environmental conditions exhibit collinearity.

To ensure that the system is stable enough to be optimized within a reasonable computation time, given the two-step optimization in the frequency and time domains, the number of design variables was minimized. Table 4-6 shows the design variables used in the concept design iteration process to ensure system stability concerning Ultimate Limit State (ULS) and Accidental Limit State (ALS).

The physical wind turbine itself was not included in the initial design concept; however, the impact of wind load was taken into consideration. The wind forces exerted on the wind turbine tower and blades were calculated based on the incoming wind speed, assuming the turbine would be operating at maximum power output under normal operating conditions. It was assumed that the wind turbine would be deactivated during stormy weather, which represents a highly turbulent sea state. The wind force acting on the FOWT was directly determined by calculating the drag on the tower and blade structures under survival conditions (refer to Fig. 4-4). In order to evaluate the models under operational conditions, the thrust force was calculated using a thrust coefficient of 0.78. A constant force was determined that acts on the projected area of the platform above sea level during storm conditions.

The initial phase of the concept design involves determining the fundamental size of the floater and the computation of the mooring system stiffness. The preliminary

design is modelled using GeniE [368], and the hydrodynamic coefficients are calculated using WADAM [454] in HydroD [369, 443], with a coupled time domain analysis conducted using DeepC. The coupled analysis is carried out under the assumption of a static wind force acting on the rotor centre to assess the geometry and mooring combinations capable of withstanding a storm event similar to that outlined in the Hywind Scotland environment documentation [455]. These conditions were taken into account at the end of the concept design stage. Subsequently, rule-based environmental design loads were calculated based on DNV during the detailed design stage. The environmental loads considered for this study is collinear due to simplify the analysis. Focusing on the combined impact of these loads in a specific direction enabling the identification of the most significant load effects on the structure that a FOWT need to withstand harsh conditions, while also optimizing material usage and construction costs.

The concept design progresses through subsequent stages to enhance the hydrodynamic analysis of the TLB floater geometry and the mooring system to meet the ULS and ALS requirements.

**Table 4-5** Hywind Scotland Wind Farm Environmental Condition

| **Hywind 100 yr. Environmental Condition** | | |
|---|---|---|
| **Weather Condition** | Operational | Survival |
| **Wave** | | |
| Wave Spectrum | JONSWAP | JONSWAP |
| Wave Height ($H_S$) (m) | 4 | 19.4 |
| Period (T) (s) | 7 | 13.2 |
| **Wind** | | |
| Wind Speed (m/s) | 11.4 | 40 |
| Wind Turbine Control | Thrust Force | Constant Force |
| **Current** | | |
| Depth (m) | Current Velocity (m/s) | |
| 25m | 0.40 | 1.42 |
| 40 m | 0.39 | 1.33 |
| 60 m | 0.27 | 1.27 |
| 90 m | 0.32 | 1.13 |
| 110 m | 0 | 0 |

**Table 4-6** Design Variables

| Property | Unit |
|---|---|
| **Diameter** | m |
| **Draft** | m |
| **No. of Fairlead Attachment Points** | |

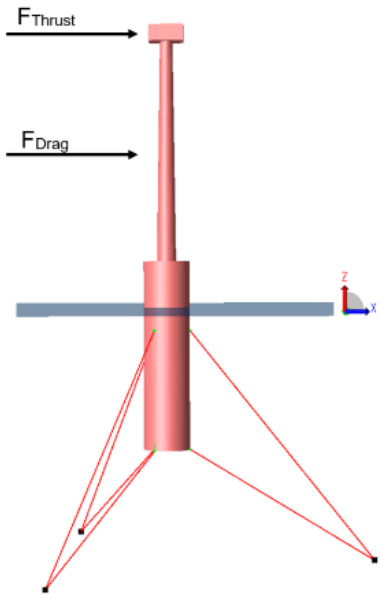


**Fig. 4-4** DeepC Model with Mooring Arrangement with Static Wind Force equivalent to Thrust Force (Operation) & Drag Force (Storm)

A mesh convergence study is conducted to determine a computational mesh that strikes a balance between computational time and accuracy. The verification of the numerical model for the TLB support platform is complex due to the requirement for supporting documentation and data. In addition, this study verified the TLB platform's software setup by comparing it to the model simulation conducted by Berg (2013) [456]. Berg experimentally investigated three prototypes and compared them to the simulation model in ANSYS APDL. The prototype TLB S model in ANSYS is used to verify the SESAM software.

## 4.3. Mesh Sensitivity and Verification Studies

In line with the recommendations outlined in the SESAM manual by DNV (2013b) [443], it is advised that the diagonal element in the panel model should not exceed one-fourth of the wavelength.

In order to compute second-order loads in Wadam, it is essential to establish a second-order free surface model. HydroMesh plays a crucial role in the HydroD/SESAM system. It can operate independently by utilizing input files generated by HydroD, in addition to an optional XML file (free surface settings file) created by HydroMesh Setup. The Wadam is used for second-order load calculations as specified by DNV (2013b) [443]. Analysing a free surface model with more than 3000 elements is impractical. To improve result accuracy, the free surface is divided into quarters while maintaining symmetry with the hull panel model.

### 4.3.1. Panel Model Convergence

At this stage, as there is a lack of field measurements for TLB platforms, a study was conducted to assess the sensitivity of mesh resolution levels and to determine the impact of different mesh sizes on the performance of the TLB I platform, including the second-order free surface, through a mesh convergence study. The hydrodynamic responses of the platform were investigated by discretizing the initial design model in GeniE and then importing it into HydroD. The mesh was refined and adjusted using a variety of mesh editing features, and its quality was subsequently verified. Table 4-7 presents six options for column surface mesh size. An initial mesh size of 3 m is adopted, which is progressively reduced to facilitate a comparison of peak amplitudes in motion responses. The determination of the mesh size is based on the point at which the peak amplitude of the motion responses stabilizes.

**Table 4-7** Mesh Density Options

| Element Per Quarter | Mesh Size (m) |
|---|---|
| 113 | 3 |
| 1009 | 1 |
| 2182 | 0.7 |
| 3200 | 0.6 |
| 4482 | 0.5 |
| 5537 | 0.45 |

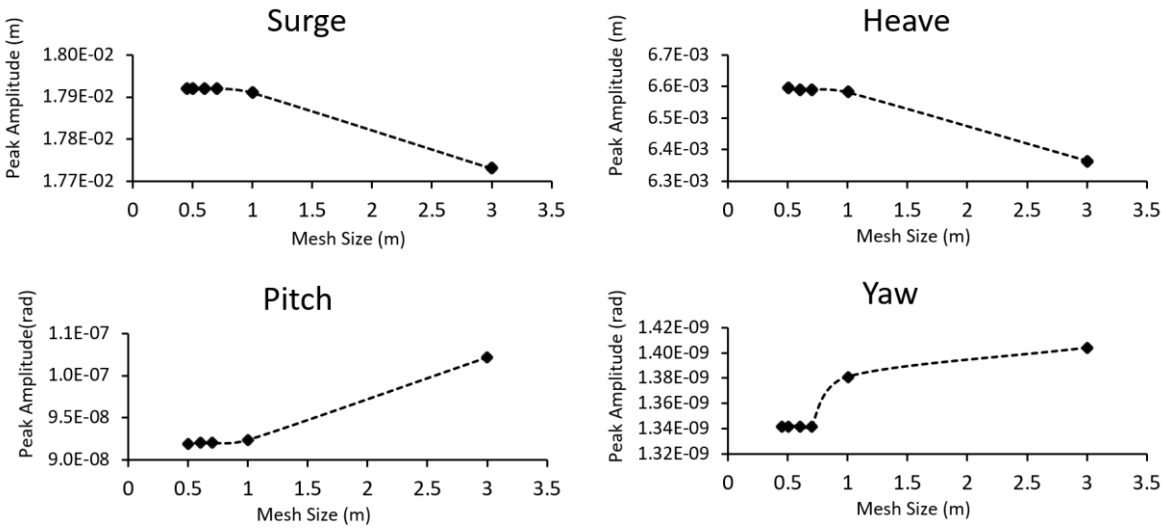


**Fig. 4-5** Peak Motion Responses Mesh Convergence

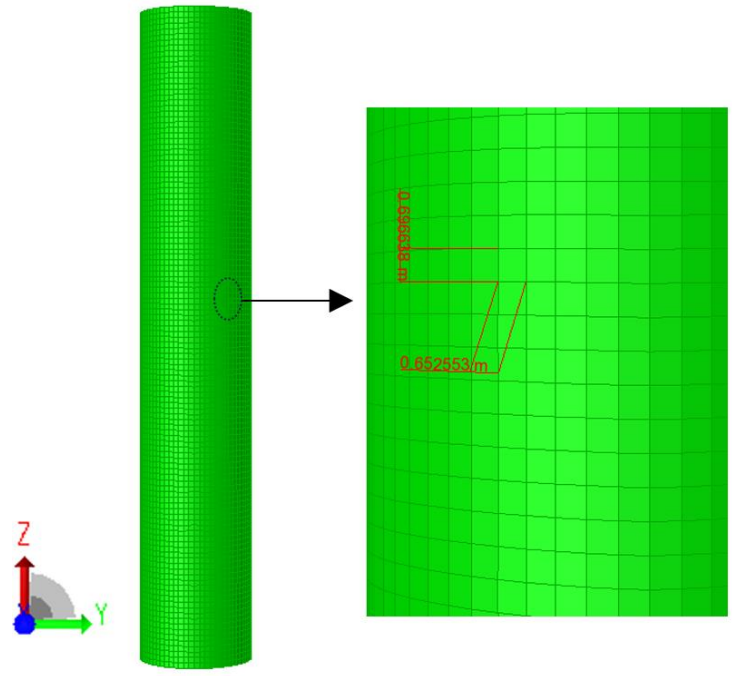


**Fig. 4-6** Panel Model Mesh Resolution (0.7 m)

The impact of varying mesh sizes on the response of heave, pitch, surge, and yaw motions is depicted in Fig. 4-5. It is evident that the motion responses of the system have stabilized at the peak amplitude for a mesh size of 0.7 m and below. Additionally, the outcomes of mesh convergence on forces, added mass, and potential damping reaffirm that the model converges at a mesh size of 0.7 m. Consequently, the final panel model of the TLB I design comprises 2,182 elements per quarter (8,728 total mesh cells), each with a mesh size of 0.7 m (refer to Fig. 4-6), based on the mesh convergence study.

### 4.3.2. Free Surface Mesh Convergence

The discretization of the free surface is necessary for computing the second-order velocity potential. The accuracy of the second-order result is influenced by the free surface mesh [457], necessitating a finer mesh to enhance accuracy. Therefore, a finer mesh is used in the free surface meshing to ensure satisfactory accuracy in the second-order results while maintaining overall computational efficiency. Mesh convergence is evaluated for five different mesh cell numbers, as detailed in Table 4-8. The surface area has a radius equivalent to 5 floater diameters [333]. Analysing a free surface model containing over 3000 basic elements is deemed unfeasible due to size limitations [443]. Therefore, an initial value of 2000 cells per quarter was arbitrarily selected to evaluate force amplitude responses. Subsequently, the number of elements was incrementally increased. The determination of mesh size being predicated on identifying the point at which the peak amplitude of motion responses reaches a stable state.

**Table 4-8** Free Surface Mesh Case Options

| Mesh Case | Cell NO |
|---|---|
| **MC1** | 8000 |
| **MC2** | 9100 |
| **MC3** | 9752 |
| **MC4** | 9840 |
| **MC5** | 9860 |

The impact of different sizes of free surface meshes on the responses of pitch, surge, and yaw motions is illustrated in Fig. 4-7. The maximum values of the amplitude of second-order forces for surge, pitch, and yaw reach a convergence point at MC3 with 2,438 elements per quarter (9,750 total mesh cells). This suggests that conducting the simulation with more than 9,750 mesh cells will have an insignificant effect on the force amplitudes.

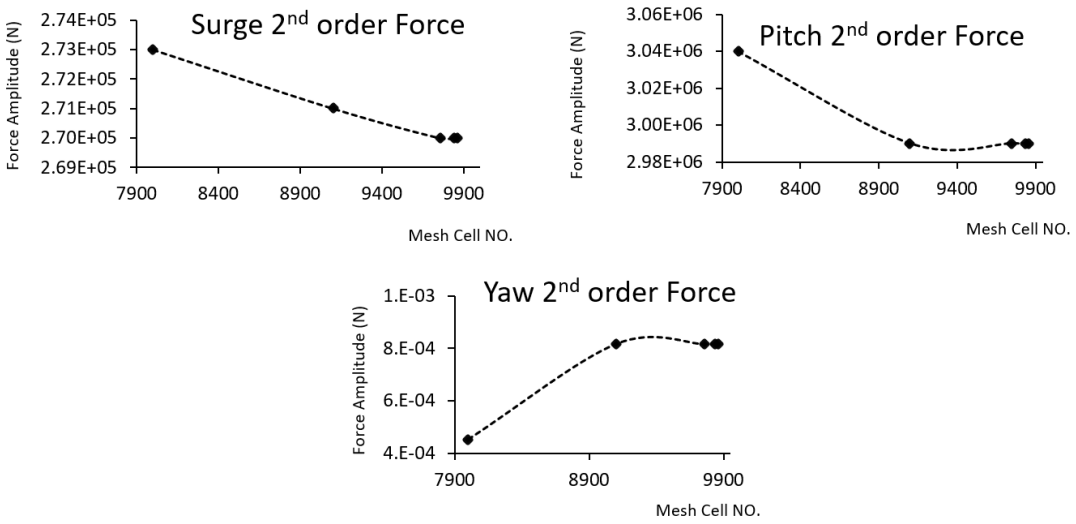


**Fig. 4-7** Second Order Free Surface Mesh Convergence

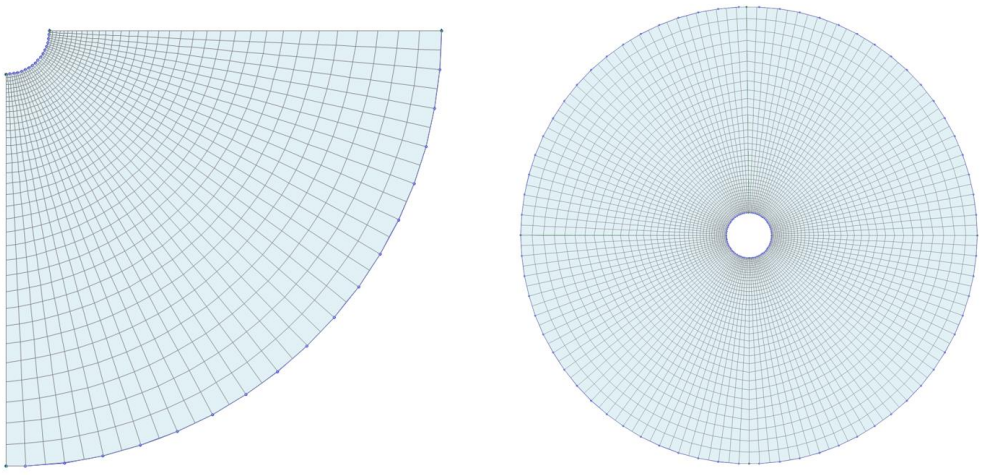

**Fig. 4-8** Free Surface Mesh Model

### 4.3.3. Model Verification

Berg (2013) [456] conducted a study to evaluate the tension leg buoy concept developed by Myhr [180] using both experimental and computational methods. Berg utilized the ANSYS APDL tool for numerical simulation. The numerical simulations were conducted using the ANSYS APDL software, with an emphasis on regular waves because the software has limitations in simulating irregular waves without extra effort. The comparison of data sets involved analysing differences for three prototypes across various load cases. The study validated the SESAM software using the prototype TLB S model. Berg emphasized the limitations of using computationally intensive simulations within time constraints and recommended adopting short simulation durations and empirical assessments. The mooring system consisted of two clusters of three sets of taut mooring lines, totalling six lines distributed at 120° angles. A significant wave height of 0.5 meters and a peak period of 2.5 seconds were used to represent the wave load. The comparison between the simulated results of the Berg study and those obtained from reproducing the setup in the current software package is presented in the following figures. The graphs included in this analysis are sourced from the research conducted by Berg. Due to restricted access to the data, it is not feasible to present response spectra. Nevertheless, to assess the discrepancies between the two results, data has been extracted from Berg's graphs. It is important to note that the reliability of the quantified results is contingent upon the precision of the data extraction from these graphs.

The comparison of translational response results in Fig. 4-9 indicates a close match in simulated time histories, with minor numerical overprediction and phase offset visible between simulations for surge and heave. The maximum surge response from the SESAM simulation was 0.78% higher than that of the Berg study. Similarly, for sway and heave responses, the SESAM simulation yielded results 0.57% and 0.70% higher than those of the Berg study, respectively. Mean value comparisons revealed insignificant differences, with a 0.07% mean difference for surge, and 0.06% and 0.14% differences for sway and heave responses. The numerical results showed excellent agreement, with only minor differences in peak responses but a close alignment of motion responses trend in all three translational directions.

The rotational responses depicted in Fig. 4-10 were compared, and the simulations conducted in this study exhibit similar trends and closely align with the findings of the Berg study.

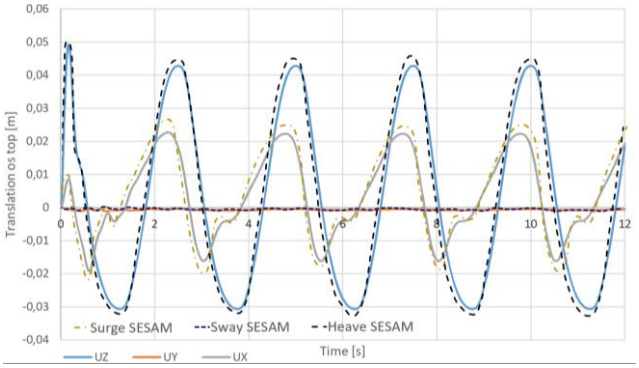


**Fig. 4-9** Comparison of Translational Responses of Berg Study with SESAM (dotted lines)

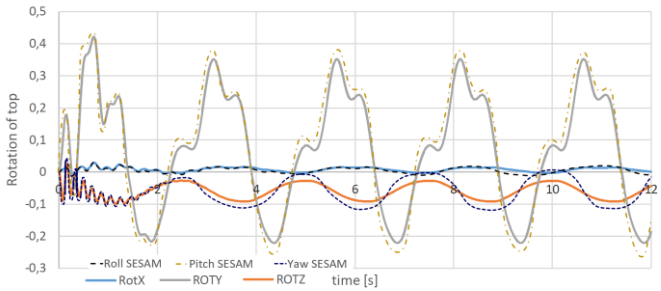


**Fig. 4-10** Comparison of Rotational Responses of Berg Study with SESAM (dotted lines)

By extracting the points from Berg graph results, it is noted that the maximum roll response in the Berg study exceeds that of the SESAM result by 0.65%, while the pitch and yaw responses from SESAM are 0.63% higher. In terms of the mean values of the rotational responses, the average roll response is consistent in both simulation results. However, the pitch mean value from the Berg study is 0.89% higher than that from the SESAM simulation, and the heave mean value of the SESAM result is 0.15% higher. Additionally, there are minor phase differences, and the magnitude of the pitch and yaw motion responses in the numerical simulation is greater. This could potentially be attributable to variations in the inclusion of mooring line effects between simulations. Fig. 4-11 and Fig. 4-12 depict the results for lower and upper mooring lines tension of Berg study and SESAM results.

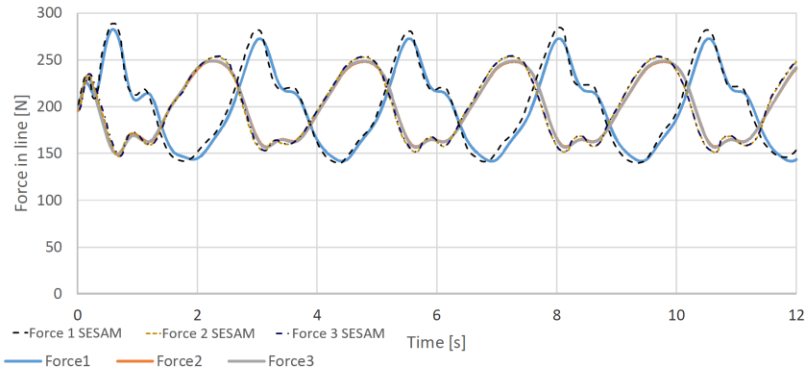


**Fig. 4-11** Comparison of Lower Mooring Lines Tension of Berg Study with SESAM (dotted lines)

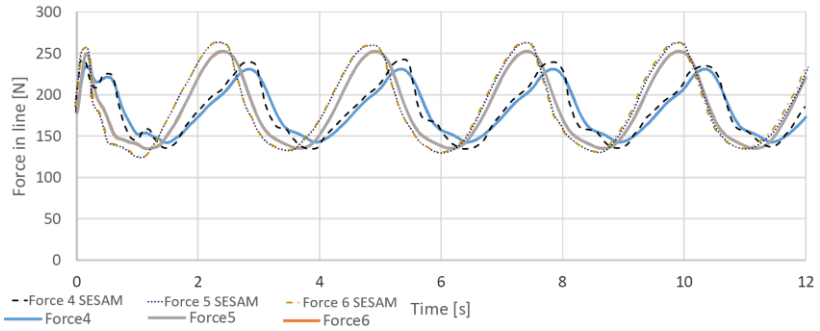


**Fig. 4-12** Comparison of Upper Mooring Lines Tension of Berg Study with SESAM (dotted lines)

The SESAM analysis indicates higher tension values for lower mooring lines compared to Berg's findings. Specifically, the maximum tension for line 1 is 0.19% higher, and for lines 2 and 3, it is 0.82% and 0.83% higher, respectively. The differences in the mean tension values among the three lines are less than 2%. Similarly, SESAM results for upper mooring lines show higher tension values compared to the Berg Study, with increases of 0.85%, 0.95%, and 0.75% for lines 4, 5, and 6, respectively. Overall, the force magnitudes show strong agreement between the SESAM and Berg Study models, with a slight phase offset observed, especially in the upper lines. This difference could be attributed to line modelling and hydrodynamic effects such as damping. It is noted that, similar to the Berg study, the mooring lines' cross-section is assumed to be a beam element, although the number of defined elements for the lines may vary. In this study, 28 elements are defined for upper lines, while 14 are defined for lower lines.

### 4.3.4. Concept Design Iteration

The initial design was created using GeniE for 3D modelling. Hydrodynamic coefficients were computed using WADAN in HydroD, and a coupled time domain analysis was conducted using DeepC to obtain the coupled response results of the floater and mooring system. The concept design progresses to subsequent phases to enhance the hydrodynamic analysis of the TLB floater geometry and the mooring system in order to meet the ULS and ALS by utilizing various combinations of input variables (refer to Table 4-6) to define the multiple configurations assessed in the design process to achieve the optimal design. The concept design iteration process is illustrated in Fig 4-13.

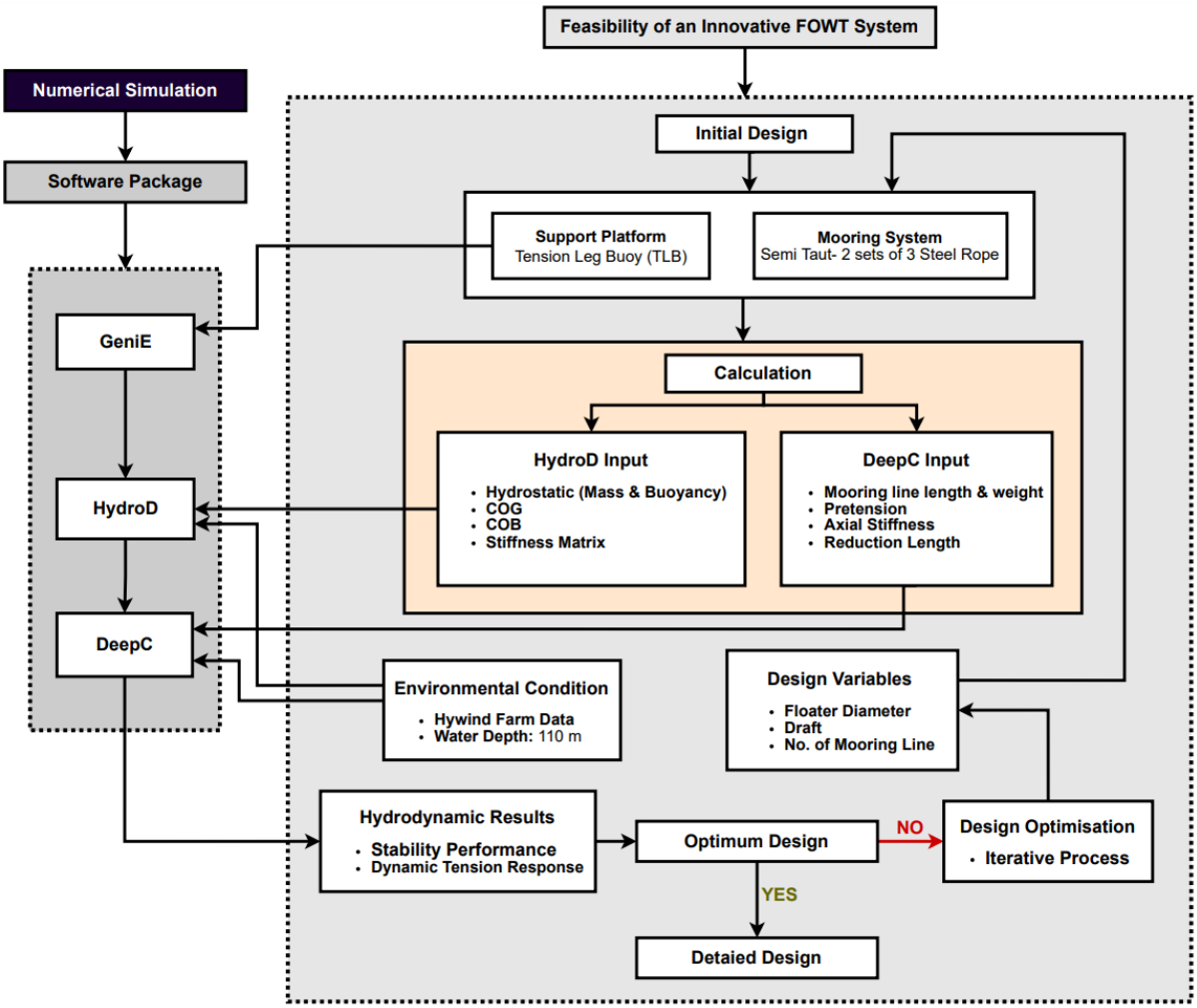


**Fig 4-13** TLB Concept Design Iteration Outline

The iterative process consists of three distinct stages. Each stage involving an assessment of the model's stability performance and the exploration of various combinations of input variables to achieve the optimal design. In the early stages of the iterative design process, two initial models (referred to as Model A and B models) were created with varying draft sizes, and the stability of the system was assessed. However, it was found that the system was unstable under both environmental conditions. Consequently, a new model (referred to as Model C) was developed, which maintained the same diameter while incorporating two different draft sizes.

A summary of the concept design iterations from Stage I and the stability performance of each design is presented in Table 4-9.

**Table 4-9** Overview of Concept Design Stage I Iterations

| **Design Iteration Process** | | | | | | |
|---|---|---|---|---|---|---|
| **Model** | A | | B | | C | |
| **Iterative NO.** | **I** | **II** | **III** | **IV** | **V** | **VI** |
| **Draft (m)** | **52** | **52** | **62** | **62** | **52** | **62** |
| **Diameter (m)** | **9.5** | **10.5** | **9.5** | **10.5** | **20** | **20** |
| **Platform (ton)** | 575 | 619 | 658 | 709 | 1267 | 1443 |
| **Turbine (ton)** | 1324 | 1324 | 1324 | 1324 | 1324 | 1324 |
| **Total Mass (ton)** | 1879 | 1923 | 1962 | 2013 | 2591 | 2747 |
| **COG (m)** | 52.32 | 50.55 | 47.65 | 45.59 | 33.3 | 28.23 |
| **EB (MN)** | 23.87 | 25.78 | 24.56 | 32.92 | 138.85 | 168.91 |
| **DeepC Model** | 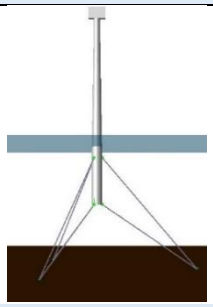 | | 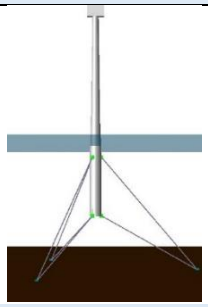 | | 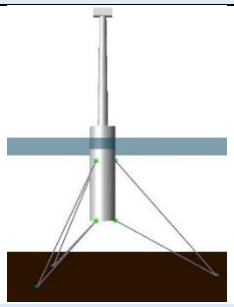 | |
| **Model Name** | 3M-9.5d-52D | | 3M-10.5d-62D | | 3M-20d-62D | |
| **Note:** M = Mooring Lines NO. d = diameter, D = Draft | | | | | | |
| **Description** | Up scaled version of NTU TLB & taper to match turbine tower diameter. | | Additional excess buoyancy through increased draft | | Significantly increased excess buoyancy through large diameter & simplified structure without taper section | |
| **Stability Performance** | Unstable in operating conditions with wind force active | | Stable in operating conditions, unstable in storm conditions above $H_s$=5m | | unstable in storm conditions above $H_s$=14m | Increased stability with a large pitching motion & tension response |

In the initial stage of the design iteration process, multiple design iterations were conducted to enhance the pre-tension and stiffness of the overall system dimensions to prevent structural failure during extreme weather events. After identifying an appropriate level of stiffness and pre-tension, adjustments were made to the floater dimensions and overall system stiffness to accommodate the typical strength characteristics of steel mooring lines. However, instability issues arose during operational conditions due to the mass of the 10MW wind turbine generator. Increasing the floater diameter to 10.5 meters for greater pre-tension and stiffness did not resolve the instability (model AII). Consequently, the draft was increased to 62 meters for Model B to provide additional buoyancy and stability, and the performance of two models with different diameters (Model BIII and Model BIV) was evaluated. Although Model B showed improved stability compared to Model A, it still exhibited insufficient stability and stiffness in harsh environmental conditions for both Models BIII and BIV. Subsequently, the design of model C was further refined to enhance the system's stiffness and pre-tension by increasing the floater diameter. Model C underwent several design iterations to address these issues and prevent failure in harsh environmental conditions. The responses for Model CII, with a 20 m diameter and 62 m draft, under Hywind 50-year return operational and survival environmental conditions, were calculated and presented in Table 4-10. It was observed that the pitch and yaw motion responses exceeded the recommended limits in the rules and regulations of DNVGL-RP-0286 [440]. Additionally, the maximum tension values surpassed the assumed MBL of the steel wire of 5000 tons under both operational and survival conditions.

Fig. 4-14 illustrates the temporal progression of the peak event surge, pitch, and yaw motion responses, as well as the dynamic tension of the most heavily loaded line for both operational condition (a) and survival condition (b) for model 3M-20d-62D iteration IV. In operational conditions, the highest tension on the most heavily loaded line was observed due to the combined surge, pitch, and yaw motion responses. Conversely, in survival conditions, the highest tension was observed on the most heavily loaded line due to the combined surge, followed by significant pitch and yaw responses. Despite an improvement in system stability, the 3M-20d-62D model exhibited significant pitching and yawing movements, surpassing the maximum dynamic tension value beyond the assumed MBL of the steel wire. Consequently,

further refinement is required to develop a system with motion responses that comply with DNV regulations and tension responses within material specifications.

**Table 4-10** Overview of Results of Concept Design Stage I Model C Iteration IV

| Overview of results of Iteration C Model 3M_20d_62D | | | |
|---|---|---|---|
| | | Operational | Survival |
| **Surge (m)** | Maximum | 4 to –5.45 | 8.6 to -7.3 |
| | Mean | -0.09 | -0.02 |
| **Pitch (°)** | Maximum | 4.23 to -6.67 | 8.02 to -7.4 |
| | Mean | -1.42 | -0.3 |
| **Yaw (°)** | Maximum | 5.6 to -5.9 | 9.3 to -9.6 |
| | Mean | 0.01 | -0.02 |
| **Tension (tons)** | Maximum | 4019.5 | 6703.4 |
| | Mean | 2289.4 | 2883.7 |
| **Design Configuration Stability During Time Domain Simulation** | 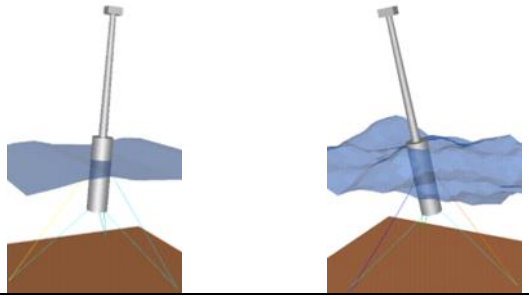 | | |

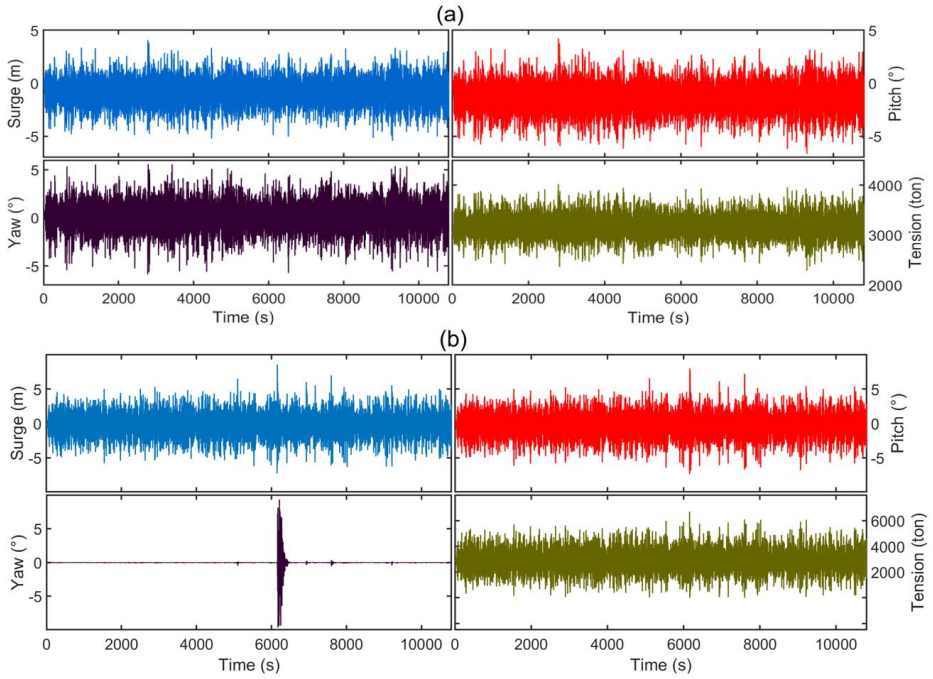


**Fig. 4-14** Model 3M-20d-62D Surge and Pitch Motion Response Time History under Operational (a) and Survival (b) Events

The tensions experienced in the mooring lines are substantial, requiring the utilization of thick steel wire rope with diameters that can reach up to 486 mm. Consequently, the subsequent phase of the project seeks to reduce the overall dimensions and tensions in the system, as well as to assess the consequences of line failure. As a result, two possible methods were evaluated to address this problem. One option was to increase the diameter of mooring lines significantly, while the alternative approach involved adding more mooring lines.

In the second phase of the design iteration process, it was deemed impractical to increase each mooring line by more than 480 mm. As a result, the number of mooring lines at each cluster was increased to four in order to alleviate the dynamic tension experienced by the mooring lines (refer to Fig. 4-15). This adjustment resulted in a total of eight mooring lines, arranged in two clusters positioned at 90° angles. The specific characteristics of the mooring line material that were taken into account during the initial design stage are detailed in Table 4-11.

**Table 4-11** Steel Wire Rope (SWR) Spiral Strand Mooring Line Characteristics of Stage 2 of Design Iteration Process

| | Diameter (mm) | $W_{in\ Air}$ (kg/m) | $W_{in\ Water}$ (kg/m) | MBL (tons) |
|---|---|---|---|---|
| **Steel** | 480 | 295 | 245.7 | 6312 |

In order to mitigate the yaw response, the yaw stiffness was determined using the approach outlined in reference [287], assuming a 20° deviation of the attachment point. This was done to simulate the impact of a bridle/delta connection and minimize the yaw movement of the platform (refer to Fig. 4-16(a)).

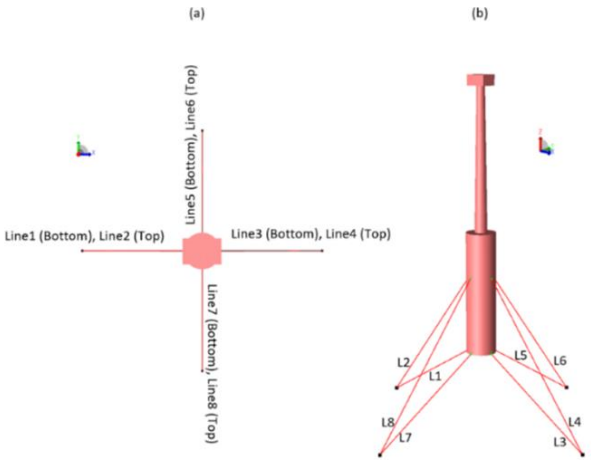


**Fig. 4-15** Model 4M-20d-62D (a) Mooring Lines Top View & (b) TLB Taut-Leg Mooring Layout

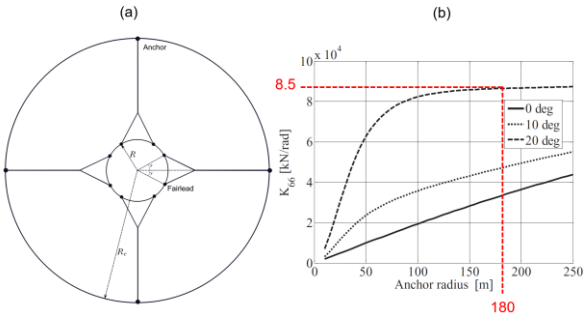


**Fig. 4-16** (a) Top View Taut Mooring System with Bridle Connection Configuration (b) Influence of Mooring System Geometry on The Stiffness

For the sake of simplicity, it was assumed that each mooring line had a single attachment point, which was then adjusted based on the mooring system stiffness matrix. A spread angle of 20° for the attachment points was also assumed to minimising the effects of a crowfoot connection in order to reduce the yaw motion of the platform. Fig. 4-16(a) illustrates the top view of the mooring configuration, which is distributed around the cylindrical floating platform. Meanwhile, Fig. 4-16(b) depicts the impact of the angle $\gamma$ on the mooring system stiffness, which was examined within a range of $R_C$. In this investigation, with $R_C = 180m$, it was found that $\gamma = 20^{\circ}$ resulted in nearly 8.5 times the yaw stiffness compared to when $\gamma = 0^{\circ}$, as indicated by the dotted line in Fig. 4-16(b). This configuration was shown to enhance the yaw response without affecting the stiffness in other directions.

The primary components of the motion response for floating offshore wind turbines occur in the wave frequency range for all translational and rotational motion. Nonlinear excitations, such as sum and difference frequency combinations, can also significantly impact the motion response at various degrees of freedom, thereby influencing the mooring line forces. Due to their increased computational complexity, preliminary designs of offshore structures often overlook higher order forces, assuming them to be at least an order of magnitude smaller than the first-order forces. However, a previous study [458] demonstrated that the second order forces for TLP-type floating offshore wind turbines are considerably higher than those for a Spar platform with catenary moorings, and can be of similar magnitude to the first-order forces. The sum frequency dominated the response in heave, while the difference frequency dominated in the surge response of the TLP. This is due to the fact that the TLP platform exhibits rigidity in the heave direction, resulting in a high heave natural frequency, which leads

to the predominance of sum frequency. Conversely, the platform demonstrates greater flexibility in the surge direction, resulting in a lower surge natural frequency, where the difference frequency becomes the dominant factor. The sum- and difference-frequency forces can lead to the generation of excitations both above and below the frequencies associated with the primary forces. This has the potential to induce vibrations at the natural frequencies of the structures. If the damping of the excited natural frequencies is sufficiently low, it can result in the development of significant, prolonged oscillations or problematic high-frequency vibrations. According to Roald's research [458], it was observed that the natural frequencies of the UMaine TLP in vertical, lateral, and rotational motion exceed the range of incident wave frequencies. This suggests that the influence of sum-frequency excitation may be significant for these modes of motion. In the event of a surge, the main reaction is ascribed to the stimulation resulting from the disparity in frequency at the natural frequency, which notably impacts the comprehensive response. With the existence of numerous slender elements in the TLP, it is expected that the viscous resistance will be relatively heightened during these surge oscillations.

In this section, the hydrodynamic analysis code WADAM will be utilized to calculate the first and second-order wave forces, added mass, and radiation damping based on potential theory. This code is integrated into the DNVGL SESAM software package through HydroD. The coupled motion response of the TLB system in defined environments for operating and storm conditions will be calculated using SIMO/RIFLEX in SESAM's DeepC program (Fig. 4-17), for excitation force, motion response, and mooring line response calculations. These simulation results will enable the evaluation of the FOWT design performance by allowing the calculation of the platform response using a first-order linear approach, first-order and wave drift forces, and a second-order approach.

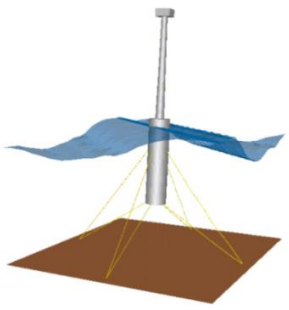

**Fig. 4-17** DeepC Time Domain Analysis of Model 4M-20d-62D

### 4.3.5. Significance of Second Order Approach

The findings for operational and survival conditions, as detailed in Table 4-5, are presented in relation to the motion and tension characteristics of the most heavily loaded line. In the scenarios examined, this pertained to the mooring line aligned with the combined wind wave and current direction. The maximum design tension for the mooring lines is determined from results obtained through extensive numerical simulations of environmental conditions. An accurate estimation of the extreme tension response is crucial at the initial stages of the design process to ensure precise prediction of mooring line loads and subsequent design optimizations. Hydrodynamic coefficients are calculated in WADAM for first-order only, first-order + wave drift, and second-order. A comparison of the surge and pitch motions and tether tension under operational and survival events will be presented (refer to Table 4-12, Fig. 4-18 and Table 4-13, Fig. 4-19). The results from the numerical simulations are presented to assess the significance of second-order effects on both motion and tension characteristics. During the initial phases of the design iteration process, it was noted that the performance of the TLB system is significantly affected by the surge, pitch, and yaw movements, which are influenced by concurrent wave, wind, and current forces. Additionally, an analysis of the results for the system with four mooring lines at each cluster indicated that yaw movements were considered negligible due to an assumed spread angle of 20° for the attachment points, which was also intended to mitigate the impact of a crowfoot connection. Other motion responses such as sway, heave, and roll were also considered minor and therefore were not considered. The presentation includes forty seconds of time history responses from three hours of time domain simulation to capture the maximum responses and the coupling effect.

Table 4-12 outlines the characteristics of the most loaded line with respect to the TLB's dynamic tension response and motion responses in operational conditions.

**Table 4-12** Model 4M-20d-62D Dynamic Tension and Motion Responses Characteristics under Operational Condition Event

| | | Time (s) | Max | Mean | SD |
|---|---|---|---|---|---|
| **1st Order** | Tension (Ton) | 4585 | 2490.1 | 1977.5 | 120.6 |
| | Pitch (°) | | 0.42 | 0.0942 | 0.0804 |
| | Surge (m) | | 0.43 | 0.0688 | 0.0898 |
| **1st Order + Drift** | Tension (Ton) | 4585 | 2495.9 | 1982.6 | 120.7 |
| | Pitch (°) | | 0.42 | 0.0981 | 0.0805 |
| | Surge (m) | | 0.42 | 0.0726 | 0.0900 |
| **1st order + 2nd Order** | Tension (Ton) | 4585 | 2199.7 | 1978.9 | 53.6 |
| | Pitch (°) | | 0.23 | 0.0953 | 0.0357 |
| | Surge (m) | | 0.22 | 0.0699 | 0.0399 |

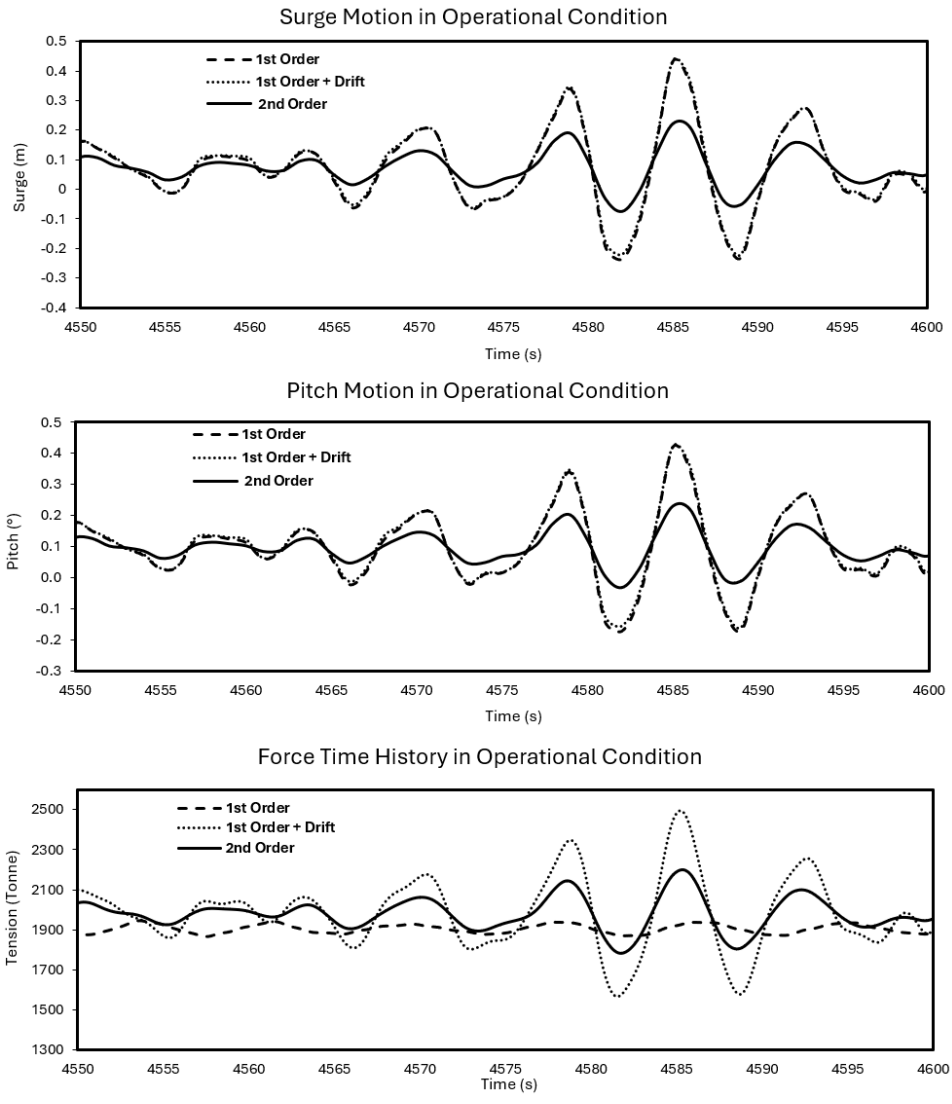


**Fig. 4-18** Model 4M-20d-62D Motions and Dynamic Tension Responses Time Series of 1st Order, 1st Order with Drift Force and 2nd Order Effects under Operational Condition

Fig. 4-18 illustrates a comparison of surge and pitch motions, along with the time series of maximum dynamic tension response for first-order, first-order with drift force, and second-order effects. The term "second order" denotes the combination of first- and second-order wave excitation forces. The maximum surge displacements over a three-hour time domain simulation are 0.43 m, 0.44 m, and 0.22 m for the first-order, first-order with drift, and second-order computations, respectively. In all cases, the pitch angle is less than 0.5°. The maximum pitch motions are consistent for first-order and first-order with drift effect, at 0.42°, but reduced to 0.23° when considering second-order effects. The maximum tension values during the operational condition simulation are 2,490 tonnes, 2,495 tonnes, and 2,200 tonnes for the first-order, first-order with drift, and second-order computations, respectively. The average tension recordings are slightly higher for second-order and drift force computations due to the mean drift forces acting on the wind turbine. Accounting for second-order effects, the maximum tension response is reduced, as evidenced by the standard deviations in Table 4-12 and Fig. 4-18, attributed to the effect of wave drift damping.

Table 4-13 presents the characteristics of the most loaded line maximum dynamic tension response and motion responses of Model 4M-20d-62D under survival condition. Fig. 4-19 allows for a comparison of surge, pitch, and most loaded dynamic tension time series for numerical calculations with first-order, first-order with drift force, and second-order effects wave force in survival condition. In harsh environment conditions, the mean difference between the first-order and second-order solution becomes smaller. However, the extreme response peaks are considerably reduced when second-order wave forces are included in the hydrodynamic analysis. The maximum pitch angles in harsh environment with a significant wave height of 19.4 m are 2.84°, 2.24°, and 2.53° for first-order, first-order with drift force, and second-order effect computational results, respectively.

**Table 4-13** Model 4M-20d-62D Dynamic Tension and Motion Responses Characteristics under Survival Condition Event

| | | Time (s) | Max | Mean | SD |
|---|---|---|---|---|---|
| **1st Order** | Tension (Ton) | 6266 | 9567.3 | 1834.2 | 571.3 |
| | Pitch (°) | | 2.84 | 0.0218 | 0.3307 |
| | Surge (m) | | 3.20 | 0.0198 | 0.4331 |
| **1st Order + Drift** | Tension (Ton) | 6261 | 7005.6 | 1953.4 | 592.98 |
| | Pitch (°) | | -3.79 | 0.0529 | 0.3324 |
| | Surge (m) | | -4.22 | 0.0506 | 0.4347 |
| **1st order + 2nd Order** | Tension (Ton) | 6266 | 5300.9 | 1971.6 | 595.3 |
| | Pitch (°) | | 2.53 | 0.0748 | 0.3331 |
| | Surge (m) | | 2.83 | 0.0689 | 0.4351 |

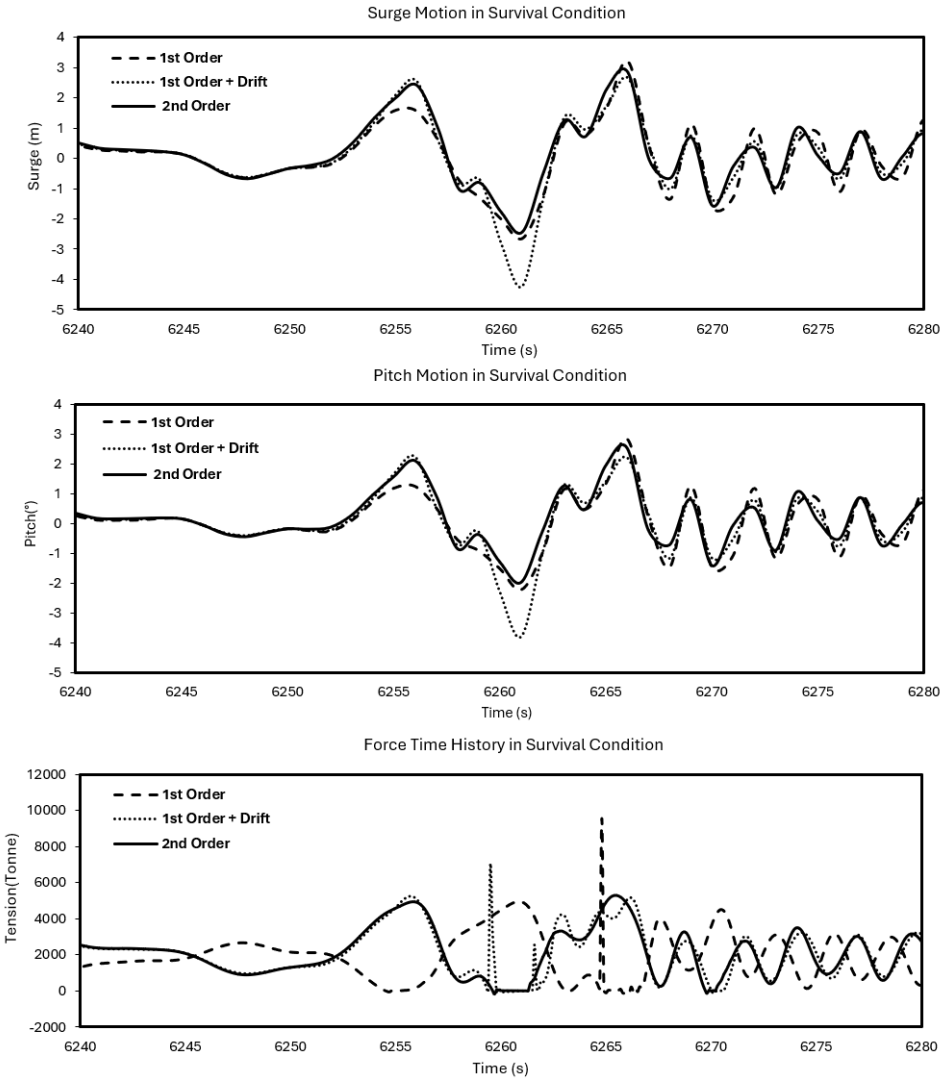


**Fig. 4-19** Model 4M-20d-62D Motions and Dynamic Tension Responses Time Series of 1st Order, 1st Order with Drift Force and 2nd Order Effects under Survival Condition

The introduction of first-order and drift forces resulted in a decrease in the maximum pitch angle, while second-order effects led to a slight increase. This phenomenon is attributed to the influence of the mean drift force acting horizontally on the floater. The coupling of surge and pitch motions in survival conditions led to the occurrence of maximum tension. When considering first-order with drift force effects, the standard deviation increased by approximately 6.5 tonnes compared to first-order alone. The difference in standard deviation between first-order with drift force effect and second-order was relatively small, being less than a tonne. Comparison of the results for first-order, first-order with drift force, and second-order effects revealed that the mean value for tension and motions were similar and slightly increased for all three cases. The maximum tension values occurred at the same time during the three-hour time domain simulation, with values of 9,567 tonnes, 7,006 tonnes, and 5,301 tonnes for the first-order, first-order with drift, and second computations, respectively.

The mean tension in the mooring lines remained relatively constant for both operating and survival conditions. However, the maximum response and standard deviation increased fourfold. The tension response in extreme weather exhibited similar trends for first-order, first-order plus drift, and combined first- and second-order, with the mean value of the most heavily-loaded mooring lines being comparable. The occurrence of large spikes can be observed for a number of simulations. To investigate spike observation under survival condition for first-order and first-order plus drift approaches, ten simulations, each utilizing different wave seeds, were conducted for each approach. The results revealed that 40% of the simulations exhibited spike when considering the first-order approach. However, this occurrence decreased by half when the first-order plus drift approach was utilized. Furthermore, all simulations showed the absence of spike when the second-order effect was considered. The identified peaks were attributed to a loss of tension caused by a decrease in buoyancy, along with the subsequent snap loads encountered in both the first-order and first-order plus drift methodologies when the platform restored its buoyancy. This occurrence highlights a reliance on environmental factors, emphasizing the necessity of integrating a thorough second-order analysis into the methodological framework. The analysis results indicated that the inclusion of second-order effects has a more pronounced impact on survival conditions compared to operational conditions. Given the crucial role of extreme environmental conditions in the design of FOWT,

incorporating second-order effects is essential for enhancing concept design and providing a more accurate prediction of forces and responses at early stages. This approach helps to prevent overdesign of the system, as significant peak responses are observed when only first-order and first-order plus drift effects are considered in the analysis. The research noted decreases in extreme tension levels when examining full second-order calculations compared to first-order and first-order plus drift methods. Furthermore, additional experimentation was carried out to evaluate the robustness of the Model 4M-20d-62D conceptual design in the event of line failure, as depicted in Fig. 4-20. Specifically, the behaviour of the system under survival conditions with a broken most heavily loaded mooring line (line 2) was examined.

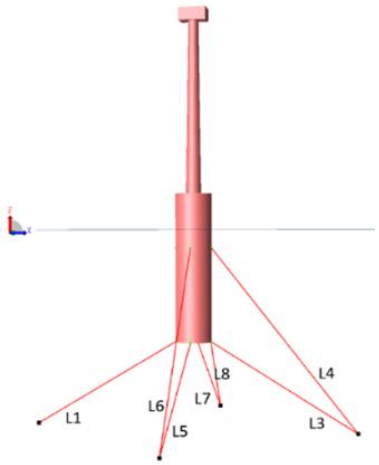


**Fig. 4-20** Model 4M-20d-62D with Broken Mooring Line 2

The analysis revealed that the system exhibits instability when one mooring line is disconnected, causing the tension in the remaining lines to exceed the MBL of the mooring line material. Even when the diameter of the mooring line is increased to the size used in the initial phase of the iteration process (480 mm), the system continues to be unstable. Consequently, further improvements are necessary in the design. In the subsequent phase, a new mooring system will be developed to investigate the hydrodynamics of the system under similar environmental conditions.

Due to the high-tension responses in relation to the MBL and the instability of the system with four mooring lines at each cluster when one line is assumed to be broken, additional design optimization is necessary. In the third stage of the design iteration

process, the number of mooring lines at each cluster is increased to six lines (refer to Fig. 4-21) due to the impracticality of increasing the mooring line beyond 480mm. As a result, the mooring system now consists of twelve mooring lines in total, distributed in two clusters at 60° angles. As the mooring line number increased, the diameter of the mooring line reduced to 240mm. The characteristics of the mooring lines material is presented in Table 4-14.

**Table 4-14** Steel Wire Rope (SWR) Spiral Strand Mooring Line Characteristics of Stage 3 of Design Iteration Process

| | Diameter (mm) | $W_{in\ Air}$ (kg/m) | $W_{in\ Water}$ (kg/m) | MBL (tons) |
|---|---|---|---|---|
| **Steel** | 240 | 221.6 | 176.6 | 3000 |

To prevent structural failure in extreme weather events, once an appropriate level of stiffness and pre-tension is determined, the dimensions of the floater and overall stiffness in the system will be reduced to accommodate the typical strength characteristics of a steel mooring line. The environmental loads are consistent with those assumed for the concept design stages I & II, as presented in Table 4-5.

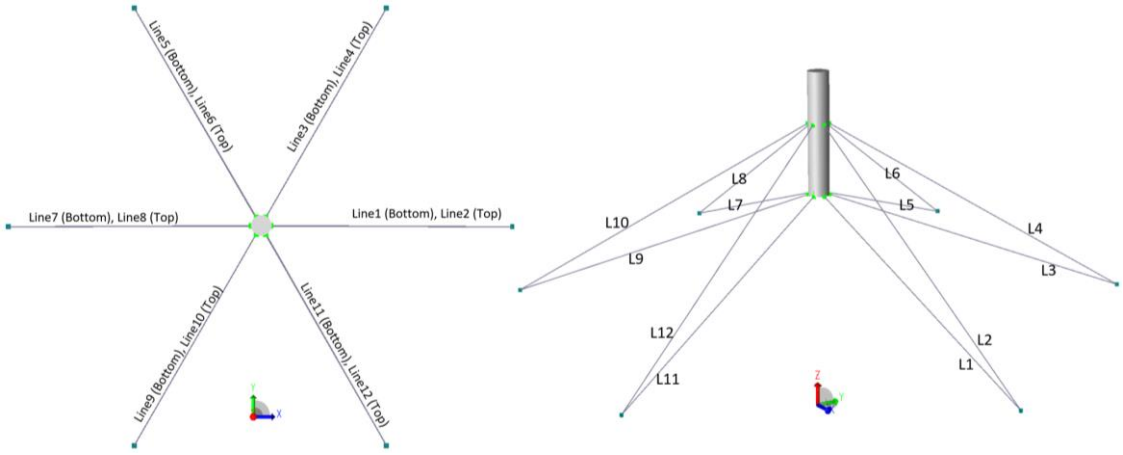


**Fig. 4-21** Model 6M-17.5d-62D (a) Mooring Lines Top View & (b) TLB Taut-Leg Mooring Layout

The study examines the operational and survival capabilities of the system, including its resilience to a fractured mooring line, through a time-domain coupled analysis carried out in DeepC. In operational scenarios, a consistent wind force with an average speed of 18 m/s is applied across the rotor area, while in survival scenarios, the wind

force with an average speed of 40 m/s is distributed over the projected area encompassing the tower and blades.

The design iterations commenced with a reduction in floater diameter from 20m to 12.5m, and three models with varying draft sizes were examined. This process of reducing the floater diameter with three draft sizes was continued to achieve an optimal design that improves stability performance. The stability of each design was evaluated using Ultimate Limit State (ULS) and Accidental Limit State (ALS) criteria. The responses for each design iteration were calculated, and the maximum motion responses and maximum dynamic tension of the most heavily loaded line for each design iteration are presented in Table 4-15 for operational conditions and Table 4-16 for survival conditions.

**Table 4-15** Motion Responses and Dynamic Tension Characteristics of Design Iteration Step III under Operational Condition Event

| Model | Surge (m) | Sway (m) | Heave (m) | Roll (°) | Pitch (°) | Yaw (°) | Tension (ton) |
|---|---|---|---|---|---|---|---|
| 6M-17.5d-62D | 3.96 | -0.59 | -2.43 | 0.41 | 1.19 | 1.33 | 2466.34 |
| 6M-17.5d-52D | 3.36 | -0.55 | -1.89 | 0.40 | 1.06 | 1.22 | 2163.45 |
| 6M-17.5d-42D | 3.18 | -0.54 | -1.74 | 0.39 | 1.02 | 1.18 | 2026.26 |
| 6M-15d-62D | 2.85 | -0.52 | -1.48 | 0.39 | 0.94 | 1.11 | 1777.42 |
| 6M-15d-52D | 2.55 | -0.50 | -1.25 | 0.38 | 0.87 | 1.05 | 1611.05 |
| 6M-15d-42D | 2.30 | -0.49 | -1.06 | 0.37 | 0.81 | 0.99 | 1444.71 |
| 6M-12.5d-62D | 2.03 | -0.46 | -0.90 | 0.36 | 0.74 | 0.93 | 1323.58 |
| 6M-12.5d-52D | 1.78 | -0.44 | -0.76 | 0.35 | 0.67 | 0.86 | 1161.03 |

**Table 4-16** Motion Responses and Dynamic Tension Characteristics of Design Iteration Step III under Survival Condition Event

| Model | Surge (m) | Sway (m) | Heave (m) | Roll (°) | Pitch (°) | Yaw (°) | Tension (ton) |
|---|---|---|---|---|---|---|---|
| 6M-17.5d-62D | 5.71 | 1.35 | -4.54 | -1.09 | 2.91 | -2.32 | 3482.94 |
| 6M-17.5d-52D | 4.84 | 1.27 | -3.54 | -1.06 | 2.59 | -2.12 | 3055.20 |
| 6M-17.5d-42D | 4.58 | 1.25 | -3.26 | -1.05 | 2.49 | -2.06 | 2861.46 |
| 6M-15d-62D | 4.10 | 1.20 | -2.77 | -1.03 | 2.30 | -1.94 | 2680.00 |
| 6M-15d-52D | 3.88 | 1.18 | -2.55 | -1.02 | 2.21 | -1.88 | 2429.15 |
| 6M-15d-42D | 3.67 | 1.15 | -2.35 | -1.01 | 2.13 | -1.83 | 2201.79 |
| 6M-12.5d-62D | 3.44 | 1.12 | -2.16 | -0.99 | 2.03 | -1.76 | 2130.83 |
| 6M-12.5d-52D | 3.03 | 1.07 | -1.83 | -0.96 | 1.85 | -1.64 | 1931.39 |

Based on the findings obtained from operational and survival conditions, it was noted that there is a reduction in motion and dynamic tension responses with a decrease in the diameter and draft of the support platform. Given the failure of model 6M-12.5d-42D, the optimal design is identified as 6M-12.5d-52D. As the system fulfils the ULS requirements, an analysis of the system with broken mooring lines will be presented. The investigation focuses on the scenario of the system under broken mooring lines for the 6M-12.5d-52D model. Specifically, the study examines the two most-loaded mooring lines that experienced maximum load in survival conditions, assumed to break and detach from the fairleads (refer to Fig. 4-22).

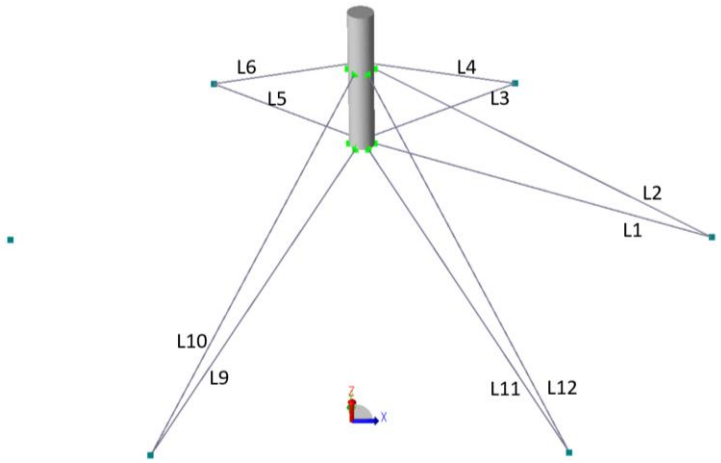


**Fig. 4-22** Disconnected lines 7 & 8 Representing Lines Broken Scenario

The primary objective is to investigate, firstly, that the TLB with disconnected mooring lines will survive, and secondly, that the motion responses do not exceed the limitations outlined in Section 2.9. Table 4-17 presents the maximum motion responses and maximum dynamic tension of the most heavily loaded line under the survival condition with two broken mooring lines for model 6M-12.5d-52D. Notably, in this scenario, the motion responses of the TLB and the dynamic tension of the most loaded mooring line, line 6, increase compared to the results from the survival event. However, despite the system's ability to survive with broken mooring lines, the maximum dynamic tension of the most loaded line exceeds the material MBL.

**Table 4-17** Motion Responses and Dynamic Tension Characteristics of Design Iteration step III under Survival Condition with Lines Broken Event

| Model | Surge (m) | Sway (m) | Heave (m) | Roll (°) | Pitch (°) | Yaw (°) | Tension (ton) |
|---|---|---|---|---|---|---|---|
| 6M-12.5d-52D | 8.25 | 3.58 | 3.37 | -5.29 | 8.57 | -7.60 | 3264.36 |

In the event of two mooring lines failing, an analysis showed that the dynamic tension in the most heavily loaded mooring line exceeded the material's MBL. This occurred as a result of simplifying environmental conditions into two sets, assumed to mirror those at the Hywind Scotland wind farm, which is characterized by a substantial significant wave height. The high tension was caused by the continuous application of wind force, which was calculated by assessing the drag on the tower and blade structures throughout the entire simulation period. In the following section, a detailed examination will be carried out to investigate the reliability of the 6M-12.5d-52D model under rule-based environmental conditions by utilizing different mooring materials. This process involved assessing various design load cases (DLCs) as outlined by DNV [422, 459, 460] to determine the expected extreme and accidental loads over the system's operational lifetime. Additionally, the effectiveness of recently developed mooring line materials, such as fibre ropes, polyester, and nylon ropes, was compared to that of steel wire rope.

## 4.4. Tension Leg Buoy Detail Analysis

This research will conduct a hydro-aero-servo-elastic analysis of a 10MW offshore wind turbine, which is supported by a TLB platform and secured by a taut mooring system carried out in SIMA (Fig. 4-23). The distinctive TLB configuration underwent a comprehensive and iterative development process to achieve an ideal prototype for deployment site. A new TLB Floating Offshore Wind Turbine (FOWT) system designed to accommodate a 10 MW wind turbine employed an innovative taut mooring system for anchoring to the seabed. An evaluation was conducted to assess the optimal design resulting from the initial conceptual phase in accordance with established criteria and standards for floating wind turbine design, incorporating nylon and polyester mooring materials. The investigation will focus on the dynamic response characteristics of the TLB under environmental conditions in the northern North Sea, where the water depth is 110 meters. Additionally, the study will compare the performance of different mooring line configurations, specifically steel, polyester, and nylon. The primary objective of the analysis is to demonstrate that the proposed TLB platform and mooring system can effectively meet the static and dynamic operational requirements, as well as the survival needs, of a 10MW FOWT. The study will also develop a control system tailored for land-based wind turbines. Furthermore, the feasibility of employing polyester or nylon mooring lines at this scale will be examined, considering their elasticity, minimum loads, and safety factors in line with the requirements of the FOWT industry. The study will assess the performance of the TLB using three different mooring materials under various environmental load conditions, including normal operation and idle states, in accordance with DNV rules and regulations outlined in Section 2.9. Furthermore, the study will examine the systems' capacity to withstand mooring line failures.

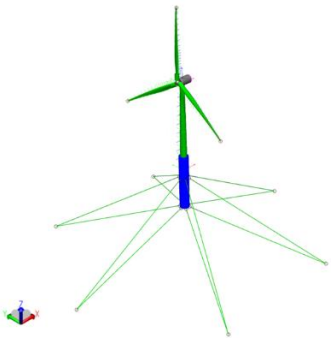

**Fig. 4-23** 10MW TLB FOWT Model in SIMA

### 4.4.1. Hydro-Aero-Servo-Elastic Coupling

In order for a FOWT model to produce accurate results, it must consider the interplay between hydrodynamic loads, aerodynamic loads, controller theory, and elasticity. When an elastic body is subjected to hydrodynamic loads, it undergoes elastic deformation, which in turn alters the load on the structure, creating a dependency between the load and the structural response. A structural model coupled with a hydrodynamic load model is referred to as a hydro-elastic model. Similarly, there is a dependency between aerodynamic loads and structural response for an elastic structure, and a structural model coupled with an aerodynamic model is known as an aero-elastic model. When combined with controller theory, these models form a hydro-aero-servo-elastic model, which accounts for the dependency of all these effects [357]. DNV's Sima software [360], is utilized hydro-aero-servo-elastic analyses. This includes environment modelling with current and wind profiles, wave modelling, and the ability to incorporate various elements such as added mass, potential damping, 1$^{st}$ and 2$^{nd}$ order, wave excitation, and viscous force elements to capture Morison forces. SIMA also calculates retardation functions from added mass and damping to consider frequency-dependent added mass and damping in time-domain calculations. Additionally, SIMA integrates the software tools Riflex and Simo, where Riflex is a non-linear finite element software for slender marine structures and Simo is a simulator for marine operations. This simulation tool utilizes the finite element solver from the combined SIMO/RIFLEX tool, transmitting position and velocity data to the aerodynamic code at the initial iteration of each time step and receiving lumped forces along the wind turbine blades. The body's fixed rotor coordinate system is assumed to have its origin at the hub centre, with the Z-axis aligned with the rotor shaft and in the direction of the hub support. Wind loads on the blades are calculated using the load coefficient description in the aerofoil library file and a double-multiple stream tube blade element momentum method, which accounts for dynamic stall effects. In the coupled analysis, SIMO and RIFLEX simulations are conducted simultaneously using a nonlinear time-domain approach for dynamic analyses. The motions of the SIMO-body are directly inputted into the RIFLEX model of the mooring system. Dynamic equilibrium is achieved at each time step, ensuring consistent treatment of the coupling effects between the floater and mooring system. This implies that the coupling effects are automatically integrated into the analysis scheme. The coupling effects

from the mooring system encompass restoring, damping, and inertia forces [461], with the primary contributors being static restoring force, current loading and its impact on the restoring force, seafloor friction, damping from mooring lines motions and current, friction forces due to hull contact, and additional inertia forces due to the mooring system. It is important to note that the quasi-static approach can accurately consider only the static restoring force, while the fully coupled analysis can account for all the coupling effects. The computational procedure of the coupled approach is described in Fig. 4-24.

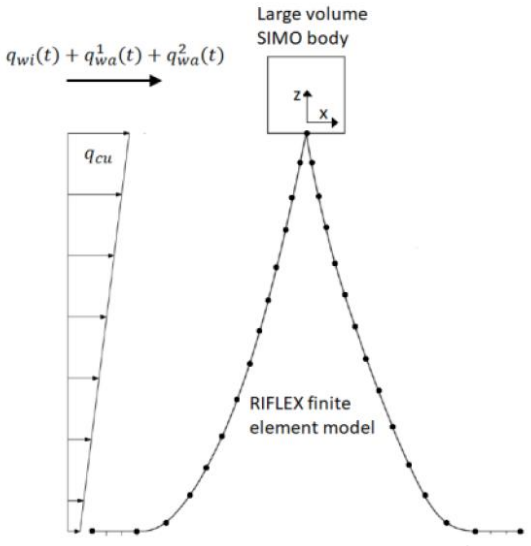


**Fig. 4-24** Coupled Analysis of Large Volume SIMO Body and Slender RIFLEX Model [286]

## 4.4.2. Wind Turbine

Based on the advancements in wind turbine capacity, this research utilizes the 10MW DTU [149] reference turbine modelled in SIMA (refer to Fig. 4-25) to conduct a comprehensive analysis of its aero-hydro-servo-elastic characteristics in this section.

In comparison to the land-based turbine discussed in the literature, modifications have been implemented in the tower sections to accommodate a 20 m decrease in height, which is attributed to the fact that the TLB platforms extend 20 m above sea level [462]. The reduction in the height of the wind turbine tower and its integration into the FOWT support platform result in significant cost savings during construction and installation

[154]. Moreover, this strategy helps improve the overturning bending forces experienced by the wind turbine [166, 427]. By reducing the tower height and incorporating it into the support platform, the hub height aligns with the designated design hub height, ensuring that it does not impact the aerodynamics of the wind turbine during power generation.

The top and bottom diameters of the tower remain consistent with the original documentation, while the middle section's diameter has been modified to accommodate the reduced length. The specifications of the 10MW DTU wind turbine are detailed in Table 4-18.

**Table 4-18** 10MW DTU Wind Turbine Property Specifications

| Property | Value |
|---|---|
| Rotor Diameter | 178.3 m |
| Hub Height | 119 m |
| Hub Diameter | 5.6 m |
| Overhang | 7.1 m |
| Rotor + Nacelle Mass | 674 tons |
| Nacelle Inertia | 7326.4 $t.m^2$ |
| Hub Mass | 105.520 tons |
| Hub Inertia | 325.671 $t.m^2$ |
| Tower Mass | 630 tons |
| Tower Length | 83 m |
| Tower Diameter | 8.3m at Base |
| | 5.5m at Hub |
| Cut in wind speed | 4 m/s |
| Cut out wind speed | 25 m/s |
| Rated wind speed | 11.4 m/s |

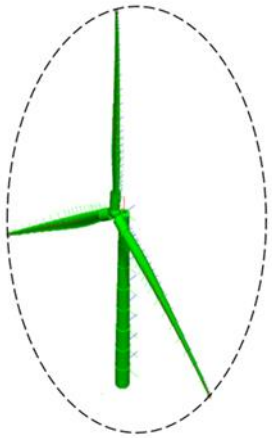

**Fig. 4-25** 10MW DTU Wind Turbine Model in SIMA

### 4.4.3. Support Platform

The optimal design, identified as 6M-12.5d-52D, has been established through conceptual design, and the system satisfies the ULS criteria. A comprehensive analysis of the 12.5-meter diameter and 52-meter draft support platform will be conducted. The configuration and characteristics of the support platform are illustrated in Fig. 4-26 and Table 4-19.

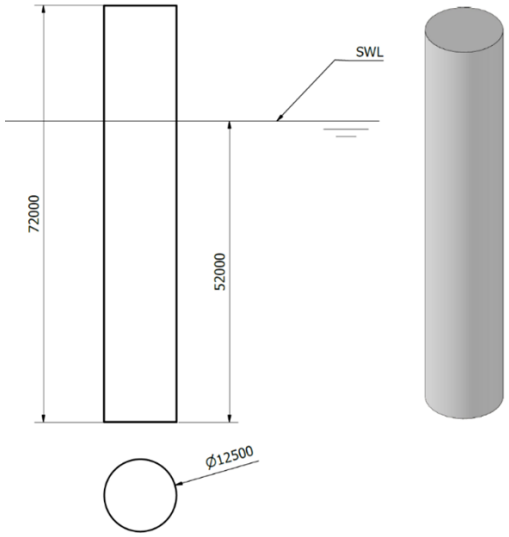


**Fig. 4-26** TLB Support Platform 3D Model (Right) & Schematic (Left)

**Table 4-19** Support Platform Specification

| 10MW TLB FOWT | |
|---|---|
| **Draft** | 52 m |
| **Diameter SWL** | 12.5 m |
| **Diameter Bottom** | 12.5 m |
| **Mass** | 791.0 t |
| **COG** | 40.95 m |
| **COB** | -26 m |
| **Pre-Tension** | 906.8 t |
| **Anchor Radius** | 180m |
| **Note: SWL serves as the point of reference.** | |

## 4.4.4. Mooring System

The mooring system is similar to the one used in the third phase of the design iteration process. In the case of a taut leg mooring system, where the line does not contact the seabed and is kept taut due to the pretension caused by the platform's excess buoyancy, most of the restoring loads are generated by the elasticity of the line. The calculation of pretension involves determining the excess buoyancy and weight and is implemented by reducing the length of the material. This reduction in length is determined by the pretension value and the axial stiffness of the material. The lines are inclined (with angle) and the anchor experiences horizontal and vertical loads. The taut mooring system comprises a total of twelve mooring lines, arranged in two clusters at two different heights: 10m below the water level (upper lines) and at the bottom of the floater (lower lines). The lines are positioned at 60° angles to each other. The configuration of the mooring system is depicted in Fig. 4-27.

The principal properties of the mooring system presented in Table 4-20.

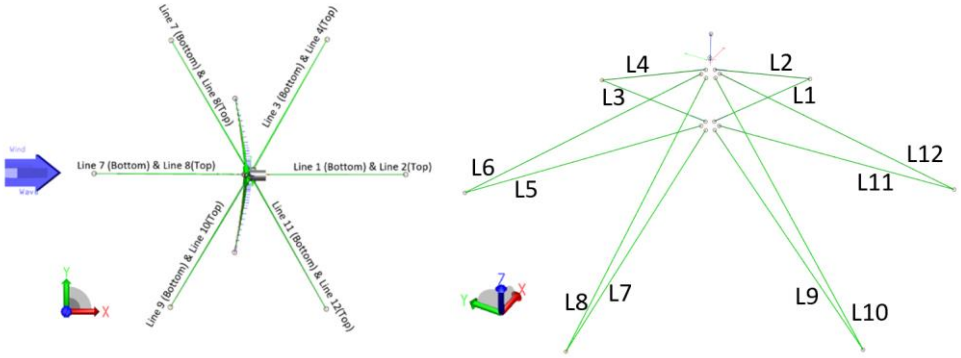


**Fig. 4-27** Mooring Lines Top View (left) and TLB Taut-Leg Mooring Layout (right)

**Table 4-20** Mooring System Principal Properties

| Taut Mooring System Characteristics | | |
|---|---|---|
| **No. of Lines** | | 2 sets of 6 lines |
| **Angle between Lines** | | 60° |
| **Radius Platform CL to Anchor** | | 180 m |
| **Fairlead below SWL** | | -10 m & -52 m |
| **Angle of attached at top Fairlead** | | 29.92° |
| **Angle of attached at bottom Fairlead** | | 18.46° |
| **Mooring Line Length** | **Upper** | 200.5 m |
| | **Lower** | 183.2 m |

### 4.4.5. Mooring Materials

Currently, floating wind projects have tended to use conventional steel chains for mooring systems, for all the top section, the main length of the line, and the bottom part that connects to the anchors. As the development of new materials continues to grow, such as synthetic fibres, there is potential for the substitution of steel chains with materials like polyester or nylon in certain or all aspects of mooring lines [257]. Consequently, the design of taut mooring systems considers the use of polyester and nylon mooring lines, which will be compared with steel wire rope. The characteristics of the mooring line materials are shown in Table 4-21 [265].

**Table 4-21** Mooring Material Specifications

| | Diameter (mm) | W $_{in\ Air}$ (kg/m) | MBF (tons) |
|---|---|---|---|
| **Steel** | 320 | 401.2 | 4104 |
| **Polyester** | 320 | 77.7 | 3097 |
| **Nylon** | 320 | 47.8 | 2247 |

Four mooring lines of 80mm are assumed to bound together to construct the nylon mooring line, whereas for polyester and steel (Spiral Strand Xtreme 1960 Grade), lines of 320mm diameter are selected [265]. The summary of simplified assumptions considered for mooring system are including uniform mooring line material cross section for calculating hydrostatic stiffness matrix, the quasi- static mooring line model, 20-degree spread of the mooring line attachment point.

For the steel line, the hydrostatic stiffness matrix is calculated (refer to appendix B) and a constant axial stiffness is considered based on the mooring line MBL. For the fibre lines, the mechanical behaviour is more complex than the corresponding behaviour of steel wire ropes. Synthetic materials such as polyester and nylon are highly nonlinear and time-dependent load-elongation, which plays an essential role in their performance [332]. Therefore, in the analysis of synthetic mooring lines, the synthetic rope's visco-elastic, visco-plastic properties as well as the dynamic stiffness are considered. The non-linear material curve used in static analysis is found by shifting the working curve and redefining the initial stress-free length, so that the working and original working curves intersect at maximum tension [293, 294]. On the

other hand, the linear material curve used in the dynamic analysis is given by dynamic stiffness coefficients using the mean tension of the segment. The initial stress-free length is then redefined, such that the tension is identical between static and dynamic analysis given the elongation of static analysis [289, 293] (Fig. 4-28).

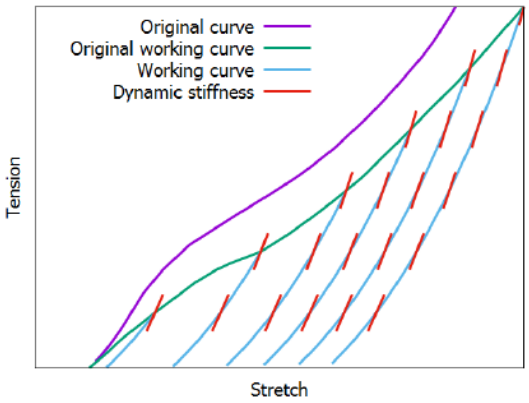


**Fig. 4-28** Tension Strain Curve (Source RIFLEX user manual 4.18.1)

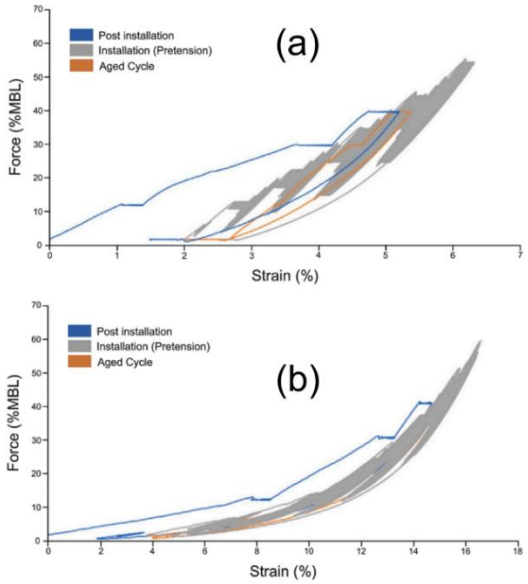


**Fig. 4-29** Polyester and (b) Nylon Dynamic Stiffness Curve (Data obtained from Bridon-Bekaert - The Ropes Group) [235, 284]

The static stiffness is utilized for the initial region of the loading curve up to the mean load, followed by the dynamic stiffness which is used to predict the cyclic part of the loading, including low frequency and wave frequencies [296, 297]. Table 4-22 displays the relationship between elongation and spliced MBL, as per the CI1500B-2015 standard provided by Bridon-Bekaert [265] which are based on dynamic stiffness

curve shown in Fig. 4-29. In contrast to steel wire rope, polyester and nylon ropes demonstrate non-linear elongation characteristics under axial load, which are influenced by loading type and can vary over time and with different loading histories.

A mooring line in a severe environment typically experiences a steady mean load and dynamic loads oscillating around the mean load. Ideally, the polyester rope's load–elongation properties should be modelled as nonlinear elastic by expressing the load–elongation relationship [296, 298]. This study considered the upper-bound and lower-bound approaches to deal with polyester and nylon ropes axial stiffness, meaning that at 10% to 20% of elongation for static axial stiffness, whilst at 20% to 50% of elongation for dynamic axial stiffness (refer to Table 4-22).

In SIMA, as depicted in Fig. 4-28, the average tension over the elements in a segment is used to compute the intersection between the working curve used in static analysis and the linear tension-strain curve used in dynamic analysis [463]. Therefore, the axial stiffness of the steel mooring line remains constant throughout the simulation length, while the axial stiffness of the fibre mooring lines will vary depending on the line elongations. The dynamic tension versus elongation of fibre mooring materials is extracted from the curves displayed in Fig. 4-29 and illustrates in Table 4-23.

**Table 4-22** Elongation Value Based on MBL Provided by Brindon[265, 444]

| | % MBL | 10 | 20 | 30 | 40 | 50 |
|---|---|---|---|---|---|---|
| Polyester | % Elongation | 0.9 | 2.6 | 4.1 | 5.6 | 7 |
| Nylon | | 5 | 7.3 | 8.6 | 9.6 | 10.3 |

**Table 4-23** Dynamic Tension-Elongation Inputs in SIMA

| Polyester | | Nylon | |
|---|---|---|---|
| Elongation (%) | Tension (N) | Elongation (%) | Tension (N) |
| 0 | 0 | 0 | 0 |
| 0.9 | 3.04E+06 | 5 | 2.20E+06 |
| 2.6 | 6.08E+06 | 7.3 | 4.41E+06 |
| 4.1 | 9.11E+06 | 8.6 | 6.61E+06 |
| 5.6 | 1.22E+07 | 9.6 | 8.82E+06 |
| 7 | 1.52E+07 | 10.3 | 1.10E+07 |
| 10 | 2.73E+07 | 14 | 1.98E+07 |

Sources of the considered nonlinearity for the present numerical study and simplified assumptions have been considered are illustrated in Table 4-24.

**Table 4-24** Nonlinearity Sources and Simplified Assumptions

| Sources of the considered nonlinearity |
|---|
| Nonlinear time domain analysis |
| Nonlinear wave included up to second order |
| Nonlinear free surface |
| Nonlinear fibre mooring lines material curve |
| **Simplified assumptions** |
| Uniform mooring line material cross section |
| Ignored |
| The mooring line inertia forces |
| The external fluid loads such as drag on the mooring line |
| Added mass forces |
| Mooring line seabed interaction forces |
| The influence of the VIV |
| Quasi–static mooring line models |
| Massless linear spring |
| 20-degree spread of the mooring line attachment point |
| Ignores the turbine blade flexibility |

These aspects could reduce the accuracy of the predicted hydrodynamic loads exerted on the platform and mooring lines particularly in low and moderate fluid speeds which may affect the resulting system response [269, 272, 464].

The present simulation also ignores the blade flexibility which could influence the system dynamics, particularly the tower elastic motion response when the rotor experiences severe aerodynamic loads at which interaction between the blade and tower elastic motions can be evident. The influence of the Vortex Induced Vibration (VIV), which can be considerable when the substructure is subject to steady current or combined current and wave loads, is also neglected. In the initial design phase, the hydrodynamic results may be affected by the assumptions utilized. These assumptions are employed to simplify the analysis during the conceptual design phase. This methodology is frequently utilized in the assessment of floating offshore wind turbines, as demonstrated by published research [465, 466] which noted that simplifications can aid in preliminary design phases.

### 4.4.6. Free Decay Test

A free-decay test is an effective method for obtaining data on the inherent periods and damping characteristics of a floating structure. The tests were conducted to determine the natural period of the system in all six degrees of freedom (DOF). This section examines the parameters of three mooring line materials in relation to the first natural frequencies and damping ratio of the body with mooring lines. The wind turbine is in a parked state with feathered blades to minimize aerodynamic damping, and no external environmental loading is present in the simulations. The systems are displaced in the degree of freedom by an applied force or moment in a similar time series. The period is defined as the distance between two turning points, two peaks, or two troughs in the time series, and the mean value of all periods is considered the natural period.

In a manner similar to the approach utilized by Borlet (2016) [467], the initial displacement in translational DOFs was induced by the application of a ramp force for a duration of 100 seconds in SIMA, followed by the application of a constant force for an additional 100 seconds. Subsequently, the force was removed, allowing the platform to oscillate freely in the specified degree of freedom (DOF) as the oscillations gradually diminished over time. The ramp force and constant force were specified using the designated force option in SIMA. Faltinsen described a method for evaluating the results of free decays to extract the linear and quadratic damping coefficients (p. 252, [220]). This method is normally used for physical tests. It can be applied to simulations that involve more than one damping mechanism [351]. By utilizing this technique, it is possible to extract both damping coefficients for the system from a single free decay data run.

The equation of motion for a body undergoing free decay is [220]:

$$M\ddot{x} + B_1\dot{x} + B_2\dot{x}|\dot{x}| + Cx = 0 \tag{12}$$

where $M$ is the mass (including added mass), $B_1$ is the linear damping, $B_2$ is the quadratic damping term, and $C$ is the restoring stiffness. In order to find the damping coefficients, the equation of motion is divided by the mass contribution, $M$. The analysis of this equation is based on the well-known solution of a linear oscillating system in combination with the technique of equivalent linearization. Equivalent

linearization involves replacing the non-linear damping term with a linear term. The equivalent linear term is determined based on the requirement of equal damping energy per cycle. This requirement is satisfied using [435]:

$$P_{EQ} = P_1 + \frac{8}{3\pi}\omega x_0 P_2 \tag{13}$$

$P_1$ and $P_2$ are the linear and quadratic damping term divided by the mass contribution, respectively. $x_0$ is the motion amplitude and $\omega$ is the oscillation frequency.

The linearized equation of motion can now be written as [468]:

$$\ddot{x} + P_{EQ}\dot{x} + P_3 x = 0 \tag{14}$$

Assuming $x_i$ and $x_{i+1}$ are two succeeding amplitudes, the logarithmic decrement can then be found for each period by taking the logarithmic value of the ratio between two amplitudes located one natural period apart [435]:

$$\Lambda = \ln\left(\frac{x_i}{x_{i+1}}\right) \tag{15}$$

The damping ratio, $\xi$, which is defined as the ratio between actual and critical damping, can then be found for each measured period. For low damping ratios (typically $\xi$ < 0.2) the formula is [468]:

$$\xi = \frac{\Lambda}{2\pi} \tag{16}$$

By examining five distinct pairs of peaks and applying the theoretical framework outlined in reference [469] calculated the damping ratio.

Fig. 4-30 to Fig. 4-32 shown the translational degrees of freedom and Fig. 4-33 to Fig. 4-35 shown the rotational degrees of freedom for TLB platform with steel, polyester, and nylon mooring lines. Table 4-25 displays the natural frequencies (in radians per second, rad/s) for different materials such as steel, polyester, and nylon in various modes of vibration and Table 4-26 presents damping ratio of TLB with three mooring materials are calculated for six degrees of freedom which are illustrated in Table 4-26.

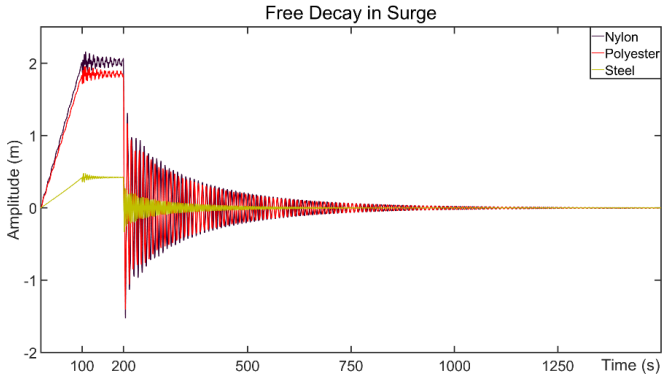


**Fig. 4-30** Free Decay in Surge for TLB with Nylon, Polyester, and Steel Mooring Lines

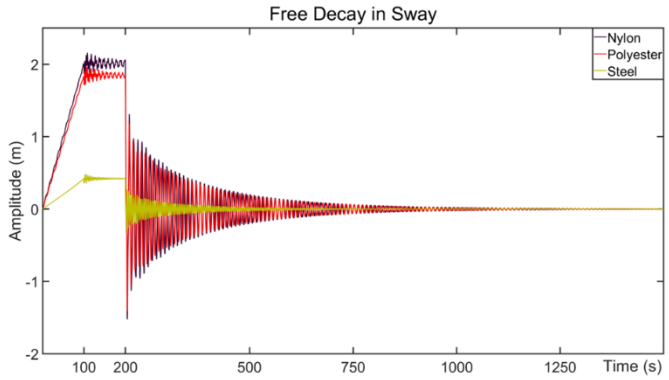


**Fig. 4-31** Free Decay in Sway for TLB with Nylon, Polyester, and Steel Mooring Lines

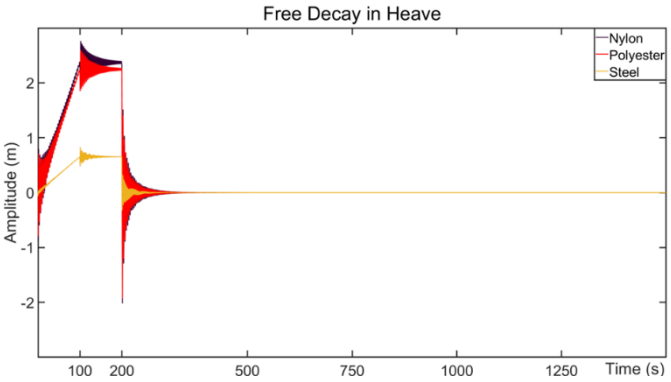


**Fig. 4-32** Free Decay in Heave for TLB with Nylon, Polyester, and Steel Mooring Lines

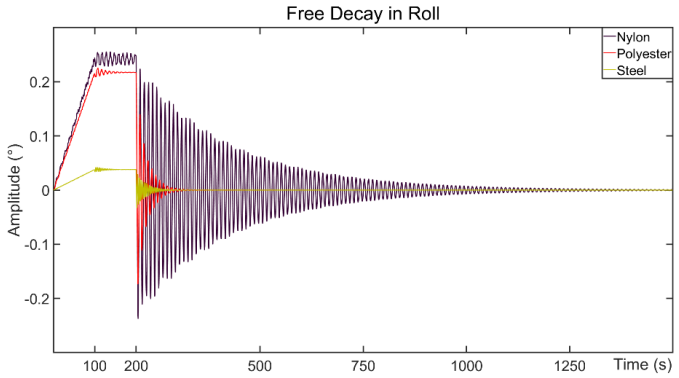


**Fig. 4-33** Free Decay in Roll for TLB with Nylon, Polyester, and Steel Mooring Lines

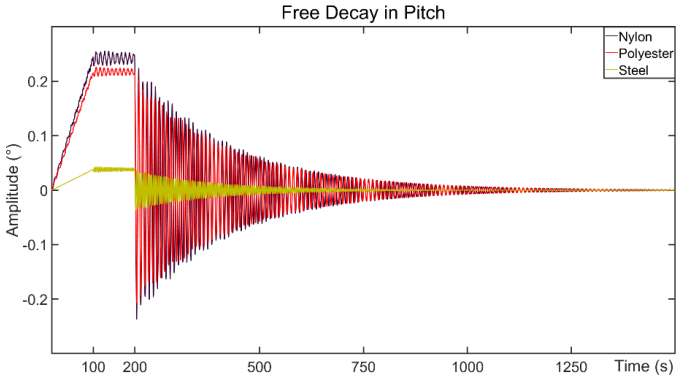


**Fig. 4-34** Free Decay in Pitch for TLB with Nylon, Polyester, and Steel Mooring Lines

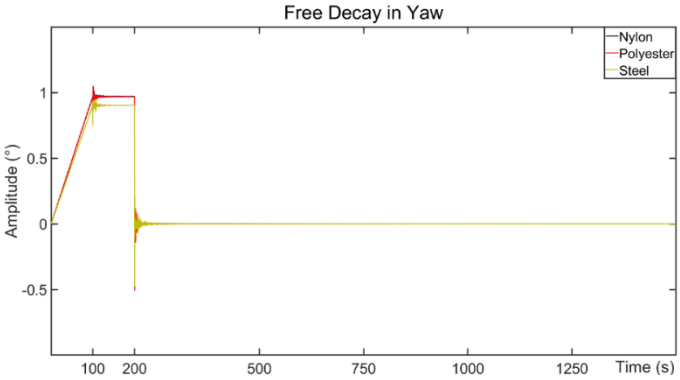


**Fig. 4-35** Free Decay in Yaw for TLB with Nylon, Polyester, and Steel Mooring Lines

**Table 4-25** Natural Frequency of 6 DOF for TLB Platform with Steel, Polyester, and Nylon Mooring Lines

| Natural Frequency (rad/s) | | | |
|---|---|---|---|
| | **Steel** | **Polyester** | **Nylon** |
| **Surge** | 0.785 | 0.331 | 0.299 |
| **Sway** | 0.785 | 0.331 | 0.299 |
| **Heave** | 2.094 | 1.047 | 1.047 |
| **Roll** | 0.785 | 0.331 | 0.299 |
| **Pitch** | 0.785 | 0.331 | 0.314 |
| **Yaw** | 2.094 | 1.571 | 1.571 |

**Table 4-26** Damping Ratio of 6 DOF for TLB Platform with Steel, Polyester, and Nylon Mooring Lines

| Damping Ratio | | | |
|---|---|---|---|
| | **Steel** | **Polyester** | **Nylon** |
| **Surge** | 0.0144 | 0.0319 | 0.0347 |
| **Sway** | 0.0135 | 0.0327 | 0.0346 |
| **Heave** | 0.0601 | 0.0936 | 0.1146 |
| **Roll** | 0.0750 | 0.0879 | 0.0956 |
| **Pitch** | 0.0246 | 0.0289 | 0.0366 |
| **Yaw** | 0.0715 | 0.0984 | 0.1064 |

In the provided table, the natural frequencies for steel, polyester, and nylon are listed for various modes of vibration. Each material exhibits unique natural frequencies for the specified modes of motion. For instance, in surge motion, steel has a natural frequency of 0.785 rad/s, while polyester and nylon have natural frequencies of 0.331 rad/s and 0.299 rad/s, respectively. Similarly, in heave motion, steel has a natural frequency of 2.094 rad/s, while both polyester and nylon have a natural frequency of 1.047 rad/s. The table provides comparable data for other modes of vibration, such as sway, roll, pitch, and yaw. The data presented in the table are valuable for engineers and researchers involved in material selection, structural analysis, and vibration control. By understanding the natural frequencies of different materials in various modes of vibration, engineers can make informed decisions regarding material choices for specific applications. Additionally, this information is crucial for predicting how structures will respond to dynamic loads and ensuring that resonant vibrations are avoided. The natural frequency of a material or structure depends on several factors, including its mass distribution, stiffness properties, boundary conditions, and damping characteristics. Changes in these factors can alter the natural frequency of a system.

The data provided includes the damping ratios for steel, polyester, and nylon across different modes of motion, such as surge, sway, heave, roll, pitch, and yaw. These damping ratios exhibit variations for each material and mode of motion, indicating the distinct responses of each material to different types of dynamic loading. The analysis of the data reveals that the TLB with a steel mooring line is a more damped system compared to those with polyester and nylon due to differences in material stiffness, internal friction. Stiffness affects the ability of a material to deform under load, with stiffer materials exhibiting lower elongation and higher resistance to deformation. Steel mooring lines are typically composed of multiple strands or wires twisted or braided together, allowing for internal friction between the strands.

### 4.4.7. Environmental Conditions

Wind turbines are exposed structures that are subject to various environmental effects, particularly the requirement to operate in medium to high-speed winds. Factors such as steady and turbulent winds are significant sources of loading for wind turbines. An example of a far-offshore FOWT location is Buchan Deep, located 25km offshore of Peterhead. Statoil installed a 30MW wind turbine farm on floating structures (Hywind Spar) to harness Scottish wind resources. The water depth at these locations ranged from 95m to 120m [22]. The northern North Sea was chosen as the deployment site for the TLB design due to its favourable wind resources, typical water depth, and distance from the shore, as indicated by previous research [61]. This study focuses on a location off the Scottish Coast with a water depth of 110 m.

DNVGL [422, 459, 460] covers critical design scenarios, including typical operational conditions and stationary states. It considers both normal and extreme external conditions as well as fault scenarios. These comprehensive environmental design load cases (DLCs) are developed through extensive research, industry-leading methodologies, and a deep understanding of the environmental factors affecting these structures. Consequently, during the initial stages of the design process, it is not necessary to consider all the load cases outlined in the design standard [470]. The selection of these specific environmental load conditions, rather than all those addressed by DNV, was based on considerations such as computational efficiency, practicality, and engineering judgment. This study focuses on the six environmental

load conditions specified in Table 4-27, in accordance with DNVGL-ST-0437 [460], for the purpose of conducting dynamic analysis at this stage of research. This approach facilitates a thorough yet manageable examination that addresses the most critical load scenarios while avoiding excessive computational demands. The analysis encompasses two distinct operational environmental conditions and survival conditions characterized by steady wind and turbulent wind, as well as an investigation of system performance under fault conditions during extreme sea states, which include turbulence and random wave height combined with steady wind. The rationale for selecting these six design load cases is to ensure coverage of various sea states, as well as to incorporate both turbulence and steady wind models, thereby addressing operational, survival, and survival scenarios with faults.

The study evaluates the impact of wind turbulence intensity on the motion responses and tension load in mooring lines during parked operation. This assessment is conducted for two design load cases, considering variations in wind models with and without turbulence. The power spectral densities characterizing the components are presented in relation to the Kaimal spectral [471]. The vertical stability of the turbine layer is determined by the dimensionless gradient Richardson number, which is set to zero for neutral conditions, a negative value for unstable conditions, or a positive value for stable atmospheric conditions [385, 472]. As stated in the Turbsim user manual, the Richardson number for EWM with turbulence input is specified as -0.05, while for EWM under steady conditions, it is assumed to be 0.05 [385]. Wind turbine generator systems (WTGS) classes based on wind speed and turbulence parameters according to IEC-61400-1 & 3 [459, 473]. Extreme wind conditions are utilized to calculate peak wind loads on Wind Turbine Generator Systems (WTGS), involving sudden changes in wind speed and direction during storms. In these extreme conditions, the potential impact of wind turbulence must be considered, necessitating the consideration of deterministic effects in the design calculations. The characteristic value of turbulence intensity is specified in TurbSim.

According to DNVGL-OS-E301 [474], ALS is implemented to ensure that the mooring system has sufficient capacity to withstand the failure of mooring lines. In cases where an anchor is shared by multiple mooring lines, the load pattern may undergo significant changes, necessitating the breaking of one line at each mooring cluster set for ALS, as detailed in DNVGL-ST-0119 [439]. Therefore, it is assumed that one mooring line

at each cluster will be disconnected after 500 seconds of the simulation, representing the ALS scenario for a parked with a fault event. The environmental loads considered in this study are assumed to be collinear in direction.

**Table 4-27** Combined Environmental Load Cases

| Event | DLC | Wind | Wave | Current |
|---|---|---|---|---|
| **Power Production** | **1.1** | NTM (Normal Turbulence Model) $U_{in} < U_{10,Hub} < U_{out}$ | NSS (Normal Sea State) $H_s = H_s \, at \, U_{10,Hub}$ | Normal Model |
| | **1.6a** | NTM $U_{in} < U_{10,Hub} < U_{out}$ | SSS $H_s = H_{S,50yr}$ | Normal Model |
| **Parked** | **6.1a** | EWM (Extreme Wind Model) Turbulent Wind,$U_{10,Hub}$ | ESS (Severe Sea State) $H_s = H_{S,50yr}$ | $V_{50yr}$ |
| | **6.2b** | EWM (Extreme Wind Model) Steady Wind,$U_{10,Hub}$ | ESS (Extreme Sea State) $H_s = H_{S,50yr}$ | $V_{50yr}$ |
| **Parked with Fault** | **7.1a** | EWM (Extreme Wind Model) Turbulent Wind,$U_{10,1yr}$ | ESS (Extreme Sea State) $H_s = H_{S,1yr}$ | $V_{1yr}$ |
| | **7.1b** | EWM (Extreme Wind Model) Steady Wind,$U_{10,1yr,Hub}$ | RWH (Random Weave Height) $H_s = \psi H_{S,1yr}$ | $V_{1yr}$ |

The initial load case, DLC 1.1, considers the environmental conditions within the operational range of the turbine, aligning wave conditions with wind velocity. Similarly, DLC 1.6 also considers wind speeds across the entire operational range of the turbine, with the sea state for each wind speed being the corresponding severe sea state $H_s$, SSS. These load cases involve examining wind speeds around both the rated wind speed and the cut-out speed. Specifically, in DLC1.6, the focus is on investigating wind speeds near or close to the cut-out speed [460]. The wind speeds used for generating power are determined based on the methodology described in the Passon study [475]. In particular, the wind speed is designated as $V_{Hub}$ = 11.4 m/s to simulate the rated wind speed, and as $V_{Hub}$ = 18 m/s to align with the turbine's full load range.

Moving on to DLC 6.1 and DLC 6.2, the turbulent wind model is combined with irregular sea state conditions. In this scenario, the 50-year recurrence value of the significant wave height and the mean wind speed is utilized [460]. For DLC 6.1b, the sea state is similar to that of DLC 6.1a, but it incorporates the extreme wind model with steady wind instead of turbulent wind.

In DLC 7.1, the fault condition shall be combined with the Extreme Wind Speed Model (EWM) and a recurrence period of a 1-year irregular sea state. DLC7.2 involves the use of irregular sea states with a 1-year recurrence value of the significant wave height representing random wave height [460].

For all DLCs, the average values of the significant wave height and the mean wind are adjusted according to the simulation time length.

### 4.4.7.1. Wind

Typical wind conditions are characterized by air density, the long-term distribution of the 10-minute average wind speed, wind shear represented by a gradient in the mean wind speed with respect to height above the sea surface, and turbulence. As outlined in DNVGL-OS-J103, Appendix B (Regional Environmental Data) [441], the 10-minute mean wind speed at a height of 10 meters above still water level for a 50-year return period in the Northern North Sea region is 43 m/s, and for a one-year return period, it is 36 m/s. Consequently, for North Sea conditions, Eq. (16) & (17) [471, 476] are utilized to compute the wind speed at the hub height. TurbSim [385] generates a summary text files for each design load, which serves as the input files for simulating the entire system in SIMA. The TurbSim employed to generate the wind profiles where the analysis duration extended to three hours, and a periodic output file is created at intervals that align with the analysis duration.

In defining the Normal Turbulence Model (NTM), the wind velocity at the hub is determined based on the data provided for the 10MW DTU, assumed to be 11.4 m/s (rated) for DLC1.1 and 18 m/s for DLC1.6a, respectively. When considering the Extreme Wind Model (EWM) to calculate the wind velocity, Eq. (17) [476] will be applied. The wind velocity for a 1-year return period can be calculated at the hub height using Eq. (18). The wind speed for each DLC is presented in Table 4-28 where $h$ = 10 m and $T_0$= 10 minutes, and $U_{10}$ is the 10-minute mean wind speed at height $h$, and $T$ is the specified averaging period.

$$U_{Hub,50yr} = U_{10}(1 + 0.137ln\frac{z}{h} - 0.047ln\frac{T}{T_0}) \quad (17)$$

$$U_{Hub,1yr} = 1.4U_{10,1yr,hub} \quad (18)$$

**Table 4-28** Wind Speed for Each DLC

| DLC | 1.1 | 1.6a | 6.1a | 6.2b | 7.1a | 7.1b |
|---|---|---|---|---|---|---|
| $V_{WIND}$ (m/s) | 11.4 | 18 | 51.6 | 51.6 | 50.4 | 50.4 |

**Table 4-29** Wind Turbine Generator System (WTGS) Classes for category for high turbulence intensity and significant wave height

| OA Wind Turbine Class | | I | II | III |
|---|---|---|---|---|
| $V_{ref}$ | (m/s) | 50 | 42.5 | 37.5 |
| $V_{ave}$ | (m/s) | 10 | 8.5 | 7.5 |
| $I_{ref}$ | | | 0.14 | |

OA: category for high turbulence intensity and significant wave height (offshore applications)
$I_{ref}$: is the characteristic value of the turbulence intensity at 15 m/s
a: is the slope parameter

In accordance with the international standard IEC 61400-1 [477, 478], wind turbine classification covers a specific range of strength defined by wind speed and turbulence parameters. This research focuses on analysing the attributes of offshore wind turbine classes as outlined in Table 2-1 of the DNVGL-ST-0437 [460]. It was assumed that the classes is characterized by high turbulence intensity and is defined by an average annual wind speed ranging from 8 to 10 m/s at a height of 100 m above sea level in the Northern North Sea [479]. This classification is specifically designated for wind that demonstrates increased turbulence characteristics, as detailed in Table 4-29.

## 4.4.7.2. Wave

The wave conditions in UK waters exhibit pronounced seasonality. As per the data provided in Appendix B Table B-1 of DNVGL-OS-J103 [441], the significant wave height for stationary sea states over a 3-hour period is considered for both one-year and 50-year return periods in the Northern North Sea region.

$$H_s = 0.00162U_{10}^2 + 0.0275U_{10} \quad (19)$$

$$H_{s,Ts} = U_{s,T_{s0}}\left(1 + \frac{ln\left(\frac{T_{s0}}{T_s}\right)}{ln(N_0T_R)}\right)^{1/\beta} \quad (20)$$

Eq. (19) and Eq. (20) [422, 460] are derived from the regulations and guidelines of DNVGL for the computation of the significant wave height $H_s$, which is generated by wind and occurs within a reference period of duration $T_S$. $N_0$ represents the number of sea states of duration, with $T_{s0}$ is one year, and $T_R$ denoting the specified return period of the significant wave height. $\beta$ stands for the Weibull parameter characterizing the long-term probability distribution of the significant wave height in the northern North Sea, as detailed in Appendix B of DNVGL-RP-C205 [476]. The determination of the significant wave height is conducted for all combination loads as specified in Table 4-30.

**Table 4-30** Significant Wave Height for Each DLC

| DLC | 1.1 | 1.6a | 6.1a | 6.2b | 7.1a | 7.1b |
|---|---|---|---|---|---|---|
| $H_s$ (m) | 4.2 | 8.8 | 16.8 | 16.8 | 11 | 8.8 |

According to DNVGL-RP-C205, $T_P$, the range for the wave periods, is calculated using Eq. (21) [441, 480] for each significant wave height illustrate in Table 4-30 to provide the average period. This study applied the mean $T_P$ for each DLC (see Table 4-31).

$$11.1\sqrt{\frac{H_S}{g}} \leq T_P \leq 14.3\sqrt{\frac{H_S}{g}} \tag{21}$$

**Table 4-31** Peak Period for Each DLC

| DLC | 1.1 | 1.6a | 6.1a | 6.2b | 7.1a | 7.1b |
|---|---|---|---|---|---|---|
| $T_P$ (s) | 9.35 | 13.54 | 18.71 | 18.71 | 15.14 | 13.54 |

Wave spectrum models are commonly employed for simulating the sea surface, with the Joint North Sea Wave Project (JONSWAP) [481] being utilized for each DLC. In accordance with the regulations specified in DNVGL-RP-C205 [476], the peak shape parameter is calculated using the Eq. (22) for JONSWAP spectrum.

$$\gamma = \begin{cases} 5 & for\ \dfrac{T_P}{\sqrt{H_s}} \leq 3.6 \\ \exp\left(5.75 - 1.15\dfrac{T_P}{\sqrt{H_s}}\right) & for\ 3.6 < \dfrac{T_P}{\sqrt{H_s}} < 5 \\ 1 & for\ 5 \leq \dfrac{T_P}{\sqrt{H_s}} \end{cases} \tag{22}$$

### 4.4.7.3. Current

Eq. (23) to (25) are utilized to account for both surface tidal current, denoted as $U_{tide}$, and wind-generated current, denoted as $U_{wind}$. Here, $z$ represents the vertical coordinate measured from the still water level, with positive values indicating an upward direction. $U_{tide0}$ denotes the tidal current at the still water level, while $U_{wind0}$ represents the wind-generated current at the same level. Additionally, $h$ denotes the water depth measured from the still water level, with positive values taken into consideration, and $h_0$ is the reference depth for wind-generated current. The constant $K$ is assigned a value of 0.33, and $U_0$ represents the 1-hour mean wind speed at a height of 10 m [482]. The Offshore Energy SEA [483] is employed to estimate the maximum surface tidal streams, which exhibit a range of 0.25 m/s to 0.5 m/s across a significant portion of the northern North Sea. Consequently,

Table ***4-32*** presents the current velocity at various heights for the wind-generated and tidal currents for 50- and 1-year return periods, respectively.

$$U_{tide}(z) = U_{tide0}\left(1+\frac{z}{h}\right)^{\frac{1}{7}} \quad for \quad z<0 \tag{23}$$

$$U_{wind}(z) = U_{wind0}\left(1+\frac{z}{h_0}\right) \quad for \quad h_0 \le z \le 0 \tag{24}$$

$$U_{wind0}(0) = k.U_0 \tag{25}$$

**Table 4-32** Current Velocity with The Height References

| Depth | $U_{Wind,50yr}$ | $U_{Tidal,50yr}$ | $U_{Tidal,1yr}$ |
|---|---|---|---|
| 0 | 0.442 | 1.42 | 0.78 |
| 25 | 0.42 | 1.41 | 0.65 |
| 40 | 0.33 | 1.33 | 0.5 |
| 52 | 0.3 | 1.3 | 0.42 |
| 62 | 0.27 | 1.27 | 0.2 |
| 90 | 0.13 | 1.13 | 0.1 |
| 100 | 0.1 | 1 | 0.01 |
| 110 | 0 | 0 | 0 |

Six design load cases were chosen from a selection of proposed load cases that combine different environmental conditions outlined in DNVGL-ST-0437 [460]. These load cases are specified for each design situation through the description of wind and marine conditions. The northern North Sea regional environmental data provided in

DNVGL-OS-J103 [441] was utilized to calculate the wind speed, significant wave height, period, and current speed. The resulting summary of the design load cases for each design situation is presented in Table 4-33.

**Table 4-33** Summary of Design Load Combinations

| DLC | Wind | | Wave | | | Current |
|---|---|---|---|---|---|---|
| | Model | $V_{Wind}$ (m/s) | Model | $H_s$ (m) | $T_P$ (s) | $V_{Maximum\ at\ SWL}$ (m/s) |
| **1.1** | NTM | 11.4 | NSS | 4.2 | 9.4 | $U_{Wind,50yr} = 0.442$ |
| **1.6a** | NTM | 18 | SSS | 8.8 | 13.5 | |
| **6.1a** | EWM, Turbulence | 51.6 | ESS | 16.8 | 18.7 | $U_{Tidel,50yr} = 1.42$ |
| **6.2a** | EWM, Steady | 51.6 | ESS | 16.8 | 18.7 | |
| **7.1a** | EWM, Turbulence | 50.4 | ESS | 11 | 15.1 | $U_{Tidel,1yr} = 0.78$ |
| **7.1b** | EWM, Steady | 50.4 | RWH | 8.8 | 13.5 | |

## 4.5. Results and Discussion

The subsequent section will present and discuss the numerical outcomes of the integrated system comprising a 10 MW DTU turbine mounted on a TLB platform, which is moored using a newly developed taut mooring system constructed from three different materials and anchored to the seabed in a systematic manner. The numerical results will be examined and presented for all load combinations, focusing on the motion response of the TLB and the dynamic tension characteristics of the most heavily loaded line. A comparison and evaluation of the dynamic responses of the TLB with the three mooring materials will be conducted in accordance with the standards and regulations outlined in Section 2.9. The maximum design tension for mooring lines will be determined based on the results obtained from extensive time-domain numerical simulations conducted under various environmental conditions.

### 4.5.1. Static Positioning

The properties of mooring lines differ based on the material employed, necessitating the calculation of hydrodynamic coefficients for each system at the appropriate floater draft. To ensure consistent draft across different mooring line materials, it is essential to compute the pretension for the lines. Additionally, the static stiffness matrix is determined for each mooring material. The initial positioning of the system moored with the three distinct line materials is presented in Table 4-34, demonstrating draft for the TLB with steel, polyester, and nylon mooring lines.

**Table 4-34** Initial Positioning of TLB with Three Mooring Line Materials

| Mooring Materials | X (m) | Y (m) | Z (m) |
|---|---|---|---|
| Steel | 0 | 0 | -0.0018 |
| Polyester | 0 | 0 | -0.0016 |
| Nylon | 0 | 0 | -0.0015 |

Table 4-35 illustrates the static positioning of the system with three different mooring line materials under operational and survival environmental conditions. The results show that the systems have effectively achieved stability and performance when exposed to environmental factors such as waves and wind. The results for sway, roll, and yaw were negligible and not significant enough to be included in the presentation.

**Table 4-35** Static Positioning

| | Environmental Case | Surge(m) | Heave(m) | Pitch (°) |
|---|---|---|---|---|
| **Steel** | Operational | 0.001620 | -0.00018 | -0.00080 |
| | Survival | 0.016427 | -0.00021 | -0.00814 |
| **Polyester** | Operational | 0.002680 | -0.00029 | -0.00133 |
| | Survival | 0.022521 | -0.00032 | -0.01116 |
| **Nylon** | Operational | 0.002877 | -0.00031 | -0.00118 |
| | Survival | 0.024003 | -0.00036 | -0.01369 |

The peak values of surge for steel, polyester, and nylon exhibit higher magnitudes when exposed to survival conditions compared to operational conditions. Polyester and nylon show more pronounced negative heave values under survival conditions, indicating a more significant downward displacement. Likewise, the pitch values for all three materials show a more negative trend under survival conditions compared to operational conditions. Overall, the results suggest that survival conditions are associated with increased surge values, enhanced downward movement (indicated by negative heave values), and a more pronounced negative pitch angle for polyester and nylon materials.

### 4.5.2. Dynamic Analysis

In this section, the outcomes derived from a three-hour simulation conducted in SIMA under environmental design load scenarios are presented, analysed, and deliberated upon.

#### 4.5.2.1. Operational Conditions

In operational conditions, the performance of the TLB platform with three mooring materials under a Normal Sea State (NSS) and a Severe Sea State (SSS), and with the wind turbine exposed to a normal turbulence wind model, will be investigated. DLC1.1 represented a normal sea state, while the DLC1.6a event was conducted to determine the operational performance boundaries of the system using three different mooring materials under severe sea conditions. This section will investigate the hydrodynamic behaviour and power production capability of the developed concept TLB designed using three different mooring materials under operational conditions. The study utilized a land-based wind turbine control system.

Statistical results of maximum motion responses and maximum tension of the most loaded mooring line for each mooring material are presented in Table 4-36. The instances of coupled motion responses of the systems highlighted in green.

Fig. 4-36 illustrates a comparative analysis of the maximum motion responses in six degrees of freedom for the system using mooring lines made of steel, polyester, and nylon materials under operational conditions.

Fig. 4-37 shows the distribution and probability density of the surge, heave, pitch, and yaw motion responses during operational events. The illustration does not include the minimal sway and roll motion responses.

Fig. 4-38 and Fig 4-39 show the surge and pitch motion responses and dynamic tension time history under DLC1.1 and DLC1.6a, respectively.

**Table 4-36** TLB Motion Responses and Maximum Loaded Line Dynamic Tension Response Characteristics of Steel, Polyester, and Nylon Mooring Lines under DLC1.1 and DLC1.6a

| | | | Time (s) | Max | Min | Mean | SD |
|---|---|---|---|---|---|---|---|
| DLC 1.1 | Steel | Surge(m) | 614 | 0.79 | -0.58 | 0.02 | 0.20 |
| | | Sway (m) | 10674 | 0.04 | -0.04 | 0.00 | 0.01 |
| | | Heave(m) | 614 | 0.06 | -0.54 | -0.10 | 0.06 |
| | | Roll (°) | 10674 | 0.06 | -0.06 | 0.00 | 0.01 |
| | | Pitch (°) | 614 | 1.24 | -0.91 | 0.08 | 0.30 |
| | | Yaw (°) | 10436 | 0.49 | -0.36 | 0.03 | 0.12 |
| | | Tension(t) | 614 | 987.3 | 224.9 | 505.6 | 108.3 |
| | Polyester | Surge(m) | 9255 | 0.94 | -0.85 | 0 | 0.24 |
| | | Sway (m) | 8927 | 0.05 | -0.05 | 0 | 0.01 |
| | | Heave(m) | 9255 | 0.07 | -0.7 | -0.04 | 0.06 |
| | | Roll (°) | 8927 | 0.08 | -0.08 | 0 | 0.02 |
| | | Pitch (°) | 9255 | 1.29 | -1.07 | 0.01 | 0.31 |
| | | Yaw (°) | 2371 | 0.18 | -0.13 | 0.01 | 0.04 |
| | | Tension(t) | 9255 | 839 | 179 | 504 | 90 |
| | Nylon | Surge(m) | 9256 | 1.22 | -1.09 | -0.03 | 0.29 |
| | | Sway (m) | 8930 | 0.06 | -0.06 | 0 | 0.01 |
| | | Heave(m) | 8970 | 0.1 | -1.06 | -0.08 | 0.15 |
| | | Roll (°) | 8930 | 0.12 | -0.12 | 0 | 0.03 |
| | | Pitch (°) | 9256 | 1.42 | -1.21 | 0.06 | 0.34 |
| | | Yaw (°) | 10759 | 0.84 | -0.75 | 0.04 | 0.21 |
| | | Tension(t) | 9256 | 799 | 178 | 473 | 79 |
| DLC 1.6a | Steel | Surge(m) | 614 | 1.14 | -1.04 | 0.00 | 0.29 |
| | | Sway (m) | 3887 | 0.08 | -0.09 | 0.00 | 0.02 |
| | | Heave(m) | 614 | 0.14 | -0.76 | -0.08 | 0.09 |
| | | Roll (°) | 3887 | 0.14 | -0.14 | -0.01 | 0.03 |
| | | Pitch (°) | 614 | 1.61 | -1.60 | -0.04 | 0.42 |
| | | Yaw (°) | 2378 | 1.28 | -1.26 | -0.066 | 0.32 |
| | | Tension(t) | 614 | 1656.6 | 97.1 | 692.7 | 215.6 |
| | Polyester | Surge(m) | 9257 | 1.94 | -1.92 | -0.02 | 0.6 |
| | | Sway (m) | 9336 | 0.19 | -0.2 | -0.01 | 0.02 |
| | | Heave(m) | 9257 | 0.16 | -1.08 | -0.01 | 0.1 |
| | | Roll (°) | 9336 | 0.74 | -0.74 | 0.01 | 0.08 |
| | | Pitch (°) | 9257 | 2.44 | -2.35 | -0.02 | 0.76 |
| | | Yaw (°) | 7693 | 2.27 | -2.31 | -0.21 | 0.6 |
| | | Tension(t) | 9257 | 1326 | -55 | 484 | 278 |
| | Nylon | Surge(m) | 3597 | 2.46 | -2.36 | 0.02 | 0.52 |
| | | Sway (m) | 3613 | 0.31 | -0.3 | 0 | 0.05 |
| | | Heave(m) | 3597 | 0.39 | -1.86 | -0.04 | 0.11 |
| | | Roll (°) | 3613 | 1.08 | -1.04 | -0.01 | 0.18 |
| | | Pitch (°) | 3597 | 3.56 | -3.61 | -0.01 | 0.78 |
| | | Yaw (°) | 10760 | 3.08 | -3.04 | 0.02 | 0.81 |
| | | Tension(t) | 3597 | 1087 | -33 | 371 | 175 |

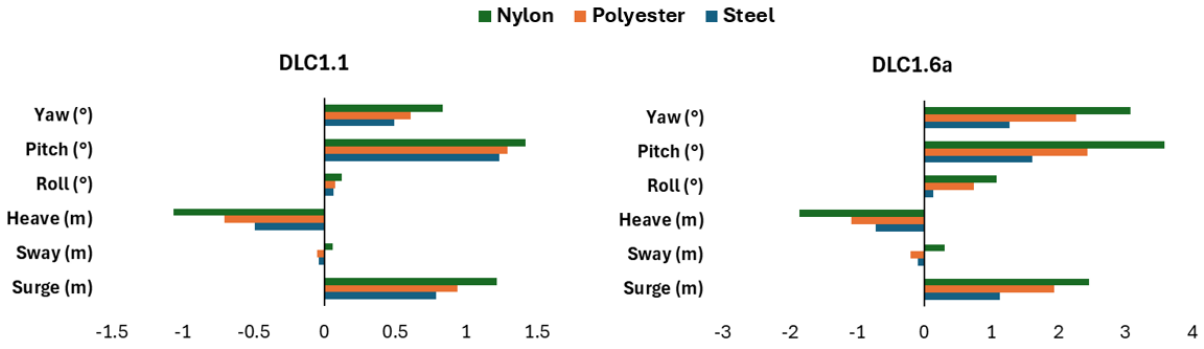


**Fig. 4-36** Statistical Six-degree Maximum Motion Responses of TLB employed Steel, Polyester, and Nylon mooring lines Under Operational Design Load Cases

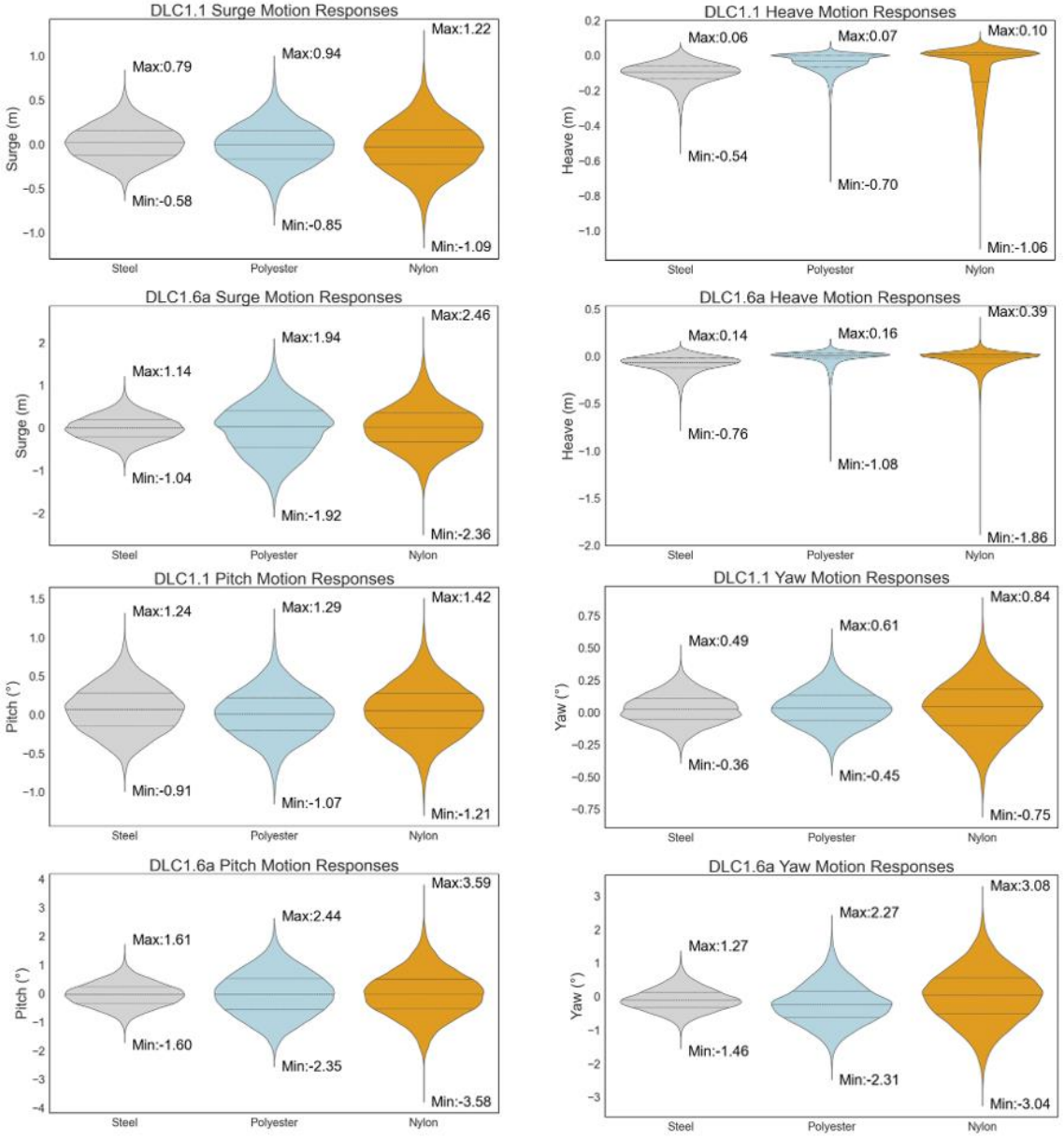


**Fig. 4-37** Surge, Heave, Pitch, and Yow Motin Responses Violin Plots under Operational Conditions

The TLB equipped with a nylon mooring line experienced a surge that was 23% higher than the surge observed in a TLB utilizing a polyester mooring line, and 35% greater than that of a TLB utilizing a steel mooring line under DLC1.1. These percentages changed to 21% and 54%, respectively under DLC1.6a. The fluctuations around the mean offset position of the TLB are reduced with steel mooring lines compared to nylon and polyester. The overall trend and distribution of surge reactions are similar in both polyester and nylon ropes. However, nylon ropes displayed more variability in surge direction and had higher maximum and minimum surge amplitudes than polyester ropes. The use of a polyester mooring line in the TLB results in higher stiffness when compared to the TLB equipped with a nylon mooring line. As a result, the inherent elasticity of the nylon rope contributes to the most pronounced surge motion observed in the TLB.

The platform experienced the heave submersion when utilizing all three types of mooring materials under operational conditions. The significant heave submersion of the platform while generating energy equipped with steel and polyester mooring line materials in severe sea state environmental condition, as compared to normal sea states, shows a similar trend. Specifically, there was a 32% increase in heave submersion for the platform with steel and a 34% increase for the platform with polyester mooring lines. In contrast, the platform utilizing nylon experienced a 43% increase in submersion under harsher environmental conditions. Through the visualization of data distribution and its shape, it becomes apparent that a majority of the values are clustered at lower levels of heave motion. This suggests that the vessel encounters more significant downward movements in comparison to upward movements. The skewed distribution towards lower values signifies a rigidity in positive heave amplitude within the system, likely attributed to factors such as line tension and excess buoyancy in the design.

The impact of concurrent environmental conditions under DLC1.1 on the pitch motion reactions of three different mooring materials is deemed to be negligible. However, when platform is subjected to severe sea states characterized by waves and NTM with higher wind speed under DLC1.6a, it was observed that the TLB with nylon material exhibited a 32% increase in pitching compared to the TLB with polyester, and a 55% increase compared to the TLB with steel mooring line.

The yaw movement of the platform equipped with three different mooring materials exhibited a notable increase under DLC1.6a conditions in comparison to findings observed under DLC1.1 conditions. Specifically, the platform utilizing steel mooring lines experienced a 61% greater degree of yawing under DLC1.6a, while platforms utilizing fibre mooring materials demonstrated a comparable increase of approximately 73%. The yaw motion response of the TLB equipped with steel ropes exhibits significantly lower magnitude compared to that of the TLB utilizing fibre ropes. This discrepancy may be attributed to the assumption of a 20-degree spread in the fairlead attachment, which aims to simulate the impact of a bridle/delta connection and mitigate the platform's yaw motion. While this approach is commonly employed with steel ropes, it may not be the most optimal configuration for polyester and nylon lines. Therefore, it is suggested that the methodology employed to determine the stiffness for modelling a bridle/delta connection be reevaluated based on the material type to ensure consistent motion response among the three configurations.

The sway and roll motion responses are minor under operational conditions due to apply colinear environment with 0° direction.

Maximum tension of the most loaded line presented. The maximum load occurred on line 8 (refer to Fig. 4-27) for the three mooring materials in the normal operation events. Maximum tension values are occurring at same time for TLB with steel and polyester mooring line in both DLCs under operational conditions, while they occur at different intervals for TLB utilizing nylon mooring lines. This disparity indicates a significant influence of harsh environmental conditions on the system hydrodynamics behaviour when nylon mooring is employed. By examining the statistical results presented in Table 4-36, Fig. 4-38 and Fig 4-39, it is evident that the trend of dynamic tensions response are strongly linked to the trend of surge, pitch, and heave motion responses, indicating that these motions of the TLB and dynamic tension of the most loaded mooring line are strongly coupled and dependent on environmental conditions. It should be noted that the surge and pitch motion responses and dynamic tension occurred concurrently for TLB with nylon mooring line under DLC1.1.

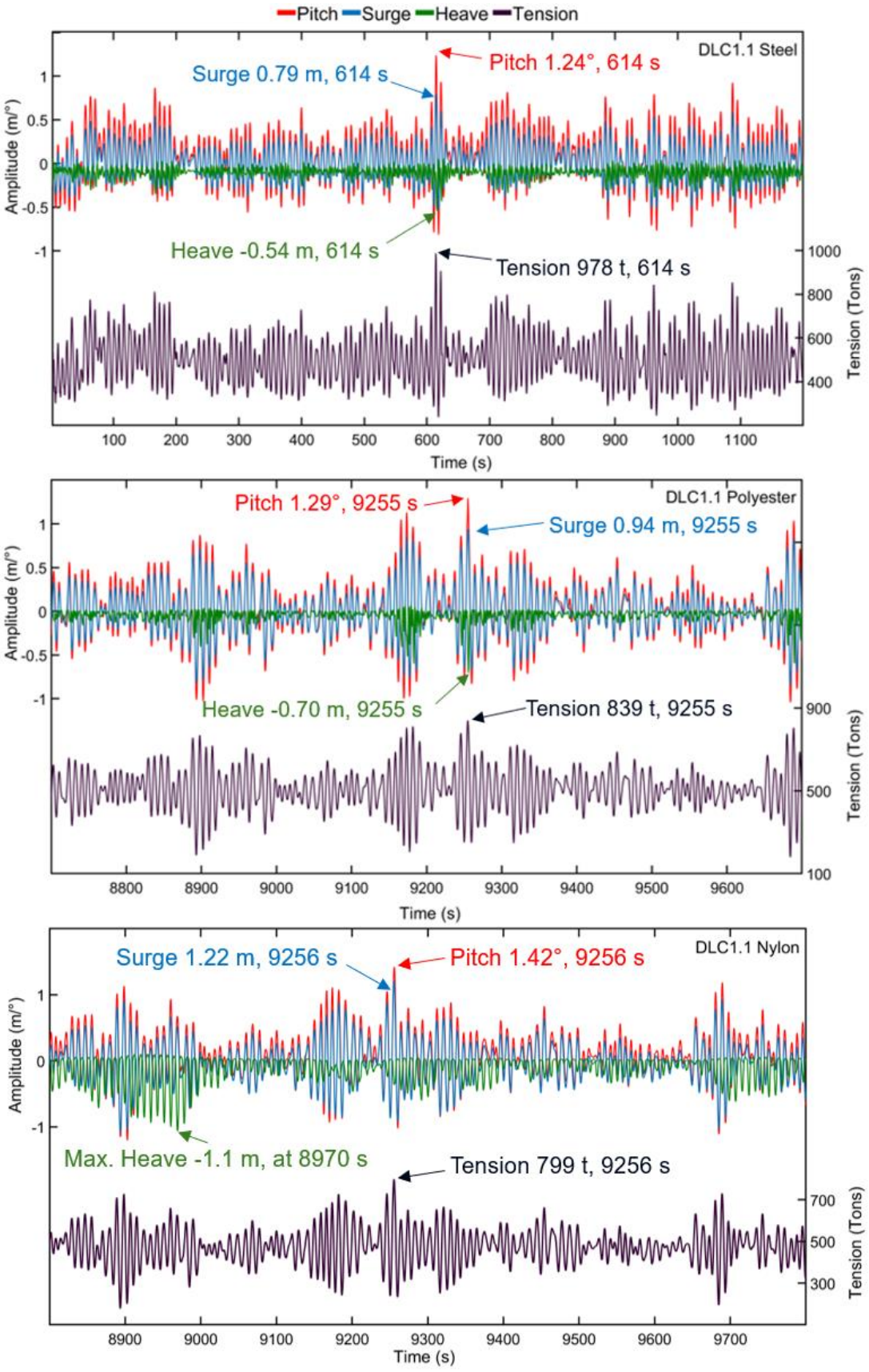


**Fig. 4-38** Time History of Coupled Responses Under DLC1.1

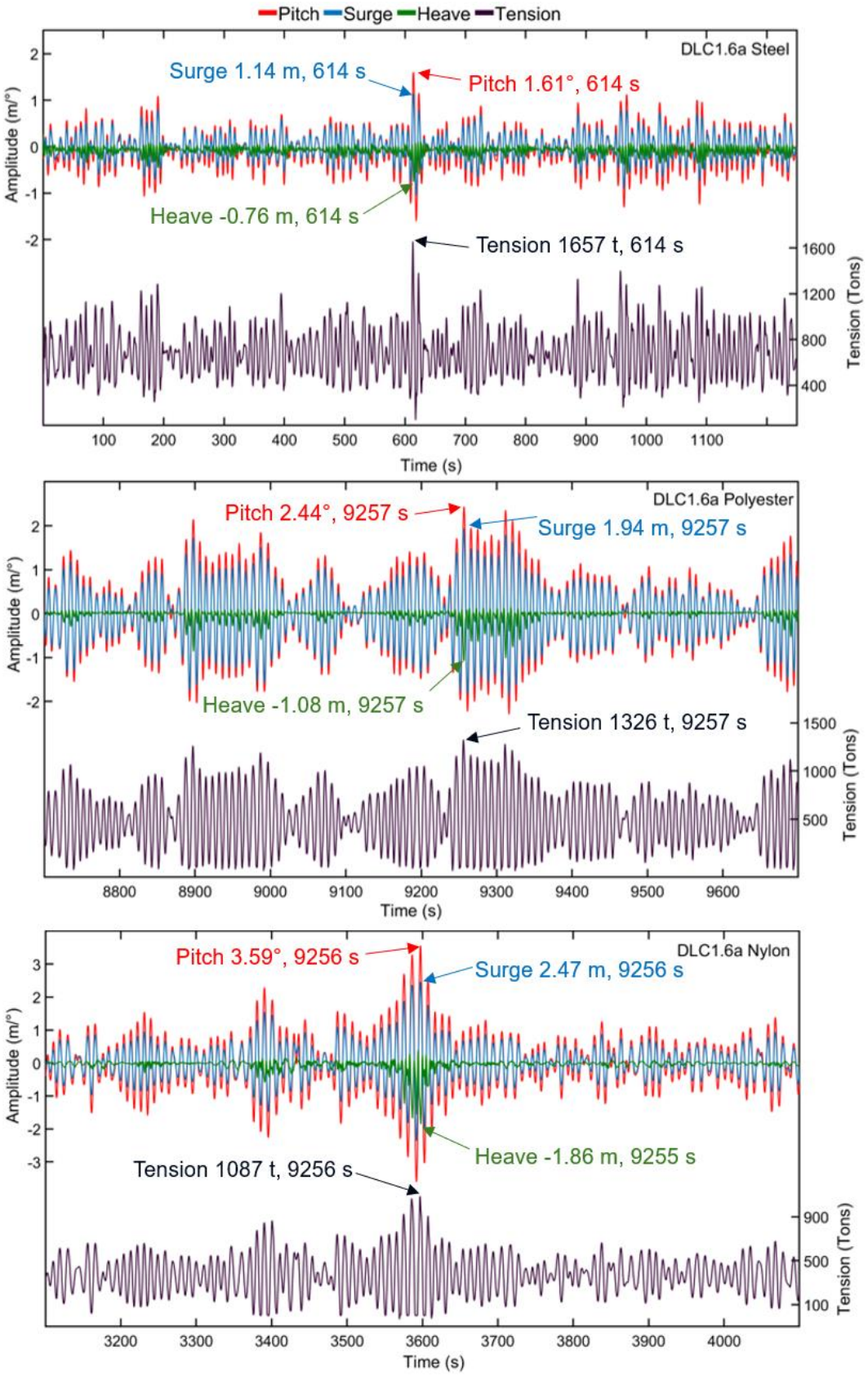


**Fig 4-39** Time History of Coupled Responses Under DLC1.6a

In a comparative analysis of extreme sea conditions and typical sea conditions, there was a significant 40% elevation in the peak loaded mooring line tension for steel and a 37% increase for polyester lines. In contrast, nylon lines demonstrated a 27% increased tension, highlighting the importance of the dynamic stiffness of the material in impacting the operational effectiveness of the system during harsh environmental conditions. The compliance with DNV regulations is evaluated through an analysis of the criteria specified in section 2.9. This analysis uses the MBL of the mooring materials as shown in Table 4-21, and the characteristic capacity of the mooring lines, $Sc$, for each mooring material is calculated using Eq. (9). The design tension is calculated using the results for mean and maximum dynamic tension presented in Table 4-36, and Eq. (8), together with the ULS safety factors for normal safety class, as given in Table 2-8. The calculations for each mooring material are shown in Table 4-37.

**Table 4-37** Characteristic Capacity of The Mooring Lines and The Design Tension Calculations for Each Mooring Material under Operational Conditions

| | $S_C\ (N)$ | $T_d\ (N)$ | |
|---|---|---|---|
| | | DLC1.1 | DLC1.6a |
| Steel | 3.82E+07 | 1.47E+07 | 2.54E+07 |
| Polyester | 2.89E+07 | 1.22E+07 | 2.06E+07 |
| Nylon | 2.09E+07 | 1.16E+07 | 1.70E+07 |

The Safety factor can be calculated using Eq. (26) as show in Table 4-38.

$$Safety\ Fator = \frac{S_C}{T_d} \tag{26}$$

**Table 4-38** Safety Factors of Most Loaded Line for Each Mooring Line Materials under Operational Conditions

| | Safety Factor | |
|---|---|---|
| | DLC1.1 | DLC1.6a |
| Steel | 1.86 | 2.38 |
| Polyester | 2.00 | 2.65 |
| Nylon | 1.91 | 2.28 |

The results obtained for the TLB with three mooring materials from 3-hour environmental conditions were used to determine the maximum motion response and mooring line tension for operational conditions (DLC1.1 & DLC1.6a) satisfy both the rule-based limitations on response motion as set by DNVGL-RP-0286 [440] and the design criterion for ULS as given in DNV-OS-J103 [441].

## 4.5.2.2. Power Production

FOWTs are rated with various power output levels when delivered. However, they will not always generate electricity at their rated power, as the generation of power is highly dependent on weather conditions, the motion responses of the system. The power production rate of a FOWT is an important element to calculate the LCOE of the system [484]. The power generation of the TLB platform utilized three mooring materials assess under two sea states. The electrical generator's output in SIMA is determined by multiplying the generator's commanded torque by its rotational speed. It should be noted that SIMA neglected to account for the generator efficiency when calculating the electrical output, instead assuming a generator efficiency of 100%. The electrical generator output time history and characteristics is shown in Fig. 4-40 and Table 4-39 under DLC1.1 and Fig. 4-41 and Table 4-40 under DLC1.6a.

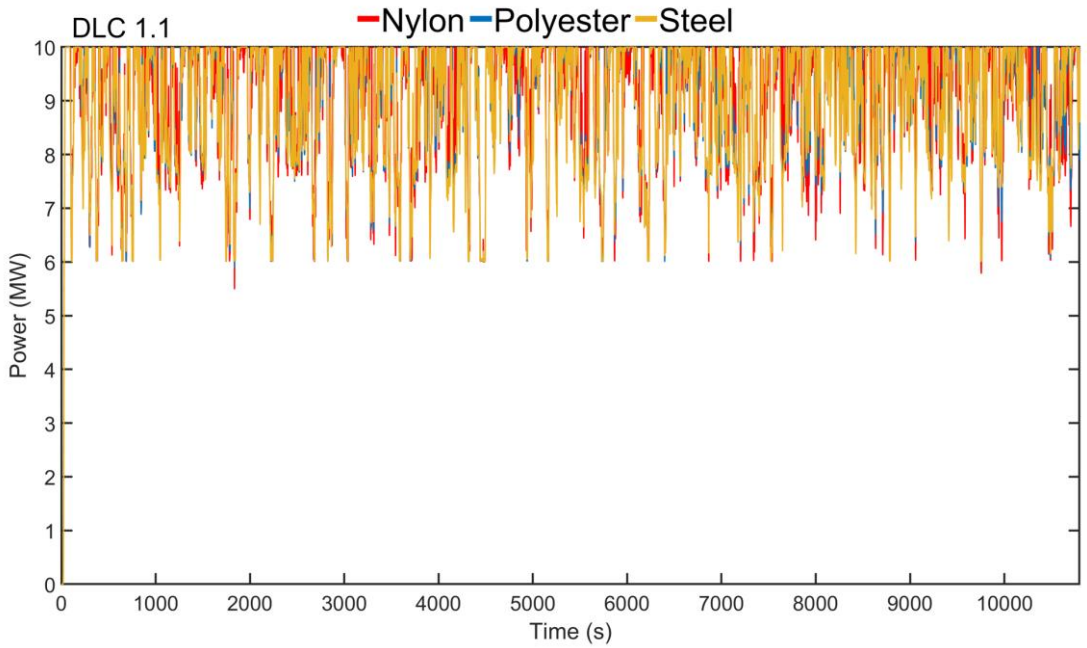


**Fig. 4-40** Power Production Time History of TLB with Steel, Polyester, and Nylon Mooring Materials under DLC 1.1 Even

**Table 4-39** TLB Power Production Characteristics of Steel, Polyester, and Nylon Mooring Lines under DLC1.1

| | Time (s) | Max | Min | Mean (MW) | SD |
|---|---|---|---|---|---|
| Steel | 4480 | 10 | 6.00 | 8.95 | 1.14 |
| Polyester | 1837 | 10 | 5.89 | 8.93 | 1.13 |
| Nylon | 1836 | 10 | 5.49 | 8.94 | 1.11 |

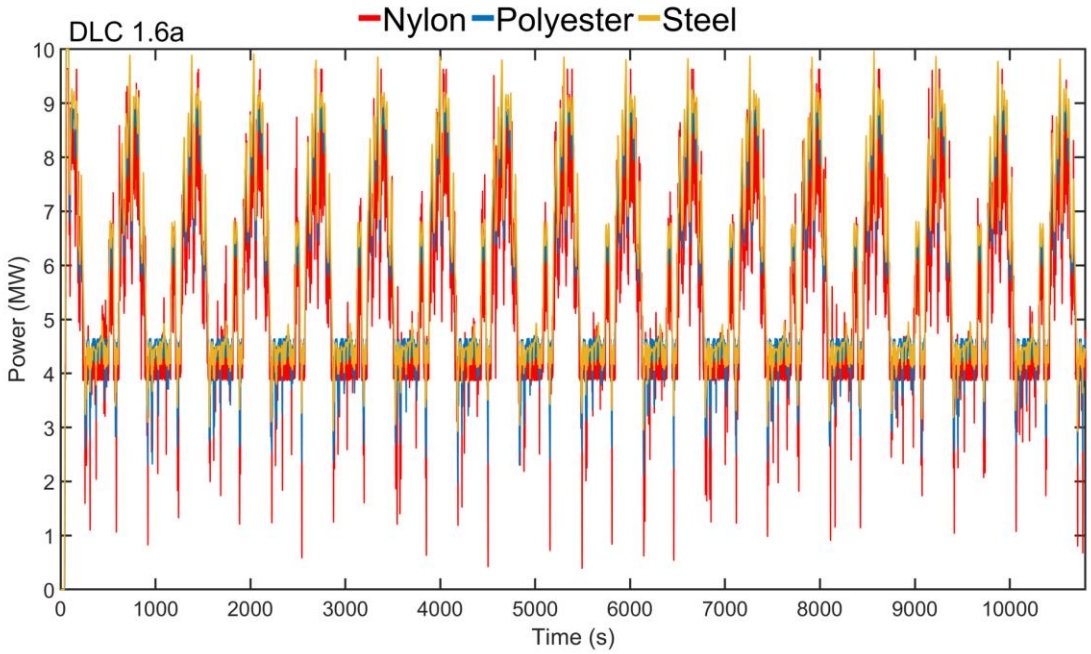


**Fig. 4-41** Power Production Time History of TLB with Steel, Polyester, and Nylon Mooring Materials under DLC 1.6a Event

**Table 4-40** TLB Power Production Characteristics of Steel, Polyester, and Nylon Mooring Lines under DLC1.6a

| | Time (s) | Max | Min | Mean (MW) | SD |
|---|---|---|---|---|---|
| Steel | 10713 | 9.97 | 2.91 | 6.04 | 1.82 |
| Polyester | 4184 | 9.74 | 1.95 | 5.82 | 1.74 |
| Nylon | 5495 | 9.64 | 0.38 | 5.45 | 1.68 |

Time is representing the minimum electrical power output in Table 4-40. The pattern of power production within three hours is almost identical for the system with three mooring materials and the mean power production rate shows that the system with nylon mooring line produced electricity slightly less than that for system with polyester and steel under DLC1.1. In DLC1.6a, the minimum electric generation capacity observed is 0.38 MW for the system utilizing nylon mooring lines. The efficiency of the system employing nylon mooring lines is 2% and 4% lower compared to the system utilizing polyester and steel mooring lines respectively. This suggests that systems employing more elastic mooring materials as exhibit higher motion responses, impacting electrical generation in challenging environmental conditions. The objective of this section was to assess the operational performance of TLB platform in varying sea states using different mooring materials, with a focus on power generation. The

findings indicate that the TLB system utilizing a steel mooring line demonstrated an average electricity production of 6 MW over a three-hour period in severe sea conditions. In comparison, TLB systems employing polyester and nylon mooring lines yielded average power outputs of 5.8 MW and 5.5 MW, respectively. The mean electricity generation of the system utilizing steel decreased by 5% when subjected to severe sea conditions, while the system employing a nylon mooring line experienced an 8% reduction in electricity production.

In summary, the TLB with steel mooring lines experienced smaller motion responses when compared with the use fibre ropes, and the motion responses obtained from TLB with polyester lines are smaller compared to results for a TLB with nylon mooring wire rope. Although the TLB moored with the steel mooring line has experienced a smaller surge amplitude than polyester and nylon ropes, it exhibited the highest tension, as would be expected due to the increased axial stiffness of the material.

The reduced motion responses observed in the system utilizing steel mooring lines compared to those employing fibre mooring lines can be attributed to the differing elastic properties of the line materials. The high stiffness of steel aids in constraining excessive movements induced by wave and wind forces. Furthermore, the motion responses in systems utilizing polyester mooring lines are found to be lower than those employing nylon, highlighting the influence of material elongation and tension characteristics of polyester. Specifically, nylon exhibits 64% greater elongation at 20% MBL and 52% greater elongation at 30% MBL compared to polyester mooring lines, as detailed in section 4.4.5.

The tilt inclination of the system utilized steel, polyester, and nylon did not exceed an average value of 5° and a maximum value of 10° during operational conditions, indicating the response of the systems are satisfied the rule-based limitation described in section 2.9. All tensions are within manufacturer described limits, the rule-based limitations, and the design criterion for ULS.

A critical consideration should therefore be the maximum allowable load and offset for a TLB, especially when thinking about closely spaced wind farm arrays. The results presented here show that a TLB with three mooring lines can operate and maintain acceptable motions in relatively severe sea states, showing the strong advantages the TLB design has over more conventional floater and mooring designs.

### 4.5.2.3. Parked (idling) Event

The parked (idling) event condition analysis represents a harsh sea state event, under which the turbine is typically switched off. An extreme sea state (ESS) with a significant wave height of 16.8m represents the survival condition wave model. Two wind models have been considered to describe the extreme wind model (EWM), one with the appearance of turbulence and another with a steady profile. The TurbSim employed to generate the wind profiles where the analysis duration extended to three hours, and a periodic output file is created at intervals that align with the analysis duration.

The maximum tidal speed of 1.42 m/s with 50-year return period is assumed. The objective of this section is to investigate the induced effect of the wind turbulence intensity on each platform's motion response performance and maximum dynamic tension on most loaded lines in the mooring systems.

Statistical results of maximum motion responses and maximum tension of the most loaded mooring line under survival conditions for each mooring materials presented in Table 4-41. The instances of coupled motion responses of the systems highlighted in green.

Fig. 4-42 illustrates the comparative analysis of the maximum motion responses in six degrees of freedom for the system utilizing mooring lines made of steel, polyester, and nylon materials under survival conditions.

Fig. 4-43 displays descriptive statistics illustrating the numerical distribution of the surge, heave, pitch, and yaw motion responses observed in operational events. The illustration ignored to included minimal sway and roll motion responses.

Fig. 4-44 to Fig. 4-46 show the time history of the coupled motion responses and dynamic tension survival conditions.

The variations in peak responses observed in the outcomes derived from DLC6.1a and DLC 6.2b for TLB systems utilizing steel, polyester, and nylon mooring lines are shows in Fig. 4-47.

**Table 4-41** TLB Motion Responses and Maximum Loaded Line Dynamic Tension Response Characteristics of Steel, Polyester, and Nylon Mooring Lines under Parked (Idling) Events

| | | | Time (s) | Max | Min | Mean | SD |
|---|---|---|---|---|---|---|---|
| DLC 6.1a | Steel | Surge(m) | 6097 | 2.19 | -2.16 | 0.02 | 0.34 |
| | | Sway (m) | 9619 | 0.26 | -0.26 | -0.01 | 0.05 |
| | | Heave(m) | 9975 | 0.25 | -2.63 | -0.16 | 0.17 |
| | | Roll (°) | 9619 | 0.36 | -0.40 | 0.00 | 0.07 |
| | | Pitch (°) | 6097 | 2.35 | -2.30 | 0.18 | 0.38 |
| | | Yaw (°) | 1735 | 2.65 | -2.64 | 0.32 | 0.56 |
| | | Tension(t) | 6097 | 3084.8 | -14.4 | 824.7 | 418.5 |
| | Polyester | Surge(m) | 8040 | 2.63 | -2.60 | 0.05 | 0.48 |
| | | Sway (m) | 7704 | 0.51 | -0.54 | -0.01 | 0.12 |
| | | Heave(m) | 8040 | 0.40 | -3.22 | -0.12 | 0.23 |
| | | Roll (°) | 7704 | 0.57 | -0.73 | -0.02 | 0.16 |
| | | Pitch (°) | 8040 | 2.98 | -2.94 | 0.14 | 0.56 |
| | | Yaw (°) | 7707 | 3.01 | -2.95 | 0.34 | 0.66 |
| | | Tension(t) | 8040 | 2647.8 | -75.7 | 634.3 | 388.2 |
| | Nylon | Surge(m) | 3439 | 4.68 | -3.57 | 0.18 | 0.91 |
| | | Sway (m) | 9207 | 0.81 | -0.66 | -0.01 | 0.14 |
| | | Heave(m) | 3438 | 0.55 | -4.27 | -0.23 | 0.45 |
| | | Roll (°) | 7871 | 0.93 | -0.95 | 0.02 | 0.20 |
| | | Pitch (°) | 3438 | 4.94 | -4.78 | 0.23 | 1.09 |
| | | Yaw (°) | 7695 | 4.55 | -3.70 | 0.32 | 0.91 |
| | | Tension(t) | 3439 | 1671.9 | -56.1 | 394.1 | 271.1 |
| DLC 6.2b | Steel | Surge(m) | 6097 | 2.14 | -2.12 | 0.02 | 0.33 |
| | | Sway (m) | 9620 | 0.24 | -0.24 | -0.01 | 0.04 |
| | | Heave(m) | 9975 | 0.23 | -2.51 | -0.15 | 0.17 |
| | | Roll (°) | 9620 | 0.34 | -0.36 | 0.00 | 0.07 |
| | | Pitch (°) | 6097 | 2.86 | -2.84 | 0.08 | 0.46 |
| | | Yaw (°) | 1735 | 2.55 | -2.54 | 0.31 | 0.54 |
| | | Tension(t) | 6097 | 2981.8 | -10.7 | 797.2 | 404.6 |
| | Polyester | Surge(m) | 8040 | 2.46 | -2.48 | 0.05 | 0.45 |
| | | Sway (m) | 8924 | 0.39 | -0.34 | 0.00 | 0.08 |
| | | Heave(m) | 8040 | 0.36 | -2.87 | -0.10 | 0.21 |
| | | Roll (°) | 5295 | 0.44 | -0.57 | -0.02 | 0.12 |
| | | Pitch (°) | 8040 | 2.80 | -2.77 | 0.13 | 0.52 |
| | | Yaw (°) | 7707 | 2.86 | -2.82 | 0.32 | 0.63 |
| | | Tension(t) | 8040 | 2473.9 | -73.4 | 592.8 | 362.6 |
| | Nylon | Surge(m) | 3439 | 4.04 | -3.38 | 0.22 | 0.81 |
| | | Sway (m) | 10288 | 0.61 | -0.61 | -0.01 | 0.08 |
| | | Heave(m) | 3439 | 0.54 | -3.83 | -0.21 | 0.41 |
| | | Roll (°) | 10288 | 0.75 | -0.75 | 0.02 | 0.10 |
| | | Pitch (°) | 3439 | 4.70 | -4.60 | 0.21 | 1.05 |
| | | Yaw (°) | 1019 | 4.10 | -3.77 | 0.39 | 0.86 |
| | | Tension(t) | 3439 | 1507.1 | -51.1 | 356.1 | 244.9 |

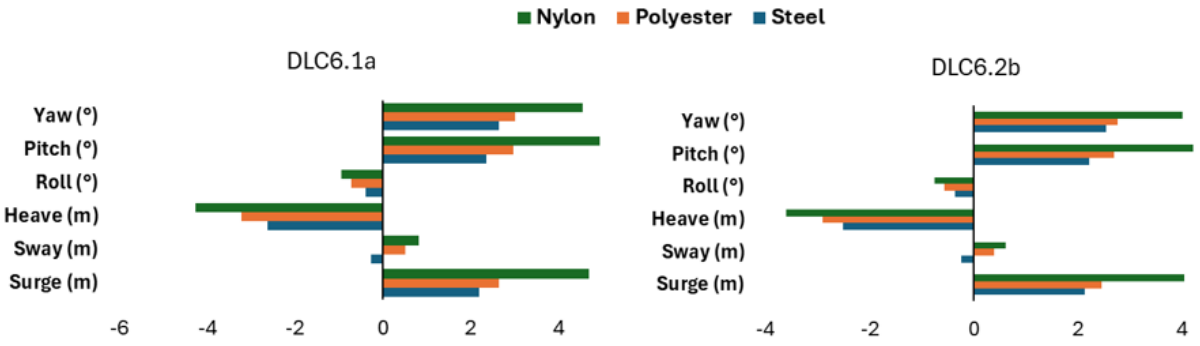


**Fig. 4-42** Statistical Six-degree Maximum Motion Responses of TLB employed Steel, Polyester, and Nylon Mooring Lines Under Survival Design Load Cases

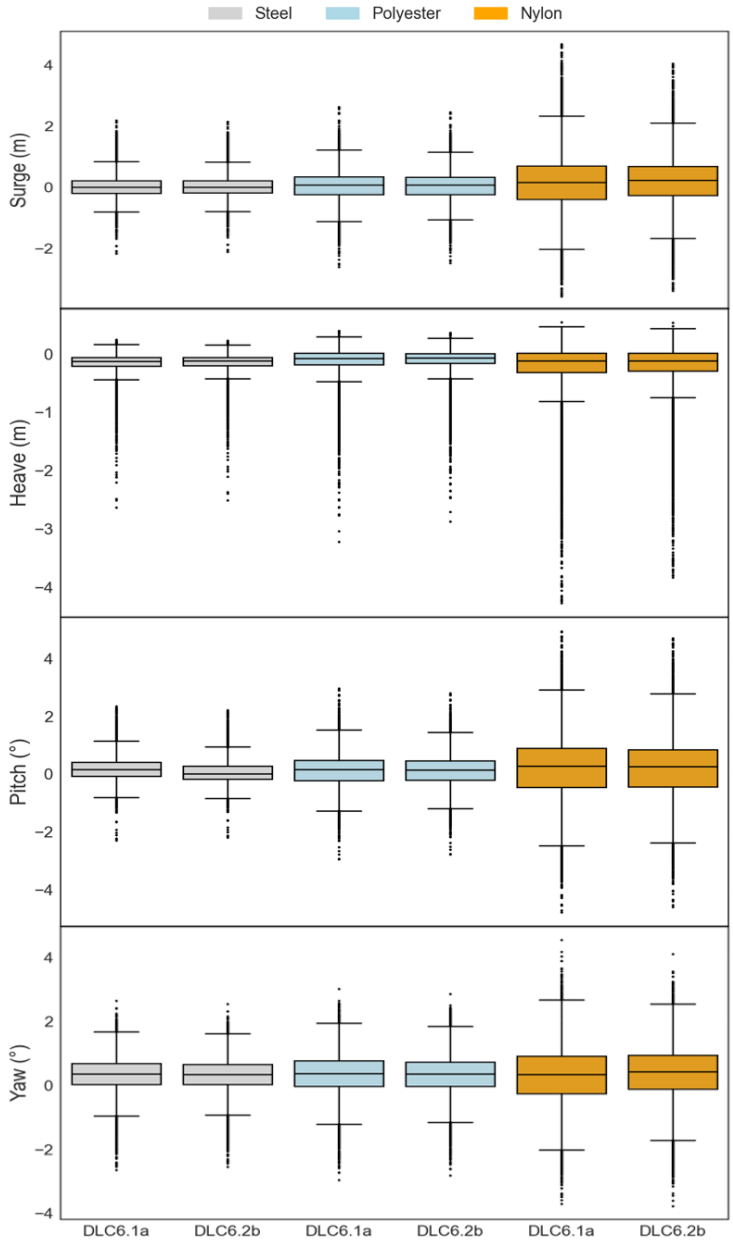


**Fig. 4-43** Surge, Heave, Pitch, and Yow Motin Responses Box Plots of TLB with Steel, Polyester, and Nylon Mooring Lines under Survival Condition

Based on the findings presented in Table 4-41 and the statistical comparison plots depicted in Fig. 4-42, it is evident that the responses of systems utilizing three distinct mooring line materials exhibit higher peak under DLC6.1a as opposed to DLC6.2b. This discrepancy in peak responses is attributed to differences in the wind model, particularly the turbulence wind, as the significant wave height and current remain constant for both DLCs.

The box plot graph presented in Fig. 4-43 demonstrates clear distinctions in the performance attributes of a TLB employing steel, polyester, and nylon mooring materials between two survival conditions design load cases.

TLB systems with steel and polyester mooring materials display consistent behaviour across motion responses, indicating performance with minimal variability. Conversely, a wider dispersion of data points across motion responses which suggest sensitivity to conditions due to material properties leading to increased fluctuation. The primary distinctions are influenced by the material properties, with steel and polyester showcasing low variability and consistent behaviour, rendering them dependable choices for applications necessitating stability during parked events in comparison to nylon material. TLB equipped with steel mooring lines experienced increased tension levels at peak surge and pitch, while systems utilizing fibre mooring materials encountered elevated tension levels due to simultaneous peak surge, pitch, and heave. This phenomenon is attributed to the complex nature of the system, its configuration, and the varying material properties of the mooring lines. Higher motion responses observed in TLB system utilized nylon material but with lower tension compared to systems employing steel mooring lines, due to the material characteristics of nylon, including its lower rigidity and greater elasticity. TLB system with nylon consistently exhibit greater variability in responses, suggesting that TLB systems with steel and polyester are suitable for applications requiring consistent behaviour due to minimal variability, while TLB systems with nylon may be less reliable for applications necessitating consistent performance.

Fig. 4-44, Fig. 4-45, and Fig. 4-46 show the trend of dynamic tensions response are strongly linked to the trend of some of motion responses.

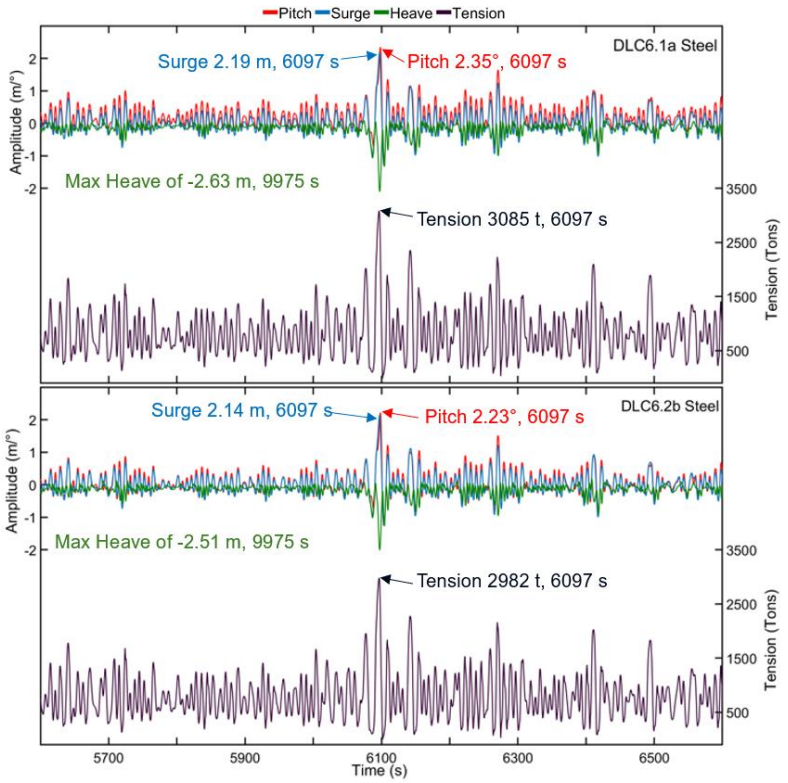


**Fig. 4-44** Time History of TLB with Steel Mooring Line Coupled Responses Under DLC6.1a & DLC6.2b

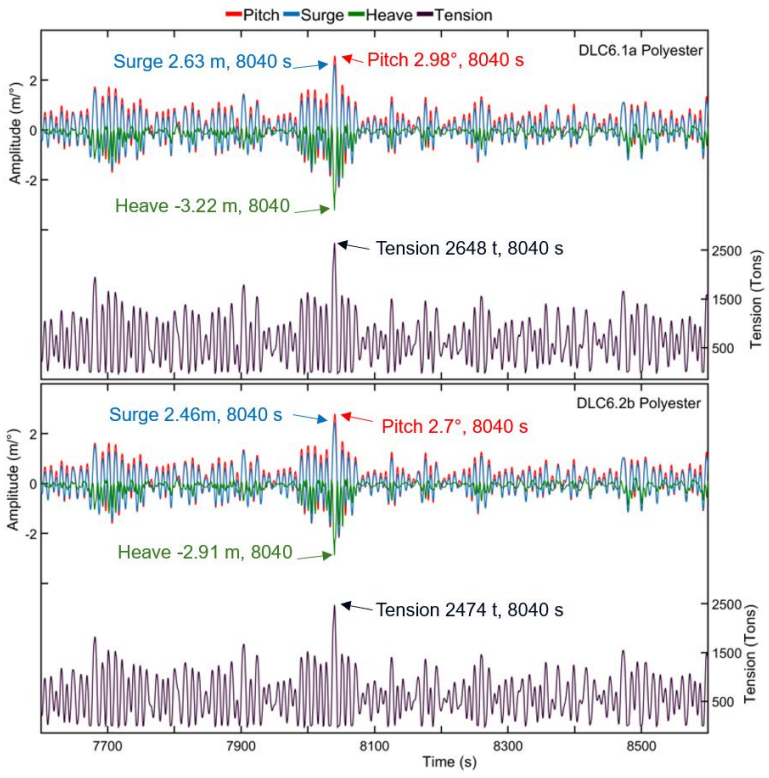


**Fig. 4-45** Time History of TLB with Polyester Mooring Line Coupled Responses Under DLC6.1a & DLC6.2b

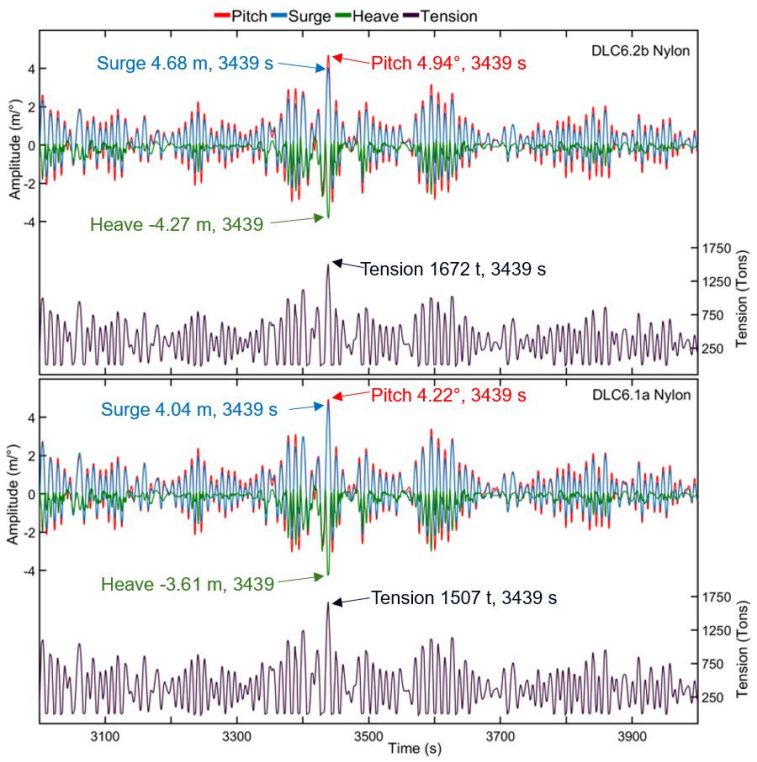


**Fig. 4-46** Time History of TLB with Nylon Mooring Line Coupled Responses Under Parked (Idling) Events

The peak responses captured in above figures indicating that the motion responses of the TLB occurred when the maximum dynamic tension of the most heavily loaded mooring line was experienced. These responses are closely interconnected and influenced by environmental factors. A significant effect was noted when substantial waves interacted with the structure during these coupled motion responses, leading to elevated tension levels.

To comply with DNV regulations, an assessment of the designated criteria detailed in section 2.9 is carried out. The design tension is calculated and illustrate in Table 4-42 by utilizing the average and maximum line dynamic tension values from Table 4-41, applying Eq. (8), and incorporating the ultimate limit state safety factors designated for the standard safety class in Table 2-8. Subsequently, the safety factor can be determined by employing Eq. (26) as illustrated in Table 4-43.

**Table 4-42** Characteristic Capacity of The Mooring Lines and The Design Tension Calculations for Each Mooring Material Under Parked (Idling) Event

| | $S_C\ (N)$ | $T_d\ (N)$ | |
|---|---|---|---|
| | | DLC6.1a | DLC6.2b |
| Steel | 3.82E+07 | 4.93E+07 | 4.77E+07 |
| Polyester | 2.89E+07 | 4.27E+07 | 3.99E+07 |
| Nylon | 2.09E+07 | 2.70E+07 | 2.43E+07 |

**Table 4-43** Safety Factors of Most Loaded Line for Each Mooring Line Materials Under Parked (Idling) Event

| | Safety Factor | |
|---|---|---|
| | DLC6.1a | DLC6.2b |
| Steel | 0.78 | 0.80 |
| Polyester | 0.68 | 0.72 |
| Nylon | 0.78 | 0.86 |

However, the safety margins are minimal, as the maximum dynamic tensions of the most heavily loaded line from the TLB systems utilizing three different mooring materials are below the manufacturer's MBLs and fall within the prescribed rule-based constraints, as well as meeting the design criteria for ULS.

## 4.5.2.4. The Impact of Wind Turbulence Modelling

Wind turbulence leads to variations in wind speeds and directions, causing dynamic aerodynamic forces on wind turbine blades. These fluctuating forces can trigger oscillations in the platform. FOWT platforms are dynamically coupled systems where wind, wave, and structural dynamics interact. Turbulent winds can provoke intricate coupled responses in the platform, resulting in increased peak responses in various degrees of freedom. Turbulent wind conditions can also interact with wave-induced movements. The collective impact of wind turbulence and wave forces can generate complex motion patterns and amplified platform reactions. According to Fig. 4-47, the importance of wind turbulence modelling is notable in systems utilizing nylon mooring materials, while its impact is minimal in systems utilizing steel mooring lines. The effect of wind turbulence intensity is more pronounced in systems using elastic mooring materials compared to those employing rigid mooring materials, suggesting that

employing steel mooring lines for TLB systems demonstrates improved resilience when subjected to turbulent wind events compared to nylon materials.

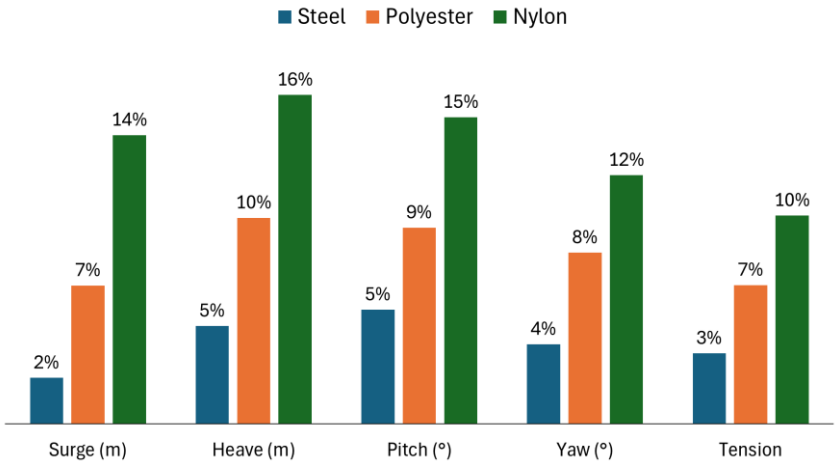


**Fig. 4-47** Variations in Maximum Responses Between DLC6.1a and DLC6.2b for TLB Utilizing Steel, Polyester, and Nylon Morring Materials

In conclusion, the results demonstrate an increase in maximum responses under DLC6.1a for systems with three mooring materials when compared against experience to a steady wind model under DLC6.2b event. TLB with steel mooring lines exhibited reduced motion responses compared to those with fibre ropes, as expected due to the higher axial stiffness of the material. Motion responses from TLB with polyester lines were also smaller compared to those with nylon mooring wire ropes, emphasizing the influence of material elongation and tension characteristics as at 50% of the MBL, the nylon material has 30% more elasticity than polyester (refer to Table 4-22).

The tilt inclination of systems utilizing steel, polyester, and nylon did not exceed a permissible maximum of 15° during non-operational conditions, indicating that the systems' responses met the rule-based limitations described in section 2.9. All tensions remained within the manufacturer's specified limits, rule-based constraints, and the design criteria for ULS.

The results presented highlight that a TLB with three mooring lines can effectively operate and maintain acceptable responses even in relatively severe sea states, showcasing the significant advantages of TLB design.

### 4.5.2.5. Parked (Idling) & Fault Event

In the context of FOWTs, similar to floating offshore structures used for oil and gas production, the ability of a FOWT to withstand extreme conditions is a crucial aspect in its design and installation. This section will concentrate on investigating the situation in which the systems encounter the failure of their two mooring lines that are subjected to significant loads during a parked (idling) event. More specifically, it will assess the scenario in which the two most heavily loaded lines rupture and separate from the fairleads at the 500-second of the simulation time. Fig. 4-48 illustrates that lines 7 and 8 are simulated to detach from the fairlead after 500 seconds of the simulation for both DLCs 7.1a and 7.1b. The results investigate to assess the survivability of the FOWT with disconnected mooring lines, ensuring that the motion responses remain within the prescribed limits outlined in industry standards (refer to Section 2.9) such as DNVGL-ST-0437 [460], DNVGL-RP-0286 [440], and maximum dynamic tension satisfy the rule-based limitations.

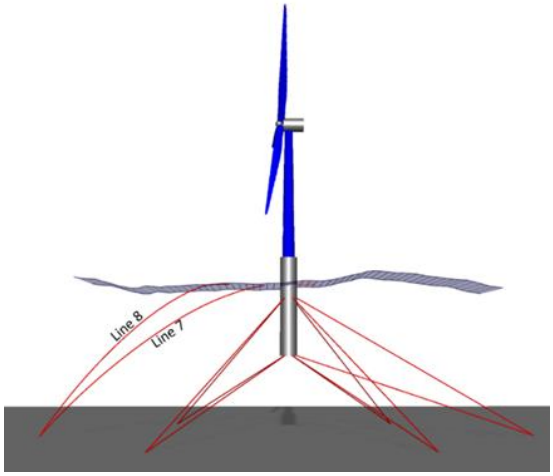


**Fig. 4-48** Disconnected lines 7 & 8 at 500 Second Representing Line Broken Scenario

Table 4-44 presents a summary of the maximum motion responses observed for parked (idling) and fault events, with the maximum dynamic tension level specified for the line subjected to the greatest load. Fig. 4-49 to Fig. 4-52 illustrate the surge, heave, pitch, and maximum tension responses. Meanwhile, Fig. 4-53 and Fig. 4-54 show the time history of the coupled motion responses and dynamic tension for DLC7.1a and

DLC7.1b respectively. Additionally, Table 4-45 displays the average offset responses both prior to and after the disconnection of the lines.

**Table 4-44** Responses Characteristics of the TLB with Steel, Polyester, and Nylon Mooring Lines for Parked (Idling) & Fault Events

| | | | Time (s) | Max | Min | Mean | SD |
|---|---|---|---|---|---|---|---|
| DLC 7.1a | Steel | Surge(m) | 8040 | 3.68 | -1.52 | 0.68 | 0.79 |
| | | Sway (m) | 7061 | 0.42 | -0.39 | 0.00 | 0.09 |
| | | Heave(m) | 6151 | 1.16 | -3.06 | 0.52 | 0.32 |
| | | Roll (°) | 7061 | 0.65 | -0.67 | 0.01 | 0.16 |
| | | Pitch (°) | 8040 | 4.26 | -2.87 | 0.32 | 1.06 |
| | | Yaw (°) | 892 | 3.70 | -3.58 | 0.23 | 0.90 |
| | | Tension(t) | 8040 | 3353.5 | 313.8 | 1807.9 | 529.2 |
| | Polyester | Surge(m) | 9688 | 6.17 | -1.88 | 0.83 | 1.12 |
| | | Sway (m) | 3367 | 0.93 | -0.92 | 0.00 | 0.18 |
| | | Heave(m) | 9688 | 2.69 | -4.06 | 0.91 | 0.60 |
| | | Roll (°) | 8102 | 1.09 | -1.03 | 0.01 | 0.23 |
| | | Pitch (°) | 9688 | 7.90 | -4.65 | 0.51 | 1.65 |
| | | Yaw (°) | 7098 | 5.07 | -3.99 | 0.30 | 1.04 |
| | | Tension(t) | 9688 | 2943.8 | -12.1 | 1176.3 | 465.6 |
| | Nylon | Surge(m) | 3439 | 6.48 | -1.93 | 0.85 | 1.15 |
| | | Sway (m) | 3889 | 1.10 | -0.54 | -0.01 | 0.15 |
| | | Heave(m) | 3439 | 3.45 | -4.57 | 1.41 | 0.63 |
| | | Roll (°) | 3889 | 1.39 | -1.56 | 0.08 | 0.29 |
| | | Pitch (°) | 3439 | 8.18 | -4.42 | 0.46 | 1.75 |
| | | Yaw (°) | 6961 | 5.61 | -4.80 | 0.70 | 1.29 |
| | | Tension(t) | 3439 | 2066.1 | -45.3 | 945.0 | 347.5 |
| DLC 7.1b | Steel | Surge(m) | 4584 | 3.25 | -1.15 | 0.61 | 0.69 |
| | | Sway (m) | 2049 | 0.35 | -0.29 | -0.02 | 0.08 |
| | | Heave(m) | 1761 | 1.00 | -2.60 | 0.46 | 0.28 |
| | | Roll (°) | 2048 | 0.51 | -0.55 | 0.03 | 0.13 |
| | | Pitch (°) | 4584 | 3.72 | -2.46 | 0.25 | 0.97 |
| | | Yaw (°) | 3638 | 3.03 | -2.71 | 0.37 | 0.70 |
| | | Tension(t) | 4584 | 3201.8 | 3.9 | 1694.1 | 521.7 |
| | Polyester | Surge(m) | 6777 | 5.20 | -1.56 | 0.78 | 1.03 |
| | | Sway (m) | 3883 | 0.85 | -0.61 | -0.04 | 0.15 |
| | | Heave(m) | 6777 | 1.88 | -3.83 | 0.73 | 0.36 |
| | | Roll (°) | 3888 | 1.56 | -1.33 | 0.06 | 0.22 |
| | | Pitch (°) | 6777 | 6.54 | -4.16 | 0.38 | 1.54 |
| | | Yaw (°) | 6778 | 4.70 | -3.83 | 0.52 | 0.95 |
| | | Tension(t) | 6777 | 2580.4 | 70.6 | 1261.4 | 448.0 |
| | Nylon | Surge(m) | 3430 | 5.96 | -1.91 | 0.79 | 1.06 |
| | | Sway (m) | 1412 | 0.80 | -0.58 | 0.01 | 0.16 |
| | | Heave(m) | 3430 | 2.72 | -3.95 | 1.01 | 0.59 |
| | | Roll (°) | 1413 | 1.07 | -1.18 | 0.01 | 0.27 |
| | | Pitch (°) | 3430 | 7.79 | -3.93 | 0.54 | 1.61 |
| | | Yaw (°) | 7098 | 4.97 | -4.36 | 0.28 | 0.92 |
| | | Tension(t) | 3430 | 1850.0 | -26.3 | 782.7 | 317.0 |

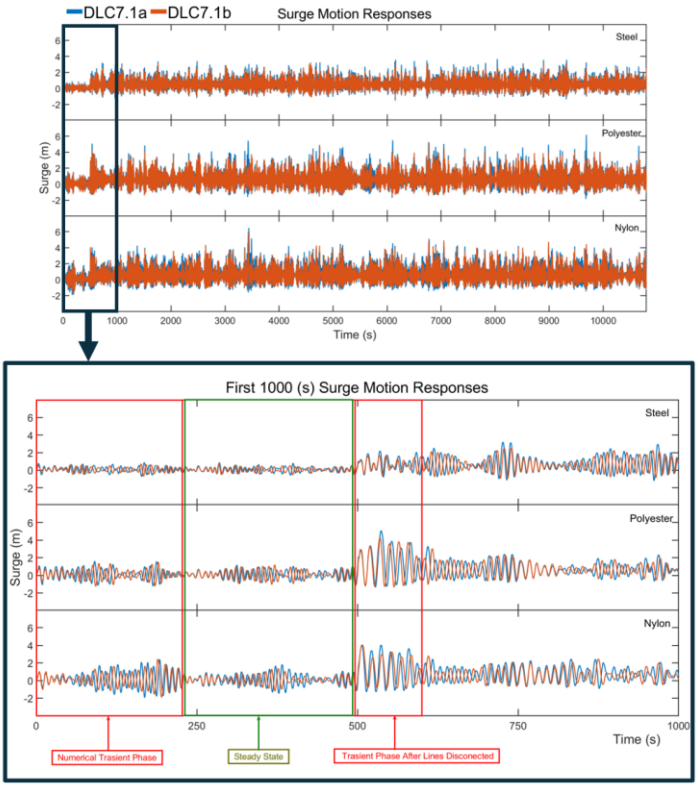


**Fig. 4-49** DLC7.1a & 7.1b Surge Response Motion Full Time History (Top) and First 1000s (bottom) for TLB with Steel, Polyester, and Nylon Mooring Lines

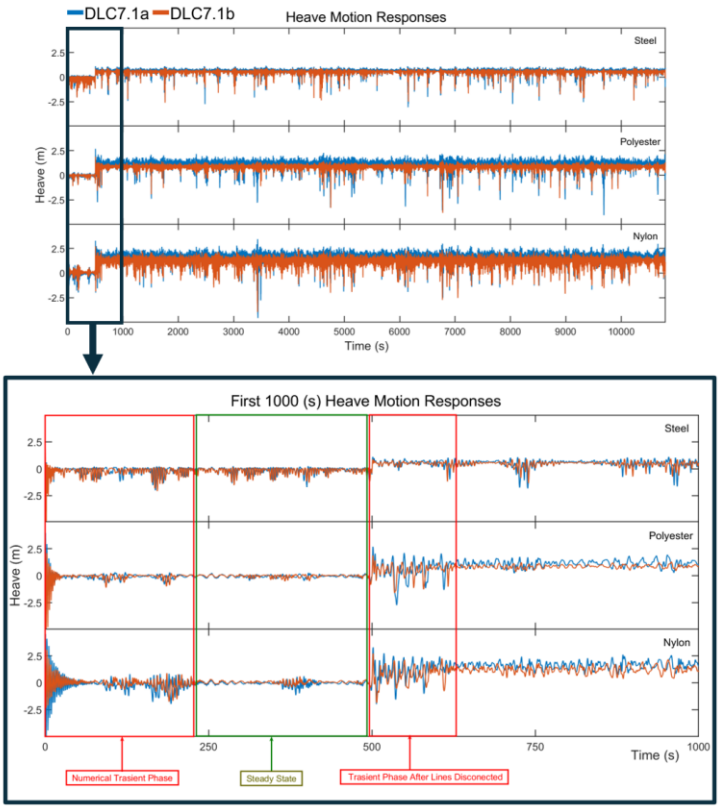


**Fig. 4-50** DLC7.1a & 7.1b Heave Response Motion Full Time History (Top) and First 1000s (bottom) for TLB with Steel, Polyester, and Nylon Mooring Lines

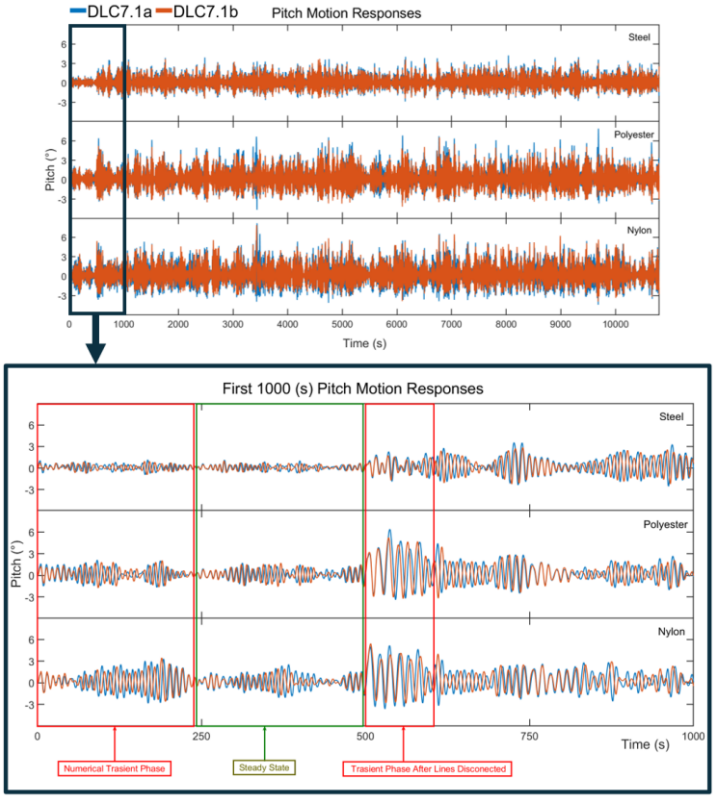


**Fig. 4-51** DLC7.1a & 7.1b Pitch Response Motion Full Time History (Top) and First 1000s (bottom) for TLB with Steel, Polyester, and Nylon Mooring Lines

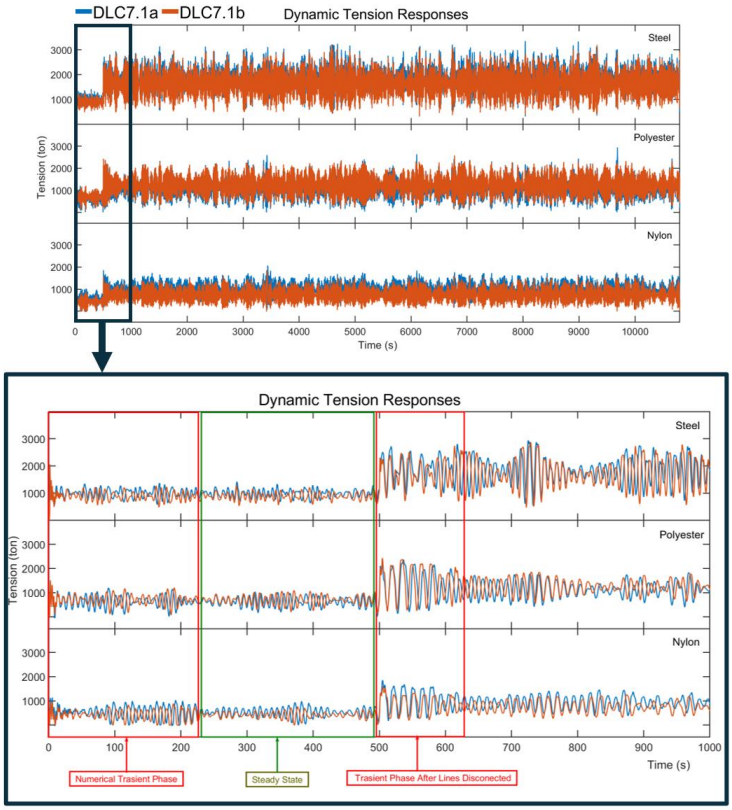


**Fig. 4-52** DLC7.1a & 7.1b Tension Response Motion Full Time History (Top) and First 1000s (bottom) for TLB with Steel, Polyester, and Nylon Mooring Lines

Comparing the behaviour of the three mooring materials before, during and after disconnecting the most loaded lines illustrated in Fig. 4-49 to Fig. 4-52 shows that the initial unsteady transient phase ended after approximately 250 seconds, with the system allowed to reach a steady state response before disconnecting of the lines. This behaviour has been observed for the system with three mooring materials. The sudden shift observed in motion responses after disconnection of the lines is higher for the TLB with nylon rope than the polyester and steel mooring lines. The platform's motion responses trend with fibre mooring lines are similar, with higher amplitude in the transient phase for TLB with nylon rope after line disconnected. The elasticity of nylon material caused higher amplitude in the responses. The systems experienced transient phase after the lines disconnected, and the platform with fibre ropes shows higher responses than for the platform with more rigid lines; the TLB with a steel mooring line material had lower oscillations. For the TLB with nylon lines, a sharp, high amplitude of surge and heave responses occurred in the transient phase after the lines disconnected, due to elasticity of the material. The high rigidity with higher axial stiffness for the steel material caused a lower magnitude, whilst the platforms with fibre mooring lines oscillate more after lines disconnect.

Table 4-45 presents the average responses of surge, heave, pitch, and tension for the system employed steel, polyester, and nylon mooring materials under DLC7.1a and DLC7.1b, both before and after failure of the mooring line. The changes (Δ) in each parameter after failure are highlighted in red.

The results of systems under both DLCs show considerable increases in heave and surge after failure, with DLC7.1a showing a slightly higher increase due to environmental conditions. System with nylon mooring line experiences the largest changes in heave after failure compared to system with polyester and steel, especially in DLC7.1a, indicating more flexibility but less stability under failure conditions. System with polyester mooring line exhibits larger changes in surge and heave after failure compared to steel. System with steel mooring line shows substantial increases in tension, indicating that steel lines experience high stress after failure. The tension on the polyester increase is less compared to steel, indicating that Polyester handles post-failure stress better in terms of tension. The increased tension on nylon line is the smallest among the three materials, suggesting that nylon, while more flexible, does not accumulate as much stress post-failure.

**Table 4-45** Mean Offset Comparison of Responses under DLC7.1a & 7.1b Beforehand and Afterward Disconnected Lines

| | | | Average of Responses | | | |
|---|---|---|---|---|---|---|
| **Mooring Material** | **DLC** | **Line Status** | **Surge (m)** | **Heave (m)** | **Pitch (°)** | **Tension (ton)** |
| **Steel** | DLC7.1a | Before Failure | 0.0886 | -0.1780 | 0.1132 | 996.1 |
| | | After Failure | 0.6947 | 0.5013 | 0.3273 | 1827.0 |
| | | Δ | 0.6060 | 0.6793 | 0.2141 | 830.9 |
| | DLC7.1b | Before Failure | 0.0701 | -0.2488 | 0.0911 | 895.8 |
| | | After Failure | 0.6211 | 0.4563 | 0.2567 | 1712.9 |
| | | Δ | 0.5510 | 0.7051 | 0.1655 | 817.1 |
| **Polyester** | DLC7.1a | Before Failure | 0.1159 | -0.0995 | 0.1634 | 632.6 |
| | | After Failure | 0.8500 | 0.9291 | 0.5217 | 1186.7 |
| | | Δ | 0.7341 | 1.0286 | 0.3583 | 554.1 |
| | DLC7.1b | Before Failure | 0.1024 | -0.0656 | 0.1391 | 695.1 |
| | | After Failure | 0.7976 | 0.7497 | 0.3899 | 1272.2 |
| | | Δ | 0.6952 | 0.8152 | 0.2508 | 577.1 |
| **Nylon** | DLC7.1a | Before Failure | 0.1378 | -0.2010 | 0.1854 | 523.1 |
| | | After Failure | 0.8671 | 1.4082 | 0.4616 | 953.1 |
| | | Δ | 0.7294 | 1.6092 | 0.2762 | 430.0 |
| | DLC7.1b | Before Failure | 0.1365 | -0.0698 | 0.1886 | 424.0 |
| | | After Failure | 0.8020 | 1.0119 | 0.5470 | 789.6 |
| | | Δ | 0.6655 | 1.0818 | 0.3584 | 365.6 |

The steel mooring line offers high stability before failure but experiences significant stress and motion changes post-failure indicating however it is suitable for applications where pre-failure stability is crucial; the maintenance of the mooring line is vital. The polyester mooring line provides a balanced performance with moderate increases in post-failure parameters with a good compromise between stability and flexibility compared with steel and nylon materials. The nylon mooring line shows the highest changes in motion parameters post-failure, indicating high flexibility and least increase in tension, suggesting it could be used with careful consideration of post-failure behaviour.

Fig. 4-53 and Fig. 4-54 show when coupled motion responses caused maximum dynamic tension. The maximum responses of TLB with three mooring materials under DLC7.1a and DLC7.1b captured and presented.

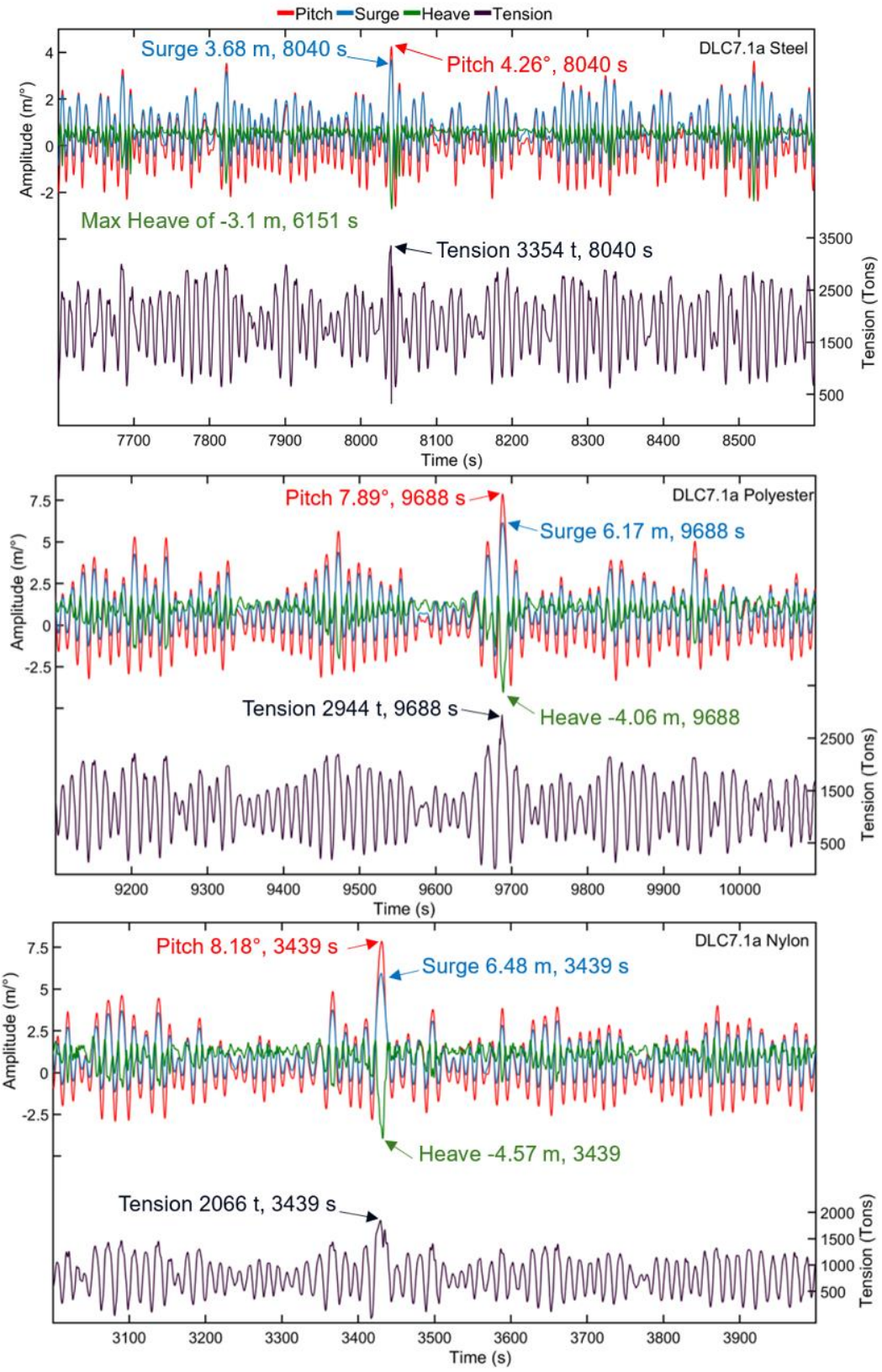


**Fig. 4-53** Time History of Coupled Responses Under DLC7.1a

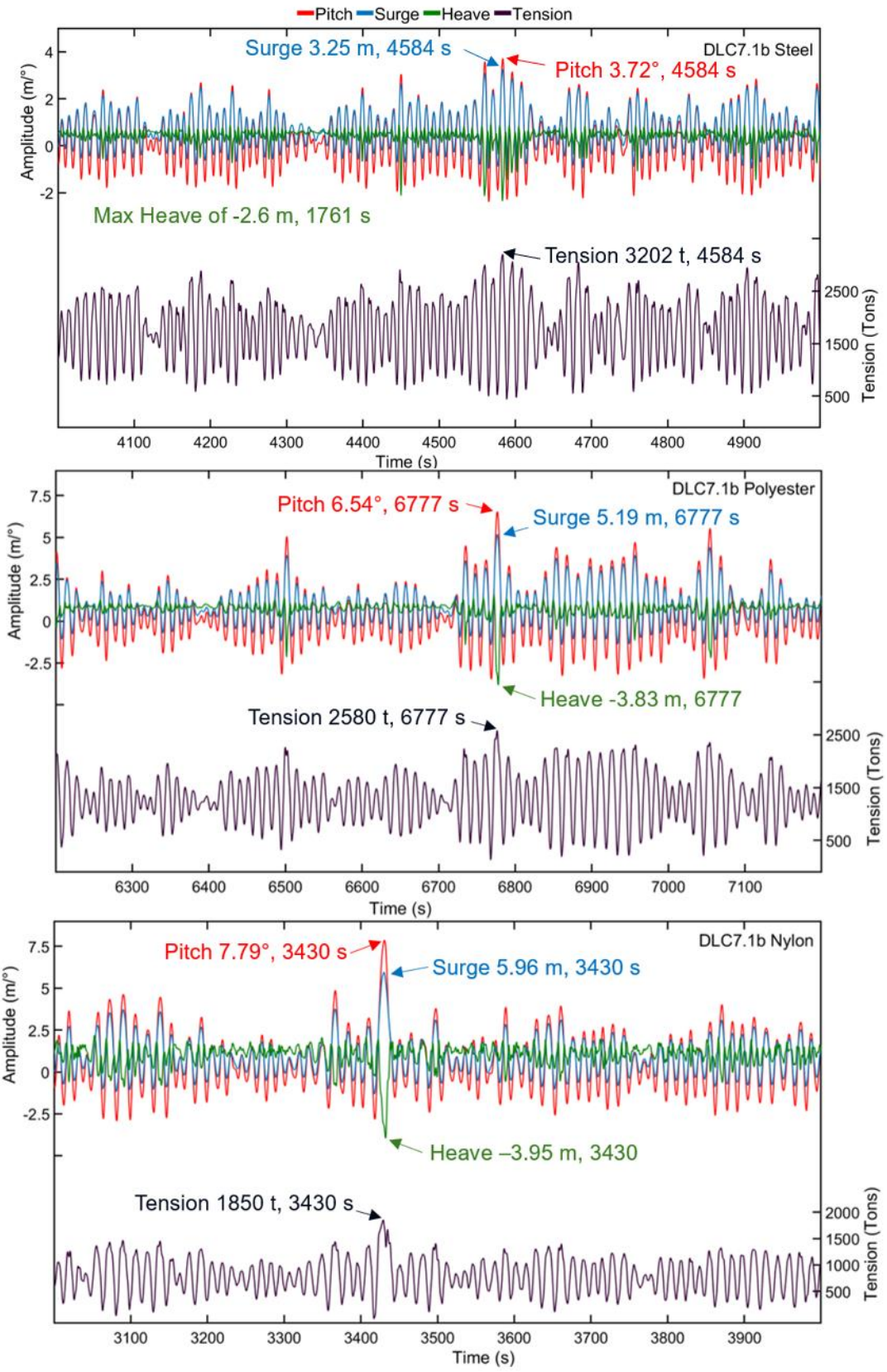


**Fig. 4-54** Time History of Coupled Responses Under DLC7.1b

The trend of motion responses and dynamic tension showed that the occurrence of surge and pitch in the TLB with steel mooring lines coincided with the highest tension levels whilst the system utilizing fibre mooring materials experienced surge, pitch, and heave simultaneously, resulting in increased tension levels. This occurrence attributed to a significant wave or a sequence of waves impacting the structure during the period when the motion responses are coupled, resulting in increased levels of tension.

To comply with DNV regulations, an assessment of the designated criteria detailed in section 2.9 is carried out. The design tension is calculated and illustrate in Table 4-46 by utilizing the average and maximum line dynamic tension values from Table 4-44, applying Eq. (8), and incorporating the ultimate limit state safety factors designated for the standard safety class in Table 2-8. Subsequently, the safety factor can be determined by employing Eq. (26) as illustrated in Table 4-47.

**Table 4-46** Characteristic Capacity of The Mooring Lines and The Design Tension Calculations for Each Mooring Material under Parked (Idling) Event

| | $S_C\ (N)$ | $T_d\ (N)$ | |
|---|---|---|---|
| | | DLC1.1 | DLC1.6a |
| Steel | 3.82E+07 | 3.44E+07 | 3.29E+07 |
| Polyester | 2.89E+07 | 3.06E+07 | 2.66E+07 |
| Nylon | 2.09E+07 | 2.14E+07 | 1.92E+07 |

**Table 4-47** The Utilization Factors for Each Mooring Line under Parked (Idling) Event

| | Safety Factor | |
|---|---|---|
| | DLC1.1 | DLC1.6a |
| Steel | 1.11 | 1.16 |
| Polyester | 0.94 | 1.08 |
| Nylon | 0.98 | 1.09 |

Based on the results of the motion responses, the angle of inclination after damage (idling with fault event) did not exceed 17° tilt inclination limitation [439]. TLB design using either of the three mooring line materials survived in an extreme sea state with wind turbulence, even while the two most-loaded lines from parked events are disconnected. Furthermore, following DNV-OS-J103 [441], the results of safety factors showed that the design tension of three mooring materials satisfy all criteria.

In summary, the selection of mooring lines for a TLB floating wind turbine is conditional upon specific criteria such as strength, elasticity, durability, weight, cost, and environmental factors. Steel, polyester, and nylon are the primary materials considered for these applications. Steel is favoured for primary mooring lines due to its superior tensile strength, which is essential for withstanding heavy loads and constant tension in TLB systems. Polyester, offering a good balance between strength and flexibility, is suitable for medium to large mooring applications. Nylon, while possessing high strength, is typically used for additional support or auxiliary moorings rather than as the primary mooring line due to its elasticity.

Steel's minimal elasticity ensures stable mooring and limited movement of the TLB, crucial for high stress on mooring lines. Polyester, with low elasticity, provides stability while allowing some flexibility to absorb dynamic loads, thereby preventing excessive tension and potential damage. Conversely, nylon's high elasticity, while beneficial for shock absorption, may result in excessive TLB movement, impacting turbine performance and structural stability.

Steel is recommended for primary mooring lines due to its high strength, low elasticity, and durability, ensuring stable TLB positioning critical for high stress. Polyester can serve as a suitable alternative or complement, providing a balance of strength and flexibility. Nylon is best suited for mooring lines where shock absorption is necessary but is less ideal as the primary mooring line due to its high elasticity and potential for excessive movement. In conclusion, steel is generally preferred for primary mooring lines in TLB floating wind turbines, with polyester offering a viable alternative or supplement due to its strength and flexibility.

### 4.5.3. Nacelle Accelerations

Nacelle accelerations directly impact the dynamic loads on the turbine structure. High accelerations can lead to increased stress and strain on the components, potentially causing structural damage or failure. Nacelle motion affects the alignment of the rotor with the wind direction. Significant accelerations can cause misalignment, reducing the efficiency of energy capture and overall power production [485]. Therefore, investigating nacelle accelerations in floating wind turbines is essential for ensuring structural integrity, optimizing performance, maintaining safety, understanding environmental interactions, improving design, and enhancing economic viability. According to DNVGL-RP-0286 [440] which provides guidance on limitations, the maximum nacelle acceleration should be 0.3 g (2.943 m/s$^2$) in the time series for the operational load cases, and should have a limit of 0.6 g (5.886 m/s$^2$) in the time series for the survival events.

Table 4-48 and Fig. 4-55 present the maximum nacelle accelerations, which include both translational and resultant components, recorded for systems utilizing each of the three mooring materials over the complete simulation period under all DLCs where X, Y, and Z signify the acceleration in the x, y, and z-directions respectively. The resultant acceleration, denoted as R, represents the magnitude of the acceleration vector. Resultant acceleration is the magnitude of the acceleration vector.

**Table 4-48** Maximum Translational and Resultant Nacelle Acceleration

| Nacelle Acceleration (m/s$^2$) | | | | | | | | | |
|---|---|---|---|---|---|---|---|---|---|
| **DLC** | Material | **X** | **Y** | **Z** | **R** | **X** | **Y** | **Z** | **R** |
| Power Production | | DLC1.1 | | | | DLC1.6a | | | |
| | Steel | 1.343 | 0.059 | 0.524 | 1.347 | 2.394 | 0.165 | 0.990 | 2.406 |
| | Polyester | 1.593 | 0.103 | 0.273 | 1.598 | 2.496 | 0.823 | 0.797 | 2.509 |
| | Nylon | 1.810 | 0.135 | 0.273 | 1.945 | 2.668 | 0.491 | 1.036 | 2.685 |
| Parked | | DLC6.1a | | | | DLC6.2b | | | |
| | Steel | 3.420 | 0.433 | 1.380 | 3.440 | 3.248 | 0.400 | 1.328 | 3.266 |
| | Polyester | 4.676 | 0.511 | 2.281 | 4.699 | 4.359 | 0.369 | 2.135 | 4.376 |
| | Nylon | 5.155 | 0.679 | 2.292 | 5.157 | 4.774 | 0.643 | 2.091 | 4.774 |
| Parked & Fault | | DLC7.1a | | | | DLC7.1b | | | |
| | Steel | 4.245 | 0.341 | 3.063 | 4.251 | 3.971 | 0.219 | 2.878 | 3.971 |
| | Polyester | 5.031 | 0.615 | 2.899 | 5.060 | 4.556 | 0.278 | 2.292 | 4.619 |
| | Nylon | 5.859 | 0.566 | 2.542 | 5.861 | 5.197 | 0.739 | 2.383 | 5.198 |

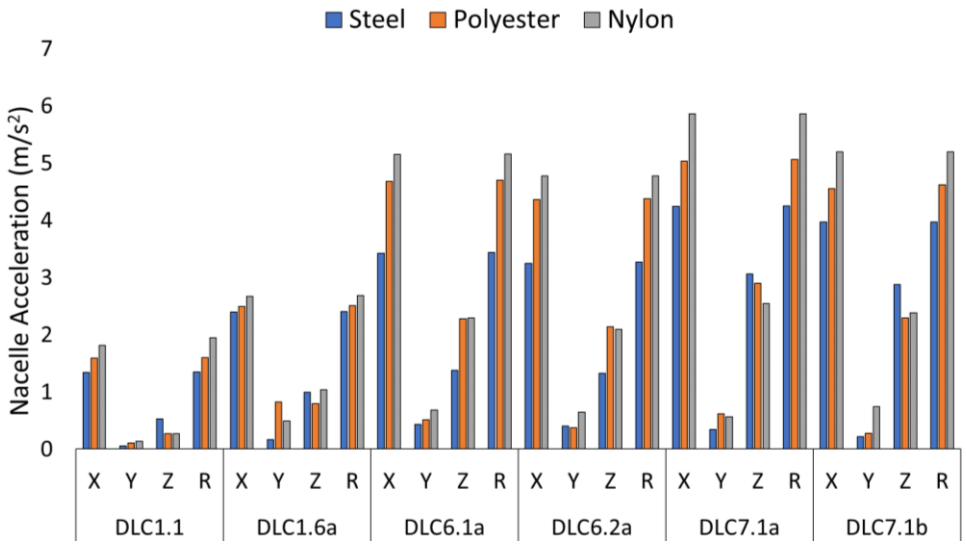


**Fig. 4-55** TLB Moored with Polyester, Nylon, and Steel Wire Ropes Maximum Nacelle Acceleration under DLCs

There is a noticeable correlation between the maximum resultant acceleration, denoted as R, and a single acceleration experienced by all mooring line materials across all DLCs. The resultant acceleration reaches its peak when the acceleration in the x-direction is maximized for three distinct mooring materials across all environmental scenarios. The nacelle acceleration of the system with nylon obtained the highest values under all DLCs. The impact of wind turbulence on nacelle acceleration was observed by analysing the outcomes of systems operating under DLC6.1a and DLC6.2b. The system utilizing a steel mooring line exhibited a 5% increase in resultant acceleration, whereas the system employing fibre mooring material demonstrated a 7% rise in acceleration when subjected to wind turbulence as opposed to steady wind conditions.

In conclusion, the design of the TLB with a taut mooring system utilizing various line materials meets the DNVGL criteria for nacelle acceleration in both operational (<0.3g) and non-operational conditions (<0.6g). However, it is observed that the system employing nylon under DLC7.1a experiences maximum acceleration levels near the specified limit. Notably, factors such as wind turbulence and external forces from environmental conditions, as outlined in the load cases, exert a considerable influence on nacelle acceleration. Furthermore, across all load cases, it is evident that employing a more rigid mooring system leads to a reduction in nacelle acceleration for the FOWT system.

# 5. Benchmarking Study

This section presents a benchmarking study of four floating wind platforms' motion responses and dynamic tension responses to verify an innovative design with the intention of overall responses whilst producing a durable, reliable and safe design. The benchmarking analysis in this study focuses on scaled models of Semi-Submersible, Spar, and TLP platform types. It is important to note that these models are not representative of all Semi-Submersible, Spar, and TLP platform categories. Therefore, the findings and conclusions drawn from this study are limited to the platforms examined and should not be concluded to include all types of platforms.

An aero-hydro-servo-elastic code is applied to benchmark a 10MW TLB floating wind turbine, as introduced in previous section, to the current leading technology types for floating offshore wind platforms, specifically Spar Buoy, Semi-Submersible and TLP floating wind turbines. The DTU 10MW wind turbine is considered [149]. The characteristics of the tower is adjusted similarly to explained for TLB system [189].

## 5.1. Floating Systems

Four floating systems (Spar, Semi-Submersible, TLP) are considered in this section, with each design scaled to support a 10MW wind turbine using methodology provide in Section 2.2.2.1 [189] enabling the same energy generation. These types of platforms are selected because they are most favourable support platforms in FOWT industry.

### 5.1.1. Support Platforms

The Semi-Submersible and Spar platforms have been scaled to support a 10MW wind turbine using the methodology described in Section 2.2.2.1, while the TLP design is derived from the TLP transport design by Aina Crozier [153]. In this study, these models have been reconfigured to generate results to examine their hydrodynamics behaviour under consistent environmental circumstances.

The process of scaling up the Semi-Submersible and Spar systems is based on uses a mass-depending factor, resulting in the scaled design, followed by a modification to ensure the draft remains the same as the original non-scaled design; this is then referred to as the reduced draft design. The main difference between the scaled and the reduced draft design lies in the geometry of the offset columns for a Semi-Submersible system. The offset columns' relative position to each other and the central column of the platform stays unchanged for the respective power rating of the system. The reduced draft design for both is lighter and will reduce material costs. The overall weight of the systems is kept constant by adjusting the amount of ballast water.

The TLP design is adopted from Aina Crozier TLP transported design remodelled and verification study carried out [153] where two TLP designs for the 10 MW wind turbine have been developed by applying the static design process. Aina Crozier TLP transported design obtained from an iterative design process to reproducing the MIT TLP properties from Tracy [421].

The Semi-Submersible system (Fig. 5-1) was developed based on the 5MW platform used in the OC4-DeepCwind project phase II (Offshore Code Comparison Collaboration Continuation) [486].

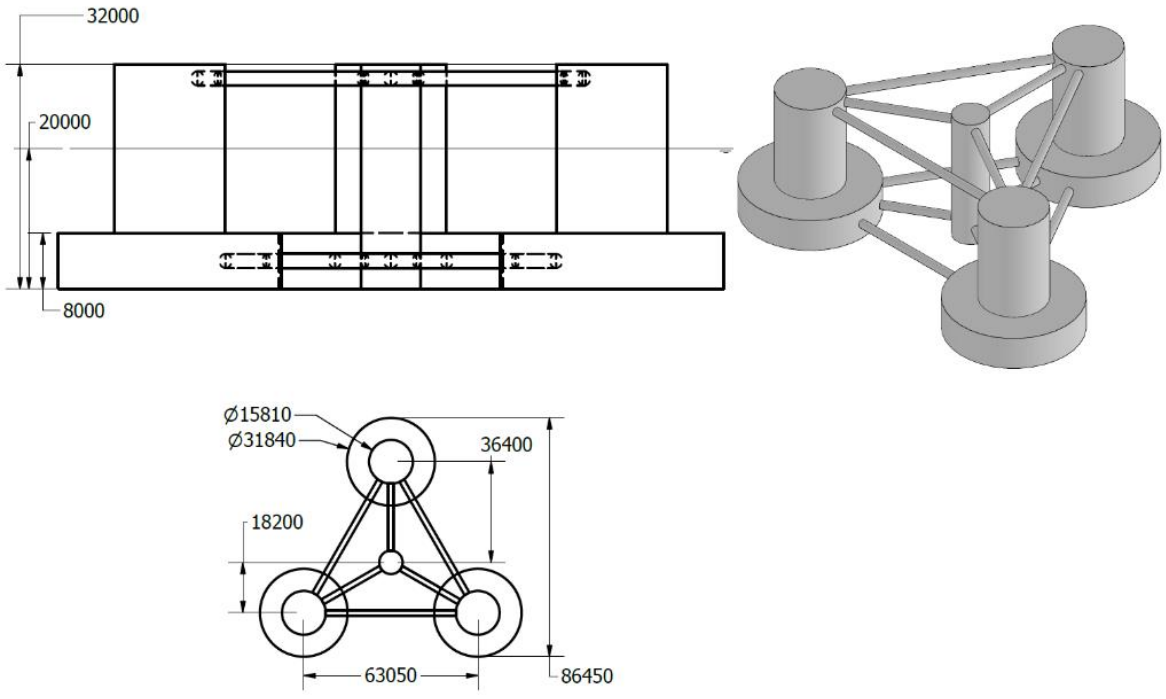


**Fig. 5-1** Semi-Submersible Support Platform 3D Model (Right) & Schematic (Left)

The Spar system (Fig. 5-2) was scaled up based on the OC3-Hywind Spar-Buoy, which used the turbine specifications of the National Renewable Energy Laboratory (NREL) offshore 5MW baseline wind turbine [364]. The TLP system is scaled to support the 10MW DTU wind turbine from [153] (Fig. 5-3) is based on a 5MW TLP designed, developed from the Massachusetts Institute of Technology (MIT) design [421] and referred to as MIT/NREL TLP herein [331].

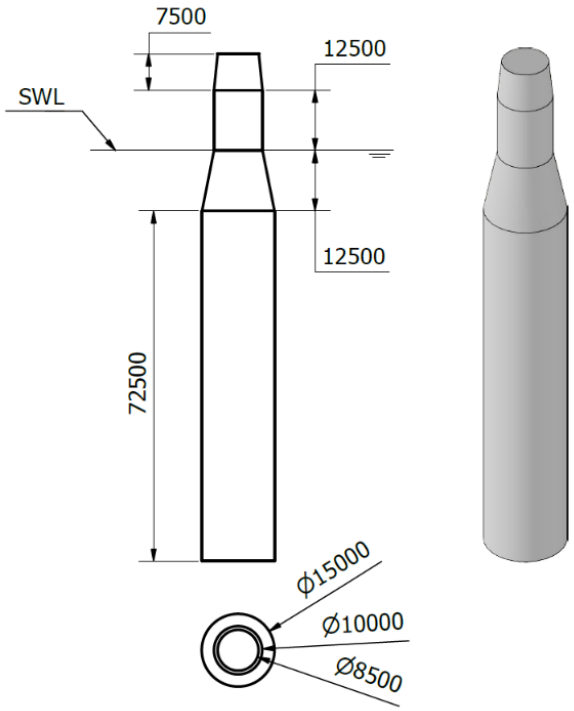


**Fig. 5-2** Spar Support Platform 3D Model (Right) & Schematic (Left)

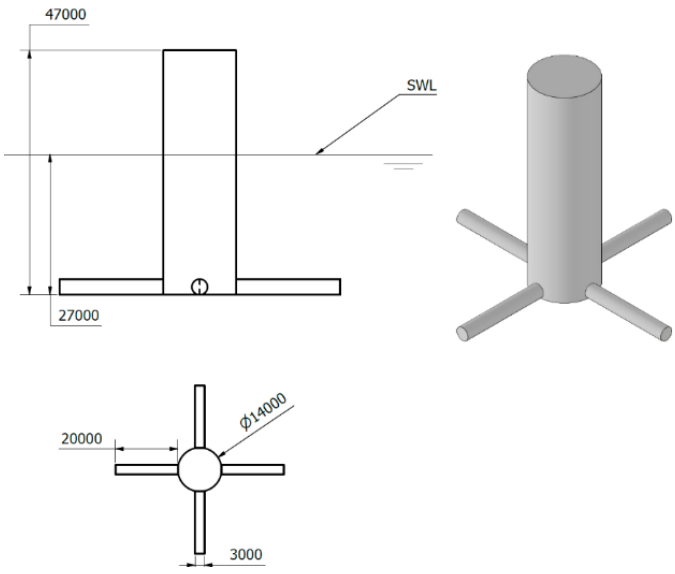


**Fig. 5-3** TLP Support Platform 3D Model (Right) & Schematic (Left)

The hydrostatic calculation of each platform is carried out and the platform characteristics of the four different designs are presented in Table 5-1. The mass value is the platform weight, and also noted that the centre of gravity (COG) and centre of buoyancy for each platform, calculated for the complete system, including the tower, rotor and nacelle, platform, ballast and mooring weights.

The scaled design of the platforms is modelled in SIMA as illustrated in Fig. 5-4.

**Table 5-1** 10MW Floating Offshore Wind Turbine Support Platforms Description

| Platform | Draft (m) | COG (m) | COB | Mass (tons) |
|---|---|---|---|---|
| Semi-Submersible | 20 | -8.7 | -13.25 | 2645.3 |
| Spar | 85 | -51.8 | -44.2 | 2488.7 |
| TLP | 27 | -21.1 | -14.9 | 1389.5 |
| TLB | 52 | -29.48 | -26 | 791 |

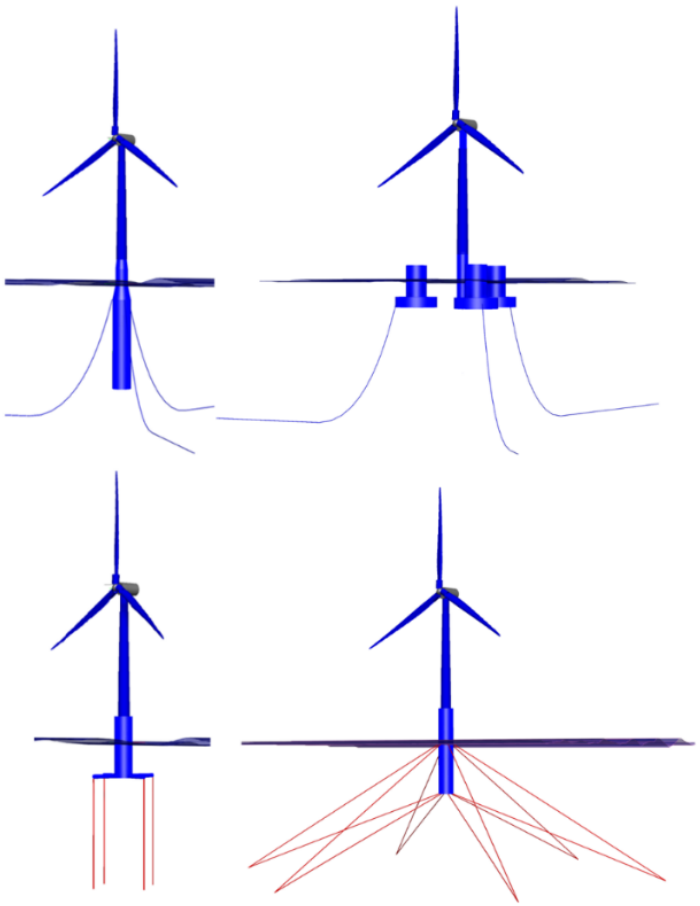

**Fig. 5-4** Offshore Floating Concepts, clockwise from top-left: Spar, Semi-Submersible, TLB, and TLP

### 5.1.2. Mooring System

The Spar and Semi-Submersible platforms using catenary mooring systems using a conventional 3-line mooring system. The mooring system for a TLP system consists of four tethers. The mooring system configurations of the various platforms are shown in Fig. 5-5, where L marks the mooring line.

In order to determine the mooring system stiffness matrix for use in HydroD when no line is present, this study adopted the approach outlined by Al-Solihat [287] for catenary of Semi-Submersible and Spar platforms and tensioned for TLP platform where to simplify the analysis of the mooring system, several assumptions are made. Firstly, homogenous line is assumed, with properties derived as the weighted-average values of the mass, weight, and stiffness (weighted based on the unstretched lengths of each segment). Secondly, all the mooring system damping, including the hydrodynamic and line-to-seabed drag, is neglected. To simplifying the modelling 20° spread of the attachment points of mooring lines to fairleads, a single attachment point for each mooring line was assumed and then modified according to the mooring system stiffness matrix, with an assumed angle of 20° spread of the attachment points to replicate the effects of a crowfoot connection to reduce the yaw motion of the platform. In the SIMA software, the RIFLEX model is constructed using supernodes and lines. The supernodes are linked to each other through lines, which are composed of one or more segments. each segment can be subdivided into multiple elements for the FEM formulation. The relationship between lines, segments, and elements is illustrated in Fig. 3-13 [487]. The FEM analysis used beam element for mooring analysis is considered in SIMA.

Apart from the TLP mooring system, the mooring lines attach to the platform via a so-called crowfoot, or delta connection, to increase the moorings' yaw stiffness [488].

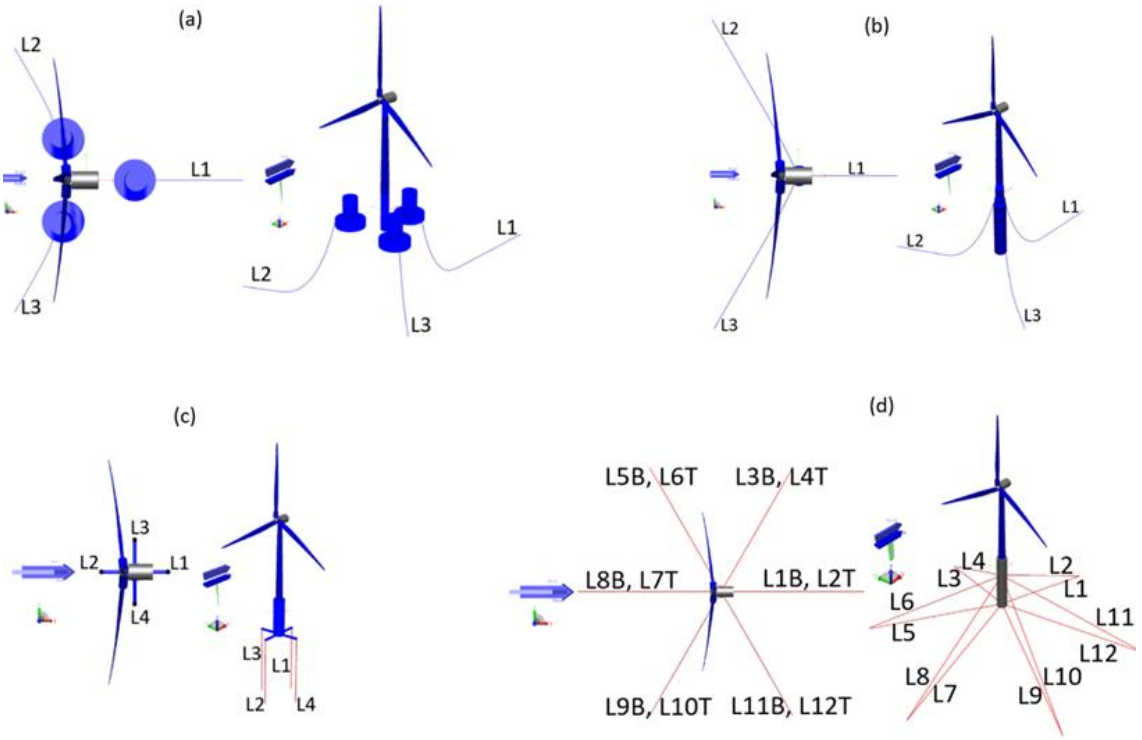


**Fig. 5-5** Mooring System Layout for Semi-Submersible (a), Sapar (b), TLP (c), and TLB (d) Platforms - Note: L, B, and T are the abbreviation formed of Line, Bottom and Top

The Spar system fairleads are located 12.5m below the still water level with a radius of 7.5m from the platform centreline. The anchors are located 110m below the still water level, at a radius of 853m from the platform centreline. One line is directed along the positive x-axis (in the XZ-plane), with the two remaining lines distributed uniformly around the platform, such that each line, the fairleads, and the anchors are 120° apart when viewed from above (see Fig. 5-5(b)). Each of the three studless chain lines has an unstretched length of 902m, a diameter of 0.166m, an equivalent mass per unit length of 400kg/m, an equivalent axial stiffness of 3.84243E+08N, a bending stiffness of 8.02E+07Nm, and finally a torsional stiffness of 6.3E+07 Nm/rad.

The Semi-Submersible mooring system is similar to the Spar mooring system, but the fairleads are located at a depth of 16m below the SWL and a radius of 52.32m from the platform centreline (see Fig. 5-5(a)). The anchor's radius is 806.2m from the platform centreline, with an unstretched length of 857.6m and the same line properties as the Spar mooring line.

The mooring system designed for the TLP system uses four tethers anchored on the seabed (see Fig. 5-5(c)). The tether is constructed of an 83m-long steel wire rope with a diameter of 0.48m. It has an equivalent mass per unit length of 494.5kg/m, with an axial stiffness of 1.73E+10N. The TLP system fairleads are located 27m below the SWL along a radius 27m from the platform centreline. The restoring coefficients are calculated by applying a small angle approximation whilst neglecting the tether mass. These restoring coefficients are calculated as an input in HydroD where no mooring line no line is present based on procedure presented in [153, 351]. However, the model employed in a fully coupled simulation incorporates all individual forces, such as lines, buoyancy, gravity, produce the restoring effect.

The hydrodynamic responses of the TLB system using a 320mm diameter steel wire rope will be compared to those of Semi-Submersible, Spar, and TLP systems. BRIDON BEKAERT [448] provided the data for steel wire rope, while ACTEON [489] provided data for the R5 studdles mooring chain. The mooring system characteristics for each platform are illustrated in Table 5-2.

**Table 5-2** Mooring Systems Characteristics

| Platform | Mooring Type | Dimension (m) | Length (m) | | Weight (kg/m) | MBL (N) |
|---|---|---|---|---|---|---|
| **Semi-Submersible** | Chain | 0.166 | 857.6 | | 400 | 2.73E+07 |
| **Spar** | Chain | 0.166 | 904.7 | | 400 | 2.73E+07 |
| **TLP** | Wire rope | 0.48 | 83 | | 494.5 | 6.38E+07 |
| **TLB** | Wire rope | 0.32 | Upper | Lower | | 2.94E+07 |
| | | | 200.5 | 183.2 | | |

The mooring system characteristics were deemed appropriate for ensuring stability and seakeeping of the systems in the prevailing environmental conditions. It is important to acknowledge that these characteristics may not represent the most optimal mooring system features for such platforms as this study only focused on designing optimum mooring system for TLB platform.

## 5.2. Numerical Methodology

The numerical and simulation methodologies outlined in Section 3.2 are applied to conduct hydrodynamics assessments of Semi-Submersible, Spar, and TLP FOWTs. The designs are first created in GeniE and then the FEM files are transferred to HydroD for conducting frequency domain hydrodynamic analysis in order to determine the Response Amplitude Operator (RAO) through the hydrodynamic wave-body interaction software. Subsequently, the hydrodynamic coefficients obtained for the platform are imported into SIMA for carrying out Aero-hydro-servo-elastic analysis using SIMO/RIFLEX to derive the integrated response results of the floater and mooring system. The aerodynamic forces are calculated in TurbSim and implemented in SIMA as an external force (refer to Fig. 5-6). The analyses involved in both the frequency domain and the time domain. The theoretical principles are elaborated upon in Section 3.1, while the detailed theoretical methodologies and formulations are provided in appendices A and B.

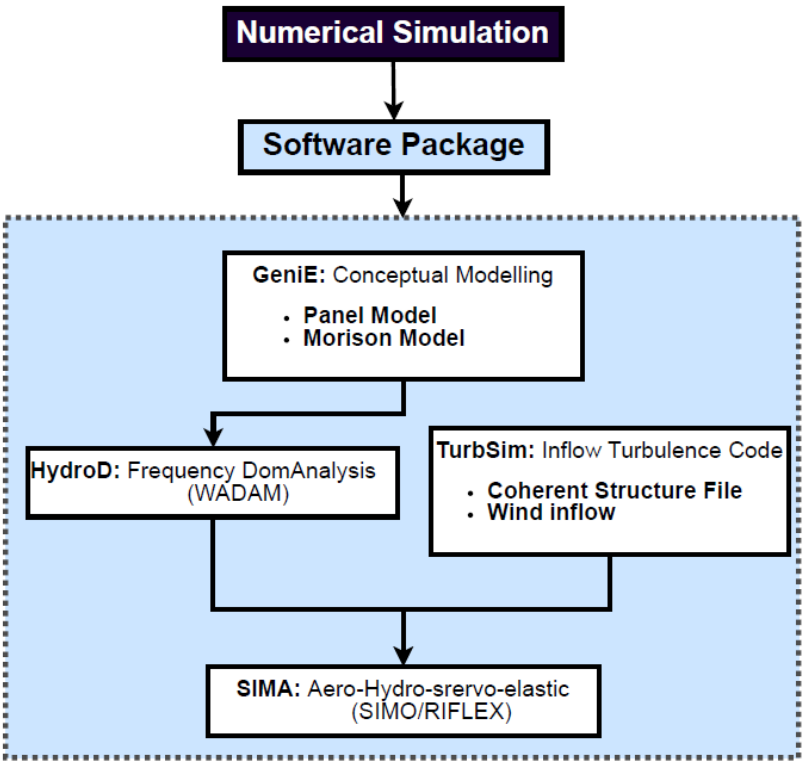


**Fig. 5-6** Numerical Simulation Workflow

## 5.3. Discretization of Platforms

The influence of different mesh sizes on the performance of each platform was investigated. It should be noted that symmetry was used in all models except for the Semi-Submersible. The influence of different mesh sizes on the result of the motion response of the platforms for surge, heave, and pitch motions (shown on the left-hand side) and forces (shown on the right-hand side) are presented in the following figures. Based on the mesh convergence study, the final panel model of the platforms is indicated in red in the following tables. It should be noted that the bracing and pontoon spokes are not discretised for both the TLP and Semi-Submersible platforms, since their mass is negligible. In conclusion, the mesh resolution was selected to cover all the critical scales in the hydrodynamic computation process.

**Table 5-3** Spar Model Mesh Options

| Mesh Size (m) | 3 | 2 | 1 | 0.5 | 0.3 | 0.25 |
|---|---|---|---|---|---|---|
| Element No/Quarter | 176 | 410 | 1314 | 5459 | 15262 | 21790 |

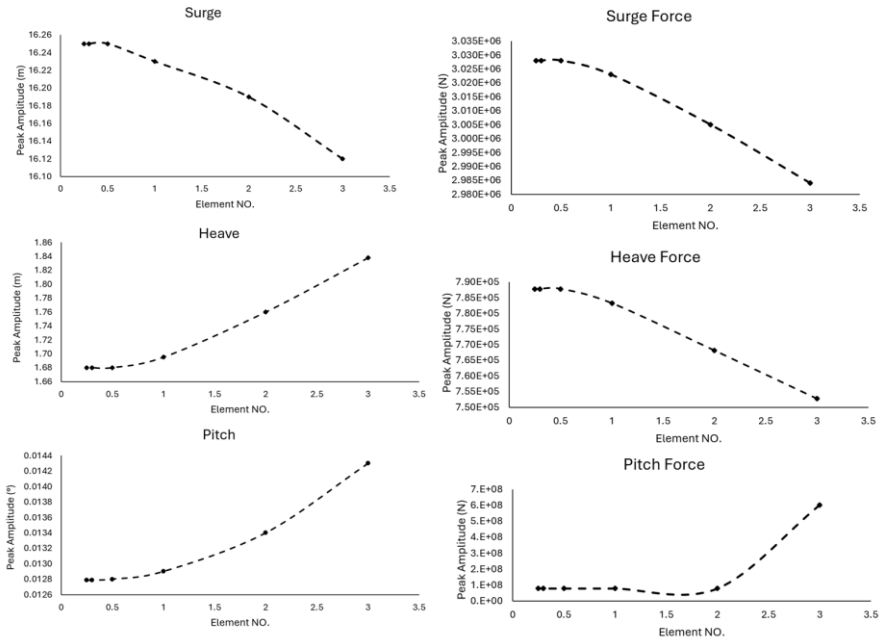


**Fig. 5-7** Spar Platform Motion Response Mesh Convergence

**Table 5-4** Semi-Submersible Model Mesh Options

| Mesh Size (m) | 5 | 3 | 1 | 0.8 | 0.7 | 0.5 |
|---|---|---|---|---|---|---|
| **Element No** | 5564 | 10534 | 26852 | 45653 | **51129** | 88235 |

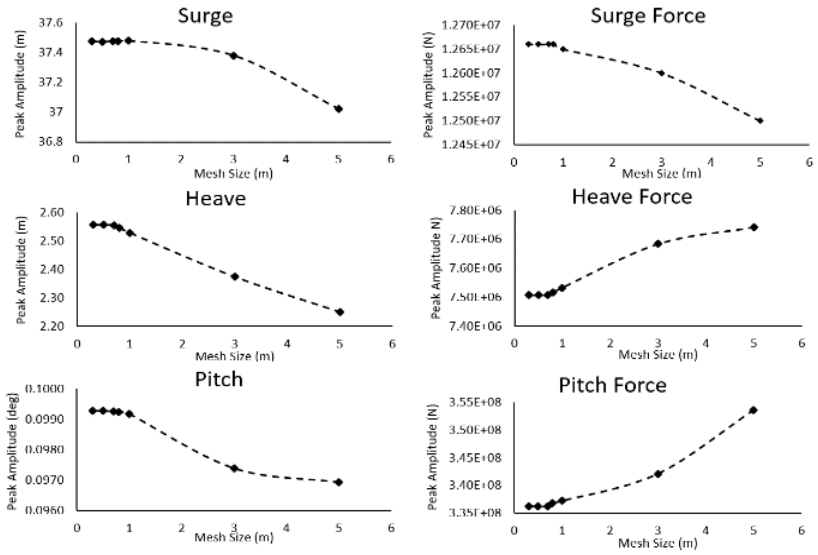


**Fig. 5-8** Semi-Submersible Platform Motion Response Mesh convergence

**Table 5-5** TLP Model Mesh Options

| Mesh Size (m) | 3 | 1 | 0.8 | 0.7 | 0.5 | 0.3 |
|---|---|---|---|---|---|---|
| **Element No/ Quarter** | 93 | 832 | 3665 | **4992** | 6015 | 8466 |

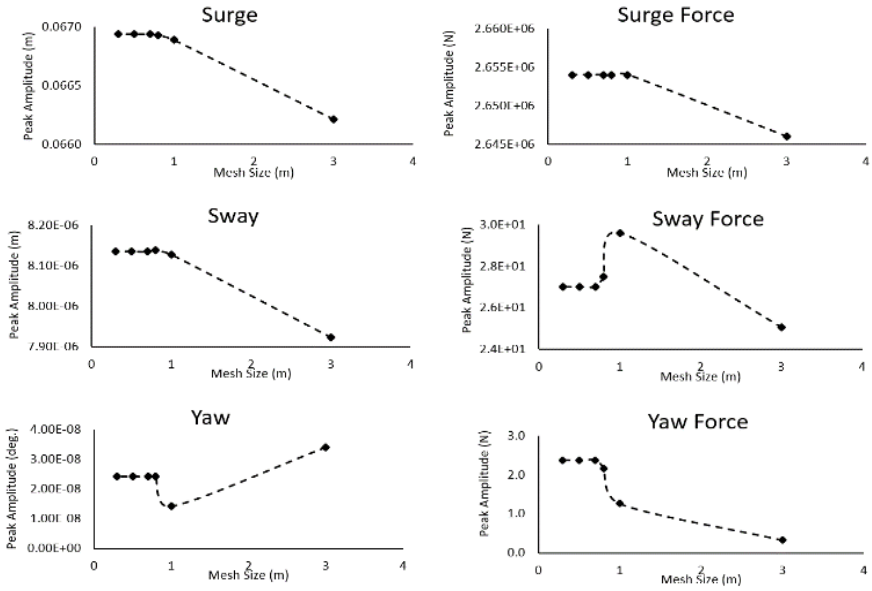


**Fig. 5-9** TLP Platform Motion Response Mesh convergence

Table 5-3, Table 5-4, and Table 5-5 illustrate the options considered when investigating the influence of different mesh sizes on the result of the motion response of the Spar, Semi-Submersible, and TLP platforms. Fig. 5-7, Fig. 5-8, and Fig. 5-9 show the results of the motion response of the Spar, Semi-Submersible, and TLP platforms for varied mesh sizes. Six mesh sizes were originally considered and the results of the mesh convergence of the Spar design indicated that the system motion responses have reached the stabilised peak amplitude by the mesh size of 0.5 m. The final panel model of the Spar floating structure consists of 5,459 elements per quarter, or 21,836 total elements given a 0.5 m mesh size.

The panel model of the complete Semi-Submersible floating structure was modelled with seven different mesh sizes. By investigating the influence of different mesh sizes on the result of motion responses of the Semi-Submersible platform, it can be seen that the model is converged with a mesh size of 0.7m. The final panel model of the Semi-Submersible floating structure consists of 51129 total element numbers. The effect of different mesh sizes on the motion responses for the TLP panel model shown that the TLP panel model reached the stabilised peak amplitude by the mesh size of 0.7m and less. The final panel model of the Semi-Submersible floating structure consists of 51,129 total element numbers.

The TLP panel model shows that the panel model reached the stabilised peak amplitude by the mesh size of 0.7m. The final panel model of the TLP platform consists of 4,992 elements per quarter, or19,968 elements in total given a mesh size of 0.7m.

The influence of different mesh sizes on the performance of each platform was investigated, with Table 5-6. illustrates the total number of panels and converged mesh size for the support structure shown in Fig. 5-10.

**Table 5-6** Mesh Size Converged and Element Number

| Platform | Mesh Size (m) | Element NO. |
|---|---|---|
| **Semi-Submersible** | 0.7 | 51129 |
| **Spar** | 0.5 | 5459 |
| **TLP** | 0.7 | 4992 |
| **TLB** | 0.6 | 3200 |

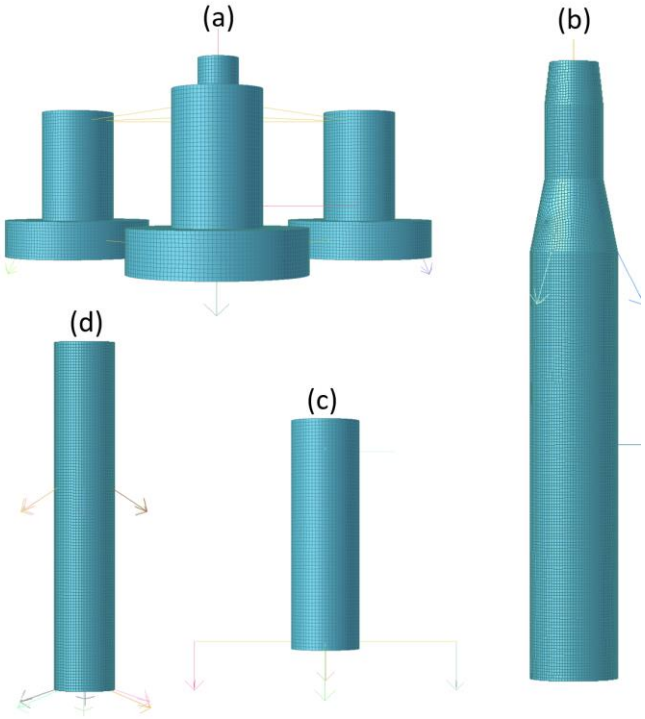


**Fig. 5-10** Mesh Converged Resolution of Semi-Submersible (a), Spar (b), TLP (c), and TLB (d) Platforms

## 5.4. Model Verification

The properties of platforms were modelled and run against available data sets to verify and validate the methodology process. The comprehensive validation for the TLB platform is carried out by Ramzanpoor [490]. The software verification for the Semi-Submersible, Spar, and TLP platforms are presented in the following section.

### 5.4.1. Spar

Model verification for the Spar platform was carried out by considering the OC3-Hywind Spar buoy [364], as this data is openly accessible and there is no data available for 10MW Spar . The comparison of the hydrodynamic wave excitations from linear diffraction is shown in Fig. 5-11. The actual figures of the results extracted from Jonkman study [364] results obtained from SESAM analysis are plotted on top (black dotted lines). The hydrodynamic damping matrices from the linear radiation problem for modes of motion of the platform are shown as a function of the oscillation frequency

in Fig. 5-12. It can be seen that the shape and magnitude of the results achieved from SESAM software are similar to the results obtained from Jonkman [364]. The dotted lines are the outcome of the results of SESAM simulations.

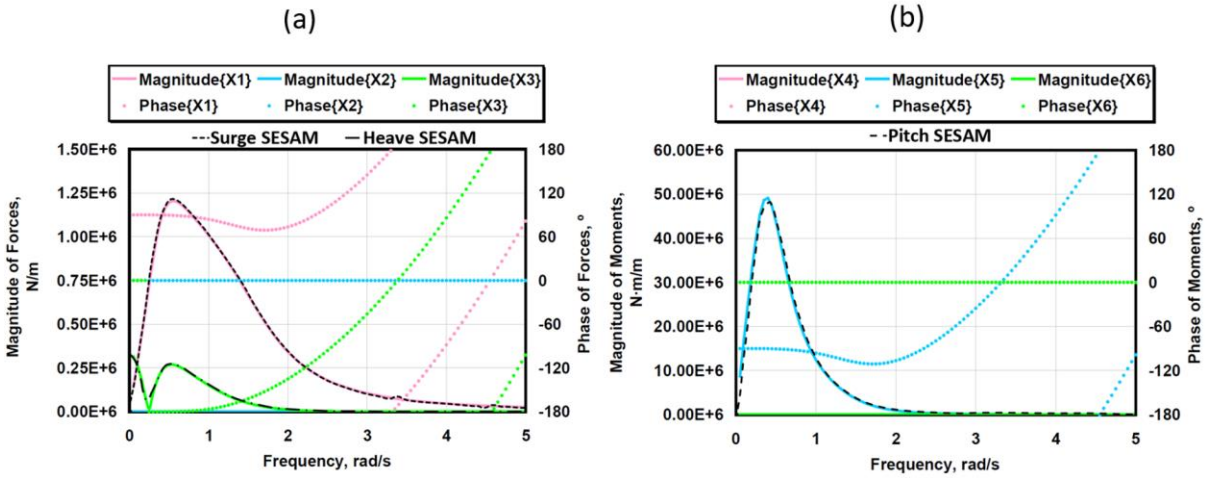


**Fig. 5-11** (a) Transitional and (b) Rotational Forces Per Unit Amplitude ( Actual Figures Of The Results Are From OC3-Hywind Spar buoy and SESAM Results (Black Dotted Lines) Plotted On For The Comparison)

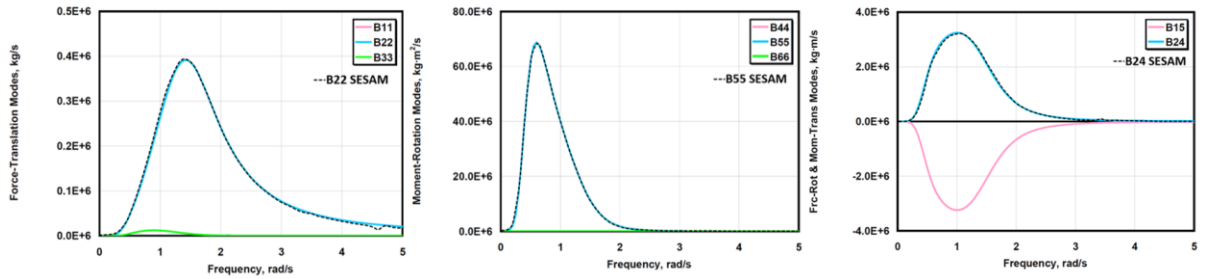


**Fig. 5-12** Hydrodynamics Damping Comparison (Actual Figures Of The Results Are From OC3-Hywind Spar buoy and SESAM Results (Black Dotted Lines)Plotted On For The Comparison)

## 5.4.2. Semi-Submersible

The SESAM software is used to validate the Semi-Submersible system to test against the published results from Johannes George study [189] who is evaluated the platform behaviour of a scaled-up a 5MW Semi-Submersible system to 7.5 MW and 10MW systems and then reduced the draft of scaled system. The George study simulated the model using FAST 8. Turbulent wind flow files were generated using TurbSim, whilst stochastic inflow turbulence code and the computations of WADAM are applied to provide inputs for the HydroDyn module of FAST.

The structural properties of a 10MW reduced draft (10MW-RD) Semi-Submersible model are very close to that of George's designed platform. The total mass of the George model structure, incorporating the mass of the wind turbine and blasting, is 26,988 tons, compared to 26,679 tons as calculated in this study using hydrostatic calculations. The variance between the two is 1%. Additionally, there is a 1.5% disparity in the COG between the two models.

Three studless chain mooring lines are used to fix the FOWT to the seabed; the diameter of lines is 107 mm each, with a weight of 229 kg/m. Free decay tests are considered to verify the validation. The comparison of the surge, heave and pitch motion responses obtained from SESAM simulation plotted on top of the figures of results from George study are shown in Fig. 5-13 to Fig. 5-15.

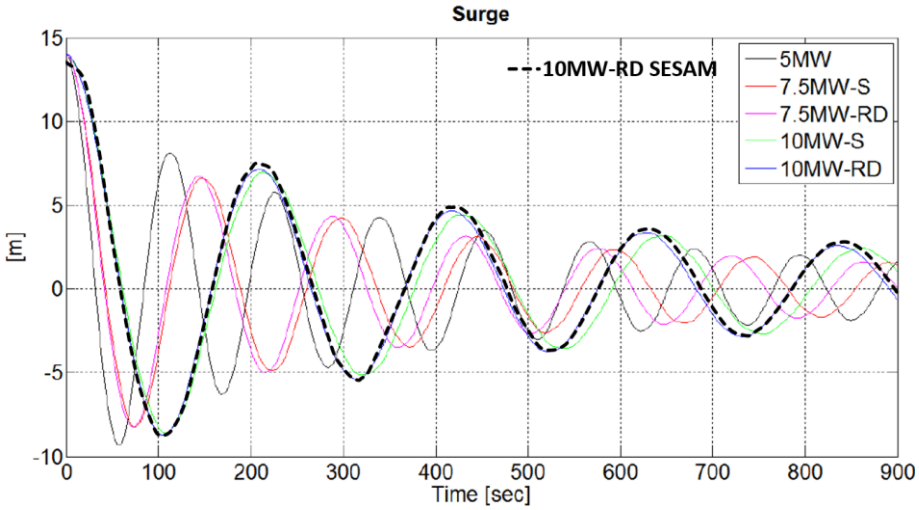


**Fig. 5-13** Surge Motion Response Comparison (Actual Figures of The Results Are from George study and SESAM Results (Black Dotted Lines) Plotted on For the Comparison)

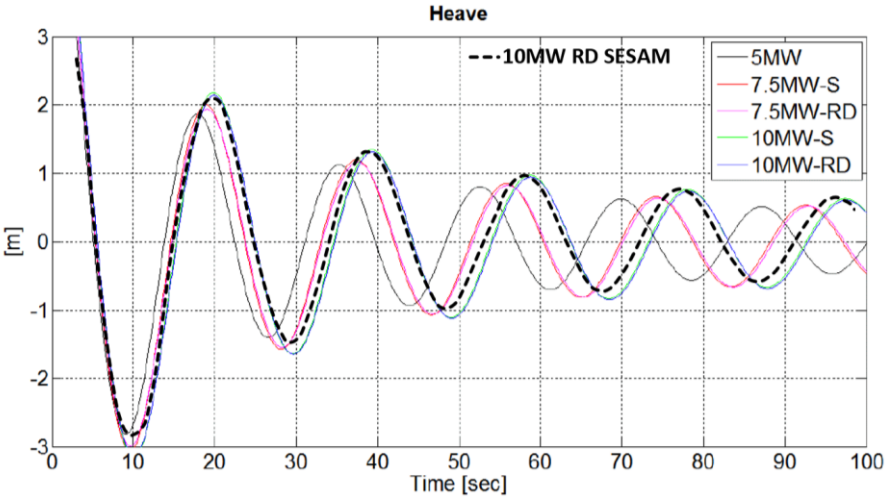


**Fig. 5-14** Heave Motion Response Comparison (Actual Figures of The Results Are from George study and SESAM Results (Black Dotted Lines) Plotted on For the Comparison)

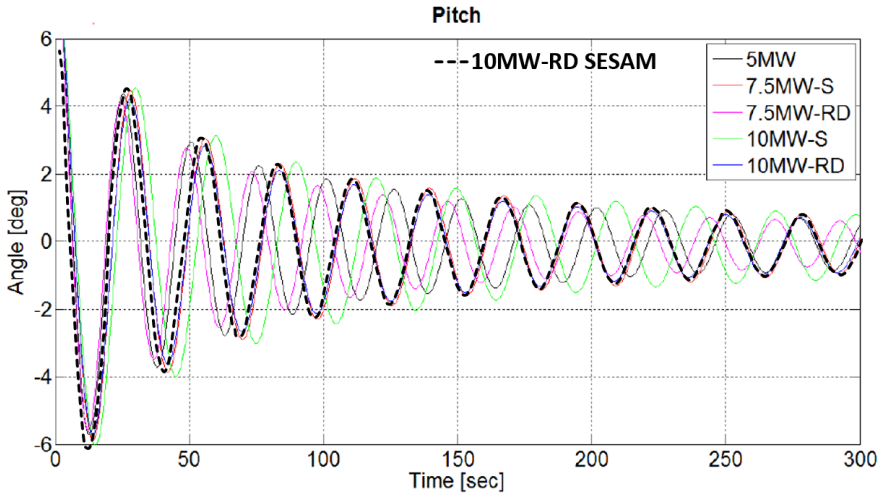


**Fig. 5-15** Pitch Motion Response Comparison (Actual Figures of The Results Are from George study and SESAM Results (Black Dotted Lines) Plotted on For the Comparison)

Comparing the heave and pitch motion responses in Fig. 5-14 and Fig. 5-15 showed that the SESAM model's amplitude is minimally higher than the George model. In general, agreement between results was excellent across the motion responses. Although the damping is similar, the natural frequencies of the models are differed. The surge natural frequency of the model simulated in SESAM has approximately a 2.1% greater than the George model similarly the differences between two models heave and pitch natural frequencies are 2.31% and 2.89% respectively. This is due to weight differences between the SESAM and George model, as the George model is slightly heavier. This weight variance is due to differences in the discretisation of the model.

### 5.4.3. TLP

This study considered the 10 MW TLB Transported design from Aina Crozier have been developed by applying the static design process where used Iterative Design Process by reproducing the MIT TLP properties from Tracy [421], which are also summarized in Matha [491]. Fig. 5-16 shows the platform RAOs for TLP Transported (green line) calculated in frequency domain (WADAM) from Aina Crozier thesis study [153] with comparison of the results obtained from the TLP modelled scaled up in this study and run in SESAM (black dotted lines). The original figures are copied from the Aina Crozier thesis study and the SESAM results are plotted on top. By adopting the TLP design from Aina Crozier's study, the results demonstrate a strong correlation between the numerical analyses.

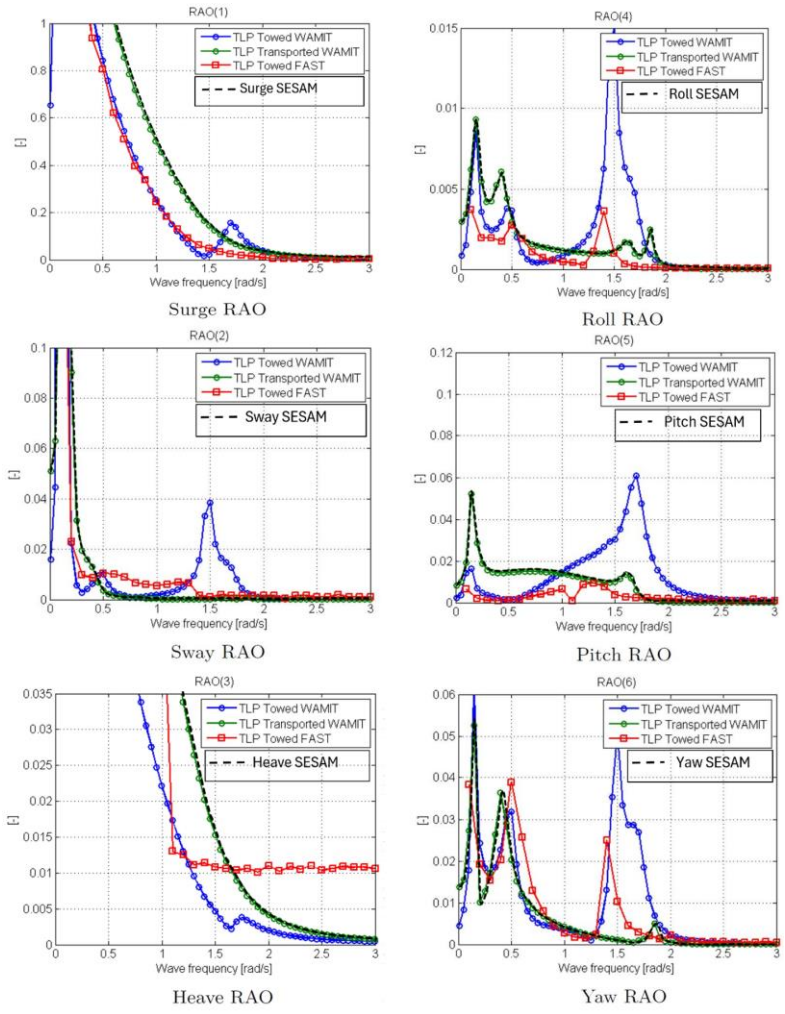


**Fig. 5-16** Comparison of the Model RAO Simulated in HydroD SESAM with Response Amplitude Operators of TLP Transported Model Simulated by Aina Crozier

## 5.5. Free Decay Test

In a manner similar to the methodology described in section 4.4.6, experiments were carried out to investigate the primary natural frequencies and damping ratios of Semi-Submersible, Spar, and TLP platforms along with their mooring lines through free decay tests. These tests involved monitoring the decay of motion in all six degrees of freedom for the mentioned platforms by initiating displacements in translational and rotational movements using specified forces at the beginning of simulations. The procedure adopted and the methodology employed to determine the natural frequency and damping ratio resemble those explained for the TLB platform in section 4.4.6. Fig 5-17 and Fig. 5-18 illustrate the translational and rotational degrees of freedom for the Semi-Submersible, Spar, and TLP platforms. The natural period and damping ratio of platforms are calculated from free decay test illustrate in Table 5-7.

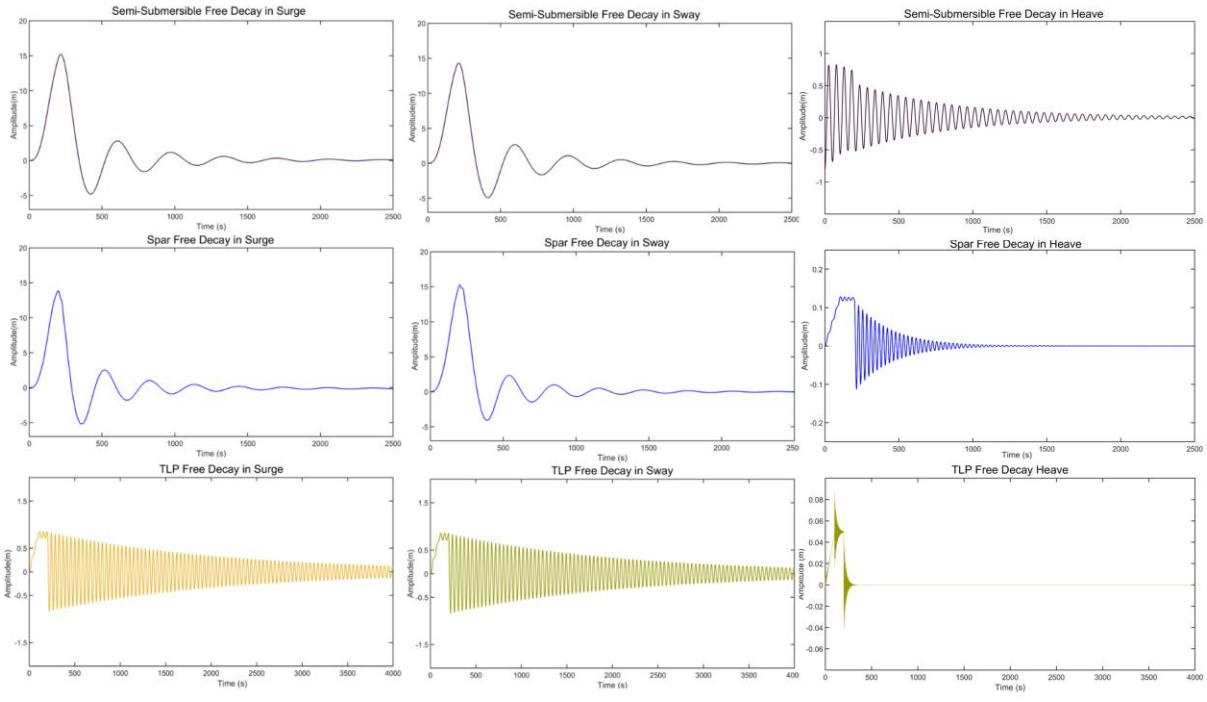


**Fig 5-17** Translational Free Decay Test for Semi-Submersible, Spar, and TLP Platforms

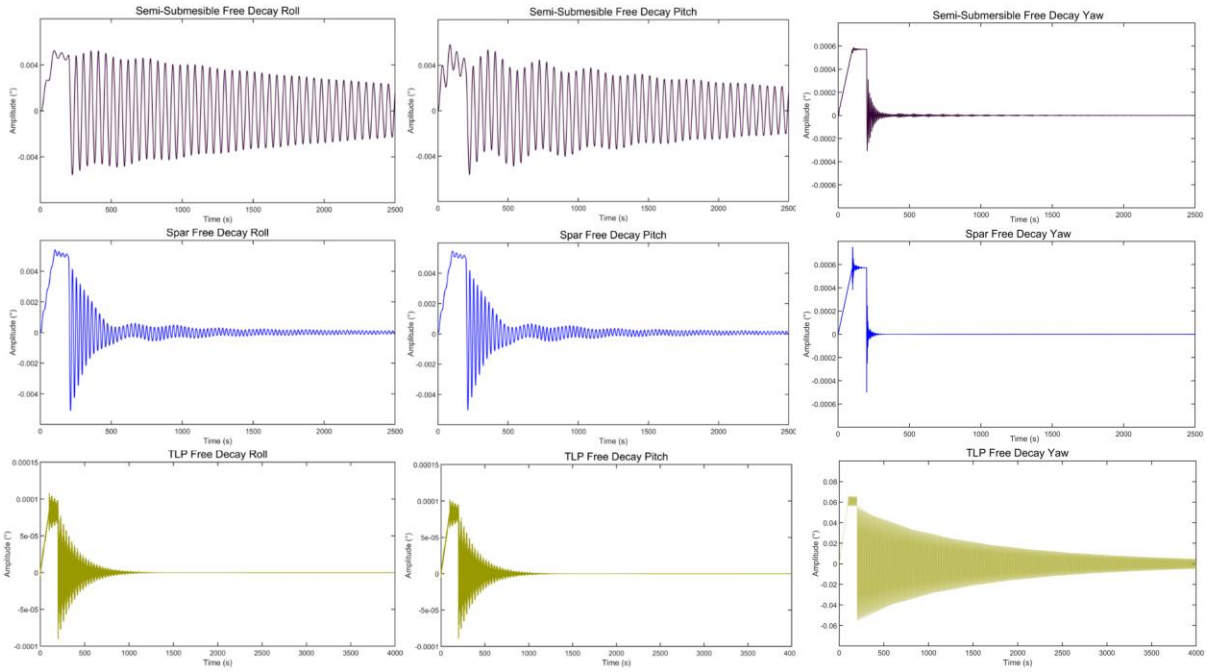


**Fig. 5-18** Rotational Free Decay Test for Semi-Submersible, Spar, and TLP Platforms

**Table 5-7** Natural Frequency (Hz) and Damping Ratio

| Natural Frequency (Hz) | | | | | | |
|---|---|---|---|---|---|---|
| | Surge | Sway | Heave | Roll | Pitch | Yaw |
| Semi-Submersible | 0.0080 | 0.0088 | 0.0661 | 0.0571 | 0.0582 | 0.2992 |
| Spar | 0.0109 | 0.0269 | 0.1142 | 0.0123 | 0.1102 | 0.1571 |
| TLP | 0.0757 | 0.0731 | 2.0944 | 1.5708 | 1.5708 | 0.4833 |
| **Damping Ratio** | | | | | | |
| | Surge | Sway | Heave | Roll | Pitch | Yaw |
| Semi-Submersible | 0.1285 | 0.1331 | 0.0450 | 0.0172 | 0.0297 | 0.0836 |
| Spar | 0.1271 | 0.1373 | 0.0511 | 0.0716 | 0.0719 | 0.1120 |
| TLP | 0.0234 | 0.0232 | 0.0191 | 0.0704 | 0.0704 | 0.0261 |

The Semi-Submersible structure typically exhibits low natural frequencies, indicating a high degree of structural flexibility and an extended oscillation period. Notably, its highest natural frequency is observed in yaw, suggesting a relatively rigid rotation around the vertical axis compared to other movements. In contrast, the Spar structure showed similarities with the Semi-Submersible in terms of natural frequencies but demonstrates slightly higher frequencies in surge, sway, heave, and pitch. This design feature enhances stability in heave and pitch, emphasizing a focus on vertical and pitch stability. On the other hand, the TLP displayed significantly higher natural

frequencies in heave, roll, and pitch due to the stiffness provided by its tensioned legs. While TLP exhibits lower frequencies in surge and sway, indicating increased flexibility in horizontal movements, it is overall the stiffest among the three structures, emphasizing a design aimed at minimizing vertical and rotational displacements.

Moreover, the Semi-Submersible structure is characterized by higher damping ratios in surge and sway, suggesting greater energy dissipation in these horizontal motions. Conversely, it shows lower damping in heave, roll, and pitch, indicating less damping in these modes and contributing to longer oscillations. The Spar structure demonstrates slightly higher damping ratios across various motions compared to the Semi-Submersible, particularly in roll and pitch, implying enhanced stability in these modes. In contrast, the TLP generally exhibits lower damping ratios, especially in surge, sway, and Heave, indicating reduced energy dissipation and the potential for longer oscillations in these modes. Higher damping in roll and pitch compared to heave suggests a design focus on minimizing rotational movements.

The distinctive design characteristics of each structure align with their specific stability requirements. TLP necessitates higher stiffness, resulting in elevated natural frequencies in vertical and rotational motions. Semi-Submersibles, due to their flexibility, showcased lower natural frequencies and higher damping ratios in horizontal motions. Spar platforms strike a balance between Semi-Submersibles and TLP, featuring intermediate natural frequencies and damping ratios to ensure stable operations in deeper waters.

## 5.6. Environmental Conditions

For specific design of the floater operational area, pre-defined design load cases (DLCs) are required to benchmark the response and performance characteristics. The platforms are expected to be deployed in the Northern North Sea, with a water depth of 110m. For this location, the DNVGL design standard specifies several Design Load Cases (DLC) [441]. Considering all the load cases prescribed by the design standard for this preliminary load analysis is unnecessary. Instead, this study aims to benchmark the TLB and compare it with three platforms by utilizing the ultimate load type during survival and operational conditions. The environmental conditions remain consistent with those outlined in section 4.4.7.

For the purpose of conducting a benchmarking study, two Distinct Load Cases (DLCs) were selected. DLC1.1 and DLC6.1a were chosen to represent operational conditions, while DLC6.1a and DLC6.2b were chosen to represent survival conditions (refer to Table 4-27 and Table 4-33). The parked with fault mooring lines scenario is neglected. The summary of the combined DLC illustrate in Table 5-8.

**Table 5-8** Summary of Design Load Combinations

| DLC | Wind | | Wave | | | Current |
|---|---|---|---|---|---|---|
| | Model | Speed (m/s) | Model | $H_s$ (m) | $T_p$ (s) | Max Speed at SWL (m/s) |
| **1.1** | NTM | 11.4 | NSS | 4.2 | 9.4 | $U_{Wind,50yr}$ = 0.442 |
| **1.6a** | NTM | 18 | SSS | 8.8 | 13.5 | |
| **6.1a** | EWM Turbulence | 51.6 | ESS | 16.8 | 16.6 | $U_{Tidel,50yr}$ = 1.42 |
| **6.2a** | EMW Steady | 51.6 | ESS | 16.8 | 16.6 | |

## 5.7. Results and Discussion

Three-hour time domain simulations were conducted to accurately assess the impact of design load effects on the operational performance of Semi-Submersible, Spar, and TLP FOWT platforms within defined DLCs. These platforms were designed to accommodate a 10MW DTU wind turbine and were situated in the environmental conditions of the Northern North Sea at a water depth of 110 meters. Although the platforms exhibit distinct characteristics, the study focused on analysing their motion and dynamic tension responses. The results, which will be presented in detail, will be compared based on their peak responses and evaluated in accordance with relevant industry guidelines and standards, as described in section 2.9.

### 5.7.1. Operational Condition (Power Production)

DLC1.1 represents a Normal Sea State (NSS), whilst DLC1.6a is used to represent a Severe Sea State (SSS) to investigate the FOWTs performance during power production state.

Table 5-9 provides a summary of the maximum motion responses and maximum tension of the primary line for Semi-Submersible, Spar, TLP, and TLB platforms when subjected to operational design load cases. In Fig. 5-19, a statistical comparative exploration is presented the maximum sway, heave, roll, pitch, and yaw responses of Semi-Submersible, Spar, TLP, and TLB FOWTs under operational conditions. Additionally, Fig. 5-20 displays the time history of sway, heave, roll, pitch, and yaw motion responses for Semi-Submersible, Spar, TLP, and TLB platforms under operational conditions. Furthermore, Fig. 5-21 illustrates the surge motion response and dynamic tension time history of the most loaded line for Semi-Submersible and Spar platforms under operational conditions, while Fig. 5-22 presents the time history of surge motion response and dynamic tension for TLP and TLB platforms under similar operational conditions.

**Table 5-9** Maximum Motions Responses & Most Loaded Line Maximum Tension Summary Statistics of Semi-Submersible, Spar, TLP, and TLB Platforms under Operational Conditions

| | | DLC1.1 | | | | | DLC1.6a | | | | |
|---|---|---|---|---|---|---|---|---|---|---|---|
| | | Time (s) | Max | Min | Mean | SD | Time (s) | Max | Min | Mean | SD |
| Semi-Submersible | Surge(m) | 8050 | 65.3 | -0.08 | 61.04 | 4.70 | 6776 | 90.38 | 0.00 | 79.21 | 6.23 |
| | Sway(m) | 9893 | 0.49 | -0.53 | -0.04 | 0.22 | 6479 | 1.18 | -1.3 | 0.03 | 0.48 |
| | Heave(m) | 2035 | 0.31 | -0.31 | -0.03 | 0.12 | 7050 | 2.14 | -2.1 | -0.03 | 0.58 |
| | Roll (°) | 4128 | 0.36 | -0.33 | 0.00 | 0.15 | 4537 | 1.28 | -1.2 | 0.03 | 0.45 |
| | Pitch (°) | 7374 | 2.66 | -1.88 | 0.20 | 0.91 | 5798 | 5.36 | -5.4 | -0.01 | 1.86 |
| | Yaw (°) | 1161 | 0.99 | -0.85 | 0.06 | 0.27 | 8601 | 3.66 | -3.6 | 0.20 | 0.82 |
| | Tension(t) | 8050 | 146 | 102 | 122 | 6.4 | 6776 | 927 | 0.1 | 267 | 147 |
| Spar | Surge(m) | 8043 | 50.8 | 48.5 | 49.4 | 0.3 | 6776 | 68.98 | 59.1 | 64.24 | 1.37 |
| | Sway(m) | 4302 | 0.24 | -0.19 | -0.02 | 0.05 | 5504 | 0.97 | -0.8 | 0.03 | 0.24 |
| | Heave(m) | 7518 | 0.25 | -0.21 | 0.00 | 0.06 | 10791 | 1.87 | -1.7 | 0.04 | 0.50 |
| | Roll (°) | 2779 | 0.33 | -0.32 | 0.00 | 0.10 | 2779 | 1.07 | -1.1 | 0.01 | 0.31 |
| | Pitch (°) | 1741 | 2.34 | -2.41 | 0.07 | 0.68 | 1741 | 4.91 | -5.1 | 0.14 | 1.44 |
| | Yaw (°) | 7909 | 0.78 | -0.77 | 0.02 | 0.16 | 7909 | 3.28 | -3.2 | 0.08 | 0.67 |
| | Tension(t) | 8043 | 125 | 49 | 120 | 7 | 6776 | 748.6 | 589 | 656.6 | 18.3 |
| TLP | Surge(m) | 4911 | 3.57 | -3.76 | 0.41 | 0.88 | 3374 | 18.61 | -15 | 0.76 | 6.86 |
| | Sway(m) | 2721 | 0.39 | -0.34 | 0.00 | 0.09 | 6103 | 0.87 | -0.8 | 0.00 | 0.26 |
| | Heave(m) | 4911 | 0.00 | -0.19 | -0.01 | 0.02 | 3374 | 0.00 | -2.15 | -0.42 | 0.38 |
| | Roll (°) | 529 | 0.01 | 0.00 | 0.00 | 0.00 | 7822 | 0.05 | -0.04 | 0.00 | 0.01 |
| | Pitch (°) | 4911 | 0.04 | -0.03 | 0.00 | 0.00 | 3374 | 0.89 | -0.8 | 0.02 | 0.15 |
| | Yaw (°) | 3361 | 0.22 | -0.22 | 0.00 | 0.04 | 4560 | 1.51 | -1.2 | 0.06 | 0.34 |
| | Tension(t) | 4911 | 1284 | 120 | 226.4 | 96.5 | 3374 | 2172 | 88.1 | 434.0 | 295 |
| TLB | Surge(m) | 614 | 0.79 | -0.58 | 0.02 | 0.20 | 614 | 1.14 | -1 | 0.00 | 0.29 |
| | Sway(m) | 10674 | 0.04 | -0.04 | 0.00 | 0.01 | 3887 | 0.08 | -0.1 | 0.00 | 0.02 |
| | Heave(m) | 614 | 0.06 | -0.54 | -0.10 | 0.06 | 614 | 0.14 | -0.8 | -0.08 | 0.09 |
| | Roll (°) | 10674 | 0.06 | -0.06 | 0.00 | 0.01 | 3887 | 0.14 | -0.14 | -0.01 | 0.03 |
| | Pitch (°) | 614 | 1.24 | -0.91 | 0.08 | 0.30 | 614 | 1.61 | -1.6 | -0.04 | 0.42 |
| | Yaw (°) | 10436 | 0.49 | -0.36 | 0.03 | 0.12 | 2378 | 1.27 | -1.3 | -0.07 | 0.32 |
| | Tension(t) | 614 | 987 | 225 | 505.6 | 108 | 614 | 1657 | 97.1 | 692.7 | 216 |

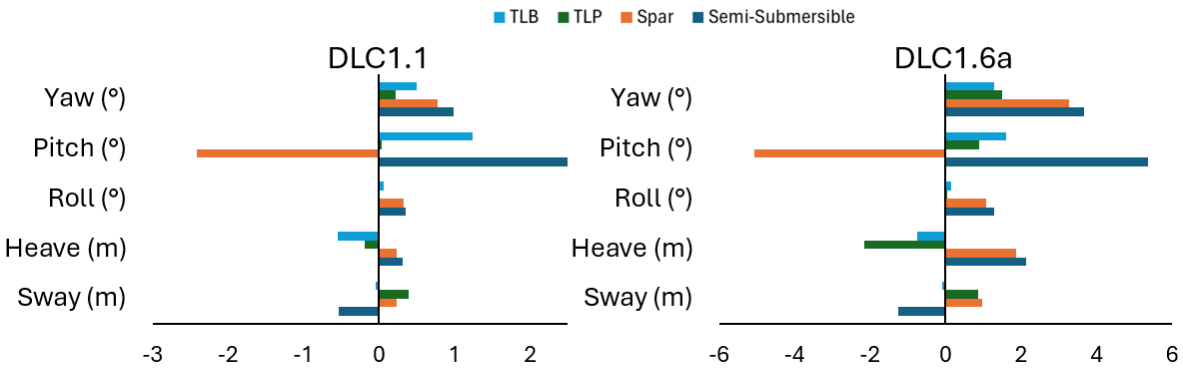


**Fig. 5-19** Statistical Comparison of Sway, Heave, Roll, Pitch, and Yaw Maximum Motion Responses of Semi-Submersible, Spar, TLP, and TLB Platforms Under Operational Design Load Cases

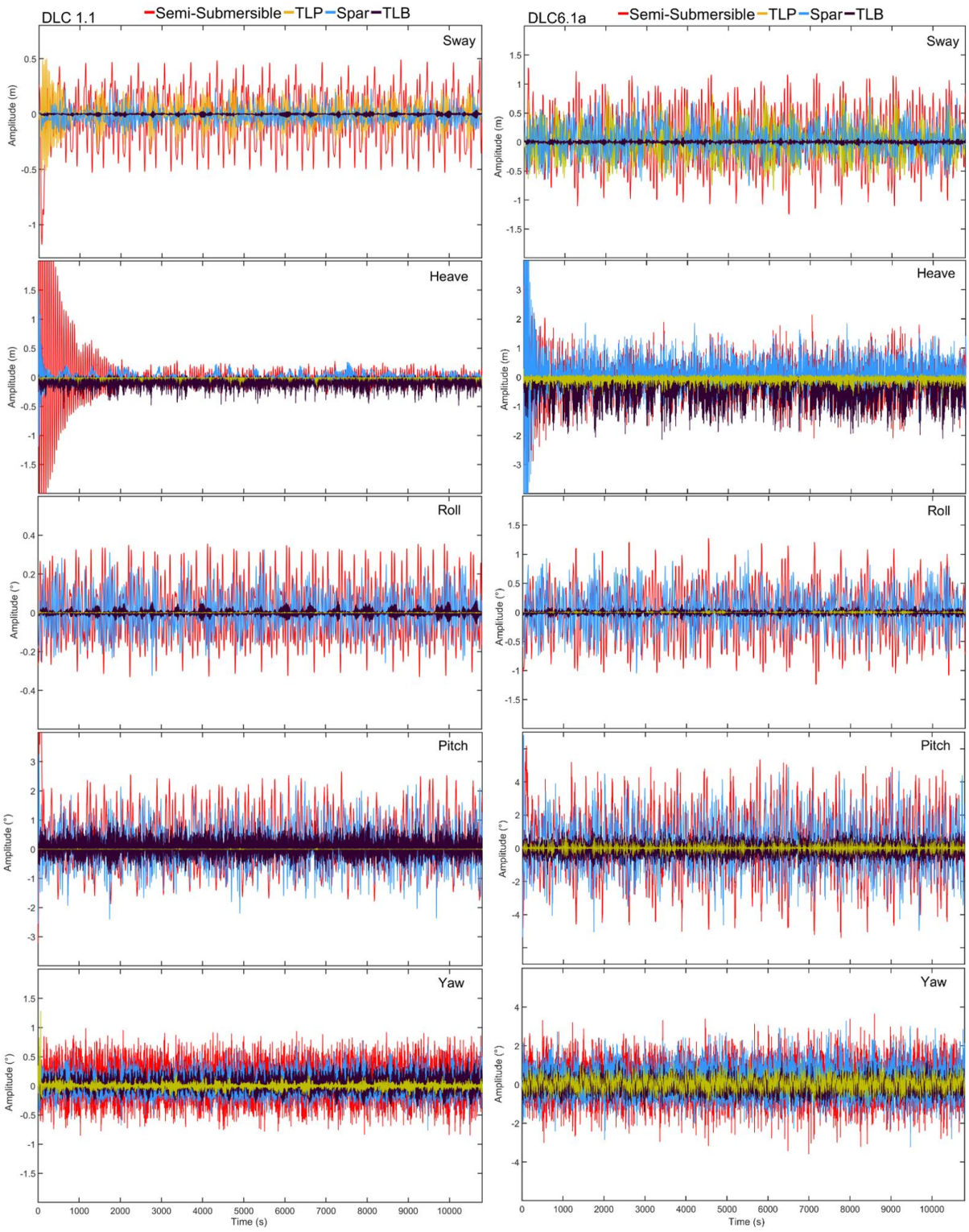


**Fig. 5-20** Time History of Sway, Heave, Roll, Pitch, and Yaw Motion Response for Semi-Submersible, Spar, TLP, and TLB under Operational Conditions (DLC1.1 (LHS) and DLC1.6a (RHS))

According to the data presented in Table 5-9, the highest dynamic tension of the most loaded line experienced by the Semi-Submersible and Spar platforms is primarily influenced by the maximum surge motion response. In contrast, the maximum tension observed in the TLP and TLB platforms is associated with the maximum surge, heave, and pitch motion responses, aligning with the peak tension levels. The instances of maximum responses are highlighted in green within Table 5-9.

The data presented in Table 5-9, Fig. 5-19 and Fig. 5-20 indicated that there was minimal sway and roll responses observed under both DLCs as a result of the collinear environmental forces acting on the structure.

The Semi-Submersible and Spar platforms exhibited increased maximum heave response when subjected to DLC1.6a conditions, which is expected due to their design, which allows for vertical compliance indicating different wave or current conditions affecting these types of platforms compared to TLB platform. In contrast, TLP platforms demonstrated maximum negative heave (set down) attributed to significant surge offset under DLC1.6a.

The Semi-Submersible and Spar Platforms consistently exhibited significant pitch motions in both DLCs. However Semi-Submersible maximum pitch response is 10% higher than that for Spar likely due to the existence of multiple columns and pontoons for the Semi-Submersible design to achieve stability compared with Spar platforms where the stability provided by the deep draft and the weight distribution.

The yaw motions are generally minimal but show more variability in DLC6.1a. This suggests different environmental conditions and mooring system responses affecting the rotational stability of the structures.

Overall, the results suggest that the Spar and Semi-Submersible structures exhibited higher motion responses than TLP and TLB platforms. The TLP and TLB platforms generally showed moderate responses across all motion types. These differences are influenced by the design and mooring configurations of each structure, affecting their responses to the dynamic loading conditions represented by DLC1.1 and DLC6.1a.

The Semi-Submersible platform recorded higher motion responses in both DLCs than the Spar platform motion responses, likely due to the existence of multiple columns

and pontoons for the Semi-Submersible design to achieve stability compared with a buoyant cylinder with a deep draft.

Apart from surge, the TLP and TLB motion responses are similar under normal sea state conditions. The TLP surge motion response is higher than for the TLB design, especially in DLC1.6a, while the platform operates in a severe sea state. Due to the TLP platform design characteristics, which is compliant, precluding motions horizontally (surge and sway) and rotationally (yaw) and impact of severe sea state, surge, sway, and yaw motion responses of the TLP platform is higher than those for the TLB platform. As the TLP is designed to be restrained in heave, roll, and pitch, the maximum responses achieved for TLP in these directions are smaller than those for the TLB.

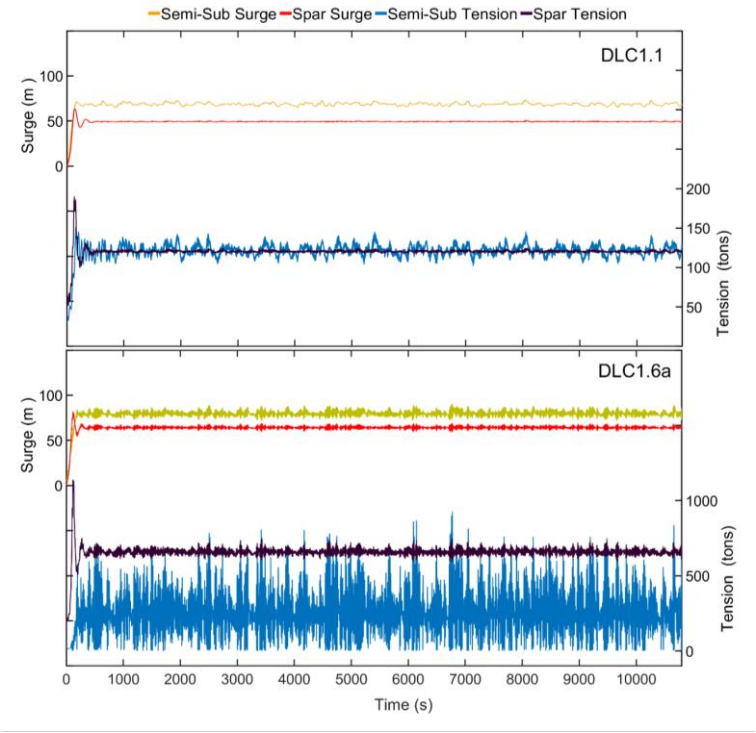


**Fig. 5-21** Time History of Surge Motion Response and Most Loaded Line Dynamic Tension for Semi-Submersible and Spar Platforms under Operational Conditions

According to Fig. 5-21, the Semi-Submersible showed a consistent surge around 61 m with fluctuation slightly more than Spar platform, the Spar showed a slightly lower surge, consistently around 49 m, with minimal fluctuations indicating stable performance under DLC 1.1 event. The Spar exhibited a tension that hangs around 120 tons with some minor oscillations. This suggests that the mooring lines are under

a steady load with small dynamic variations. The line representing the mean tension response for the Spar platform is close to that for Semi-Submersible under DLC1.1. However, the Semi-Submersible platform has higher fluctuations from the mean values. In challenging power production environmental scenario (DLC1.6a), both Semi-Submersible and Spar platforms exhibit consistent surge response similar to that observed under DLC1.1. The mean surge response of the Semi-Submersible platform remains at approximately 79 m, while that of the Spar platform is around 64 m. This indicates that the lateral displacement of both structures remains relatively stable even when exposed to more severe loading conditions. The Semi-Submersible platform showed a surge response with a higher maximum magnitude compared to the Spar platform, which is attributed to its larger water plane area resulting from the presence of multiple columns and pontoons. The tension response of the Semi-Submersible platform demonstrates greater fluctuations with a higher maximum magnitude. The average value of the dynamic tension response for the Semi-Submersible platform surpasses that of the Semi-Submersible platform, likely due to higher mean surge response of Semi-Submersible and having a shorter mooring line length than Spar platform, resulting in increased tension on the line.

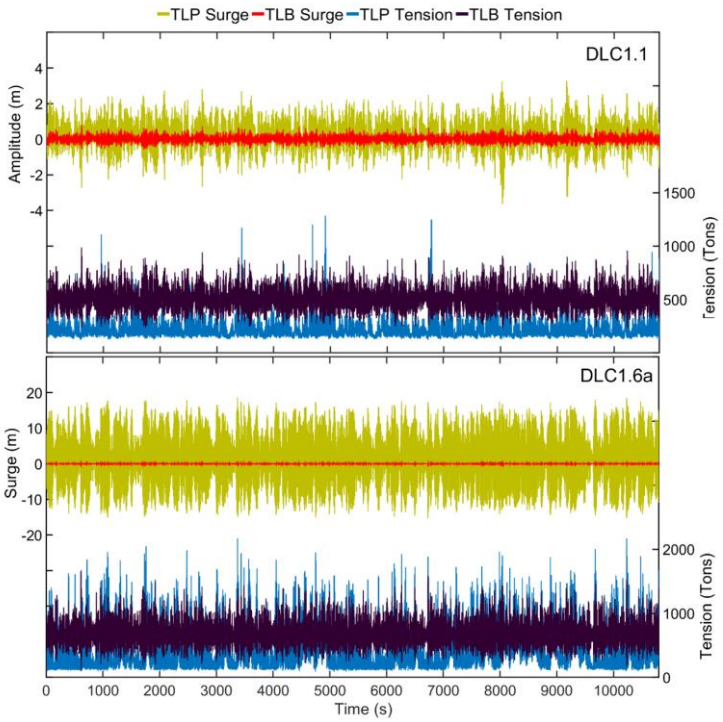


**Fig. 5-22** Time History of Surge Motion Response and Most Loaded Line Dynamic Tension for TLP and TLB Platforms under Operational Conditions

The platforms that use catenary mooring systems have higher surge responses than those with taut mooring systems or tendons and show different low-frequency motion behaviour compared to the high-frequency motions experienced by the stiff-mooring stabilised platforms. TLB and TLP surge responses are dominated by high-frequency motion, whilst the TLP has more oscillation due to the nature of its surge motion; however, the mean surge offset is almost similar. The TLB with stiff mooring characteristics results in low-magnitude motion response at high frequency. When operating in harsh environmental conditions, the magnitude of the surge response can be seen to increase significantly for TLP platform. The TLP platform has high frequency with elevated magnitude surge response. The TLB system is designed to limit the response motion, whilst the TLP is a compliant design platform in the surge direction; however, the mean line surge motion response of both platforms is closely matched. The platform design characteristics and its mooring system design are essential to platform surge responses.

The most heavily loaded tether on the TLP platform displayed an average tension of approximately 226 tons, with peak tensions reaching as high as 1284 tons under DLC1.1. Similarly, the most loaded line on the TLB showed an average tension of around 506 tons, with a maximum recorded tension of 987 tons under the same conditions. However, when subjected to DLC1.6a, the maximum tension magnitude increased by 40% for both platforms. TLPs are designed to maintain stability with minimal vertical movement, resulting in lower average tensions in their mooring lines. Environmental factors can lead to significant peak loads on TLP mooring lines, resulting in higher tension magnitudes. Conversely, TLB mooring lines with taut mooring system tend to experience higher average tensions due to the buoy's design, which allows it to move in response to waves and currents more than TLP is certain directions. Peak tensions in TLB mooring lines were lower than those in TLP because the design permits more movement, dispersing forces rather than concentrating them on the mooring lines. In summary, the distinct design and motion response characteristics of TLP and TLB systems account for the variations observed in average tension and peak tension magnitudes in their respective mooring lines.

To comply with DNV regulations, an assessment of the designated criteria detailed in section 2.9 is carried out. The design tension is calculated and illustrate in Table 5-10 by utilizing the average and maximum line dynamic tension values from Table 5-9,

applying Eq. (8), and incorporating the ultimate limit state safety factors designated for the standard safety class in Table 2-8. Subsequently, the safety factor can be determined by employing Eq. (26) as illustrated in Table 5-11.

**Table 5-10** Characteristic Capacity of The Mooring Lines and The Design Tension Calculations for Each Platform under Operational Condition DLC1.6a event

| Platform | $S_C\ (N)$ | $T_d\ (N)$ | |
|---|---|---|---|
| | | DLC1.1 | DLC1.6a |
| Semi-Submersible | 2.60E+07 | 1.96E+06 | 1.47E+07 |
| Spar | 2.60E+07 | 1.61E+06 | 9.95E+06 |
| TLP | 6.06E+07 | 2.10E+07 | 3.54E+07 |
| TLB | 3.82E+07 | 1.47E+07 | 2.54E+07 |

**Table 5-11** The Safety Factors for Each Platform Mooring Line under Operational Condition DLC1.6a event

| Platform | Safety Factor | |
|---|---|---|
| | DLC1.1 | DLC1.6a |
| Semi-Submersible | 13.26 | 1.76 |
| Spar | 16.17 | 2.61 |
| TLP | 2.88 | 1.71 |
| TLB | 2.60 | 1.51 |

The safety factors of platforms mooring lines comply with DNV regulation for mooring of FOWTs criteria. The results obtained for Semi-Submersible, Spar, and TLP from 3-hour environmental conditions were used to determine the maximum motion response and mooring line tension for operational conditions (DLC1.1 & DLC1.6a) satisfy both the rule-based limitations on motion responses as set by DNVGL-RP-0286 [440] and the design criterion for ULS as given in DNV-OS-J103 [441] described under Section 2.9.

## 5.7.2. Power Production

In order to assess the electrical power generation outputs of Semi-Submersible, Spar, TLP, and TLB platforms, Fig. 5-23 and Table 5-12 illustrate the power generation of these platforms during DLC1.1 conditions. Similarly, Fig. 5-24 and Table 5-13 the power generation under DLC6.1a conditions for comparison. The electrical generator's output in SIMA is determined by multiplying the generator's commanded torque by its rotational speed by assuming a generator efficiency of 100%.

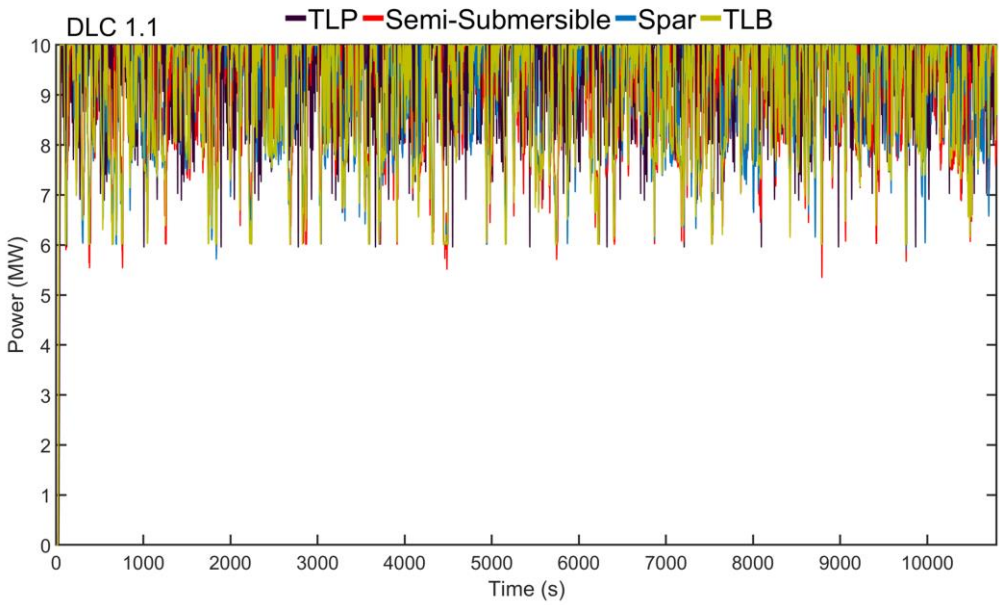


**Fig. 5-23** Power Output Time History of Semi-Submersible, Spar, TLP, and TLB Platforms under DLC1.1 Event

**Table 5-12** Electrical Generator Output (MW) of Platforms under DLC1.1 Event

| | Time | Max | Min | Mean | SD |
|---|---|---|---|---|---|
| Semi-Submersible | 8791 | 10 | 5.340 | 8.909 | 1.1 |
| Spar | 1838 | 10 | 5.708 | 8.932 | 1.1 |
| TLP | 1007 | 10 | 5.949 | 9.387 | 0.7 |
| TLB | 4480 | 10 | 6.000 | 8.951 | 1.1 |

The TLP shows the highest mean value (9.387 MW), suggesting that it experiences consistently higher mean electrical generating followed by the TLB, Spar, and Semi-Submersible, which have similar mean values around 8.9 MW under mild environmental condition. The TLP has the lowest standard deviation (0.7 MW), indicating that its measurements are more consistent and less variable. The other

platforms (Semi-Submersible, Spar, and TLB) have higher standard deviations (1.1 MW), indicating more variability around their mean values due to their pitch responses.

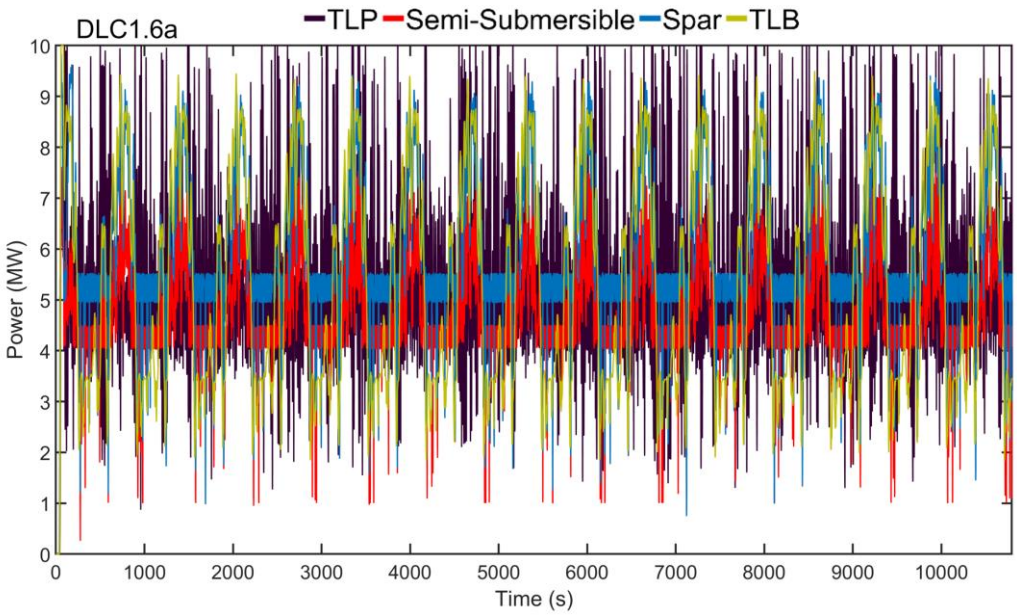


**Fig. 5-24** Power Output Time History of Semi-Submersible, Spar, TLP, and TLB Platforms under DLC1.6a Event

**Table 5-13** Electrical Generator Output (MW) of Platforms under DLC1.6a Event

| | Time | Max | Min | Mean | SD |
|---|---|---|---|---|---|
| Semi-Submersible | 2233 | 9.2 | 0.949 | 4.742 | 1.0 |
| Spar | 7122 | 9.4 | 0.747 | 6.018 | 1.3 |
| TLP | 958 | 10.0 | 0.873 | 5.493 | 1.6 |
| TLB | 10713 | 10.0 | 2.914 | 6.042 | 1.8 |

In severe sea conditions, the TLB and Spar platforms exhibit higher average power production levels (6.042 MW and 6.018 MW, respectively) compared to the Semi-Submersible platform, which has the lowest mean value (4.742 MW). This suggests that the environmental forces exerted on motion responses, particularly pitch motion, are more pronounced on the Semi-Submersible platform, leading to decreased power production. Furthermore, the power production of the TLP platform is reduced in harsh environmental conditions compared to mild conditions, as indicated by its higher maximum surge and heave motion responses in comparison to the TLB platform.

### 5.7.3. Survival Conditions (Parked (Idling))

An extreme sea state (ESS) with a significant wave height of 16.8m represents the survival condition wave model. Two wind models have been considered to describe the extreme wind model (EWM), one with the appearance of turbulence (DLC6.1a) and another with a steady profile (DLC6.2b). The maximum tidal speed of 1.42m/s at the surface level with 50-year return period is assumed to representing the current.

The study examines the performance of Semi-Submersible, Spar, TLP, and TLB systems under environmental design load scenarios. It identifies the maximum responses and dynamic tension of the most heavily loaded lines for comparison across different types of FOWTs supporting a 10MW wind turbine in a water depth of 110 meters in the Northern North Sea.

Table 5-14 displays the statistical summary of motion responses and line tension for Semi-Submersible, Spar, TLP, and TLB platforms during survival events, with and without wind turbulence (DLC6.1a and DLC6.2b, respectively). Fig. 5-25 presents a comparative analysis of the maximum sway, heave, roll, pitch, and yaw responses of these platforms under operational conditions. Additionally, Fig. 5-27 showcases the motion responses of Semi-Submersible, Spar, TLP, and TLB platforms under survival conditions using violin plots. Furthermore, Fig. 5-26 depicts the percentage difference in the impact of induced wind turbulence on the responses of Semi-Submersible, Spar, TLP, and TLB platforms.

In accordance with the maximum responses presented in Table 5-14, the Semi-Submersible and Spar platforms exhibit simultaneous peak surge and dynamic tension in the most heavily mooring line during survival design load scenarios, consistent with results observed under operational conditions. Conversely, the TLB platform demonstrates peak surge, pitch, and dynamic tension concurrently. Similarly, the TLP platform experiences peak surge, heave, pitch, and dynamic tension in the most heavily loaded line simultaneously.

The instances of coupled motion responses of the platforms highlighted in green in Table 5-14. This occurrence is attributed to the complex nature of the system, its configuration, and the mooring system configuration.

**Table 5-14** Maximum Motions Responses & Most Loaded Line Maximum Tension Summary Statistics of Semi-Submersible, Spar, TLP, and TLB Platforms under Survival Conditions

| | | DLC6.1a | | | | | DLC6.2b | | | | |
|---|---|---|---|---|---|---|---|---|---|---|---|
| | | Time (s) | Max | Min | Mean | SD | Time (s) | Max | Min | Mean | SD |
| Semi-Submersible | Surge(m) | 3431 | 117 | 0.0 | 95.31 | 6.30 | 3431 | 110.4 | 0.0 | 88.51 | 6.20 |
| | Sway(m) | 10434 | 1.97 | -1.91 | 0.01 | 0.85 | 10436 | 1.69 | -1.40 | -0.07 | 0.56 |
| | Heave(m) | 3416 | 2.80 | -2.47 | 0.15 | 0.68 | 6155 | 2.34 | -2.2 | 0.00 | 0.61 |
| | Roll (°) | 9398 | 2.45 | -2.41 | -0.20 | 0.84 | 10414 | 2.30 | -2.3 | 0.01 | 0.74 |
| | Pitch (°) | 3323 | 7.86 | -7.75 | 0.02 | 2.30 | 10420 | 7.30 | -7.3 | 0.54 | 2.37 |
| | Yaw (°) | 5215 | 6.65 | -6.54 | 0.46 | 1.50 | 7904 | 6.30 | -6.3 | 0.56 | 1.40 |
| | Tension(t) | 3431 | 1616 | 77.2 | 854.7 | 149 | 3431 | 1419 | 52.7 | 737 | 136 |
| Spar | Surge(m) | 6771 | 98.4 | 0.0 | 88.74 | 5.07 | 6771 | 91.93 | 0.0 | 82.99 | 4.57 |
| | Sway(m) | 7712 | 0.96 | -0.9 | 0.01 | 0.28 | 7713 | 0.92 | -0.8 | 0.04 | 0.24 |
| | Heave(m) | 4179 | 2.03 | -2.0 | 0.12 | 0.55 | 4179 | 1.83 | -1.8 | 0.03 | 0.51 |
| | Roll (°) | 2509 | 2.13 | -2.1 | -0.08 | 0.48 | 2509 | 2.07 | -2 | -0.15 | 0.41 |
| | Pitch (°) | 6257 | 6.64 | -6.7 | 0.03 | 1.75 | 6257 | 6.22 | -6.3 | 0.43 | 1.61 |
| | Yaw (°) | 4082 | 4.36 | -4.3 | 0.12 | 0.87 | 6927 | 4.17 | -4.1 | 0.07 | 0.86 |
| | Tension(t) | 6771 | 1561 | 924 | 1177 | 79 | 6771 | 1352 | 112 | 994 | 89.7 |
| TLP | Surge(m) | 2740 | 24.9 | -19.7 | 1.11 | 8.97 | 887 | 20.5 | -18 | 0.91 | 7.94 |
| | Sway(m) | 1946 | 1.64 | -1.64 | 0.00 | 0.53 | 1946 | 1.36 | -1.4 | 0.00 | 0.44 |
| | Heave(m) | 2740 | 0.00 | -4.85 | -0.87 | 0.77 | 887 | 0.00 | -4.56 | -0.93 | 0.83 |
| | Roll (°) | 1942 | 0.05 | -0.04 | 0.00 | 0.01 | 5588 | 0.05 | -0.04 | 0.00 | 0.01 |
| | Pitch (°) | 2740 | 1.82 | -1.53 | 0.02 | 0.27 | 887 | 1.52 | -1.4 | 0.02 | 0.25 |
| | Yaw (°) | 3485 | 3.33 | -3.27 | 0.19 | 0.68 | 3485 | 3.12 | -3.06 | 0.18 | 0.64 |
| | Tension(t) | 2740 | 4789 | 172 | 896 | 584 | 887 | 4572 | 170 | 970.1 | 634 |
| TLB | Surge(m) | 6097 | 2.19 | -2.16 | 0.02 | 0.34 | 6097 | 2.14 | -2.12 | 0.02 | 0.33 |
| | Sway(m) | 9620 | 0.26 | -0.26 | -0.01 | 0.05 | 9620 | 0.24 | -0.24 | -0.01 | 0.04 |
| | Heave(m) | 9975 | 0.25 | -2.63 | -0.16 | 0.17 | 9975 | 0.23 | -2.51 | -0.15 | 0.16 |
| | Roll (°) | 9620 | 0.36 | -0.40 | 0.00 | 0.07 | 9620 | 0.34 | -0.36 | 0.00 | 0.07 |
| | Pitch (°) | 6097 | 2.35 | -2.30 | 0.18 | 0.38 | 6097 | 2.22 | -2.19 | 0.06 | 0.35 |
| | Yaw (°) | 1735 | 2.65 | -2.64 | 0.33 | 0.55 | 1735 | 2.55 | -2.54 | 0.31 | 0.53 |
| | Tension(t) | 6097 | 3085 | -14.4 | 824.7 | 419 | 6097 | 2982 | -10.7 | 797.2 | 405 |

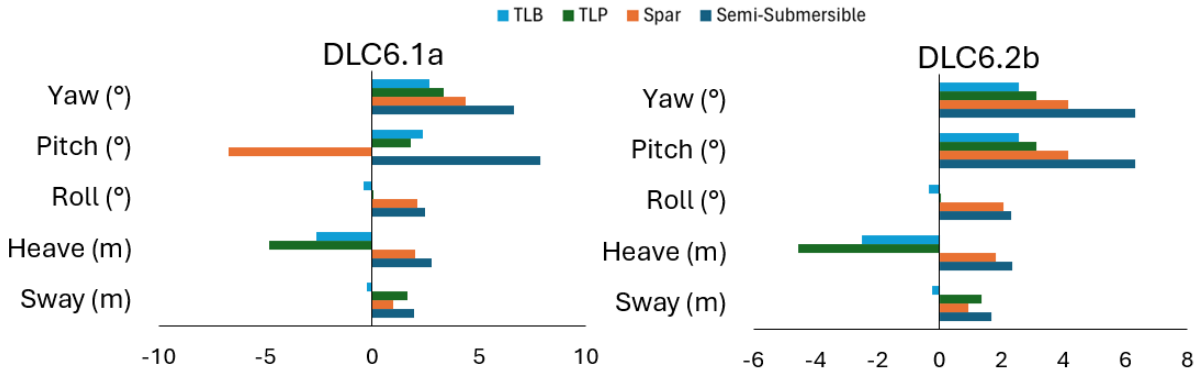


**Fig. 5-25** Statistical Six-degree Maximum Motion Responses of Semi-Submersible, Spar, TLP, and TLB Platforms Under Survival Design Load Cases

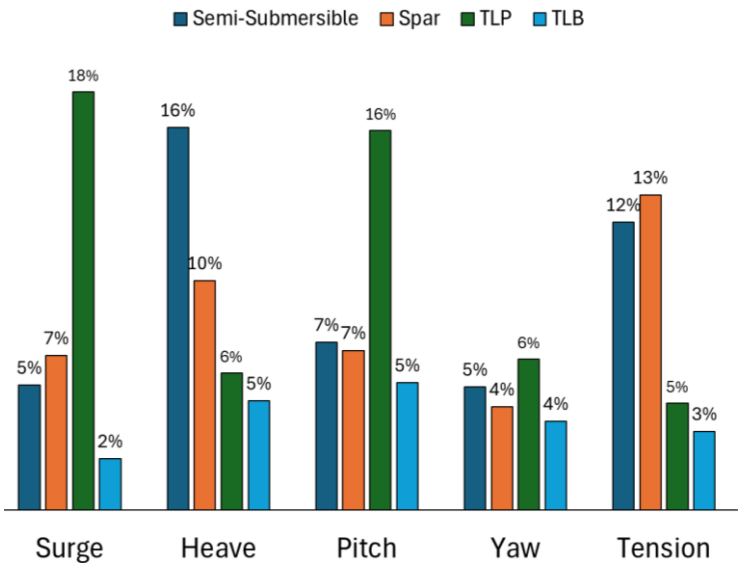


**Fig. 5-26** Comparison of Peak Motion Responses and Maximum Tension of the Most Heavily Loaded Mooring Line Differences between DLC6.1a and DLC6.2b for Semi-Submersible, Spar, TLP, and TLB Platforms

According to peak responses illustrated in Table 5-14, all platforms have higher responses under DLC6.1a compare with DLC6.2b. This due to the different wind model assumed for DLCs. Based on maximum responses presented in Table 5-14 and Fig. 5-25, it can be observed that TLP demonstrate minimal pitch and roll responses with comparison to other platforms due to its design characteristics. The rigidity of TLP design restricts vertical (heave) and rotational (pitch and roll) motions, while the presence of tensioned mooring lines contributes to platform stability. However, the influence of turbulent winds on the peak pitch response of TLP is more significant compared to other types of offshore platforms (refer to Fig. 5-26). The TLB system

The negative heave observed is attributed to the characteristics of the TLP and TLB systems. The negative heave (set down) of the TLP is a result of the surge offset. As a result of this displacement, the TLP tendons become inclined, leading to a decrease in the effective vertical tension and subsequently reducing the buoyancy force acting on the platform which results in a decreased upward force on the platform, causing platform to submerge. In comparison, Semi-Submersible platforms exhibit more pronounced responses than Spar platforms due to their larger surface area and reduced water plane area, which enhances stability but also renders them more susceptible to environmental forces. This contrasts with Spar platforms, characterized by a deep draft and cylindrical shape, which offer stability. The performance of TLB

platforms indicates a moderate level of stability, striking a balance between the structural attributes of TLPs and Spar platforms.

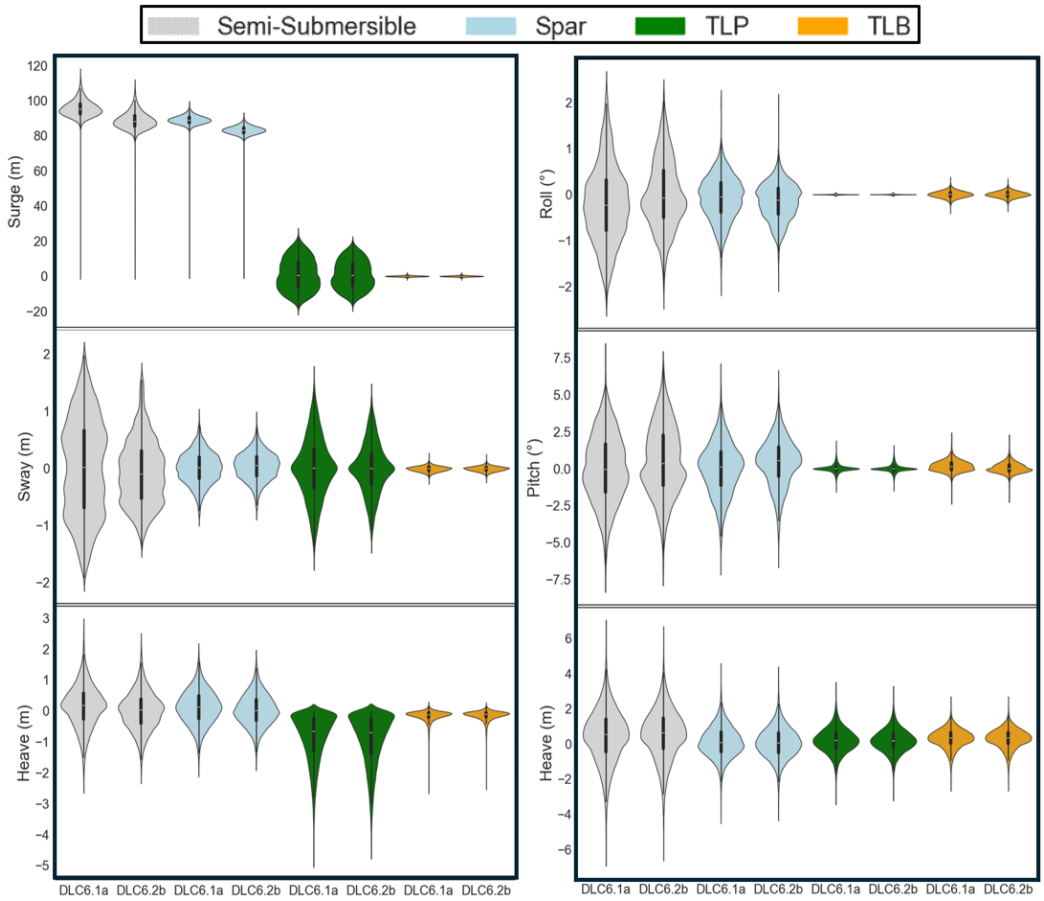


**Fig. 5-27** Semi-Submersible, Spar, TLP, and TLB Sway, Heave, Roll, Pitch, and Yow Motin Responses Violin Plots under Survival Conditions

The violin plots illustrated in Fig. 5-27 showcased the distribution of motion response values under survival conditions. The violin plots illustrate significant differences in the motion responses behaviour of Semi-Submersible, Spar, TLP, and TLB FOWT platforms under DLC6.1a and DLC6.2b. it should be noted that the plot ignored the data at the transient phase of the simulations.

The surge responses of Semi-Submersible and Spar platforms exhibited significant variability with higher median, reflecting notable horizontal displacement resulting from their specific design characteristics and mooring system configurations in challenging environmental circumstances. Conversely, the TLP surge response demonstrated moderate variability, indicating a comparatively consistent performance with horizontal displacement due to environmental influences. In contrast, the TLB platform displayed

minimal variability with almost zero median values, suggesting a high level of stability in survival conditions and minimal horizontal displacement when compared to other types of platforms.

The violin plots demonstrate that the equilibrium of sway is balanced around a central position across all platforms, although the distributions exhibit distinct shapes. Specifically, the TLB and Spar platforms exhibit reduced oscillation in the heave direction, with maximum and minimum heave responses are close to the mean values as a result of system characteristics and environmental load orientations. In contrast, the Semi-Submersible and TLP platforms display greater oscillations in the sway direction due to challenging environmental conditions, larger water plane area for Semi-submersible, and the compliant characteristics of TLP in the sway direction.

The heave response distributions of Semi-Submersible and Spar platforms exhibit broader distributions with greater magnitudes in comparison to TLP and TLB platforms. Platforms utilizing catenary mooring systems demonstrate a heave median cantered around zero, indicating a more evenly distributed heave. In contrast, TLP heave response displays a distinct, narrow shape with a wider lower tail, leading to a median slightly below zero and an extended range into negative values. A significant surge offset in a TLP can alter the geometry and tension distribution of the tendons, resulting in a downward movement of the platform.

The graphical representations of the roll and pitch reactions indicated that the system utilizing catenary mooring systems exhibited more pronounced responses in comparison to those employing tensioned mooring systems, the distinction attributed to the specific characteristics of the mooring systems. In a catenary mooring system with minimal displacements, the force exerted is small, enabling the system to undergo more substantial initial movements before the restoring force provide by mooring lines becomes substantial. Conversely, in a tensioned mooring system, the restoring force escalates more rapidly with displacement, leading to smaller initial movements and a quicker restoration to equilibrium.

The results indicated that the Semi-Submersible experienced increased yaw oscillations of greater magnitude compared to the Spar platform. This was attributed to the Semi-Submersible's larger exposed surface area to wind and waves, as well as Spar deep draft and small waterplane area, which diminish the moment arm for yaw-

inducing forces. Moreover, the submerged section of the Spar platform contributes significantly to damping yaw movements. The design characteristics of spars, such as a high centre of mass and low centre of buoyancy, enhance its stability and resistance to yaw. Yaw responses for the TLP and TLB platforms exhibited similar distributions, with median values approximating zero, indicating no substantial variance in the central tendency of yaw across the datasets. The TLB platform demonstrated lower yaw response compared to the TLP platform, attributed to the compliant nature of the TLP system in the yaw direction and the incorporation of a 20° spread in the fairlead attachment to reduce the effects of a bridle/delta connection aimed at modifying yaw motion response in the TLB platform.

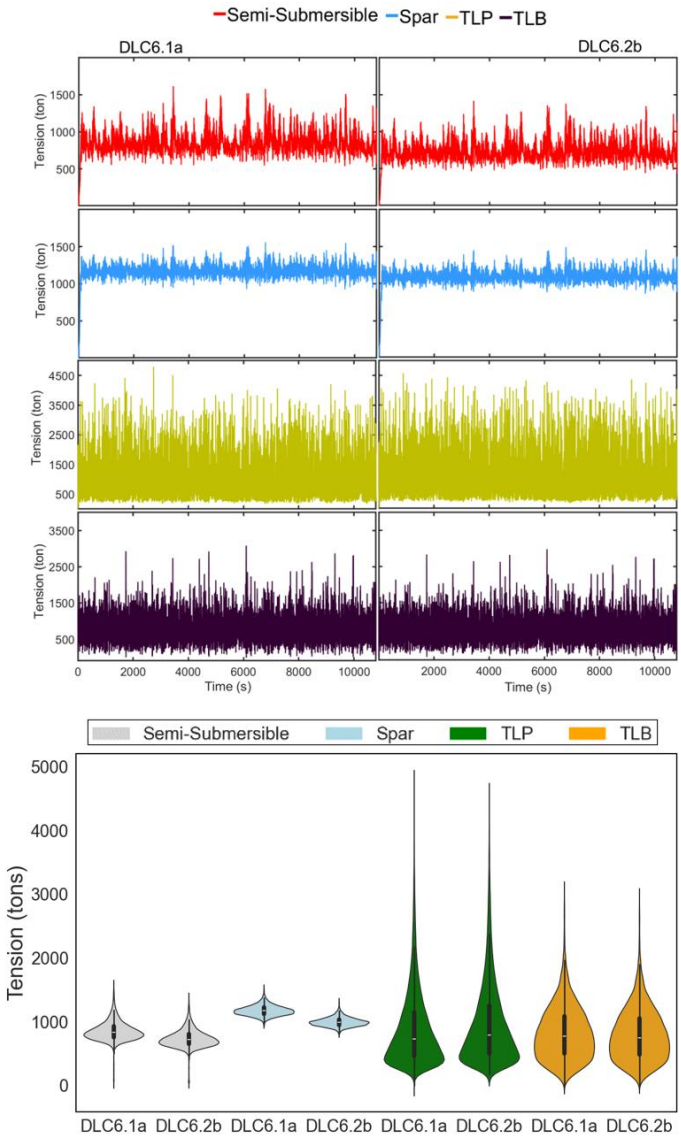


**Fig. 5-28** Most Loaded Line Maximum Dynamic Tension Time History and Distribution of Semi-Submersible, Spar, TLP, and TLB Platforms Under DLC6.1a and DLC6.2b

Fig. 5-28 illustrated the time history and distribution of dynamic tension in the most heavily loaded mooring lines for each platform under survival conditions.

The average tension experienced by platforms is decreased in the presence of steady wind conditions as per the DLC6.2b event, in contrast to the turbulent wind conditions specified in DLC6.1a. An initial spike in tension is observed, particularly for Semi-Submersible and Spar platforms, attributed to the notable surge offset resulting from the specific characteristics of the catenary mooring system.

The average tension in the mooring lines of the Spar platform exceeds that of the Semi-Submersible platform, while the peak tension in the primary mooring line of the Semi-Submersible platform surpasses that of the Spar platform. The comparison shows that the semi-submersible FOWT experienced more dynamic and variable tension in its mooring lines compared to the spar FOWT. As a results, the mooring lines of the Semi-Submersible platform exhibited lower capacity to absorb and distribute external forces compared to Spar platform as the distinct designs and buoyancy characteristics of Semi-Submersible platform influence its response to environmental forces, particularly in severe sea state conditions, which can significantly impact the tension experienced in the mooring lines. The comparison shows that the semi-submersible FOWT experienced more dynamic and variable tension in its mooring lines compared to the spar FOWT.

The TLP platform demonstrated a more consistent tension profile over time, with reduced frequency and severity of fluctuations when compared to the TLB system. The heavily loaded line on the TLB platform experiences fewer and less severe tension peaks in contrast to the TLP. This enhanced stability is attributed to the design and mooring system features of the TLB, which offer improved damping characteristics and lower susceptibility to environmental forces. In contrast, the TLP system displayed more pronounced coupling responses, leading to frequent and significant dynamic changes in tension. This suggests that the TLP is more responsive to variations in environmental conditions, such as waves and wind, potentially resulting in higher peak loads.

# 6. Anchor Sharing Concept

According to IREA (International Renewable Energy Agency), the primary challenge in floating offshore wind development is the high capital cost associated with constructing the large platforms and mooring systems needed to support the turbines [51]. The magnitude of the support structure cost relative to the total cost encourages research in support structure efficiency, which motivates the multiline anchor concept to be analysed in this section. While the anchors are shared amongst FOWTs, allowing for a smaller number of anchors, site investigations, and installation operation.

The interaction of waves with a floating structure is a significant factor in influencing the motion and loading behaviours of platforms in a multi-platform configuration, as opposed to a single floating structure. The complexity of the multi-platform situation arises from the requirement to account for not only the hydrodynamic interaction between platforms but also the comprehensive examination of interconnected platforms and their mooring systems [492]. In a multi-platform configuration, where the platforms are in close proximity to one another, the presence of multiple structures significantly influences the wave conditions surrounding each platform [345]. Waves interacting with one platform undergo reflection, diffraction, and interference due to the interactions with adjacent platforms, resulting in a complex wave pattern. This complex wave pattern influences the forces and moments experienced by each platform, thereby altering their motion responses compared to a single platform [493]. Nevertheless, while the aerodynamic spacing often dominates the overall layout of the FOWT array [494], hydrodynamic interactions are also critical for platforms are close to each other to ensure structural integrity and stability. A balanced approach considering both aerodynamic and hydrodynamic factors, supplemented by site-specific data and simulations, will lead to the optimal arrangement for a given FOWT project [495].

This study investigates the feasibility of anchor sharing in the context of the proposed TLB system by evaluating the system dynamics within a wind farm, specifically focusing on the tension applied to the mooring lines and the vertical loads on shared anchors. This innovative approach, involving multiple mooring lines applying loads on a single anchor from various directions, has not been implemented in FOWTs or thoroughly explored in theoretical frameworks. To achieve this objective, the study

focuses on the geometric configuration of a wind farm comprising FOWTs, including the arrangement of seven FOWT platforms, their wind turbines, and mooring lines.

As in the study of Hallowell [180], 1-hour simulations of a wind turbine in a survival load case scenario are conducted in FAST, and due to computational time, this study considered the simulation length to be one hour.

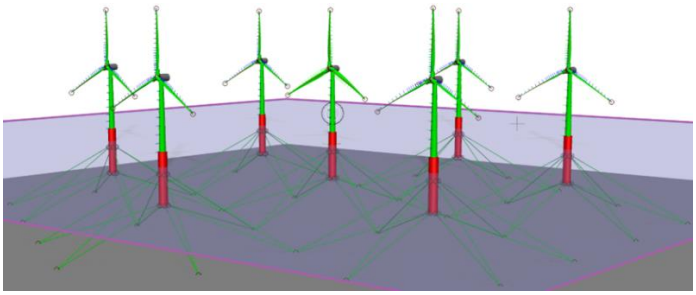

**Fig. 6-1** Anchor sharing Concept Modelled in SIMA

The arrangement of turbines within wind farms, as depicted in Fig. 6-1 may require optimization to reduce wake effects from prevailing wind directions, and the spacing between turbines should be determined to maximize the electric power output of the wind farm. The TLB concept utilizes a 180-meter anchor radius design to minimize the anchor's size and eliminate the need for long mooring lines. In addition, it is important to highlight that the current study, conducted in 2018, considered 2D distance between wind turbine platforms based on existing references [449-451]. Nevertheless, subsequent research has indicated that the ideal distance between neighbouring turbines should surpass 2D, with a preference for distances approaching 5D. Furthermore, turbines arranged in a linear configuration should maintain a separation of more than 10D [452]. Therefore, it is imperative that the design of wind farm systems integrates these updated findings to improve the wake effects encountered by the turbines.

As a result, the focus of this section does not include the assessment of wake effects on power generation under operational circumstances. This section is focused on analysing the influence of anchor sharing on the peak tension encountered by lines attached to a common anchor and the vertical load on the shared anchor. As the anchor holding capacity (vertical, horizontal or a combination) is typically 10 to 3000 tons per unit and it can be designed for all soil conditions where sufficient penetration

by under-pressure is possible [496], a suction pile anchor with holding capacity of 3000 ton is assumed. The evaluation is conducted based on the DLC6.1a criteria for survival conditions, with the assumption that the mooring material is steel wire rope with defined properties in Section 4.4.5 Table 4-21.

## 6.1. Multiline Anchor Layout Geometries

The design of a multiline anchor sharing system is based on research conducted by Casey M. Fontana [406], which examined the implementation of 3-line and 6-line anchor sharing systems. This study considered the original anchors of the single FOWT (O) are shared with its six surrounding FOWTs. The taut mooring system consists of two clusters of six sets of taut mooring lines and the first and the second cluster of mooring lines are attached to one anchor. In single-platform case anchor systems, the load on the anchor is governed by a double line connected to it; in multi-platform case systems, in which anchors are shared amongst the FOWTs, four lines are connected to one anchor.

The distance between turbine NO. 3 and NO. 5 is four times the blades diameter and the distance between turbine NO4 and original is twice the blade diameter. The anchor-sharing design pattern shown in Fig. 6-2 is schematic and does not include length scales. The original anchors of the single FOWT (O) are shared with its six surrounding FOWTs. In single-platform scenarios, the load on the anchor is determined by a dual line that is attached to it. In multi-platform situations, where anchors are utilized by multiple FOWTs, four lines are connected to a single anchor.

Fig. 6-3 shows the connection of the platform's lines to the shared anchor. For instance, lines 7 and 8 of platform (1) and lines 1 and 2 of platform (O) are connected to shared anchor (a), and similarly, lines 9 and 10 of platform (2) and lines 3 and 4 of the platform (O) are connected to shared anchor (b). In the following, the horizontal and vertical load of those shared anchors connecting platform (O) to its neighbouring platforms are considered for comparison with load on single platform anchors.

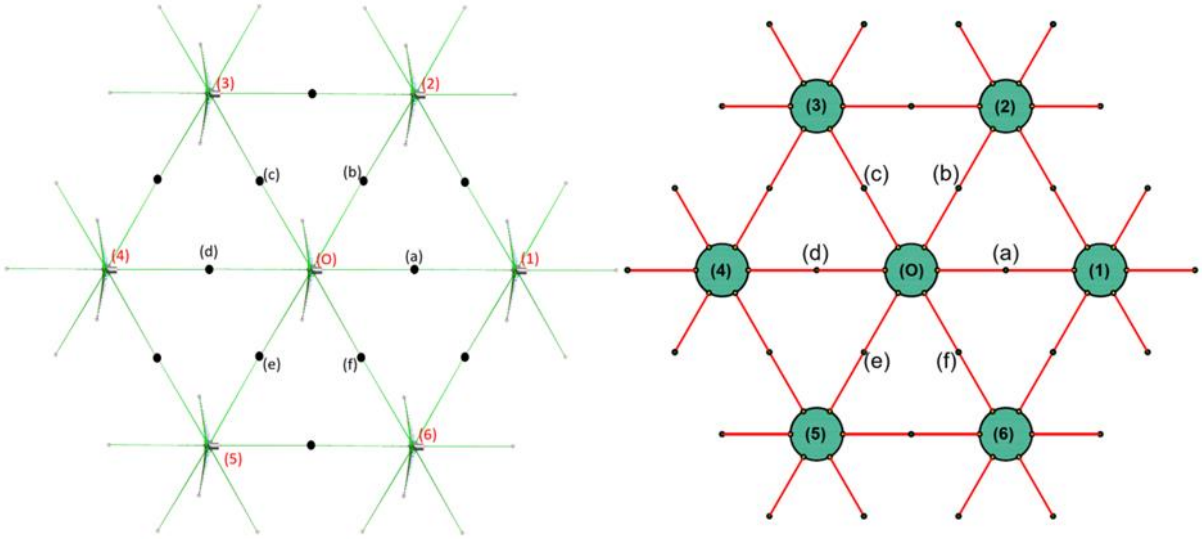


**Fig. 6-2** Wind Farm Anchor sharing Design Pattern

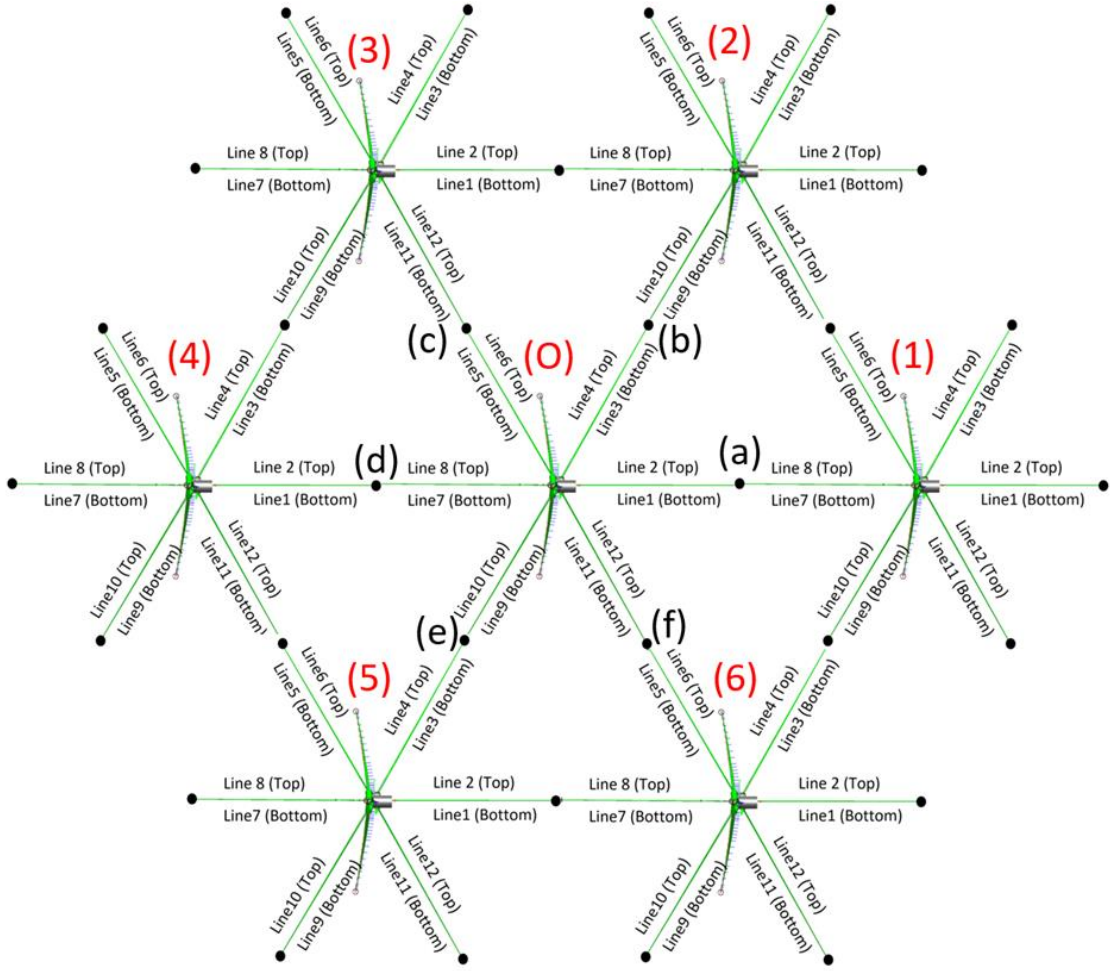


**Fig. 6-3** Mooring Lines of Platforms Attached to Shared Anchor

## 6.2. Results

The outcome derived from the interaction of a multi-platform system with a single platform is assessed in both the frequency and time domains. The motion responses and the tension on mooring lines connected to a common anchor are analysed. It is important to highlight that the tension in lines connected to the same anchor is taken into account when determining the maximum tension at the origin turbine (O) in the multi-platform scenario. Hydrodynamic characteristics are calculated utilizing WADAM through HydroD, and a coupled analysis in the time domain is carried out using SIMA.

### 6.2.1. Motion Responses

The results of the peak motion responses of the single-platform case compared to each platform in multi-platform case present in Table 6-1.

**Table 6-1** Peak Motion Responses of platforms from Multi-Platform Case and Single platform

| Case | Platform | Surge (m) | Sway (m) | Heave (m) | Roll (°) | Pitch (°) | Yaw (°) |
|---|---|---|---|---|---|---|---|
| **Single-Platform** | Single | 1.86 | -0.16 | -0.97 | 0.23 | 1.95 | 0.15 |
| **Multi-Platform** | (O) | 1.85 | 0.26 | -1.57 | -0.40 | 2.15 | 0.24 |
| | (1) | 1.91 | 0.11 | -1.29 | 0.21 | -2.40 | 0.26 |
| | (2) | 2.11 | 0.17 | -1.11 | 0.29 | 2.35 | -0.31 |
| | (3) | 1.99 | 0.15 | -1.35 | 0.27 | -2.47 | 0.13 |
| | (4) | 3.14 | 0.11 | -1.60 | 0.16 | 3.61 | 0.41 |
| | (5) | 1.99 | -0.16 | -1.31 | 0.35 | 2.35 | 0.33 |
| | (6) | 2.16 | -0.14 | -1.08 | 0.37 | 2.36 | 0.21 |

Table 6-1 provides data comparing the peak motion responses for a single-platform scenario against multiple-platform scenarios. Most multi-platform cases have surge values comparable to or slightly higher than the single-platform case, except platform (4), which has a significantly higher surge. However, the sway responses are relatively small due to the environmental loading directions, but platform (O) experienced higher sway in in the motion direction compared to the single-platform case. All multi-platform cases show higher negative values for heave compared to the single-platform case, indicating more significant vertical displacement. All multi-platform cases exhibit higher

pitch values than the single-platform case, indicating more pronounced angular motion in the longitudinal plane. Platform (0) exhibits a significantly higher yaw compared to other platforms and the single-platform case, indicating considerable rotation around the vertical axis. The results suggest that the use of multi-platform configurations can cause increased motion reactions, especially in surge, heave, and pitch, which can impact stability and operational efficiency. Multi-platform systems can exhibit resonance phenomena where the natural frequencies of the platforms and the wave frequencies interact. This can amplify certain motion responses (such as heave, pitch, or surge) when the system is excited at or near its resonant frequencies.

### 6.2.2. Anchor Load

The horizontal and vertical forces generated by the dynamic tension of individual lines attached to a shared anchor point are calculated and analysed to assess the resultant horizontal and vertical loads imposed by the mooring lines' dynamic tension. In Fig. 6-4, there are four vertical and four horizontal load components at each shared anchor, denoted as T1, T2, T3, and T4, representing the line tensions from the connected FOWTs to an anchor. When mooring lines are fastened to the fairlead at angles of 29.9° and 18.5°, the line tensions can be divided into vertical and horizontal tensions. Consequently, each shared anchor is subjected to loads from four vertical line tensions and four horizontal line tensions. The horizontal line tensions act in opposite directions, resulting in their cancellation. This research determined the point at which the highest tension occurs on the lines linked to a common anchor and also took into account the tensions of the remaining lines simultaneously.

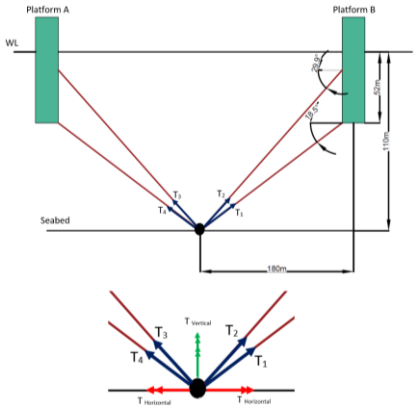


**Fig. 6-4** Vertical and Horizontal Tension Components at Shared Anchor

Table 6-2 compares the dynamic tension response of mooring lines for both multi-platform and single-platform configurations. Fig. 6-5 illustrates the maximum dynamic tension of the horizontal resultant mooring lines for a single platform, while Fig. 6-6 shows the maximum dynamic tension of the horizontal resultant mooring lines for multiple platforms. Table 6-3 displays the cumulative vertical anchor load (in tons) generated by the mooring line connected to it in scenarios involving both multi-platform and single-platform configurations.

**Table 6-2** Comparison of Mooring Lines Dynamic Tension Response of Multi-Platform with the Dynamic Tensions of Mooring Lines for Single Platform

| Platforms Dynamic Tension Response (tons) | | | | | | | | |
|---|---|---|---|---|---|---|---|---|
| Line | Multi-Platform | | | | | | | Single-Platform |
| | (4) | (5) | (6) | (O) | (3) | (2) | (1) | |
| 1 | 2181 | | | 2728 | | | | 1911 |
| 2 | 3030 | | | 2253 | | | | 2253 |
| 3 | | 2111 | | 1747 | | | | 1747 |
| 4 | | 1778 | | 1351 | | | | 1351 |
| 5 | | | 2128 | 1920 | | | | 1920 |
| 6 | | | 1430 | 1672 | | | | 2380 |
| 7 | | | | 2264 | 2167 | | | 2264 |
| 8 | | | | 2933 | 2753 | | | 2933 |
| 9 | | | | 1915 | | 2250 | | 1915 |
| 10 | | | | 1704 | | 3092 | | 2334 |
| 11 | | | | 1732 | | | 2112 | 2226 |
| 12 | | | | 1357 | | | 1874 | 1357 |

The dynamic tension response in multi-platform configurations generally varies more compared to single-platform configurations due to the fact that mooring system used to stabilize platforms in a multi-platform setup can also contribute to the interaction effects. In many cases, the multi-platform configurations exhibit higher tensions than the single-platform setup, indicating potential increased stress due to the interaction of multiple platforms.

For certain lines, single-platform configurations show higher tension than some multi-platform setups, suggesting that the distribution of forces in multi-platform systems can sometimes reduce individual line tensions. The results indicate the complexity and variability introduced by multi-platform interactions, which can lead to both increased and decreased tension responses depending on the specific configuration and line.

The multi-platform configurations exhibit higher tensions than the single-platform setup due to several factors related to the distribution of forces, load sharing, and the structural dynamics of the platforms. In a single-platform setup, the forces are concentrated and managed within a single structure, which typically leads to a straightforward distribution of tension and load however, this concentration can lead to higher tension in the lines as they bear the entire load. In multi-platform configurations, the load is distributed across multiple structures. This distribution can lead to uneven force distribution due to variations in platform stability, alignment, and connectivity, which can increase the overall tension in the system.

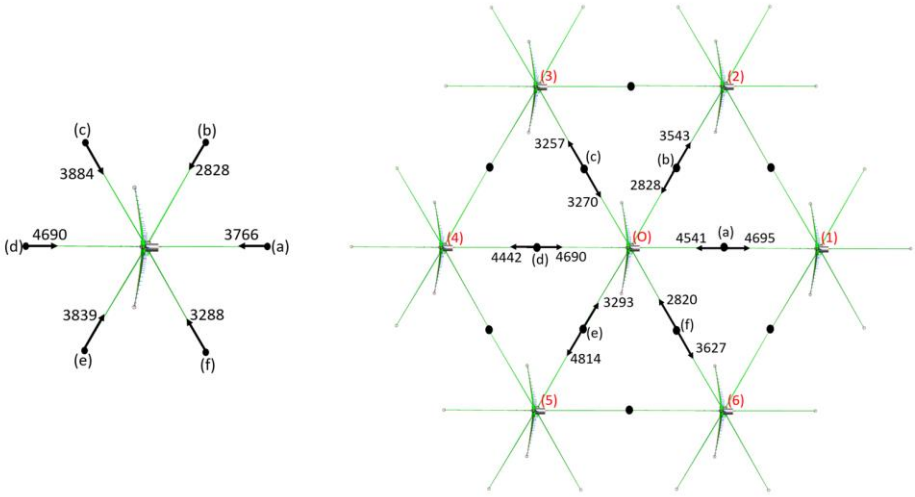


**Fig. 6-5** Single Platform and Multi-Platform Cases Mooring Lines Maximum Dynamic Horizontal Tension (tons)

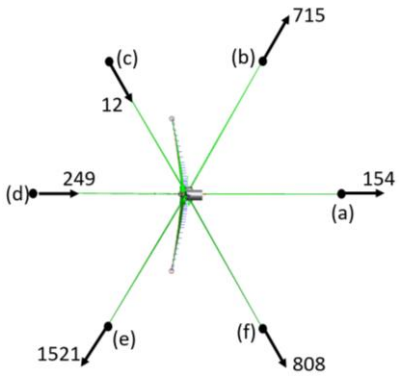


**Fig. 6-6** Total Horizontal Resultant Load (tons) on Shared Anchor in Multi-Platform Case

In the multi-platform scenario, the horizontal resultant forces counterbalance each other, leading to reducing distribution of total horizontal load on each shared anchor

as depicted in Fig. 6-6. Consequently, this occurrence suggests a decreased likelihood of experiencing an out-of-plane loading condition.

**Table 6-3** Total Vertical Anchor Load (ton) for Multi-Platform and Single-Platform Cases

| Anchor | Multi-Platform | Single-Platform | Δ |
|---|---|---|---|
| **a** | 2967 | 1729 | 42% |
| **b** | 1981 | 1227 | 38% |
| **c** | 2001 | 1795 | 10% |
| **d** | 2999 | 2180 | 27% |
| **e** | 2684 | 1771 | 34% |
| **f** | 2018 | 1382 | 32% |

The analysis conducted on vertical loads on shared anchors in multi-platform settings indicated that multi-platform configurations consistently experience higher vertical loads across all types of anchors compared to single-platform setups. This difference is primarily due to the greater load-bearing capacity needed by four mooring lines in multi-platform arrangements, as opposed to two in single-platform scenarios. This trend underscores the tendency of multi-platform layouts to raise vertical anchor loads.

Moreover, the examination of different percentage differentials revealed that the variations in vertical loads range from 10% to 42%, suggesting diverse impacts of multi-platform configurations on different types of anchors. These discrepancies linked to uneven load distribution due to variations in platform stability.

In brief, examining the motion and tension responses that apply loads on common anchors, while taking into account certain assumptions, can provide valuable insights into the viability of anchor sharing for a designed TLB using semi-taut mooring lines. The horizontal out-of-plane loading on the anchor is reduced because the opposing tensioned forces cancel out the total horizontal load. Adjustments to the capacity of the shared anchors are necessary to accommodate vertical loads. Therefore, Future innovations should prioritize the enhancement of more effective and dependable types of shared anchoring systems, including suction anchors equipped with fins, caisson-plate gravity anchors, among others. Subsequent research activities should emphasize investigating factors such as the influence of aerodynamic wake effects on various anchor sizes and the impact of non-collinear environmental conditions on the motion and tension responses of multiple platforms.

# 7. Conclusions and Future Work Recommendation

## 7.1. Conclusions

The study demonstrated the feasibility of a TLB FOWT system through extensive innovative concept design iteration approach. The results of each design iteration are assessed according to rules and regulations pertaining to Ultimate Limit State (ULS) and Accidental Limit State (ALS), as well as the evaluation of dynamic tension based on rule-based design criteria for dynamic tension characteristics.

The TLB system was specifically engineered to support a 10 MW wind turbine, secured by a unique taut mooring system that sets it apart from other designs. Notably, this system ensures that the upper cluster mooring lines are situated beneath the water surface, enabling safe access for maintenance and inspection activities by service vessels. The system utilized steel wire rope and fibre mooring materials was tested under various rule based environmental design load cases typical of the Northern North Sea and was deployed in water depths of 110 meters. Subsequently, a comparative analysis was conducted to evaluate the performance of TLB FOWT with scaled existing leading technologies for floating offshore wind platforms. Furthermore, the potential viability of an anchor sharing concept for the TLB platform was explored, utilizing steel wire rope mooring lines in survival conditions.

The hydrodynamic loads on floating platforms are modelled using well-established analysis methods previously used in the FOWT industry, such as frequency and time domain analyses. For the detail design analysis, this study conducted a coupled aero-hydro-servo-elastic analysis under combined wind, wave, and current effect. Platform motion and mooring line tension characteristics are analysed for three-hour time domain solution under various environmental conditions, including wind field descriptions covering uniform wind to fluctuating turbulent wind.

- The conducted assessment of drift force and second-order effects indicated notable spike under the first-order analysis and first-order analysis with drift whilst did not observe under the second-order effect. The emergence of these peaks was linked to tension loss and consequent snap loads in the first-order and first-order with drift analyses, contingent upon environmental conditions,

underscoring the importance of integrating full second-order considerations in the methodology.

- The iterative design process during the conceptual design phase indicated a decrease in motion and dynamic tension responses under operational and survival environmental conditions by reducing the diameter and draft of the support platform. However, during the ALS analysis, it was found that the dynamic tension in the most heavily loaded mooring line exceeded the material's MBL. This was due to simplifying environmental conditions into two sets resembling those at the Hywind Scotland wind farm, characterized by a significant wave height. The tension exceeding the material's limit was attributed to the consistent application of wind force, calculated by assessing the drag on the tower and blade structures throughout the simulation period.
- The system utilized rigid mooring line in severe sea state under operational condition produce higher mean electricity than those employed fibre materials indicating that the system's positioning relative to the incoming wind, with limited response such as pitch compared to systems oscillating more rapidly, plays a crucial role in power production efficiency.
- TLB system utilized nylon material indicate more pronounced motions but with lower tension compared to systems employing steel mooring lines, due to the material characteristics of nylon, including its lower rigidity and greater elasticity. The TLB with steel experiences less motion and higher tension on the mooring line compared to the TLB with nylon, underscoring the importance of maintaining steel mooring lines.
- The peak values indicate the severity of the event, with responses slightly lower in DLC6.2b compared to DLC6.1a at their peaks, signifying disparities in external load. The effect of wind turbulence intensity is more pronounced in systems using elastic mooring materials compared to those employing rigid mooring materials, suggesting that employing steel mooring lines for TLB systems demonstrates improved resilience when subjected to turbulent wind events compared to nylon materials.
- Subsequent to the disconnection of lines, all systems undergo an initial phase, with platforms utilizing fibre ropes displaying elevated responses in contrast to that with stiffer lines. TLB utilizing steel mooring lines exhibit reduced

oscillations. Subsequent to the disconnection of lines, all systems undergo an initial phase, with platforms utilizing fibre ropes displaying elevated responses in contrast to that with stiffer lines. TLB utilizing steel mooring lines exhibit reduced oscillations. Notably, TLB with nylon lines showcase sharp, high-amplitude surge and heave responses during the initial phase following line disconnection due to the material's elasticity.

- The results presented highlight that a TLB with three mooring lines can effectively operate and maintain acceptable motion responses even in relatively severe sea states, showcasing the significant advantages of TLB design.
- The primary distinctions are influenced by the material properties, with steel and polyester showcasing low variability and consistent behaviour, rendering them dependable choices for applications necessitating stability in comparison to nylon material.
- TLB systems with steel and polyester are suitable for applications requiring consistent behaviour due to minimal variability, while TLB systems with nylon may be less reliable for applications necessitating consistent performance.
- Steel is recommended for primary mooring lines due to its high strength, low elasticity, and durability, ensuring stable TLB positioning with critical for high stress. Polyester can serve as a suitable alternative or complement, providing a balance of strength and flexibility. Nylon is best suited for mooring lines where shock absorption is necessary but is less ideal as the primary mooring line due to its high elasticity and potential for excessive movement.
- The platforms that use catenary mooring systems have higher surge responses than those with taut mooring systems or tendons and show different low-frequency motion behaviour compared to the high-frequency motions experienced by the stiff-mooring stabilised platforms. The environmental forces exerted on motion responses, particularly pitch motion, are more pronounced on the Semi-Submersible platform, leading to decreased power production. Furthermore, the power production of the TLP platform is reduced in harsh environmental conditions compared to mild conditions, as indicated by its higher maximum surge and heave motion responses in comparison to the TLB platform.

- The Semi-Submersible platform exhibited greater motion responses than the Spar platform, likely due to the presence of multiple columns and pontoons in the Semi-Submersible design for enhanced stability in comparison to a buoyant cylinder with a deep draft. In a catenary mooring system, the recorded dynamic tension force was minimal, allowing for more significant initial movements before the mooring lines' restoring force becomes substantial. Conversely, in a tensioned mooring system, the restoring force increased more rapidly with displacement, resulting in smaller initial movements and a quicker return to equilibrium. The peak tensions in TLB mooring lines were lower than those in TLP due to the buoy's design allowing for more movement, which disperses forces rather than concentrating them on the mooring lines. Nevertheless, the findings obtained adhere to both the rule-based constraints, with the TLB platform demonstrating minimal variability and nearly zero median values, indicating a high degree of stability with minimal horizontal displacement when compared to other platform types.
- Analysing the motion and tension responses that apply loads on common anchors, while considering specific assumptions, can offer valuable insights into the feasibility of anchor sharing for a designed TLB utilizing semi-taut mooring lines.
- In the multi-platform scenario, the horizontal resultant forces counterbalance each other, leading to reducing distribution of total horizontal load on each shared anchor, suggests a decreased likelihood of experiencing an out-of-plane loading condition. Nevertheless, adjustments to the capacity of the shared anchors are required to accommodate vertical loads.

In summary, The TLB system has substantial advantages over the conventional floater and mooring types. First, as the TLB motion responses are reduced compared to other systems, the TLB design will allow for ease of adoption of land-based wind turbines without the need to re-develop control systems. The TLB design is less prone to effects in wind turbulence, at least for the non-operating conditions evaluated in this paper. The TLB design is less complex than the current leading technology types for floating offshore wind platforms, simplifying the construction process.

The dynamic response of the floater obtained for all DLCs showed slight motion and nacelle accelerations, enabling the wind turbine to be installed without significant modifications to its control systems. Therefore, the TLB design will allow for the simplicity of adopting land-based wind turbines without needing to re-develop control systems to cope with the increased motion and accelerations.

In terms of bench marking study, The TLB system has substantial advantages over the conventional floater and mooring types. First, as the TLB motion responses are reduced compared to other systems, specifically surge and pitch responses, the TLB design will allow for ease of adoption of land-based wind turbines without the need to re-develop control systems. Second, the TLB design is less prone to effects in wind turbulence, at least for the non-operating conditions evaluated in this paper. Third, the TLB design is less complex than the current leading technology types for floating offshore wind platforms, simplifying the construction process.

## 7.2. Future Work Recommendation

This study proposes the following future research directions:

1. Examination of the TLB using a combination of mooring materials using various segments of different mooring materials.
2. Examine the performance of the TLB under varying water depths.
3. Analysis of the TLB with varying anchor radii to consider the impact of wind wake effects specifically within wind farm utilizing anchor sharing concept.
4. Considered non collinear environmental conditions
5. Comprehensive cost analysis of the TLB system, comparing it with other floating wind turbine types and fixed bottom platforms at the same water depth.
6. In-depth analysis of cost reduction possibilities through the implementation of an anchor sharing concept.

# List of References


1. Carbon Trust, *Floating Offshore Wind: Market and Technology Review* 2015.
2. Carbon Trust. *Floating Wind Joint Industry Project Phase I Summary Report - Key Findings from Electrical Systems, Mooring Systems, and Infrastructure & Logistics studies*. 2018 7/11/2018]; Available from: https://www.carbontrust.com/media/675868/flw-jip-summaryreport-phase1.pdf.
3. Snieckus. *Floating wind forging 'structural shift' with sights on 15% of new offshore arrays by 2050: DNV*. 2022 [cited 2022; Available from: https://www.rechargenews.com/wind/floating-wind-forging-structural-shift-with-sights-on-15-of-new-offshore-arrays-by-2050-dnv/2-1-1196722.
4. Archer, C.L. and M.Z. Jacobson, *Evaluation of global wind power.* Journal of Geophysical Research: Atmospheres, 2005. **110**(D12).
5. Bae, Y., et al. *Influence of control strategy to FOWT hull motions by aero-elastic-control-floater-mooring coupled dynamic analysis*. in *ISOPE International Ocean and Polar Engineering Conference*. 2011. ISOPE.
6. Premalatha, M., T. Abbasi, and S.A. Abbasi, *Wind energy: Increasing deployment, rising environmental concerns.* Renewable and Sustainable Energy Reviews, 2014. **31**: p. 270-288.
7. Gill, A.B., *Offshore renewable energy: ecological implications of generating electricity in the coastal zone.* Journal of applied ecology, 2005: p. 605-615.
8. Gusatu, L.F., et al., *A spatial analysis of the potentials for offshore wind farm locations in the North Sea region: Challenges and opportunities.* ISPRS International Journal of Geo-Information, 2020. **9**(2): p. 96.
9. ACTEON, *FIXED WIND FOUNDATIONS: AN INDEPENDENT CONCEPT SCREENING APPROACH*. 24/05/2021.
10. Swart, R., et al., *Europe's onshore and offshore wind energy potential: An assessment of environmental and economic constraints*. 2009, European Environment Agency.
11. Hildebrandt, A., A. Stahlmann, and T. Schlurmann. *GIGAWIND ALPHA VENTUS GESAMTKONZEPT UND TEILASPEKTE*. in *FZK-Kolloquium–Potentiale für die Maritime Wirtschaft, FZK*. 2009.
12. Carbon Trust. *Floating Wind Joint Industry Project: Policy & Regulatory APPraisal*. 2017 10/10/2018]; Available from: https://www.carbontrust.com/media/673978/wp1-flw-jip-policy-regulatory-appraisal_final_170120_clean.pdf.
13. Spearman, D. and S. Strivens, *Phase II summary report.* Carbon Trust, 2020.
14. Henderson, A.R. and D. Witcher, *Floating offshore wind energy—a review of the current status and an assessment of the prospects.* Wind Engineering, 2010. **34**(1): p. 1-16.
15. CATAPULT. *MACROECONOMIC BENEFITS OF FLOATING OFFSHORE WIND IN THE UK*. 2018 04/02/2019]; Available from: 5bd78f98e76ae_Macroeconomic benefits of offshore wind in the UK -October 2018 (2).pdf.
16. CATAPULT. *Floating wind: technology assessment*. 2015 [cited 2/2/2018; Available from: https://ore.catapult.org.uk/app/uploads/2018/01/Floating-wind-technology-assessment-June-2015.pdf.
17. Myhr, A., et al., *Levelised cost of energy for offshore floating wind turbines in a life cycle perspective.* Renewable Energy, 2014. **66**: p. 714-728.
18. Sorensen, J.N. and W.Z. Shen, *Numerical modeling of wind turbine wakes.* J. Fluids Eng., 2002. **124**(2): p. 393-399.
19. Butterfield, S., et al., *Engineering challenges for floating offshore wind turbines*. 2007, National Renewable Energy Laboratory (NREL), Golden, CO.

20. Witte, T., S. Siegfriedsen, and M. El-Allawy, *WindDeSalter® Technology Direct use of wind energy for seawater desalination by vapour compression or reverse osmosis.* Desalination, 2003. **156**(1-3): p. 275-279.
21. Maciel, J.G., *The WindFloat Project.* Lisbon: edp, 2010: p. 24.
22. Statoil. *Statoil to build the world's first floating wind farm: Hywind Scotland*. 2017 15/01/2018]; Available from: https://www.statoil.com/en/news/hywindscotland.html.
23. Fukushima Offshore, *Fukushima Floating Offshore Wind Farm Demonstration Project Demonstration Project （Fukushima FORWARD）*. 2014.
24. Schouten, J., *Design of a vibration control system to reduce the tower forces in a tension leg platform wind turbine.* 2016.
25. Bossler, A., *Japan's floating offshore wind projects: an overview.* Maine Ocean and Wind Industry Initiative: MOWII Webinar (May 2013), 2013.
26. Nilsson, D. and A. Westin, *Floating wind power in Norway Analysis of future opportunities and challenges*. 2014, MS Thesis, Lund University, Sweden.
27. James, R. and M.C. Ros, *Floating offshore wind: market and technology review.* Carbon Trust: UK, 2015: p. 168.
28. Mast, E., R. Rawlinson, and C. Sixtensson, *Market study floating wind in the Netherlands: Potential of floating offshore wind.* TKI Wind op Zee, DNV GL, 2015.
29. Equinor. *Hywind - leading floating offshore wind solution*. 2018 6/11/2018]; Available from: https://www.equinor.com/en/what-we-do/hywind-where-the-wind-takes-us.html.
30. Agency, I.R.E., *Floating Foundations: A Game Changer for Offshore Wind Power*. 2016, International Renewable Energy Agency (IRENA) Masdar City, UAE.
31. Singhal, G., et al. *Independent Assessment of Current Floater Concepts for Floating Wind Application*. in *SNAME 26th Offshore Symposium*. 2021. OnePetro.
32. Maktabi, M. and E. Rusu, *A review concerning the perspectives in developing the floating wind farms.* 2024.
33. Mahfouz, M.Y., et al., *Response of the International Energy Agency (IEA) Wind 15 MW WindCrete and Activefloat floating wind turbines to wind and second-order waves.* Wind Energy Science, 2021. **6**(3): p. 867-883.
34. equinor. *Equinor marks 5 years of operations at world's first floating wind farm*. 2022 [cited 2023; Available from: https://www.equinor.com/news/hywind-5-years-world-first-floating-wind-farm.
35. Yoshimoto, H., et al. *Development of floating offshore substation and wind turbine for Fukushima FORWARD*. in *Proceedings of the International Symposium on Marine and Offshore Renewable Energy, Tokyo, Japan*. 2013.
36. Abin, B.A., *Japan's Energy Security: Opportunities and Challenges of Renewables in post-Fukushima Energy Scenario.* Journal of Polity & Society, 2021. **13**: p. 23-47.
37. Molins, C., A. Yagüe, and P. Trubat. *Construction possibilities for monolithic concrete spar buoy serial production*. in *Journal of Physics: Conference Series*. 2018. IOP Publishing.
38. Kolios, A., A. Rodriguez-Tsouroukdissian, and K. Salonitis, *Multi-criteria decision analysis of offshore wind turbines support structures under stochastic inputs.* Ships and offshore structures, 2016. **11**(1): p. 38-49.
39. James, R., et al., *Floating Wind Joint Industry Project—Phase I Summary Report.* Carbon Trust Tech. Rep, 2018. **19**: p. 2-20.
40. Cermelli, C., D. Roddier, and A. Weinstein. *Implementation of a 2MW floating wind turbine prototype offshore Portugal*. in *Offshore technology conference*. 2012. Offshore Technology Conference.
41. Rodrigues, S., et al., *Trends of offshore wind projects.* Renewable and Sustainable Energy Reviews, 2015. **49**: p. 1114-1135.
42. PrinciplePower. *Kincardine Offshore Windfarm* 2022 [cited 2022; Available from: https://www.principlepower.com/projects/kincardine-offshore-wind-farm.

43. Amano, R.S., *Review of wind turbine research in 21st century.* Journal of Energy Resources Technology, 2017. **139**(5).
44. PFOWF, P.F.O.W.F.-. *Environmental Statement:*

*Offshore Non-Technical Summary*. 2022 [cited 2022 23 November]; Available from: https://marine.gov.scot/sites/default/files/eia_report_volume_1_-_non-technical_summary_redacted.pdf.
45. Liu, Y., et al., *Investigation of the effects of platform motion on the aerodynamics of a floating offshore wind turbine.* Journal of Hydrodynamics, Ser. B, 2016. **28**(1): p. 95-101.
46. Musial, W., S. Butterfield, and B. Ram, *Energy from offshore wind: Preprint*. 2006, National Renewable Energy Laboratory (NREL), Golden, CO.
47. Adam, F., et al. *Scale tests of the GICON®-TLP for wind turbines*. in *ASME 2014 33rd International Conference on Ocean, Offshore and Arctic Engineering*. 2014. American Society of Mechanical Engineers Digital Collection.
48. Vita, L., et al. *Comparison of numerical models and verification against experimental data, using Pelastar TLP concept*. in *ASME 2015 34th International Conference on Ocean, Offshore and Arctic Engineering*. 2015. American Society of Mechanical Engineers.
49. Villoslada, D., M. Santos, and M. Tomás-Rodríguez, *General methodology for the identification of reduced dynamic models of barge-type floating wind turbines.* Energies, 2021. **14**(13): p. 3902.
50. FLOATGEN. *BW Ideol's first floater in operation*. 2018 [cited 2022; Available from: https://www.ideol-offshore.com/en/floatgen-demonstrator.
51. International renewable Energy Agancey (IRENA). *FLOATING FOUNDATIONS: A GAME CHANGER FOR OFFSHORE WIND POWER*. 2016 12/03/2019]; Available from: https://www.irena.org/-/media/Files/IRENA/Agency/Publication/2016/IRENA_Offshore_Wind_Floating_Foundations_2016.pdf.
52. Castro-Santos, L., *Decision variables for floating offshore wind farms based on life-cycle cost: The case study of Galicia (North-West of Spain).* Ocean Engineering, 2016. **127**: p. 114-123.
53. Castro-Santos, L. and V. Diaz-Casas, *Floating offshore wind farms*. 2016: Springer.
54. Borg, M. and M. Collu, *Offshore floating vertical axis wind turbines, dynamics modelling state of the art. Part III: Hydrodynamics and coupled modelling approaches.* Renewable and Sustainable Energy Reviews, 2015. **46**: p. 296-310.
55. Taboada, J.V., *Comparative Analysis Review on Floating Offshore Wind Foundations (FOWF).* 2015.
56. Strivens, S., et al., *Floating Wind Joint Industry Project Phase III Summary Report.* The Carbon Trust: London, UK, 2021.
57. WindFloat. *The WindFloat Project*. 2017 11/10/2018]; Available from: eusew.eu/sites/default/files/programme-additional-docs/WindFloat%20Project%20Update.pdf.
58. Tisheva, P. *Hywind Scotland trumpets 65% capacity factor*. 2018 [cited 2018 Feb 15]; Available from: https://renewablesnow.com/news/hywind-scotland-trumpets-65-capacity-factor-601823/.
59. Durakovic, A. *WindFloat Atlantic Fully Up and Running*. 2020 [cited 2020.
60. Musial, W., et al., *Offshore Wind Market Report: 2022 Edition*. 2022, National Renewable Energy Lab.(NREL), Golden, CO (United States).
61. Zwick, D. and M. Muskulus, *Simplified fatigue load assessment in offshore wind turbine structural analysis.* Wind Energy, 2016. **19**(2): p. 265-278.
62. Tillenburg, D., *Technical challenges of floating offshore wind turbines-An overview.* 2021.
63. Chitteth Ramachandran, R., et al., *Floating wind turbines: marine operations challenges and opportunities.* Wind Energy Science, 2022. **7**(2): p. 903-924.

64. Chen, J. and M.-H. Kim, *Review of recent offshore wind turbine research and optimization methodologies in their design.* Journal of Marine Science and Engineering, 2021. **10**(1): p. 28.
65. Komusanac, I., D. Fraile, and G. Brindley, *Wind energy in Europe in 2019-Trends and statistics.* Wind Europe, 2019: p. 9-10.
66. Broom, D. *These 3 countries are global offshore wind powerhouses*. 2019 [cited 2020; Available from: https://www.weforum.org/agenda/2019/04/these-3-countries-are-global-offshore-wind-powerhouses.
67. Global, W.F.O.W.W. *WFO Global Offshore Wind Report*. 2023 [cited 2023; Available from: https://wfo-global.org/wp-content/uploads/2023/10/WFO-Global-Offshore-Wind-Report-HY1-2023-1.pdf.
68. Memija, A. *China's Deep-Sea Floating Wind Platform Heads Offshore*. 2023 [cited 2023; Available from: https://www.offshorewind.biz/2023/03/27/chinas-deep-sea-floating-wind-platform-heads-offshore/#:~:text=The%20platform%2C%20named%20CNOOC%20Guanlan,on%20the%20Chinese%20Government's%20website.
69. Liu, Y., et al., *Developments in semi-submersible floating foundations supporting wind turbines: A comprehensive review.* Renewable and Sustainable Energy Reviews, 2016. **60**: p. 433-449.
70. Smith, A. *2021 Offshore Wind Energy Update and Outlook*. 2020 [cited 2020; Available from: https://www.orrick.com/en/Insights/2021/07/2021-Offshore-Wind-Energy-Update-and-Outlook.
71. Zhao, Y., J. Yang, and Y. He, *Preliminary design of a multi-column TLP foundation for a 5-MW offshore wind turbine.* Energies, 2012. **5**(10): p. 3874-3891.
72. Zhao, J., L. Zhang, and H. Wu, *Motion performance and mooring system of a floating offshore wind turbine.* Journal of Marine Science and Application, 2012. **11**(3): p. 328-334.
73. WindEurope. *Offshore Wind in Europe Key trends and statistics 2019*. 2019 [cited 2023; Available from: https://windeurope.org/wp-content/uploads/files/about-wind/statistics/WindEurope-Annual-Offshore-Statistics-2019.pdf.
74. Díaz, H., et al., *Market needs, opportunities and barriers for the floating wind industry.* Journal of Marine Science and Engineering, 2022. **10**(7): p. 934.
75. SimplyBlueGroup. *Erebus | Blue Gem Wind*. 2020 [cited 2020; Available from: https://simplybluegroup.com/project/erebus-blue-gem-wind/.
76. Hannon, M., et al., *Offshore wind, ready to float? Global and UK trends in the floating offshore wind market.* 2019.
77. Greaves, D., et al., *UK perspective research landscape for offshore renewable energy and its role in delivering Net Zero.* Progress in Energy, 2022. **4**(4): p. 042012.
78. Ibrion, M. and A.R. Nejad. *On a road map for technology qualification, innovation and cost reduction in floating offshore wind: learning from Hywind and Norwegian approach*. in *Journal of Physics: Conference Series*. 2023. IOP Publishing.
79. Buljan, A. *200 MW Floating Wind Farm in South Korea Moves Forward*. 2021 [cited 2022; Available from: https://www.offshorewind.biz/2021/05/07/200-mw-floating-wind-farm-in-south-korea-moves-forward/.
80. Vu, D.Q., et al., *Evaluation of resource spatial-temporal variation, dataset validity, infrastructures and zones for Vietnam offshore wind energy.* Vietnam Journal of Sciences, Technology and Engineering (Serie C), 2020. **62**(1): p. 03-16.
81. Musial, W. and S. Butterfield, *Future for offshore wind energy in the United States*. 2004, National Renewable Energy Lab., Golden, CO (US).
82. REUTERSEVENT. *Floating Wind USA 2023*. 2023 [cited 2023; Available from: https://events.reutersevents.com/renewable-energy/floating-wind-usa#:~:text=With%20ambitious%20goals%20to%20install,billions%20into%20its%20green%20economy.

83. CARBONTRUST. *FLOATING WIND JOINT INDUSTRY PROGRAMME-Phase IV-Summary Report*. 2022 [cited 2022; Available from: https://www.carbontrust.com/our-work-and-impact/impact-stories/floating-wind-joint-industry-programme-jip/floating-wind-jip-2.
84. Energy, U.D.o., *Offshore wind market report: 2022 Edition.* Technical Report, 2022.
85. Musial, W., et al., *Offshore Wind Market Report: 2023 Edition*. 2023, National Renewable Energy Laboratory (NREL), Golden, CO (United States).
86. Edie. *Renewables Obligation Certificates (ROCs)*. 2014 27/02/2018]; Available from: https://www.edie.net/library/Edie-explains-Renewables-Obligation-Certificates-ROCs/6538.
87. O'Keeffe, A. and C. Haggett, *An investigation into the potential barriers facing the development of offshore wind energy in Scotland: Case study–Firth of Forth offshore wind farm.* Renewable and Sustainable Energy Reviews, 2012. **16**(6): p. 3711-3721.
88. Toke, D., *The UK offshore wind power programme: A sea-change in UK energy policy?* Energy Policy, 2011. **39**(2): p. 526-534.
89. GWEC, G.W.E.C., *Global offshore wind report 2020.* URL https://gwec. net/global-offshore-wind-report-2020, 2020.
90. Higgins, P. and A. Foley, *The evolution of offshore wind power in the United Kingdom.* Renewable and sustainable energy reviews, 2014. **37**: p. 599-612.
91. CrownEstateScotland. *ScotWind offshore wind leasing delivers major boost to Scotland's net zero aspirations*. 2022 [cited 2023; Available from: https://www.crownestatescotland.com/news/scotwind-offshore-wind-leasing-delivers-major-boost-to-scotlands-net-zero-aspirations.
92. CrownEstate. *Early-commercial scale and full-commercial scale projects*. 2022 [cited 2022 9 March]; Available from: https://www.thecrownestate.co.uk/en-gb/what-we-do/on-the-seabed/energy/floating-offshore-wind/#:~:text=The%20Crown%20Estate%20has%20published,industrial%20sector%20for%20the%20UK.
93. James, R. and M.C. Ros, *Floating offshore wind: market and technology review.* The Carbon Trust, 2015.
94. Zhang, H. and M. Pollitt, *Comparison of policy instruments in the development process of offshore wind power in North Sea countries.* 2023.
95. Kleyver, M., *Will Europe achieve its Offshore Floating Wind energetic targets for 2050?* 2023, uis.
96. Lerch, M., et al., *Sensitivity analysis on the levelized cost of energy for floating offshore wind farms.* Sustainable Energy Technologies and Assessments, 2018. **30**: p. 77-90.
97. Buljan, A. *Scotland's New Floating Wind Projects – What We Know So Far*. 2022 [cited 2022; Available from: https://www.offshorewind.biz/2022/01/18/scotlands-new-floating-wind-projects-what-we-know-so-far/.
98. Scotland, C.E. *ScotWind Clearing process*. 2022 2022]; Available from: https://www.crownestatescotland.com/our-projects/scotwind#:~:text=What%20is%20ScotWind%3F,wind%20farms%20in%20Scottish%20waters.
99. Leimeister, M., A. Kolios, and M. Collu. *Critical review of floating support structures for offshore wind farm deployment*. in *Journal of Physics: Conference Series*. 2018. IOP Publishing.
100. Edwards, E.C., et al., *Evolution of floating offshore wind platforms: A review of at-sea devices.* Renewable and Sustainable Energy Reviews, 2023. **183**: p. 113416.
101. Thiagarajan, K. and H. Dagher, *A review of floating platform concepts for offshore wind energy generation.* Journal of offshore mechanics and Arctic engineering, 2014. **136**(2).
102. Spearman, D. and S. Strivens, *Floating Wind Joint Industry Project-Phase II Summary Report. UK: Carbon Trust*. 2020.

103. Layman's Report. *The BLUETEC Project*. 2016 27/03/2018]; Available from: http://www.bluewater.com/wp-content/uploads/2014/06/Bluetec-LIFE-Laymans-report.pdf.
104. Huber, F. *The first floating wind turbines*. in *Proceedings of the 2nd International Conference on Ocean Energy (ICOE 2008), Brest, France*. 2008.
105. Atcheson, M., et al., *Floating offshore wind energy.* by Joao Cruz and Mairead Atcheson. Springer International Publishing. Chap. Looking back. doi, 2016. **10**(1007): p. 978-3.
106. Koh, J., et al., *Building and calibration of a fast model of the sway prototype floating wind turbine*. 2013, National Renewable Energy Lab.(NREL), Golden, CO (United States).
107. Koh, J.H., et al. *Validation of SWAY wind turbine response in FAST, with a focus on the influence of tower wind loads*. in *ISOPE International Ocean and Polar Engineering Conference*. 2015. ISOPE.
108. Mathern, A., C. von der Haar, and S. Marx, *Concrete support structures for offshore wind turbines: Current status, challenges, and future trends.* Energies, 2021. **14**(7): p. 1995.
109. Hand, B. and A. Cashman, *A review on the historical development of the lift-type vertical axis wind turbine: From onshore to offshore floating application.* Sustainable Energy Technologies and Assessments, 2020. **38**: p. 100646.
110. Pedersen, T.F., *Design and Manufacture of an Offshore Concept Wind Turbine–the.* 2013.
111. Utsunomiya, T., et al. *Experimental validation for motion of a spar-type floating offshore wind turbine using 1/22.5 scale model*. in *International Conference on Offshore Mechanics and Arctic Engineering*. 2009.
112. Ishida, S., et al. *At-sea experiment of a hybrid spar type offshore wind turbine*. in *International Conference on Offshore Mechanics and Arctic Engineering*. 2013. American Society of Mechanical Engineers.
113. Utsunomiya, T., et al. *Dynamic response analysis of a floating offshore wind turbine during severe typhoon event*. in *ASME 2013 32nd International Conference on Ocean, Offshore and Arctic Engineering*. 2013. American Society of Mechanical Engineers.
114. Kokubun, K., et al. *Model experiment of a SPAR type offshore wind turbine in storm condition*. in *International Conference on Offshore Mechanics and Arctic Engineering*. 2012. American Society of Mechanical Engineers.
115. Fowler, M.J., et al. *1: 52 Scale Testing of the First US Commercial Scale Floating Wind Turbine, VolturnUS: Testing Overview and the Evolution of Scale Model Testing Methods*. in *ASME 2017 36th International Conference on Ocean, Offshore and Arctic Engineering*. 2017. American Society of Mechanical Engineers.
116. Allen, C., et al., *Definition of the UMaine VolturnUS-S reference platform developed for the IEA wind 15-megawatt offshore reference wind turbine*. 2020, National Renewable Energy Lab.(NREL), Golden, CO (United States); Univ. of ….
117. Viselli, A.M., et al., *Design and model confirmation of the intermediate scale VolturnUS floating wind turbine subjected to its extreme design conditions offshore Maine.* Wind Energy, 2016. **19**(6): p. 1161-1177.
118. Young, A.C., et al. *VolturnUS 1: 8-Scale FRP Floating Wind Turbine Tower: Analysis, Design, Testing and Performance*. in *International Conference on Offshore Mechanics and Arctic Engineering*. 2014. American Society of Mechanical Engineers.
119. Yamaguchi, H. and A. Imakita. *Learning from Field Test Regarding Damping of a Floater Motion-2mw Fowt "Fukushima Mirai"*. in *Grand Renewable Energy proceedings Japan council for Renewable Energy (2018)*. 2018. Japan Council for Renewable Energy.
120. Akel, N., *Grid stability benefits with Seatwirl vs horizontal shaft windpower plant.* 2017.
121. Ohta, M., et al. *Development of a V-shaped semi-submersible floating structure for 7MW offshore wind turbine*. in *Proceedings of the international symposium on marine and offshore renewable energy, Tokyo, Japan*. 2013.

122. Alexandre, A., et al. *Coupled analysis and numerical model verification for the 2MW Floatgen demonstrator project with IDEOL platform*. in *ASME 2018 1st International Offshore Wind Technical Conference*. 2018. American Society of Mechanical Engineers Digital Collection.
123. Guyot, M., et al. *Experimental offshore floating wind turbine prototype and numerical analysis during harsh and production events*. in *International Conference on Offshore Mechanics and Arctic Engineering*. 2019. American Society of Mechanical Engineers.
124. Connolly, A., et al. *Fully coupled aero-hydro-structural simulation of new floating wind turbine concept*. in *International Conference on Offshore Mechanics and Arctic Engineering*. 2018. American Society of Mechanical Engineers.
125. Baita-Saavedra, E., et al., *An economic analysis of an innovative floating offshore wind platform built with concrete: The SATH® platform.* Applied Sciences, 2020. **10**(11): p. 3678.
126. Vittori, F., et al., *Model tests of a 10 MW semi-submersible floating wind turbine under waves and wind using hybrid method to integrate the rotor thrust and moments.* Wind Energy Science Discussions, 2021. **2021**: p. 1-20.
127. Marijuán, A., *Offshore Floating Plataforms: Analysis of a solution for motion mitigation.* KTH Royal Institute of Technology, Stockholm, 2017.
128. Borg, M., et al., *Technical definition of the tetraspar demonstrator floating wind turbine foundation.* Energies, 2020. **13**(18): p. 4911.
129. Borg, M., et al. *Physical Model Testing of the TetraSpar Demo Floating Wind Turbine Prototype*. in *International Conference on Offshore Mechanics and Arctic Engineering*. 2019. American Society of Mechanical Engineers.
130. CSSC-HZ. *Floating wind power*. 2021 [cited 2023; Available from: http://cssc-hz.com/?en/Technologies/Floating/.
131. OffshoreWINDbiz. *CSSC installing largest floating wind turbine in China*. 2022 [cited 2023; Available from: https://www.offshorewind.biz/2022/05/30/cssc-installing-largest-floating-wind-turbine-in-china/.
132. Legaz, M.J., et al. *Study of a hybrid renewable energy platform: W2Power*. in *International Conference on Offshore Mechanics and Arctic Engineering*. 2018. American Society of Mechanical Engineers.
133. Hanssen, J.E., et al. *Design and performance validation of a hybrid offshore renewable energy platform*. in *2015 Tenth International Conference on Ecological Vehicles and Renewable Energies (EVER)*. 2015. IEEE.
134. Power, P. *W2Power*. 2010 [cited 2023; Available from: http://www.pelagicpower.no/index.html.
135. EnBW. *Floating wind turbine: Nezzy2.* 2022 [cited 2023; Available from: https://www.enbw.com/renewable-energy/wind-energy/our-offshore-wind-farms/nezzy2-floating-wind-turbine/.
136. Yde, A., et al., *Experimental and theoretical analysis of a combined floating wave and wind energy conversion platform.* 2014.
137. Ohya, Y., et al., *Wind lens technology and its application to wind and water turbine and beyond.* Renewable Energy and Environmental Sustainability, 2017. **2**: p. 2.
138. Ramakumar, R., J. Slootweg, and L. Wozniak, *Guest editorial: introduction to the special issue on wind power.* IEEE Transactions on Energy Conversion, 2007. **22**(1): p. 1-3.
139. Jonkman, J., et al., *Definition of a 5-MW reference wind turbine for offshore system development*. 2009, National Renewable Energy Lab.(NREL), Golden, CO (United States).
140. Beiter, P., et al., *Wind power costs driven by innovation and experience with further reductions on the horizon.* Wiley Interdisciplinary Reviews: Energy and Environment, 2021. **10**(5): p. e398.
141. Gaertner, E., et al., *IEA wind TCP task 37: definition of the IEA 15-megawatt offshore reference wind turbine*. 2020, National Renewable Energy Lab.(NREL), Golden, CO (United States).

142. Oceanwind, O. *DNV awards Approval in Principle for the Deepsea Semi™ floating wind foundation*. 2022 [cited 2022 Feb 2022]; Available from: https://knowledge.odfjell-oceanwind.com/news/dnv-awards-approval-in-principle-for-the-deepsea-semi-floating-wind-foundation.
143. DVVMediaGroupGmH, *AiP for floating offshore wind foundation*, in *Ship & Offshore*. 2022. p. 31.
144. Astolfi, D., R. Byrne, and F. Castellani, *Estimation of the performance aging of the vestas v52 wind turbine through comparative test case analysis.* Energies, 2021. **14**(4): p. 915.
145. Remy, T., A. Mbistrova, and I. Pineda, *Offshore Wind in Europe: Key trends and statistics 2017.* Wind Europe: Brussels, Belgium, 2018: p. 36.
146. Shahan, Z. *History of Wind Turbines*. 2014 2/3/2019]; Available from: https://www.renewableenergyworld.com/ugc/articles/2014/11/history-of-wind-turbines.html.
147. Bilgili, M., et al., *Effect of growth in turbine size on rotor aerodynamic performance of modern commercial large-scale wind turbines.* Arabian Journal for Science and Engineering, 2021. **46**(8): p. 7185-7195.
148. Desmond, C., *Summary description of LEANWIND 8 MW reference turbine 2015: 12*.
149. Bak, C., et al. *The DTU 10-MW reference wind turbine*. in *Danish Wind Power Research 2013*. 2013.
150. Wang, Q., *Design and dynamic analysis of a steel pontoon-type semi-submersible floater supporting the dtu 10mw reference turbine*. 2014, NTNU.
151. Rojas Castro, I., *Design of a 10MW Wind Turbine Rotor Blade for Testing of a Scaled-down Floating Offshore Support Structure.* 2017.
152. Tian, X., *Design, Numerical Modelling and Analysis of TLP Floater Supporting the DTU 10MW Wind Turbine*. 2016, NTNU.
153. Crozier, A., *Design and dynamic modeling of the support structure for a 10 MW offshore wind turbine*. 2011, Institutt for energi-og prosessteknikk.
154. Hegseth, J.M., E.E. Bachynski, and J.R. Martins, *Integrated design optimization of spar floating wind turbines.* Marine Structures, 2020. **72**: p. 102771.
155. Wang, S., et al., *Effects of bedplate flexibility on drivetrain dynamics: Case study of a 10 MW spar type floating wind turbine.* Renewable Energy, 2020. **161**: p. 808-824.
156. Hegseth, J.M. and E.E. Bachynski, *A semi-analytical frequency domain model for efficient design evaluation of spar floating wind turbines.* Marine Structures, 2019. **64**: p. 186-210.
157. Son, D., R. Pinguet, and D. Roddier. *Global Sizing of the WindFloat for a 10 MW Generic Wind Turbine*. in *ASME 2018 1st International Offshore Wind Technical Conference*. 2018. American Society of Mechanical Engineers.
158. Islam, M.T., *Design, Numerical Modelling and Analysis of a Semi-submersible Floater Supporting the DTU 10MW Wind Turbine*. 2016, NTNU.
159. Xue, W., *Design, numerical modelling and analysis of a spar floater supporting the DTU 10MW wind turbine*. 2016, NTNU.
160. Sclavounos, P., *Floating offshore wind turbines.* Marine Technology Society Journal, 2008. **42**(2): p. 39-43.
161. Bento, N. and M. Fontes, *Emergence of floating offshore wind energy: Technology and industry.* Renewable and Sustainable Energy Reviews, 2019. **99**: p. 66-82.
162. Mäkitie, T., et al., *The green flings: Norwegian oil and gas industry's engagement in offshore wind power.* Energy Policy, 2019. **127**: p. 269-279.
163. Bachynski, E.E., *Fixed and floating offshore wind turbine support structures.* Offshore wind energy technology, 2018: p. 103-142.
164. Borg, M. and M. Collu, *A comparison between the dynamics of horizontal and vertical axis offshore floating wind turbines.* Philosophical Transactions of the Royal Society A: Mathematical, Physical and Engineering Sciences, 2015. **373**(2035): p. 20140076.

165. Van Hees, M., et al., *Study of feasibility of and boundary conditions for a floating offshore wind turbines.* TNO, ECN, TUD, MARIN, lagerweij the Windmaster, 2002.
166. Roddier, D., et al., *WindFloat: A floating foundation for offshore wind turbines.* Journal of renewable and sustainable energy, 2010. **2**(3): p. 033104.
167. Collu, M., F. Brennan, and M. Patel, *Conceptual design of a floating support structure for an offshore vertical axis wind turbine: the lessons learnt.* Ships and Offshore Structures, 2014. **9**(1): p. 3-21.
168. Wayman, E.N., et al. *Coupled dynamic modeling of floating wind turbine systems*. in *Offshore technology conference*. 2006. Offshore Technology Conference.
169. Proskovics, R., *Floating offshore wind: A situational analysis.* Ore Catapult, 2018.
170. Sclavounos, P., et al. *Floating offshore wind turbines: tension leg platform and taught leg buoy concepts supporting 3-5 MW wind turbines*. in *European wind energy conference EWEC*. 2010.
171. Zamora-Rodriguez, R., et al. *Model scale analysis of a TLP floating offshore wind turbine*. in *ASME 2014 33rd International Conference on Ocean, Offshore and Arctic Engineering*. 2014. American Society of Mechanical Engineers.
172. Govindji, A., R. James, and A. Carvallo, *Appraisal of the Offshore Wind Industry in Japan.* Carbon Trust, 2014: p. 6-25.
173. Olondriz, J., et al., *An advanced control technique for floating offshore wind turbines based on more compact barge platforms.* Energies, 2018. **11**(5): p. 1187.
174. Arrambide, I., I. Zubia, and A. Madariaga, *Critical review of offshore wind turbine energy production and site potential assessment.* Electric Power Systems Research, 2019. **167**: p. 39-47.
175. Johannessen, M., *Concept Study and Design ofFloating Offshore Wind TurbineSupport Structure*. 2018.
176. El Beshbichi, O., Y. Xing, and M.C. Ong, *Comparative dynamic analysis of two-rotor wind turbine on spar-type, semi-submersible, and tension-leg floating platforms.* Ocean Engineering, 2022. **266**: p. 112926.
177. Zhou, Y., et al., *Initial Design of a Novel Barge-Type Floating Offshore Wind Turbine in Shallow Water.* Journal of Marine Science and Engineering, 2023. **11**(3): p. 464.
178. Andersen, B., *Design and analysis of a tension-leg-buoy floating wind turbine*. 2022, Norwegian University of Life Sciences, Ås.
179. Myhr, A., et al., *A comparison of existing and conceptual designs for floating wind turbines.* 2010.
180. Myhr, A., *Developing offshore floating wind turbines: the Tension-Leg-Buoy design.* 2016.
181. Myhr, A., K.J. Maus, and T.A. Nygaard. *Experimental and computational comparisons of the OC3-HYWIND and Tension-Leg-Buoy (TLB) floating wind turbine conceptual designs*. in *The Twenty-first International Offshore and Polar Engineering Conference*. 2011. International Society of Offshore and Polar Engineers.
182. Myhr, A. and T.A. Nygaard. *Load reductions and optimizations on tension-leg-buoy offshore wind turbine platforms*. in *The Twenty-second International Offshore and Polar Engineering Conference*. 2012. International Society of Offshore and Polar Engineers.
183. Sclavounos, P., C. Tracy, and S. Lee. *Floating offshore wind turbines: Responses in a seastate pareto optimal designs and economic assessment*. in *ASME 2008 27th International Conference on Offshore Mechanics and Arctic Engineering*. 2008. American Society of Mechanical Engineers.
184. Hall, M., B. Buckham, and C. Crawford, *Hydrodynamics-based floating wind turbine support platform optimization: A basis function approach.* Renewable Energy, 2014. **66**: p. 559-569.
185. Barter, G.E., A. Robertson, and W. Musial, *A systems engineering vision for floating offshore wind cost optimization.* Renewable Energy Focus, 2020. **34**: p. 1-16.

186. UpWind, N., *Design limits and solutions for very large wind turbines.* EWEA, Brussels, Belgium, 2011.
187. Leimeister, M., et al., *Rational upscaling of a semi-submersible floating platform supporting a wind turbine.* Energy Procedia, 2016. **94**: p. 434-442.
188. Kikuchi, Y. and T. Ishihara. *Upscaling and levelized cost of energy for offshore wind turbines supported by semi-submersible floating platforms*. in *Journal of physics: conference series*. 2019. IOP Publishing.
189. George, J., *WindFloat design for different turbine sizes.* Master's Thesis Project, Instituto Superior Técnico Technical University of Lisbon, Portugal, MS, 2014.
190. Wu, J. and M.-H. Kim, *Generic upscaling methodology of a floating offshore wind turbine.* Energies, 2021. **14**(24): p. 8490.
191. Jamieson, P., *Innovation in wind turbine design*. 2018: John Wiley & Sons.
192. Castillo Capponi, P., et al., *A Non-Linear Upscaling Approach for Wind Turbines Blades Based on Stresses.* EWEA 2011: Europe's Premier Wind Energy Event, Brussels, Belgium, 14-17 March 2011, 2011.
193. Sergiienko, N., et al., *Review of scaling laws applied to floating offshore wind turbines.* Renewable and Sustainable Energy Reviews, 2022. **162**: p. 112477.
194. Benassai, G., et al., *Optimization of mooring systems for floating offshore wind turbines.* Coastal Engineering Journal, 2015. **57**(04): p. 1550021.
195. Campanile, A., V. Piscopo, and A. Scamardella, *Mooring design and selection for floating offshore wind turbines on intermediate and deep water depths.* Ocean Engineering, 2018. **148**: p. 349-360.
196. Davidson, J. and J.V. Ringwood, *Mathematical modelling of mooring systems for wave Energy converters—A review.* Energies, 2017. **10**(5): p. 666.
197. He, Z., et al. *Mooring System Design for Floating Offshore Wind Turbine Working in Intermediate Water*. in *International Conference on Offshore Mechanics and Arctic Engineering*. 2022. American Society of Mechanical Engineers.
198. Xu, K., et al., *Design and comparative analysis of alternative mooring systems for floating wind turbines in shallow water with emphasis on ultimate limit state design.* Ocean Engineering, 2021. **219**: p. 108377.
199. Benassai, G., et al., *Mooring control of semi-submersible structures for wind turbines.* Procedia Engineering, 2014. **70**: p. 132-141.
200. Xu, K., Z. Gao, and T. Moan. *Effect of hydrodynamic load modelling on the response of floating wind turbines and its mooring system in small water depths*. in *Journal of Physics: Conference Series*. 2018. IOP Publishing.
201. Harrold, M.J., et al., *Large-scale testing of a hydraulic non-linear mooring system for floating offshore wind turbines.* Ocean Engineering, 2020. **206**: p. 107386.
202. Harrold, M.J., et al. *Demonstration of the intelligent mooring system for floating offshore wind turbines*. in *International Conference on Offshore Mechanics and Arctic Engineering*. 2019. American Society of Mechanical Engineers.
203. Longridge, K. *FLOATING WIND: WHAT ARE THE MOORING OPTIONS?* . 2020 [cited 2020 2021]; Kent Longridge, Principal Engineer, InterMoor, an Acteon company, answers our questions about the various mooring options for floating wind turbines.]. Available from: https://acteon.com/blog/floating-wind-mooring-options/.
204. Ren, X., et al. *Interaction of offshore support vessel with adjacent offshore wind turbine during maintenance operation*. in *International Conference on Offshore Mechanics and Arctic Engineering*. 2022. American Society of Mechanical Engineers.
205. Lin, Z., X. Liu, and S. Lotfian, *Impacts of water depth increase on offshore floating wind turbine dynamics.* Ocean Engineering, 2021. **224**: p. 108697.

206. Ma, K.-t., et al. *Mooring Designs for Floating Offshore Wind Turbines Leveraging Experience From the Oil & Gas Industry*. in *International Conference on Offshore Mechanics and Arctic Engineering*. 2021. American Society of Mechanical Engineers.
207. Han, Y., et al., *Stability and dynamic response analysis of a submerged tension leg platform for offshore wind turbines.* Ocean Engineering, 2017. **129**: p. 68-82.
208. Jeon, S., et al., *Dynamic response of floating substructure of spar-type offshore wind turbine with catenary mooring cables.* Ocean Engineering, 2013. **72**: p. 356-364.
209. Xu, K., *Design and analysis of mooring system for semi-submersible floating wind turbine in shallow water.* 2020.
210. Wang, J. *Novel Small Footprint Shared Anchor Mooring System for Deepwater Floating Wind Turbines*. in *ISOPE International Ocean and Polar Engineering Conference*. 2023. ISOPE.
211. Ma, Y., et al., *Research on motion inhibition method using an innovative type of mooring system for spar floating offshore wind turbine.* Ocean Engineering, 2021. **223**: p. 108644.
212. Pham, H.-D., et al., *Dynamic modeling of nylon mooring lines for a floating wind turbine.* Applied Ocean Research, 2019. **87**: p. 1-8.
213. Xiang, G., X. Xiang, and X. Yu, *Dynamic Response of a SPAR-Type Floating Wind Turbine Foundation with Taut Mooring System.* Journal of Marine Science and Engineering, 2022. **10**(12): p. 1907.
214. Azcona, J. and F. Vittori. *Mooring System Design for the 10MW Triple Spar Floating Wind Turbine at a 180 m Sea Depth Location*. in *Journal of Physics: Conference Series*. 2019. IOP Publishing.
215. Brommundt, M., et al., *Mooring system optimization for floating wind turbines using frequency domain analysis.* Energy Procedia, 2012. **24**: p. 289-296.
216. Benassai, G., et al., *Ultimate and accidental limit state design for mooring systems of floating offshore wind turbines.* Ocean Engineering, 2014. **92**: p. 64-74.
217. Trolle, J. and F. Hornbak, *Optimization of Tension Leg Buoy with regards to Stabilization Failure*, in *Department of Civil Engineering*

*Division of Structures, Materials and Geotechnics*. 2016, Aalborg University Esbjerg

Esbjerg, Denmark.
218. Wu, Y., et al. *A New Mooring System for Floating Offshore Wind Turbines: Theory, Design and Industrialization*. in *Offshore Technology Conference*. 2023. OTC.
219. Chakrabarti, S., *Handbook of Offshore Engineering (2-volume set)*. 2005: Elsevier.
220. Faltinsen, O., *Sea loads on ships and offshore structures*. Vol. 1. 1993: Cambridge university press.
221. Ma, K.-T., et al., *Mooring System Engineering for Offshore Structures*. 2019: Gulf Professional Publishing.
222. Li, Y., et al., *Analysis on restoring stiffness and its hysteresis behavior of slender catenary mooring-line.* Ocean Engineering, 2020. **209**: p. 107521.
223. Montasir, O., A. Yenduri, and V. Kurian, *Effect of mooring line configurations on the dynamic responses of truss spar platforms.* Ocean Engineering, 2015. **96**: p. 161-172.
224. Guo, S., W. Chen, and Y. Fu, *Non-linearly restoring performance of SFT's catenary mooring-lines under consideration of its dynamic behaviors.* Procedia engineering, 2016. **166**: p. 202-211.
225. Adam, F., et al., *Evaluation of internal force superposition on a TLP for wind turbines.* Renewable Energy, 2014. **71**: p. 271-275.
226. Zang, J., et al. *Steep wave and breaking wave impact on offshore wind turbine foundations–ringing re-visited*. in *25th International Workshop on Water Waves and Floating Bodies*. 2010.
227. Ridge, I., S. Banfield, and J. Mackay. *Nylon fibre rope moorings for wave energy converters*. in *OCEANS 2010 MTS/IEEE SEATTLE*. 2010. IEEE.

228. Løvstad, T., J. Namork, and A. Nilsen. *Features of a Taut Leg Mooring System For Deep Water*. in *ISOPE International Ocean and Polar Engineering Conference*. 1995. ISOPE.
229. Masuda, K., T. Ikoma, and T. Nagai. *Springing responses of a taut-moored column-footing type floating body*. in *The Fifth International Offshore and Polar Engineering Conference*. 1995. OnePetro.
230. Qiao, D. and J. Ou, *Global responses analysis of a semi-submersible platform with different mooring models in South China Sea.* Ships and Offshore Structures, 2013. **8**(5): p. 441-456.
231. Yuan, Z.-M., A. Incecik, and C. Ji, *Numerical study on a hybrid mooring system with clump weights and buoys.* Ocean engineering, 2014. **88**: p. 1-11.
232. Haslum, H., *Developer perspective and lessons learnt*, in *Subsea UK: Mooring and Anchoring Systems*. 2020.
233. Jump, E., *Mooring and Anchoring Systems-Market Projections*. 2021, Technical report no. ORE Catapult.
234. Liu, S., et al., *Proposal and Performance Study of a Novel Mooring System with Six Mooring Lines for Spar-Type Offshore Wind Turbines.* Applied Sciences, 2021. **11**(24): p. 11665.
235. Fan, H., et al. *A Novel Design of Hybrid Mooring Systems for Floating Structure in Shallow Water*. in *ISOPE International Ocean and Polar Engineering Conference*. 2022. ISOPE.
236. Pillai, A., et al., *Anchor loads for shallow water mooring of a 15 MW floating wind turbine—Part II: Synthetic and novel mooring systems.* Ocean Engineering, 2022. **266**: p. 112619.
237. Festa, O., S. Gourvenec, and A. Sobey. *Analytical model of non-linear load reduction devices for catenary moorings*. in *International Conference on Offshore Mechanics and Arctic Engineering*. 2023. American Society of Mechanical Engineers.
238. Golden, D., et al., *The Use of the Load Reduction Device and High Modulus Synthetic Lines for Improved Semi-submersible Station Keeping Performance.* 2023.
239. Zhang, Z. and C. Høeg, *Inerter-enhanced tuned mass damper for vibration damping of floating offshore wind turbines.* Ocean Engineering, 2021. **223**: p. 108663.
240. Stewart, G.M., *Load reduction of floating wind turbines using tuned mass dampers.* 2012.
241. Golden, D. *Introducing the LRD, a passive Load Reduction Device for Floating Wind Dr Tom Doyle, Dublin Offshore*. 2021 [cited 2021; Available from: https://www.researchgate.net/publication/357017723_Introducing_the_LRD_a_passive_Load_Reduction_Device_for_Floating_Wind_Dr_Tom_Doyle_Dublin_Offshore.
242. Luxmoore, J.F., et al., *Analytical performance assessment of a novel active mooring system for load reduction in marine energy converters.* Ocean Engineering, 2016. **124**: p. 215-225.
243. Harrold, M.J., et al. *Dynamic load reduction and station keeping mooring system for floating offshore wind*. in *International Conference on Offshore Mechanics and Arctic Engineering*. 2018. American Society of Mechanical Engineers.
244. Castillo, F.T.S., *Floating Offshore Wind Turbines: Mooring System Optimization for LCOE Reduction*. 2020.
245. Bjørnsen, E., *Chains in mooring systems*. 2014, Institutt for konstruksjonsteknikk.
246. Stenlund, T., *Mooring system design for a large floating wind turbine in shallow water*. 2018, NTNU.
247. Rocha, M.M., et al., *Inverse catenary load attenuation along embedded ground chain of mooring lines.* Ocean Engineering, 2016. **122**: p. 215-226.
248. Niedzwecki, J.M. *A comparison of non-metallic ropes with wire rope and chain mooring lines for deep water applications*. in *Offshore Technology Conference*. 1978. OnePetro.
249. Liu, L., et al., *Optimal structural patterns of multi-strand wire ropes.* International Journal of Solids and Structures, 2021. **225**: p. 111070.
250. DNV, G., *Design of Floating Wind Turbine Structures; 2018*. DNVGL-ST-0119. https://rules.dnvgl. com/docs/pdf/DNVGL/ST/2018-07/DNVGLST ….
251. BRIDONBEKAERT. *Drag Rope*. [cited 2023; Available from: https://www.bridon-bekaert.com/en-us/steel-and-synthetic-ropes/surface-mining/dragline-machine/drag-rope.

252. Xiang, L., et al., *Modeling of multi-strand wire ropes subjected to axial tension and torsion loads.* International Journal of Solids and Structures, 2015. **58**: p. 233-246.
253. Ghoreishi, S.R., et al., *Validity and limitations of linear analytical models for steel wire strands under axial loading, using a 3D FE model.* International Journal of Mechanical Sciences, 2007. **49**(11): p. 1251-1261.
254. Usabiaga, H. and J. Pagalday, *Analytical procedure for modelling recursively and wire by wire stranded ropes subjected to traction and torsion loads.* International Journal of Solids and Structures, 2008. **45**(21): p. 5503-5520.
255. Erdonmez, C. and C.E. Imrak, *A finite element model for independent wire rope core with double helical geometry subjected to axial loads.* Sadhana, 2011. **36**: p. 995-1008.
256. Liu, L., S. Zheng, and D. Liu, *Effect of lay direction on the mechanical behavior of multi-strand wire ropes.* International Journal of Solids and Structures, 2020. **185**: p. 89-103.
257. Ford, N. *Floating wind mooring shifts from steel to synthetic fibres*. 2020 [cited 2020; Available from: https://www.reutersevents.com/renewables/wind/floating-wind-mooring-shifts-steel-synthetic-fibres.
258. Rossi, R., C.J. Del Vecchio, and R.C.F. Gonçalves. *SS: Fiber Moorings, Recent Experiences and Research: Moorings with Polyester Ropes in Petrobras: Experience and the Evolution of Life Cycle Management*. in *Offshore Technology Conference*. 2010. OnePetro.
259. Bugg, D., D. Vickers, and C. Dorchak. *Mad Dog project: Regulatory approval process for the new technology of synthetic (polyester) moorings in the Gulf of Mexico*. in *Offshore Technology Conference*. 2004. OTC.
260. West, W., et al. *The influence of synthetic mooring line stiffness model type on global floating offshore wind turbine performance*. in *Journal of physics: conference series*. 2020. IOP Publishing.
261. generation, C.n. *CETO Technology*. 2020 [cited 2022; Available from: https://www.carnegiece.com/.
262. Johanning, L. and G. Smith, *Consideration of the cost implications for mooring MEC devices.* Deliverable D7, 2009. **3**.
263. Weller, S., P. Davies, and L. Johanning, *The influence of load history on synthetic rope response.* 2013.
264. Weller, S., et al., *Synthetic mooring ropes for marine renewable energy applications.* Renewable energy, 2015. **83**: p. 1268-1278.
265. BRINDON.BEKAERT. *MoorLine Polyester*. 2018 7/9/2019]; Available from: https://www.bridon-bekaert.com/en-gb/steel-and-synthetic-ropes/offshore-production/mooring.
266. ENERGY, O. *Petrobras Selects Dyneema Fibers for MODU Mooring Ropes*. 2011 2018]; Available from: https://www.offshore-energy.biz/the-netherlands-petrobras-selects-dyneema-fibers-for-modu-mooring-ropes/.
267. Cribbs, A., et al. *Mooring system considerations for renewable energy standards*. in *Offshore Technology Conference*. 2017. OTC.
268. Sørum, S.H., et al., *Assessment of nylon versus polyester ropes for mooring of floating wind turbines.* Ocean Engineering, 2023. **278**: p. 114339.
269. Chrolenko, M.O., *Dynamic analysis and design of mooring lines*. 2013, Institutt for marin teknikk.
270. Ma, G., et al., *Effects of different influence factors on static and dynamic analysis of mooring line.* International Journal of Engineering and Technology, 2015. **7**(2): p. 95.
271. Yang, M. and B. Teng, *Static and dynamic analysis of mooring lines by nonlinear finite element method.* China Ocean Engineering, 2010. **24**(3): p. 417-430.
272. Brown, D.T. and S. Mavrakos, *Comparative study on mooring line dynamic loading.* Marine Structures, 1999. **12**(3): p. 131-151.

273. Tahar, A. and M.H. Kim, *Coupled-dynamic analysis of floating structures with polyester mooring lines.* Ocean Engineering, 2008. **35**(17): p. 1676-1685.
274. Skop, R., *Mooring systems: a state-of-the-art review.* 1988.
275. Herbich, J.B. and K.A. Ansari, *Developments in offshore engineering.* Chapter, 1999. **5**: p. 195-255.
276. Fan, T., D. Qiao, and J. Ou, *Innovative approach to design truncated mooring system based on static and damping equivalent.* Ships and Offshore Structures, 2014. **9**(6): p. 557-568.
277. Konovessis, D., K.H. Chua, and D. Vassalos, *Stability of floating offshore structures.* Ships and offshore structures, 2014. **9**(2): p. 125-133.
278. Mavrakos, S., et al., *Deep water mooring dynamics.* Marine structures, 1996. **9**(2): p. 181-209.
279. Pascoal, R., et al., *Equivalent force model for the effect of mooring systems on the horizontal motions.* Applied Ocean Research, 2005. **27**(3): p. 165-172.
280. Pascoal, R., et al., *Assessment of the effect of mooring systems on the horizontal motions with an equivalent force to model.* Ocean engineering, 2006. **33**(11-12): p. 1644-1668.
281. Jain, R., *A simple method of calculating the equivalent stiffnesses in mooring cables.* Applied Ocean Research, 1980. **2**(3): p. 139-142.
282. Hall, M., B. Buckham, and C. Crawford, *Evaluating the importance of mooring line model fidelity in floating offshore wind turbine simulations.* Wind energy, 2014. **17**(12): p. 1835-1853.
283. Kallesøe, B.S. and A.M. Hansen. *Dynamic mooring line modeling in hydro-aero-elasticwind turbine simulations*. in *ISOPE International Ocean and Polar Engineering Conference*. 2011. ISOPE.
284. Hole, K.B., *Design of Mooring Systems for Large Floating Wind Turbines in Shallow Water*. 2018, NTNU.
285. Ghigo, A., et al. *Mooring System Design and Analysis for a Floating Offshore Wind Turbine in Pantelleria*. in *Turbo Expo: Power for Land, Sea, and Air*. 2022. American Society of Mechanical Engineers.
286. Tomren, M., *Design and Numerical Analysis of Mooring Systems for Floating Wind Turbines–Comparison of Concepts for European Waters*. 2022, NTNU.
287. Al-Solihat, M.K. and M. Nahon, *Stiffness of slack and taut moorings.* Ships and Offshore Structures, 2016. **11**(8): p. 890-904.
288. Kaasen, K.E., et al. *Development of time domain model for synthetic rope mooring systems*. in *International Conference on Offshore Mechanics and Arctic Engineering*. 2014. American Society of Mechanical Engineers.
289. Falkenberg, E., L. Yang, and V. Åhjem. *The Syrope method for stiffness testing of polyester ropes*. in *International Conference on Offshore Mechanics and Arctic Engineering*. 2018. American Society of Mechanical Engineers.
290. Falkenberg, E., V. Åhjem, and L. Yang. *Best practice for analysis of Polyester rope mooring systems*. in *Offshore Technology Conference*. 2017. OnePetro.
291. DNV, G. *DNV-RP-E305 Design, testing and analysis of offshore fibre ropes*. 2019 [cited 2020; Available from: https://www.dnv.com/oilgas/download/dnv-rp-e305-design-testing-and-analysis-of-offshore-fibre-ropes.html.
292. Flory, J.F., V. Ahjem, and S.J. Banfield. *A new method of testing for change-in-length properties of large fiber-rope deepwater mooring lines*. in *Offshore Technology Conference*. 2007. OnePetro.
293. Sørum, S.H., et al., *Modelling of Synthetic Fibre Rope Mooring for Floating Offshore Wind Turbines.* Journal of Marine Science and Engineering, 2023. **11**(1): p. 193.
294. Weller, S., S. Banfield, and J. Canedo. *Parameter estimation for synthetic rope models*. in *International Conference on Offshore Mechanics and Arctic Engineering*. 2018. American Society of Mechanical Engineers.

295. Falkenberg, E., L. Yang, and V. Åhjem. *Spring-dashpot simulations of polyester ropes: validation of the syrope model*. in *International Conference on Offshore Mechanics and Arctic Engineering*. 2019. American Society of Mechanical Engineers.
296. Francois, M. and P. Davies. *Fibre rope deep water mooring: a practical model for the analysis of polyester mooring systems*. in *Proceedings of Oil Gas Conference, Rio de Janeiro*. 2000.
297. ABS. *THE APPLICATION OF FIBER ROPE FOR OFFSHORE MOORING*. 2014 2/8/2019]; Available from: https://ww2.eagle.org/content/dam/eagle/rules-and-guides/current/offshore/90_fiberrope/fiber_rope_gn_e-feb14.pdf.
298. Chaplin, C. and C. Del Vecchio. *Appraisal of lightweight moorings for deep water*. in *Offshore Technology Conference*. 1992. Offshore Technology Conference.
299. RP, A., *Design, Manufacture, Installation, and Maintenance of Synthetic Fiber Ropes for Offshore Mooring.* 2014.
300. Francois, M., et al. *Modelling fiber rope load-elongation properties-Polyester and other fibers*. in *Offshore Technology Conference*. 2010. OnePetro.
301. Fernandes, A., C. Del Vecchio, and G. Castro, *Mechanical properties of polyester mooring cables.* International Journal of Offshore and Polar Engineering, 1999. **9**(03).
302. Huntley, M.B. *Fatigue and modulus characteristics of wire-lay nylon rope*. in *OCEANS 2016 MTS/IEEE Monterey*. 2016. IEEE.
303. Group, B.-B.R. *SuperLine™ & MoorLine ™ Nylon*. 2019 [cited 2019 02/02/2019]; 05/2018:[Available from: https://www.bridon-bekaert.com/en-gb.
304. Fontana, C.M., et al., *Multiline anchor force dynamics in floating offshore wind turbines.* Wind Energy, 2018. **21**(11): p. 1177-1190.
305. Arany, L. and S. Bhattacharya, *Simplified load estimation and sizing of suction anchors for spar buoy type floating offshore wind turbines.* Ocean Engineering, 2018. **159**: p. 348-357.
306. Zhang, L., et al., *Second-order hydrodynamic effects on the response of three semisubmersible floating offshore wind turbines.* Ocean Engineering, 2020. **207**: p. 107371.
307. Calderer, A., et al., *Fluid–structure interaction simulation of floating structures interacting with complex, large-scale ocean waves and atmospheric turbulence with application to floating offshore wind turbines.* Journal of Computational Physics, 2018. **355**: p. 144-175.
308. Jonkman, J.M., *Dynamics of offshore floating wind turbines—model development and verification.* Wind energy, 2009. **12**(5): p. 459-492.
309. Engebretsen, E., H. Haslum, and O. Aagaard. *Distributed potential theory and its application for spar-type floating offshore wind turbines*. in *International Conference on Offshore Mechanics and Arctic Engineering*. 2020. American Society of Mechanical Engineers.
310. Zhu, K., et al., *Wave diffraction and radiation from a semi-submersible floating foundation for wind turbines: A semi-analytical study.* Physics of Fluids, 2023. **35**(5).
311. Faltinsen, O.M., J. Newman, and T. Vinje, *Nonlinear wave loads on a slender vertical cylinder.* Journal of Fluid Mechanics, 1995. **289**: p. 179-198.
312. Yucheng, L. and T. Bin, *Wave action on maritime structures*. 2002, China Ocean Press Beijing.
313. Beskos, D.E., *Boundary element methods in dynamic analysis.* 1987.
314. Shoele, K., et al., *Dynamic and structural modeling of a floating wind turbine.* International Journal of Offshore and Polar Engineering, 2011. **21**(02).
315. Netzband, S., C.W. Schulz, and M. Abdel-Maksoud. *A fully coupled simulation method for floating offshore wind turbine dynamics using a boundary element method in time domain*. in *10th International Workshop on Ship and Marine Hydrodynamics IWSH*. 2017.
316. Gueydon, S., T. Duarte, and J. Jonkman. *Comparison of second-order loads on a semisubmersible floating wind turbine*. in *International Conference on Offshore Mechanics and Arctic Engineering*. 2014. American Society of Mechanical Engineers.
317. Le Roux, J., *An extension of the Airy theory for linear waves into shallow water.* Coastal Engineering, 2008. **55**(4): p. 295-301.

318. Lee, C.-H. and J. Newman, *Computation of wave effects using the panel method.* WIT Transactions on State-of-the-art in Science and Engineering, 2005. **18**.
319. Tang, J., et al. *The frequency domain analysis of a novel extended tension leg platform*. in *OCEANS 2016-Shanghai*. 2016. IEEE.
320. Lee, C.-H. and J.N. Newman, *WAMIT User manual.* WAMIT, Inc, 2006.
321. Azcona, J., et al., *State-of-the-art and implementation of design tools for floating structures*. Deliverable.
322. Bae, Y.H. and M.H. Kim, *Aero-Elastic-Control-Floater-Mooring Coupled Dynamic Analysis of Floating Offshore Wind Turbine in Maximum Operation and Survival Conditions.* Journal of Offshore Mechanics and Arctic Engineering, 2014. **136**(2).
323. Deng, S., Y. Liu, and D. Ning, *Fully coupled aero-hydrodynamic modelling of floating offshore wind turbines in nonlinear waves using a direct time-domain approach.* Renewable Energy, 2023. **216**: p. 119016.
324. Yu, Z., et al., *Fully-coupled and decoupled analysis comparisons of dynamic characteristics of floating offshore wind turbine drivetrain.* Ocean Engineering, 2022. **247**: p. 110639.
325. Håland, F., *Combining fully coupled analysis and linear potential theory time domain analysis to obtain cross sectional loads in the substructure of a floating offshore wind turbine*. 2022, NTNU.
326. Antonutti, R., et al., *The effects of wind-induced inclination on the dynamics of semi-submersible floating wind turbines in the time domain.* Renewable Energy, 2016. **88**: p. 83-94.
327. Jiang, Y., et al. *Hydrodynamic performance of a novel floating foundation for offshore wind turbine*. in *ISOPE International Ocean and Polar Engineering Conference*. 2018. ISOPE.
328. Shi, W., et al. *A comparative study on the dynamic response of three semisubmersible floating offshore wind turbines*. in *International Conference on Offshore Mechanics and Arctic Engineering*. 2019. American Society of Mechanical Engineers.
329. Zhao, Z., et al., *Analysis of dynamic characteristics of an ultra-large semi-submersible floating wind turbine.* Journal of Marine Science and Engineering, 2019. **7**(6): p. 169.
330. Shi, W., et al., *Numerical study of ice-induced loads and responses of a monopile-type offshore wind turbine in parked and operating conditions.* Cold regions science and technology, 2016. **123**: p. 121-139.
331. Coulling, A.J., et al., *Importance of Second-Order Difference-Frequency Wave-Diffraction Forces in the Validation of a FAST Semi-Submersible Floating Wind Turbine Model.* 2013(55423): p. V008T09A019.
332. Yan, J., et al., *Computational free-surface fluid–structure interaction with application to floating offshore wind turbines.* Computers & Fluids, 2016. **141**: p. 155-174.
333. Göbel, M., *Meshing Tool HydroMesh.* Projektionisten GmbH, Laboratory for Software Development, 2002.
334. JN, N. *Second-order slowly varying forces on vessels in irregular waves*. in *Proceedings of the international symposium on dynamics of marine vehicles and structures in waves. London, UK, 1974*. 1974.
335. Xu, K., et al., *A study on fully nonlinear wave load effects on floating wind turbine.* Journal of Fluids and Structures, 2019. **88**: p. 216-240.
336. Fonseca, N., J.o. Pessoa, and C. Guedes Soares. *Calculation of second order drift forces on a FLNG accounting for difference frequency components*. in *International Conference on Offshore Mechanics and Arctic Engineering*. 2008.
337. Newman, J.N., *The drift force and moment on ships in waves.* Journal of ship research, 1967. **11**(01): p. 51-60.
338. Pessoa, J.o., N. Fonseca, and C. Guedes Soares. *Experimental and numerical study of the depth effect on the first order and slowly varying motions of a floating body in bichromatic waves*. in *International Conference on Offshore Mechanics and Arctic Engineering*. 2010.

339. Bayati, I., et al. *The effects of second-order hydrodynamics on a semisubmersible floating offshore wind turbine*. in *Journal of Physics: Conference Series*. 2014. IOP Publishing.
340. Jiawen Li, A., B. Yougang Tang, and C.R.W. Yeung, *Effects of second-order difference-frequency wave forces on a new floating platform for an offshore wind turbine.* Journal of renewable and sustainable energy, 2014. **6**(3): p. 033102.
341. Roald, L., et al., *The effect of second-order hydrodynamics on floating offshore wind turbines.* Energy Procedia, 2013. **35**: p. 253-264.
342. Zhao, Z., et al. *Effects of second-order hydrodynamics on an ultra-large semi-submersible floating offshore wind turbine*. in *Structures*. 2020. Elsevier.
343. Cao, Q., et al., *Second-order responses of a conceptual semi-submersible 10 MW wind turbine using full quadratic transfer functions.* Renewable Energy, 2020.
344. Goupee, A.J., et al. *Model tests for three floating wind turbine concepts*. in *Offshore technology conference*. 2012. Offshore Technology Conference.
345. Koo, B.J., et al., *Model tests for a floating wind turbine on three different floaters.* Journal of Offshore Mechanics and Arctic Engineering, 2014. **136**(2): p. 020907.
346. Goupee, A.J., et al., *Experimental comparison of three floating wind turbine concepts.* Journal of Offshore Mechanics and Arctic Engineering, 2014. **136**(2): p. 020906.
347. Bulder, B., et al., *Study to feasibility of and boundary conditions for floating offshore wind turbines.* ECN, MARIN, TNO, TUD, MSC, Lagerway the Windmaster, 2002. **26**: p. 70-81.
348. Lee, K.H., *Responses of floating wind turbines to wind and wave excitation*. 2005, Massachusetts Institute of Technology.
349. Wayman, E.N., et al., *Coupled Dynamic Modeling of Floating Wind Turbine Systems: Preprint*. 2006, National Renewable Energy Lab.(NREL), Golden, CO (United States).
350. Fulton, G., D. Malcolm, and E. Moroz. *Design of a semi-submersible platform for a 5MW wind turbine*. in *44th AIAA Aerospace Sciences Meeting and Exhibit*. 2006.
351. Withee, J.E., *Fully coupled dynamic analysis of a floating wind turbine system*. 2004, Monterey California. Naval Postgraduate School.
352. Nielsen, F.G., T.D. Hanson, and B.r. Skaare. *Integrated dynamic analysis of floating offshore wind turbines*. in *25th International Conference on Offshore Mechanics and Arctic Engineering*. 2006. American Society of Mechanical Engineers.
353. Smith, K., *WindPACT turbine design scaling studies technical area 2: turbine, rotor and blade logistics*. 2001, National Renewable Energy Lab.(NREL), Golden, CO (United States).
354. Larsen, K. and P.C. Sandvik. *Efficient methods for the calculation of dynamic mooring line tension*. in *The First ISOPE European Offshore Mechanics Symposium*. 1990. OnePetro.
355. Park, S. and J. Choung, *Structural Design of the Substructure of a 10 MW Floating Offshore Wind Turbine System Using Dominant Load Parameters.* Journal of Marine Science and Engineering, 2023. **11**(5): p. 1048.
356. Jonkman, J.M., *Dynamics modeling and loads analysis of an offshore floating wind turbine*. 2007: University of Colorado at Boulder.
357. Svendsen, K.F., *Structural design and dynamic analysis of a tension leg platform wind turbine, considering elasticity in the hull*. 2016, NTNU.
358. Jonkman, J.M. and M.L. Buhl, *FAST user's guide*. Vol. 365. 2005: National renewable energy Laboratory Golden, CO, USA.
359. Larsen, T.J. and A.M. Hansen, *How 2 HAWC2, the user's manual*. 2007: Risø National Laboratory.
360. DNV. *Marine operations and mooring analysis software - Sima*. 2023 [cited 2023; Available from: https://www.dnv.com/services/marine-operations-and-mooring-analysis-software-sima-2324.
361. Ross, A. and G. McKinnon, *Orcina Project 1405 Wind Turbine Validation Report.* Orcina Ltd, 2018.

362. Laino, D.J. and A.C. Hansen, *User's guide to the wind turbine dynamics aerodynamics computer software AeroDyn.* Salt Lake City, UT: Windward Engineering LLC, Prepared for the National Renewable Energy Laboratory under Subcontract No. TCX-9-29209-01, 2002.
363. Moriarty, P. and A. Hansen, *AeroDyn Theory Manual, latest ed*. 2005, NREL/EL-500-36881, Golden, CO: National Renewable Energy Laboratory, December.
364. Jonkman, J., *Definition of the Floating System for Phase IV of OC3*. 2010, National Renewable Energy Laboratory (NREL), Golden, CO.
365. Jonkman, J.M., A. Robertson, and G.J. Hayman, *HydroDyn user's guide and theory manual.* National Renewable Energy Laboratory, 2014.
366. DNV, G., *Homepage of DNV GL SESAM package*. 2020.
367. DNV. *SESAM FEATURE DESCRIPTION*. 2022 [cited 2022; Available from: https://www.dnv.com/Images/Sesam-Feature-Description_tcm8-58834.pdf.
368. DNV, G., *Sesam User Manual-GeniE.* DNV GL Software, 2016.
369. DNV. *HydroD*. 2021 [cited 2021; Wave load & stability analysis of fixed and floating structures]. Available from: https://sesam.dnv.com/status/hydrod/status/hydrod_releasenotes_6.0.0.pdf.
370. Ojo, A., M. Collu, and A. Coraddu. *Parametrisation scheme for multidisciplinary design analysis and optimisation of a floating offshore wind turbine substructure–OC3 5MW case study*. in *Journal of Physics: Conference Series*. 2022. IOP Publishing.
371. Lygren, J.E.L., *Dynamic response analysis of a tension-leg floating wind turbine*. 2011, Norges teknisk-naturvitenskapelige universitet, Fakultet for ….
372. Solberg, T., *Dynamic response analysis of a spar type floating wind turbine*. 2011, Norges teknisk-naturvitenskapelige universitet, Fakultet for ….
373. Wang, Y., et al., *Linear and quadratic damping coefficients of a single module of a very large floating structure over variable bathymetry: Physical and numerical free-decay experiments.* Journal of Ocean Engineering and Science, 2022. **7**(6): p. 607-618.
374. Ormberg, H., H. Lie, and C. Stansberg, *Coupled analysis of offshore floating systems.* WIT Transactions on State-of-the-art in Science and Engineering, 2005. **18**.
375. SINTEF, O., *RIFLEX theory manual.* SINTEF Ocean: Trondheim, Norway, 2021.
376. Marintek, *SIMO—Theory Manual Version 4.0*. 2012, Marintek Trondheim, Norway.
377. SINTEF. *SIMA*. 2023; Available from: https://www.sintef.no/en/software/sima/.
378. Karimirad, M. and T. Moan, *A simplified method for coupled analysis of floating offshore wind turbines.* Marine Structures, 2012. **27**(1): p. 45-63.
379. Kvittem, M.I., E.E. Bachynski, and T. Moan, *Effects of hydrodynamic modelling in fully coupled simulations of a semi-submersible wind turbine.* Energy Procedia, 2012. **24**: p. 351-362.
380. Karimirad, M. and C. Michailides, *Fault condition effects on the dynamic response of V-shaped offshore wind turbine.* Journal of Marine Science and Technology, 2019. **24**(1): p. 34-45.
381. MARINTEK, *SIMO—User's Manual Version 3.6.* 2007.
382. Marintek, *RIFLEX User's Manual*. 2013, Sintef Ocean Trondheim, Norway.
383. Skaare, B., et al. *Integrated dynamic analysis of floating offshore wind turbines*. in *European Wind Energy Conference, Milan, Italy*. 2007. Citeseer.
384. Manwell, J.F., J.G. McGowan, and A.L. Rogers, *Wind energy explained: theory, design and application*. 2010: John Wiley & Sons.
385. Jonkman, B., *Turbsim user's guide v2. 00.00.* Natl. Renew. Energy Lab, 2014.
386. Hansen, M., *Aerodynamics of wind turbines*. 2015: Routledge.
387. Jonkman, J. and P. Sclavounos. *Development of fully coupled aeroelastic and hydrodynamic models for offshore wind turbines*. in *44th AIAA Aerospace Sciences Meeting and Exhibit*. 2006.

388. Masciola, M., et al. *Investigation of a FAST-OrcaFlex coupling module for integrating turbine and mooring dynamics of offshore floating wind turbines*. in *International Conference on Offshore Wind Energy and Ocean Energy, Beijing, China, Oct*. 2011. Citeseer.
389. Paduano, B., et al., *Experimental validation and comparison of numerical models for the mooring system of a floating wave energy converter.* Journal of Marine Science and Engineering, 2020. **8**(8): p. 565.
390. Chen, P., J. Chen, and Z. Hu, *Review of experimental-numerical methodologies and challenges for floating offshore wind turbines.* Journal of Marine Science and Application, 2020. **19**: p. 339-361.
391. Bashetty, S. and S. Ozcelik, *Review on dynamics of offshore floating wind turbine platforms.* Energies, 2021. **14**(19): p. 6026.
392. Innosea. *INNOSEA: Marine Renewable Energy Engineering Consultants*. 2023 [cited 2023; Available from: https://innosea.fr/.
393. Siemens. *Siemens Gamesa Renewable Energy*. 2023 [cited 2023; Available from: https://www.siemensgamesa.com/en-int.
394. Arramounet, V., et al. *Development of coupling module between BHawC aeroelastic software and OrcaFlex for coupled dynamic analysis of floating wind turbines*. in *Journal of Physics: Conference Series*. 2019. IOP Publishing.
395. Atalay, G.B., *FOWT Hybrid Substructure Analyses: A comparison between Orcaflex and Sima software.* 2022.
396. Wendt, F.F., A.N. Robertson, and J.M. Jonkman, *FAST model calibration and validation of the OC5-DeepCwind floating offshore wind system against wave tank test data.* International Journal of Offshore and Polar Engineering, 2019. **29**(01): p. 15-23.
397. Matha, D., et al., *Efficient preliminary floating offshore wind turbine design and testing methodologies and application to a concrete spar design.* Phil. Trans. R. Soc. A, 2015. **373**(2035): p. 20140350.
398. Laura, C.-S. and D.-C. Vicente, *Life-cycle cost analysis of floating offshore wind farms.* Renewable Energy, 2014. **66**: p. 41-48.
399. Ioannou, A., et al., *A preliminary parametric techno-economic study of offshore wind floater concepts.* Ocean Engineering, 2020. **197**: p. 106937.
400. Hall, M., B. Buckham, and C. Crawford. *Evolving offshore wind: A genetic algorithm-based support structure optimization framework for floating wind turbines*. in *2013 MTS/IEEE OCEANS-Bergen*. 2013. IEEE.
401. Thomsen, J.B., F. Ferri, and J.P. Kofoed. *Experimental testing of moorings for large floating wave energy converters*. in *Progress in Renewable Energies Offshore: Proceedings of the 2nd International Conference on Renewable Energies, 2016 (RENEW2016)*. 2016. Taylor & Francis Books Ltd.
402. Thomsen, J.B., et al., *Cost optimization of mooring solutions for large floating wave energy converters.* Energies, 2018. **11**(1): p. 159.
403. Bach-Gansmo, M.T., et al., *Parametric study of a taut compliant mooring system for a FOWT compared to a catenary mooring.* Journal of Marine Science and Engineering, 2020. **8**(6): p. 431.
404. West, W., et al., *Development of a multi-objective optimization tool for screening designs of taut synthetic mooring systems to minimize mooring component cost and footprint.* Modelling, 2021. **2**(4): p. 728-752.
405. Hallowell, S.T., et al. *Reliability of mooring lines and shared anchors of floating offshore wind turbines*. in *ISOPE International Ocean and Polar Engineering Conference*. 2017. ISOPE.
406. Fontana, C.M., et al. *Efficient multiline anchor systems for floating offshore wind turbines*. in *International Conference on Offshore Mechanics and Arctic Engineering*. 2016. American Society of Mechanical Engineers.

407. Goldschmidt, M. and M. Muskulus, *Coupled mooring systems for floating wind farms.* Energy Procedia, 2015. **80**: p. 255-262.
408. Hall, M. and P. Connolly. *Coupled dynamics modelling of a floating wind farm with shared mooring lines*. in *International Conference on Offshore Mechanics and Arctic Engineering*. 2018. American Society of Mechanical Engineers.
409. Chan Chow, M.N., *Mooring system design for a floating wind farm in very deep water-European Wind Energy Master Thesis*. 2019, NTNU.
410. Connolly, P. and M. Hall, *Comparison of pilot-scale floating offshore wind farms with shared moorings.* Ocean Engineering, 2019. **171**: p. 172-180.
411. Hallowell, S.T., et al., *System reliability of floating offshore wind farms with multiline anchors.* Ocean Engineering, 2018. **160**: p. 94-104.
412. Diaz, B.D., et al. *Multiline anchors for floating offshore wind towers*. in *OCEANS 2016 MTS/IEEE Monterey*. 2016. IEEE.
413. Ojo, A., M. Collu, and A. Coraddu, *Multidisciplinary design analysis and optimization of floating offshore wind turbine substructures: A review.* Ocean Engineering, 2022. **266**: p. 112727.
414. Stehly, T. and P. Duffy, *2020 cost of wind energy review*. 2021, National Renewable Energy Lab.(NREL), Golden, CO (United States).
415. Fingersh, L., M. Hand, and A. Laxson, *Wind turbine design cost and scaling model*. 2006, National Renewable Energy Lab.(NREL), Golden, CO (United States).
416. López-Queija, J., et al., *Review of control technologies for floating offshore wind turbines.* Renewable and Sustainable Energy Reviews, 2022. **167**: p. 112787.
417. Patryniak, K., M. Collu, and A. Coraddu, *Multidisciplinary design analysis and optimisation frameworks for floating offshore wind turbines: State of the art.* Ocean Engineering, 2022. **251**: p. 111002.
418. Muskulus, M. and S. Schafhirt, *Design optimization of wind turbine support structures-a review.* Journal of Ocean and Wind Energy, 2014. **1**(1): p. 12-22.
419. Faraggiana, E., et al., *An efficient optimisation tool for floating offshore wind support structures.* Energy Reports, 2022. **8**: p. 9104-9118.
420. Leimeister, M. and A. Kolios, *Reliability-based design optimization of a spar-type floating offshore wind turbine support structure.* Reliability Engineering & System Safety, 2021. **213**: p. 107666.
421. Tracy, C.C.H., *Parametric design of floating wind turbines*. 2007, Massachusetts Institute of Technology.
422. Veritas, D.N., *DNV-OS-J101-Design of offshore wind turbine structures.* Det Norske Veritas, 2004.
423. Yu, W., K. Müller, and F. Lemmer, *Qualification of innovative floating substructures for 10 MW wind turbines and water depths greater than 50 m*. 2015, University of Stuttgart.
424. Lefebvre, S. and M. Collu, *Preliminary design of a floating support structure for a 5MW offshore wind turbine.* Ocean Engineering, 2012. **40**: p. 15-26.
425. Matha, D., et al., *Challenges in simulation of aerodynamics, hydrodynamics, and mooring-line dynamics of floating offshore wind turbines*. 2011, National Renewable Energy Laboratory (NREL), Golden, CO.
426. Elia, A., et al., *Wind turbine cost reduction: A detailed bottom-up analysis of innovation drivers.* Energy Policy, 2020. **147**: p. 111912.
427. Zhang, J., et al., *Fatigue degradation of wind turbines considering dynamic wake meandering effects.* Engineering Structures, 2024. **300**: p. 117132.
428. Al-Sanad, S., et al., *Reliability-based design optimisation framework for wind turbine towers.* Renewable Energy, 2021. **167**: p. 942-953.

429. Papi, F. and A. Bianchini, *Technical challenges in floating offshore wind turbine upscaling: A critical analysis based on the NREL 5 MW and IEA 15 MW Reference Turbines.* Renewable and Sustainable Energy Reviews, 2022. **162**: p. 112489.
430. Azcona, J., *Design Solutions for 10 MW Floating Offshore Wind Turbines.* INNWIND Report, 2017.
431. Pegalajar-Jurado, A., et al., *D4. 5 State-of-the-art models for the two LIFES50+ 10MW floater concepts*. 2018, Technical report, Technical University of Denmark.
432. Crowle, A. and P. Thies, *Installation Innovation for floating offshore wind.* 2021.
433. Crome, T., *Hywind floating wind turbine project.* 2010.
434. Ramachandran, C., et al., *Floating offshore wind turbines: Installation, operation, maintenance and decommissioning challenges and opportunities.* Wind. Energy Sci. Discuss, 2021. **2021**: p. 15.
435. Steen, K.E. *Hywind Scotland – status and plans*. 2016 [cited 2016 2018]; Available from: https://marine.gov.scot/sites/default/files/00516548.pdf.
436. Jiang, Z., *Installation of offshore wind turbines: A technical review.* Renewable and Sustainable Energy Reviews, 2021. **139**: p. 110576.
437. eDF. *R&D up to the challenges of floating offshore wind*. 2022 [cited 2022; Available from: https://www.edfenergy.com/energywise/solutions-for-challenges-floating-offshore-wind-energy.
438. Statoil. *Hywind Scotland Pilot Park Project Plan for Construction Activities 2017*. 2017 [cited 2019; Available from: https://marine.gov.scot/sites/default/files/00516548.pdf.
439. Dnv, G., *DNVGL-ST-0119: Floating wind turbine structures.* DNV GL, 2018.
440. DNV, G., *Recommended Practice: Coupled analysis of floating wind turbines*. 2019, DNVGL-RP-0286. DNV GL AS, Høvik, Oslo, Norway.
441. Veritas, D.N., *DNV-OS-J103: Design of Floating Wind Turbine Structures.* Nor-way: DNV, DNV, 2013.
442. Veritas, D.N., *WADAM—Wave Analysis by Diffraction and Morison Theory.* SESAM user's manual, Høvik, 1994.
443. DNV, G., *Sesam user manual, HydroD: Wave loads & stability analysis of fixed and floating structures.* Oslo, Norway: DNV, GL, 2017.
444. BRIDONBEKAERT. *SuperLine Nylon*. 2022 [cited 2022; Available from: https://www.bridon-bekaert.com/en-gb/steel-and-synthetic-ropes/offshore-production/mooring/single-point-mooring-lines/superline-nylon.
445. SESAM. *FEATURE DESCRIPTION* Sesam

Software suite for hydrodynamic and structural analysis of

renewable, offshore and maritime structures 2023 [cited 2023; Available from: https://sesam.dnv.com/download/documents/SesamFeatureDescription.pdf.
446. Silva de Souza, C.E. and E.E. Bachynski, *Effects of hull flexibility on the structural dynamics of a tension leg platform floating wind turbine.* Journal of Offshore Mechanics and Arctic Engineering, 2020. **142**(1): p. 011903.
447. DNV. *DNV-RP-C202*. 2013 [cited 2019; Available from: https://dokumen.tips/documents/dnv-rp-c202-buckling-strength-of-shells.html?page=1.
448. BRIDON BEKAERT. *Permanent Mooring Spiral strand*. 2018 15/11/2018]; Available from: https://www.bridon-bekaert.com/en-gb/steel-and-synthetic-ropes/offshore-production/mooring/permanent-mooring-lines/spiral-strand.
449. Sørensen, T., et al., *Adapting and calibration of existing wake models to meet the conditions inside offshore wind farms.* EMD International A/S. Aalborg, 2008.
450. Monzón Alejandro, O.A., *Diseño De Una Central De Generacion Eolica De 20 Mw.* 2010.
451. Attias, K. and S.P. Ladany. *Optimal layout for wind turbine farms*. in *World Renewable Energy Congress-Sweden; 8-13 May; 2011; Linköping; Sweden*. 2011.

452. Yang, K. and X. Deng, *Layout optimization for renovation of operational offshore wind farm based on machine learning wake model.* Journal of Wind Engineering and Industrial Aerodynamics, 2023. **232**: p. 105280.
453. Mathiesen, M., A.K. Meyer, and B. Kvingendal, *Hywind Buchan Deep Metocean Design Basis RE2014-002*. 2014, Tech. rep., Norway, http://marine. gov. scot/sites/default/files ….
454. Veritas, D.N., *Wave analysis by diffraction and morison theory (Wadam).* SESAM User's Manual, Det Norske Veritas (DNV): Høvik, Norway, 1994.
455. Statoil. *Physical environment* 2014 20/08/2018]; Hywind Scotland Pilot Park Project – Environmental Statement]. Available from: https://www.equinor.com/content/dam/statoil/documents/impact-assessment/Hywind/Statoil-Chapter%208%20Physical%20environment.pdf.
456. Berg, J.M., *Experimental and computational study of tension leg buoy concepts for floating wind turbines*. 2013, Norwegian University of Life Sciences, Ås.
457. Sun, L., R.E. Taylor, and P.H. Taylor, *First-and second-order analysis of resonant waves between adjacent barges.* Journal of Fluids and Structures, 2010. **26**(6): p. 954-978.
458. Roald, L., J. Jonkman, and A. Robertson, *The Effect of Second-Order Hydrodynamics on a Floating Offshore Wind Turbine*. 2014, National Renewable Energy Laboratory (NREL): www.nrel.gov/publications. p. 156.
459. Commission, I.E., *Wind Turbines—Part 1: Design Requirements: International Standard IEC 61400-1.* International Electrotechnical Commission, 2005.
460. DNVGL-ST-0437, *Loads and site conditions for wind turbines*. 2016, Tech. rep., DNVGL.
461. DNV, *DNV Offshore Standard DNV-OS-E301. Position Mooring*. 2010, DNV Oslo, Norway.
462. Zhao, Z., et al., *Dynamic analysis of a novel semi-submersible platform for a 10 MW wind turbine in intermediate water depth.* Ocean Engineering, 2021. **237**: p. 109688.
463. SINTEF, O., *Simo theory manual.* SINTEF Ocean: Trondheim, Norway, 2020.
464. Cecilia, S., *Quasi-dynamic modelling of shared mooring lines for floating wind turbines*. 2022, NTNU.
465. Reig, M., I. Mendikoa, and V. Petuya. *An efficient frequency-domain based methodology for the preliminary design of FOWT substructures*. in *Journal of Physics: Conference Series*. 2024. IOP Publishing.
466. Li, Y., et al., *Influence of Vortex-Induced Loads on the Motion of SPAR-Type Wind Turbine: A Coupled Aero-Hydro-Vortex-Mooring Investigation.* Journal of Offshore Mechanics and Arctic Engineering, 2018. **140**(5).
467. Borlet, R.M., *Design and Optimization of Mooring Systems for Floating Wind Turbines*. 2016, NTNU.
468. Espedal, M.H., *Numerical Analysis of a Floating Wind Turbine-Global Load Effects in the Tower Structure*. 2016, NTNU.
469. Huang, F.-L., et al., *A new approach to identification of structural damping ratios.* Journal of Sound and Vibration, 2007. **303**(1-2): p. 144-153.
470. Jonkman, J.M. and M.L. Buhl Jr. *Loads analysis of a floating offshore wind turbine using fully coupled simulation*. in *Wind Power Conference and Exhibition, Los Angeles, CA*. 2007.
471. TC88, W., *IEC 61400-3 Wind turbines: Design requirements for offshore wind turbines*. 2005, IEC.
472. Dewan, E. and R. Good, *Saturation and the "universal" spectrum for vertical profiles of horizontal scalar winds in the atmosphere.* Journal of Geophysical Research: Atmospheres, 1986. **91**(D2): p. 2742-2748.
473. Commission, I.E., *IEC 61400-3 wind turbines Part3: design requirements for offshore wind turbines.* International Electrotechnical Commission: Geneva, Switzerland, 2009.
474. DNV, G., *DNVGL-OS-E301 Position Mooring.* DNV GL, Oslo, 2015.
475. Passon, P., et al. *OC3—Benchmark exercise of aero-elastic offshore wind turbine codes*. in *Journal of Physics: Conference Series*. 2007. IOP Publishing.

476. Gl, D., *Dnvgl-rp-c205: Environmental conditions and environmental loads.* DNV GL: Oslo, Norway, 2017.
477. Madsen, P.H. and D. Risø, *Introduction to the IEC 61400-1 standard.* Risø National Laboratory, Technical University of Denmark, 2008.
478. Imamura, H., et al. *Evaluation of turbulence model in IEC 61400-3 by NEDO guideline measurement data*. in *Proc. Jpn. Wind Energy Symp*. 2009.
479. Coelingh, J., A. Van Wijk, and A. Holtslag, *Analysis of wind speed observations on the North Sea coast.* Journal of Wind Engineering and Industrial Aerodynamics, 1998. **73**(2): p. 125-144.
480. Veritas, D.N., *DNV RP E305, On-Bottom Stability Design of Submarine Pipeline*. 1988, Oslo: Det Norske Veritas.
481. Spiess, F., *JOINT NORTH SEA WAVE PROJECT (JONSWAP) PROGRESS---AN OBSERVER'S REPORT*. 1975.
482. Veritas, D.N., *Recommended practice DNV-RP-C205: environmental conditions and environmental loads.* DNV, Norway, 2010.
483. Offshore Energy SEA. *Appendix 3 - Environmental baseline*. 2009 03/03/2019]; Available from: https://assets.publishing.service.gov.uk/government/uploads/system/uploads/attachment_data/file/194342/OES_A3d_Water.pdf.
484. Bjerkseter, C. and A. Ågotnes, *Levelised costs of energy for offshore floating wind turbine concepts.* 2013.
485. Wang, S. and T. Moan, *Serviceability limit state assessment of semi-submersible floating wind turbines.* Journal of Offshore Mechanics and Arctic Engineering, 2024. **146**(2).
486. Robertson, A., et al., *Definition of the semisubmersible floating system for phase II of OC4*. 2014, National Renewable Energy Lab.(NREL), Golden, CO (United States).
487. Godø, S.N., *Trondheim, 2013*. 2013, Norwegian University of Science and Technology.
488. Robertson, A.N. and J.M. Jonkman, *Loads Analysis of Several Offshore Floating Wind Turbine Concepts*, in *The Twenty-first International Offshore and Polar Engineering Conference*. 2011, International Society of Offshore and Polar Engineers: Maui, Hawaii, USA.
489. ACTEON. *INTERMOOR- WORLD LEADER IN MOORING TECHNOLOGY*. 2021 2021]; Available from: https://acteon.com/moorings-anchors/intermoor/.
490. Ramzanpoor, I., *Coupled Aero-Hydro-Elastic Analysis of 10MW TLB Floating Offshore Wind Turbine.* Ocean Engineering and Science, 2022.
491. Matha, D., *Model development and loads analysis of an offshore wind turbine on a tension leg platform with a comparison to other floating turbine concepts: April 2009*. 2010, National Renewable Energy Lab.(NREL), Golden, CO (United States).
492. Ren, X., *Nonlinear hydrodynamic interaction analysis of multi-platform system.* 2021.
493. Cheng, P., Y. Huang, and D. Wan, *A numerical model for fully coupled aero-hydrodynamic analysis of floating offshore wind turbine.* Ocean Engineering, 2019. **173**: p. 183-196.
494. Lackner, M.A., N. deVelder, and T. Sebastian, *On 2D and 3D potential flow models of upwind wind turbine tower interference.* Computers & Fluids, 2013. **71**: p. 375-379.
495. Subbulakshmi, A., et al., *Recent advances in experimental and numerical methods for dynamic analysis of floating offshore wind turbines—An integrated review.* Renewable and Sustainable Energy Reviews, 2022. **164**: p. 112525.
496. Alderlieste, E. and M. Dekker. *Suction pile design and installation challenges for the Ophir WHP*. in *Proceedings of the 1st Vietnam Symposium on Advances in Offshore Engineering: Energy and Geotechnics*. 2019. Springer.
497. Liu, S. and I. Janajreh, *Development and application of an improved blade element momentum method model on horizontal axis wind turbines.* International Journal of Energy and Environmental Engineering, 2012. **3**: p. 1-10.

498. Hansen, M.O.L., et al., *State of the art in wind turbine aerodynamics and aeroelasticity.* Progress in aerospace sciences, 2006. **42**(4): p. 285-330.
499. Glauert, H., *Airplane propellers.* Aerodynamic theory, 1935: p. 169-360.
500. Glauert, H., *The Analysis of Experimental Results in the Windmill Brake and Vortex Ring States of an Airscrew, R & M No. 1026.* British ARC, 1926.
501. Snel, H. and J. Schepers, *Joint investigation of dynamic inflow effects and implementation of an engineering method.* 1995.
502. Kelley, N.D. and B.J. Jonkman, *Overview of the TurbSim stochastic inflow turbulence simulator*. 2005, National Renewable Energy Lab.(NREL), Golden, CO (United States).
503. Kelley, N.D., *Full vector (3-D) inflow simulation in natural and wind farm environments using an expanded version of the SNLWIND (Veers) turbulence code*. 1992, National Renewable Energy Lab., Golden, CO (United States).
504. Jonkman, B. and L. Kilcher, *TurbSim user's guide: version 1.06. 00.* National Renewable Energy Laboratory: Golden, CO, USA, 2012.
505. Commission, I.E., *IEC 61400–2: Wind turbines—part 2: small wind turbines*. 2013, IEC, Geneva.
506. SINTEF, O., *Riflex 4.23. 0 Theory Manual.* SINTEF Ocean: Trondheim, Norway, 2022.
507. Veers, P., *Three-dimensional wind simulation, SAND88-0152.* Sandia National Laboratories, Albuquerque, NM, Tech. Rep, 1988.
508. TC88-MT, I., *Iec 61400-3: Wind turbines–part 1: Design requirements.* International Electrotechnical Commission, Geneva, 2005. **64**.
509. Commission, I.E., *IEC 61400-1.* International Standard on Wind Turbines, Part, 2005. **1**: p. 1301-1328.
510. Kreyszig, E., *Advanced Engineering Mathematics 9th Edition with Wiley Plus Set*. 2007: John Wiley & Sons.
511. Cochran, W.T., et al., *What is the fast Fourier transform?* Proceedings of the IEEE, 1967. **55**(10): p. 1664-1674.
512. Newland, D.E., *An introduction to random vibrations, spectral & wavelet analysis*. 2012: Courier Corporation.
513. Cooley, J.W. and J.W. Tukey, *An algorithm for the machine calculation of complex Fourier series.* Mathematics of computation, 1965. **19**(90): p. 297-301.
514. Chakrabarti, S.K., *Hydrodynamics of offshore structures*. 1987: WIT press.
515. Newman, B.G., *The spacing of wind turbines in large arrays.* Energy Conversion, 1977. **16**(4): p. 169-171.
516. Luo, X.-H., Xiao, R.-C., and Xiang, H.-F., *Cable element based on exact analytical expressions.* Journal of Tongji University, 2005. **33**: p. 5.
517. Yang, Y. and J.-Y. Tsay, *Geometric nonlinear analysis of cable structures with a two-node cable element by generalized displacement control method.* International Journal of Structural Stability and Dynamics, 2007. **7**(04): p. 571-588.
518. Irvine, M. *Local bending stress in cables*. in *ISOPE International Ocean and Polar Engineering Conference*. 1992. ISOPE.
519. Engineering, A.U.S.o. *MEC-E2004 Ship Dynamics (L) -Lecture 3 – Ocean waves*. [cited 2020; Available from: file:///C:/Users/xdb17245/Downloads/02.%20Lecture_SD03.pdf.
520. Hess, J.L. and A.M.O. Smith, *Calculation of nonlifting potential flow about arbitrary three-dimensional bodies.* Journal of ship research, 1964. **8**(04): p. 22-44.
521. Journée, J.M. and W. Massie, *Offshore hydromechanics.* 2000.
522. Hedges, T., *An empirical modification to linear wave theory.* Proceedings of the Institution of Civil Engineers, 1976. **61**(3): p. 575-579.
523. Lee, C., *Theory Manual.* 1995.
524. Zheng, Z., et al., *Hydrodynamic responses of a 6 MW spar-type floating offshore wind turbine in regular waves and uniform current.* Fluids, 2020. **5**(4): p. 187.

525. Sebastian, T. and M. Lackner. *A comparison of first-order aerodynamic analysis methods for floating wind turbines*. in *48th AIAA Aerospace Sciences Meeting Including the New Horizons Forum and Aerospace Exposition*. 2010.
526. Kooijman, H., et al., *DOWEC Dutch Offshore Wind Energy Converter 1997-2003 Public Reports, DOWEC 10046-009*. 2003, ECN-CX–01-135, Petten, the Netherlands: Energy Research Center of the ….
527. Newman, J.N. and C.-H. Lee, *Boundary-element methods in offshore structure analysis.* J. Offshore Mech. Arct. Eng., 2002. **124**(2): p. 81-89.
528. Ogilvie, T.F., *First-and second-order forces on a cylinder submerged under a free surface.* Journal of Fluid Mechanics, 1963. **16**(3): p. 451-472.
529. Lopez-Pavon, C., et al., *Influence of Wave Induced Second-Order Forces in Semisubmersible FOWT Mooring Design.* Journal of Offshore Mechanics and Arctic Engineering, 2015. **137**(3): p. 031602.
530. Chen, J., et al., *Coupled aero-hydro-servo-elastic methods for floating wind turbines.* Renewable Energy, 2019. **130**: p. 139-153.
531. Kim, H. and M. Kim, *Global performances of a semi-submersible 5 MW wind-turbine including second-order wave-diffraction effects.* Ocean Syst. Eng, 2015. **5**(3): p. 139-160.
532. Kim, E., A. Platt, and J. Jonkman, *2nd-order Wave Kinematics Within HydroDyn.*
533. Lee, C.-H., *On the evaluation of quadratic forces on stationary bodies.* Journal of Engineering Mathematics, 2007. **58**(1-4): p. 141-148.
534. Sebastian, T. and M. Lackner, *Characterization of the unsteady aerodynamics of offshore floating wind turbines.* Wind Energy, 2013. **16**(3): p. 339-352.
535. Isaacson, M. and K.-F. Cheung, *Time-domain solution for second-order wave diffraction.* Journal of waterway, port, coastal, and ocean engineering, 1990. **116**(2): p. 191-210.
536. Cheung, K.F., *Time-domain solution for second-order wave diffraction*. 1991, University of British Columbia.
537. Frank, W., *Oscillation of cylinders in or below the free surface of deep fluids*. Vol. 2375. 1967: Naval Ship Research and Development Center.
538. Lee, C.-H. and P. Sclavounos, *Removing the irregular frequencies from integral equations in wave-body interactions.* Journal of Fluid Mechanics, 1989. **207**: p. 393-418.
539. Chakrabarti, S.K., *Application and verification of deepwater Green function for water waves.* Journal of ship research, 2001. **45**(03): p. 187-196.
540. Liang, H., H. Wu, and F. Noblesse, *Validation of a global approximation for wave diffraction-radiation in deep water.* Applied Ocean Research, 2018. **74**: p. 80-86.
541. Newman, J.N., *Algorithms for the free-surface Green function.* Journal of engineering mathematics, 1985. **19**(1): p. 57-67.
542. Noblesse, F., *The Green function in the theory of radiation and diffraction of regular water waves by a body.* Journal of Engineering Mathematics, 1982. **16**(2): p. 137-169.
543. Ponizy, B., et al., *Numerical evaluation of free-surface Green functions.* Journal of ship research, 1994. **38**(03): p. 193-202.
544. Telste, J. and F. Noblesse, *Numerical evaluation of the Green function of water-wave radiation and diffraction.* Journal of Ship Research, 1986. **30**(02): p. 69-84.
545. Kara, F., *Coupled dynamic analysis of horizontal axis floating offshore wind turbines with a spar buoy floater.* Wind Engineering, 2023: p. 0309524X221150220.
546. Liang, H., Y. Shao, and J. Chen, *Higher-order derivatives of the Green function in hyper-singular integral equations.* European Journal of Mechanics-B/Fluids, 2021. **86**: p. 223-230.
547. Zhang, W. and O. el Moctar, *Numerical prediction of wave added resistance using a Rankine Panel method.* Ocean Engineering, 2019. **178**: p. 66-79.
548. BECK, R.F., et al., *Modern computational methods for ships in a seaway. Discussion. Author's closure.* Transactions-Society of Naval Architects and Marine Engineers, 2001. **109**: p. 1-51.

549. Wehausen, J.V. and E.V. Laitone, *Surface waves*, in *Fluid Dynamics/Strömungsmechanik*. 1960, Springer. p. 446-778.
550. Newman, J.N., *Wave effects on deformable bodies.* Applied ocean research, 1994. **16**(1): p. 47-59.
551. Qian, Y. and B. Teng, *A modified method for the singular spatial derivative of velocity potential at corners of 2D bodies and its application to second-order radiation problems.* Ocean Engineering, 2022. **243**: p. 110188.
552. Lee, C. *Second-order wave loads on a stationary body*. in *6th International Workshop on Water Waves and Floating Bodies, Woods Hole*. 1991.
553. Kim, M.-H. and D.K. Yue, *The complete second-order diffraction solution for an axisymmetric body Part 1. Monochromatic incident waves.* Journal of Fluid Mechanics, 1989. **200**: p. 235-264.
554. John, F., *On the motion of floating bodies II. Simple harmonic motions.* Communications on pure and applied mathematics, 1950. **3**(1): p. 45-101.
555. Wang, J., et al., *Investigation of second-order low-frequency wave forces approximations for moored floating structures.* Ocean Engineering, 2023. **282**: p. 114987.
556. Kim, M.-H. and D.K. Yue, *The complete second-order diffraction solution for an axisymmetric body Part 2. Bichromatic incident waves and body motions.* Journal of Fluid Mechanics, 1990. **211**: p. 557-593.
557. Gerhart, A.L., J.I. Hochstein, and P.M. Gerhart, *Munson, Young and Okiishi's Fundamentals of Fluid Mechanics*. 2020: John Wiley & Sons.
558. Ronold, K.O., et al. *Guideline for offshore floating wind turbine structures*. in *International Conference on Offshore Mechanics and Arctic Engineering*. 2010.
559. Zhao, Y., et al., *Dynamic response analysis of a multi-column tension-leg-type floating wind turbine under combined wind and wave loading.* Journal of Shanghai Jiaotong University (Science), 2016. **21**: p. 103-111.
560. Niu, W.-B., et al. *Motion Response and Aero-Elastic Analysis of Floating Offshore Wind Turbine*. in *ISOPE International Ocean and Polar Engineering Conference*. 2023. ISOPE.
561. Mohazzab, P., *Archimedes' principle revisited.* Journal of Applied Mathematics and Physics, 2017. **5**(04): p. 836.
562. Chan, G.K.Y., et al. *Computation of nonlinear hydrodynamic loads on floating wind turbines using fluid-impulse theory*. in *International Conference on Offshore Mechanics and Arctic Engineering*. 2015. American Society of Mechanical Engineers.
563. Newland, D.E., *Random Vibrations, Spectral & Wavelet Analysis.* (No Title), 1993.
564. Veritas, D.N., *Global performance analysis of deepwater floating structures.* Recommended Practice, DNV-RP-F205, 2010.
565. Ocean, D.S. *RIFLEX 4.12.2 Theory Manual*. 2018; Available from: https://home.hvl.no/ansatte/tct/FTP/H2021%20Marinteknisk%20Analyse/SESAM/SESAM%20UM%20Brukermanualer/RIFLEX%20User%20Manual.pdf.
566. Larsen, C., *Marine dynamics: TMR4182 Marine dynamics.* Akademika forlag Kompendieforlaget, Trondheim, 2014.
567. Langen, I. and R. Sigbjörnsson, *Dynamisk analyse av konstruksjoner: Dynamic analysis of structures*. 1979: Tapir.
568. Clough, R. and J. Penzien, *Of structures*. 1975: McGraw-Hill.

# Appendix A

# 1. Wind Turbine Aerodynamics

## 1.1. One-dimensional Momentum Theory

Hansen (2015) [386] conducted an in-depth analysis of wind turbine aerodynamics and aeroelasticity, providing detailed insights into the subject matter. However, the current discussion will focus on presenting the fundamental principles of aerodynamics as they relate to wind turbines. A simplified one-dimensional model representing an ideal disk is shown in Fig. 1-1, where the airflow is confined within the tube boundaries and moves from the inlet to the outlet through the rotor. This model consists of two control volumes: one from the inlet to side A, and the other from side B to the outlet. In this model, $P_0$ represents the inlet pressure, and $V_0$ signifies the inflow velocity, and $T$ inflow velocity represents the thrust force generated by the disk.

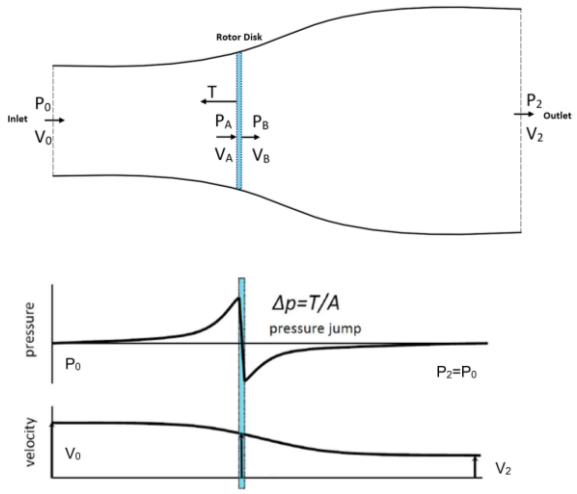


**Fig. 1-1** One-Dimensional Actuator Disk Model and Pressure and velocity drop over disk [386]

In accordance with the principle of momentum conservation from the entry to the exit, Eq. (1-1) considers the alteration in momentum due to the thrust force, $T$, the density of the fluid, $\rho$. Subsequently, by incorporating the conservation of mass within the defined control volumes (Eq. (1-2)) and utilizing the mass flow rate, $\dot{m}$, it becomes

feasible to integrate Eq. (1-1) and (1-2) to express the thrust force, $T$, as depicted in Eq. (1-3).

$$T = v_0(\rho A_0 v_0) - v_1(\rho A_1 v_1) \tag{1-1}$$

$$\rho A_0 v_0 = \rho A_1 v_1 = \dot{m} \tag{1-2}$$

$$T = \dot{m}(v_0 - v_1) \tag{1-3}$$

Bernoulli's equation is subsequently utilized on both sides of the rotor, initially assuming the presence of a pressure discontinuity across the rotor as indicated in Eq. (1-4) and (1-5).

$$P_0 + \frac{1}{2}\rho v_0^2 = P_A + \frac{1}{2}\rho v_A^2 \tag{1-4}$$

$$P_B + \frac{1}{2}\rho v_B^2 = P_1 + \frac{1}{2}\rho v_1^2 \tag{1-5}$$

Since there is no disruption in flow across the rotor and the pressure is equivalent to the surrounding ambient pressure at a distance from the disk, the velocities $v_A$ and $v_B$ are equal, and the pressures $P_0$ and $P_1$ are also equal. Therefore, Eq. (1-6) represents the pressure decrease across the rotor disk, and the resultant thrust force is equivalent to the pressure drop multiplied by the area of the rotor disk, denoted as $A$, as illustrated in Eq. (1-7).

$$P_A - P_B = \frac{1}{2}\rho(v_0^2 - v_1^2) \tag{1-6}$$

$$T = \dot{m}(v_0 - v_1) = \frac{1}{2}\rho(v_0^2 - v_1^2) \tag{1-7}$$

Since the mass flow remains constant across the rotor, it can be inferred that:

$$v_A = \frac{1}{2}(v_0 - v_1) \tag{1-8}$$

By incorporating the axial induction factor, denoted as $a$, as follows:

$$a = \frac{v_0 - v_A}{v_0} \tag{1-9}$$

It is shown that:

$$v_A = v_0(1-a) \quad \& \quad v_B = v_0(1-2a) \tag{1-10}$$

To calculate the wind power, one may consider the change in kinetic energy, or the thrust multiplied by velocity. Eq. (1-11) represents the power in relation to the induction factor. The power coefficient, as defined in Eq. (1-12), is the ratio of the power extracted by the rotor disk to the power in the incoming wind, with a speed of $v_0$, i within the area of the rotor disk.

$$P = \frac{1}{2}\rho A v_0^3 4a(1-a)^2 \tag{1-11}$$

$$C_P = \frac{P}{\frac{1}{2}\rho A v_0^3} \tag{1-12}$$

From Eq. (1-11) and (1-12), it can then be shown that:

$$C_P = 4a(1-a)^2 \tag{1-13}$$

## 1.2. Blade Element/Momentum Method

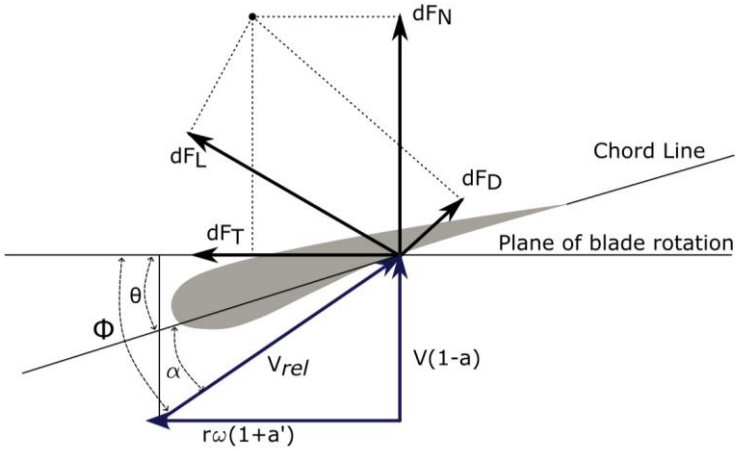


**Fig. 1-2** Velocities at The Rotor Plane [120]

Fig. 1-2 illustrates a fundamental airfoil arrangement [497], in which the vertical force acting on the rotor plane is referred to as $F_N$, with $F_D$ and $F_T$ representing the lift and drag forces, respectively. The tangential force to the rotor plane is designated as $F_T$, where $\theta$ indicates the local blade pitch angle, defined as the angle between the chord and the rotational plane at a specific location. Moreover, $r$ denotes the distance from the centre of rotation, while $\omega$ signifies the angular velocity. The wind velocity, denoted as $V_0$, is directed perpendicular to the rotor plane, and $\phi$ represents the flow angle. Additionally, $\alpha$ is the attacking angle.

The airfoil generates lift force perpendicular to the wind speed and drag force opposing it. The lift force is mainly due to pressure differences on the airfoil's surfaces, with the top surface typically experiencing higher flow velocity leading to lower pressure compared to the lower surface resulting in higher pressure. Conversely, drag force is caused by pressure variations and viscous forces [386]. By utilizing a Blade Element/Momentum Method (BEM) code within RIFLEX, it becomes feasible to compute steady loads, including thrust and power, for different wind speed, rotational speed, and pitch angle configurations [375] .

In a BEM model, certain assumptions are made [386, 498] such as

1. There is no radial dependency present which indicates that changes or interventions occurring at one element do not impact or influence the others.
2. The blades exert a continuous force on the flow within each segment, resembling a rotor with a theoretically unlimited number of blades.

In the context of an ideal rotor under the specified assumptions, the incremental axial or thrust force denoted as $dT$ and the angular torque denoted as $dQ$ on blade sectors can be determined through the application of axial and angular momentum conservation principles. These quantities are expressed in Eq. (24) and Eq. (25) as outlined by Manwell [384, 386] where, $\rho$ represents the air density, $V_0$ denotes the average air flow velocity, $r$ signifies the local blade radius, $\omega$ represents the angular rotational speed of the blade, and $a$ and $\acute{a}$ correspond to the axial and tangential induction factors, respectively.

$$dT = 4a\rho V_0^2(1-a)\pi r\, dr \tag{1-14}$$

$$dQ = 4\acute{a}\,\rho V_0 \omega(1-a)\pi r^3\,dr \tag{1-15}$$

According to the BEM approach outlined in reference [386], the respective normal coefficient $C_n$ and thrust coefficient $C_t$ can be found in Eq. (26) and Eq. (27), with $\emptyset$ denoting the angle of relative wind, and $C_l$ and $C_d$ representing the lift and drag coefficients, respectively.

$$C_n = C_l\,cos\emptyset - C_d\,sin\emptyset \tag{1-16}$$

$$C_t = C_l\,sin\emptyset - C_d\,cos\emptyset \tag{1-17}$$

The axial induction factors are outlined in Eq. (28) and Eq. (29), with $\sigma$ denoting the local solidity, which can be computed as $\sigma = Bc/2\pi r$; in this equation, $B$ represents the number of blades and $c$ signifies the local blade chord length.

$$a = \left(1 + \frac{4sin^2\emptyset}{\sigma C_n}\right)^{-1} \tag{1-18}$$

$$a' = \left(1 + \frac{4sin\emptyset cos\emptyset}{\sigma C_t}\right)^{-1} \tag{1-19}$$

Eq. (1-18) and Eq. (1-19) provide formulations for determining the values of the unknown variables $a$ and $a'$. The parameters $\emptyset$, $C_n$, and $C_t$ are dependent on these unknowns. A common approach involves the following steps [152]:

1. Initial estimation of $a$ and $a'$.
2. Computation of $\emptyset$ leading to the determination of $\alpha, C_l$ and $C_d$.
3. Iterative update of $a$ and $a'$ using Eq. (1-18) and Eq. (1-19).
4. Verification of convergence within a specified tolerance; if not met, return to step 3.

Various adjustments, such as Prandtl's tip loss factor and Glauert corrections, are essential for the successful application of the BEM method to ensure accurate outcomes.

A significant drawback of the original BEM theory is its neglect of tip loss effects and the assumption of an infinite number of blades. As illustrated in Fig. 1-3, airflow tends

to circulate around the blade tip, generating tip vortices that form multiple helical structures in the wake [363].

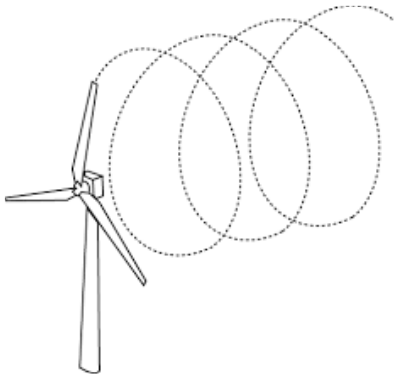

**Fig. 1-3** Helical wake pattern of single tip vortex [363]

Prandtl's tip loss factor corrects the second basic assumption that turbines function with an infinite number of blades. Hansen (2006) [498] developed a correction factor denoted as F for the equations related to thrust and torque (Eq. (1-14) and Eq. (1-15)), as presented in Eq. (1-20), where $B$ represents the blade count, $R$ signifies the overall rotor radius, $r$ denotes the local radius, and $\emptyset$ represents the flow angle.

$$F = \frac{2}{\pi}\cos^{-1}(\exp(-\frac{B(1-\frac{r}{R})}{\frac{2r\sin\emptyset}{R}}) \quad (1\text{-}20)$$

his correction factor results in adjusted equations for thrust and torque [499].

$$dT = 4\emptyset r\rho V_0^2 a(1-a)Fdr \quad (1\text{-}21)$$

$$dQ = 4\pi r^3 \rho V_0 \omega\, \acute{a}(1-a)Fdr \quad (1\text{-}22)$$

When the axial induction factor a exceeds 0.4, the BEM theory becomes invalid [497] (refer Fig. 1-4). This situation typically arises in turbines operating at high tip speed ratios, such as constant speed turbines under low wind conditions, leading to the rotor transitioning into a state known as the "turbulent wake state" [498]. During this phase, the airflow behind the rotor decelerates while the thrust on the rotor disk continues to rise. The breakdown of the BEM theory in this scenario is attributed to the

phenomenon where some of the flow in the distant wake begins to move upstream, thereby contravening the theory's second fundamental assumption [500]. In order to address this phenomenon, Glauert [500] a correction method utilizing empirical data, commonly referred to as the Glauert correction as presented in Eq. (1-23).

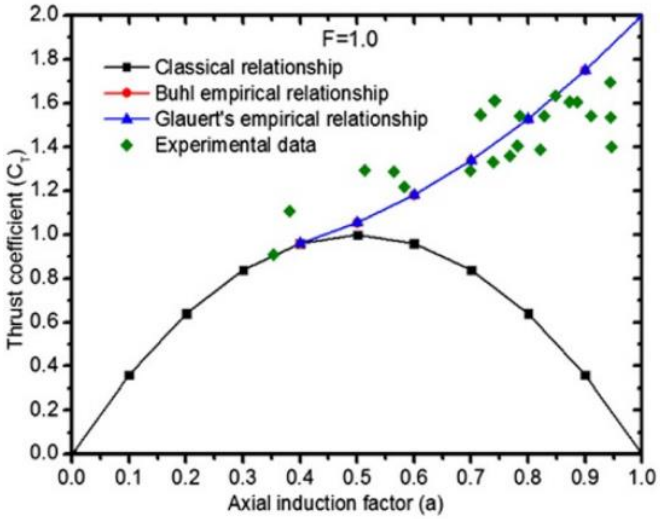


**Fig. 1-4** Different expressions for the thrust coefficient versus the axial induction factor a [497]

$$C_T = \begin{cases} 4a(1-a)F, & for\ a \le \frac{1}{3} \\ 4a\left(1-\frac{1}{4}(5-3a)a\right)F, & for\ a > \frac{1}{3} \end{cases} \quad (1\text{-}23)$$

The BEM procedure can be considered as quasi-static, where adjustments to the induction factor or output occur promptly in response to variations in wind speed, blade pitch angle, or rotor speed [352, 383]. in practical applications, wind turbines exhibit a delay in responding to these updates known as the "Dynamic wake effect," which is attributed to the time lag in induced velocities caused by the shedding and downstream convection of velocity [498]. To account for this effect in the BEM code, the "Stig Øye dynamic inflow model" can be implemented, serving as a filter for induced velocities as presented in Eq. 1-24 and Eq. 1-25 [501]. In these equations, $W_{qs}$ represents the quasi-static induced velocity vector, and $W$ denotes the new induced velocity vector, and $\tau_1$ and $\tau_2$ denote the time constants.

$$W + \tau_2 \frac{dW}{dt} = W_{int} \tag{1-24}$$

$$W_{int} + \tau_1 \frac{dW_{int}}{dt} = W_{qs} + 0.6\tau_1 \frac{dW_{qs}}{dt} \tag{1-25}$$

## 1.3. TurbSim

TurbSim [502] is a computational tool designed to simulate inflow turbulence, capable of representing all three components of the turbulent wind vector and replicating turbulent conditions observed between 50m and 120m elevations. It serves as a realistic inflow simulator, utilizing boundary layer turbulence theory to model heights of up to 200m, thus accommodating even the largest and tallest rotors. The underlying code in TurbSim bears resemblance to the preceding SNLWIND-3D [503] turbulence simulator codes. Initially, TurbSim processes a text input file to establish the necessary parameters for program execution. Fig 1-5 depicts the coordinates of a TurbSim wind field with mean flow angles of 15° horizontally and 8° vertically, while Table 1-1 illustrates the definition of the component coordinate systems. The TurbSim input data, based on the 10MW DTU Turbine, is outlined in Table 1-2.

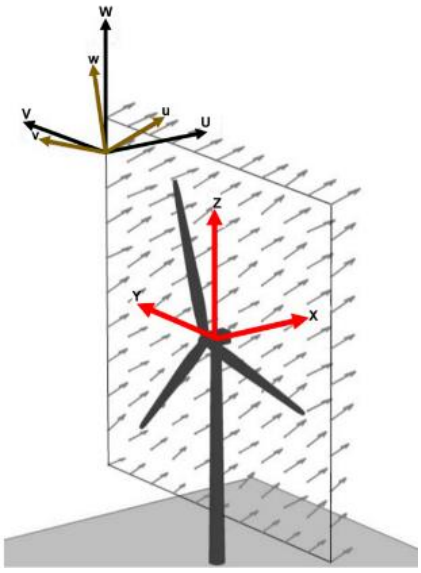


**Fig 1-5** TurbSim Wind Field Coordinates [504]

**Table 1-1** Definitions of TurbSim Wind-Component Coordinate Systems [504]

| Inertial Reference Frame | |
|---|---|
| **U** | Along positive X (nominally downwind) |
| **V** | Along positive Y (to the left when looking along X) |
| **W** | Up, along positive Z (opposite gravity) |
| **Aligned with the Mean Wind** | |
| **u** | Streamwise (longitudinal) |
| **v** | Transverse (crosswise) |
| **w** | Vertical |

**Table 1-2** TurbSim Input Data Based on the Turbine Configuration

| Input | Description | Value |
|---|---|---|
| **NumGrid_Z** | Vertical grid-point matrix dimension | 15 |
| **NumGrid_Y** | Horizontal grid-point matrix dimension | 15 |
| **HubHt** | Hub height [m] (should be > 0.5*Grid Height) | 119 |
| **GridHeight** | Grid height [m] | 200 |
| **GridWidth** | Grid width [m] (should be >=2*(Rotor Radius + Shaft Length)) | 200 |

The IEC Kaimal turbulence model is utilized to determine the velocity spectra and standard deviations for each load case and simulation [459, 505], as outlined in Table 1-3. The selected IECKAI spectral model ensures that the velocity spectra remain consistent across the grid. However, some minor variations in the u-component standard deviation may arise due to the spatial coherence model. The IEC 61400-3 [473] standard for offshore wind turbines is employed to provide input for scaling parameters, with the specific IEC turbulence type being determined for each load case. The $U_{Ref}$ values are calculated based on the load case.

**Table 1-3** TurbSim Input Data Based on the Each Load Case and Simulation

| Input | Description |
|---|---|
| **TurbModel** | Turbulence model |
| **IECstandard** | Number of the IEC standard (61400-x, x=1,2,3) with optional 61400-1 |
| **IEC_WindType** | IEC turbulence type ("NTM", "xETM", "xEWM1", or "xEWM50" for x=class 1, 2, or 3) |
| **$U_{Ref}$** | Mean wind speed at the reference height [m/s] |

The flowchart of TurbSim is depicted in Fig 1-6. The time step is configured to 0.05 seconds, as advised for the majority of simulations and the highest frequency employed in the inverse Fast Fourier Transform (FFT). The total duration of the data under analysis spans three hours.

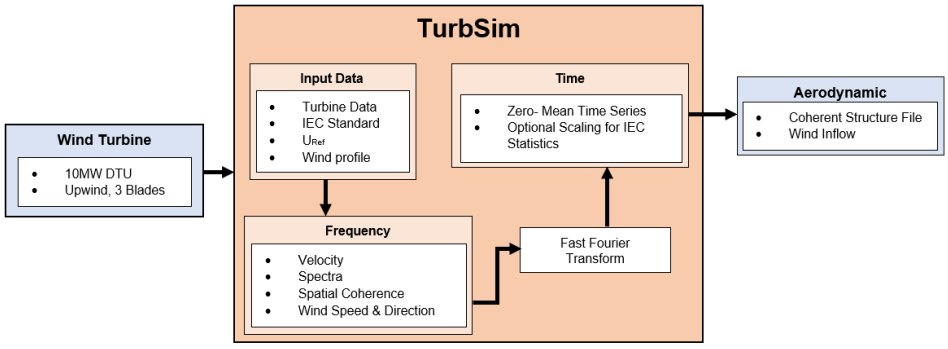


**Fig 1-6** Overview of the TurbSim Simulation Method

The aerodynamic model implemented in Riflex is based on the blade element momentum theory [384]. Dynamic stall and dynamic wake effects are accounted for with the Øye models [386], Glauert's correction is used for high induction factors outside the validity range of the BEM theory, and Prandtl's correction is used for hub and tip losses [446]. Riflex elements can be bar elements or beam elements, and further theory on the element formulations in Riflex can be found in SINTEF Ocean (2022a) [506]. TurbSim employs interpolation techniques to create wind speed grids in both temporal and spatial dimensions. It is capable of generating input files for software applications like SIMA. TurbSim utilizes an inverse fourier transform method to produce time series, incorporating velocity components and spatial coherence in the frequency domain, which are defined by spectra. This approach assumes stationarity, leading TurbSim to overlay coherent turbulent structures onto the stationary time series (Jonkman and Kilcher 2022) [385].

This simulation tool utilizes the finite element solver from the combined SIMO/RIFLEX tool, transmitting position and velocity data to the aerodynamic code at the initial iteration of each time step and receiving lumped forces along the wind turbine blades. The body's fixed rotor coordinate system is assumed to have its origin at the hub centre, with the Z-axis aligned with the rotor shaft and in the direction of the hub support. Wind loads on the blades are calculated using the load coefficient description in the aerofoil library file and a double-multiple stream tube blade element momentum method, which accounts for dynamic stall effects.

## 1.4. Spectra Models

TurbSim uses a modified version of the Sandia method [507] to generate time series based on spectral representation. Several different spectral models are available, including two IEC models, the Risø smooth-terrain model, and several NREL site-specific models. Standard deviations, σ, have been calculated by integrating the velocity spectra, S:

$$\sigma^2 = \int_0^\infty S\,(f)df$$

The IEC Kaimal model is defined in IEC 61400-1 2nd [477], and 3rd ed. [478, 508]. The spectra for the three wind components, K = u, v, w, are given by

$$S_K(f) = \frac{4f\ {\sigma_K}^2 \left(\frac{L_K}{U_{Hub}}\right)}{\left(1 + 6f\left(\frac{L_K}{U_{Hub}}\right)\right)^{5/3}}$$

Where $S_K(f)$ is the single-sided velocity component spectrum, $\sigma_K$ is the velocity component standard deviation, $f$ is the frequency in Hertz, $K$ is the index referring to the velocity component direction, $L_K$ is the velocity component integral scale parameter. For further info please refer to [385, 509].

## 1.5. The Fast Fourier Transform Algorithm

The fundamental principle underlying the Fourier transform is the representation of a piecewise continuous and integrable function $f$ as a combination of sinusoidal oscillations across all possible frequencies (Kreyszig, 2007, p. 520) [510] . The Fourier transform is employed to analyse the frequency composition within a function $f$, with the individual harmonics comprising $f$ being termed as Fourier components. The frequency composition of a function is typically illustrated in a frequency spectrum. Furthermore, the Fourier transform has a corresponding inverse known as the inverse Fourier transform. The Fourier transform and its inverse are denoted by Eq. (1-25) and

Eq. (1.26), respectively. The operators for the Fourier transform and inverse Fourier transform are commonly represented as $\mathcal{F}$ and $\mathcal{F}^{-1}$, while the Fourier transform of the function $f$ f is often denoted as $\hat{f}$. The Fourier transform maps the input function $f(t)$ to another function $\hat{f}(\omega)$ that is dependent on frequency and is therefore commonly referred to as the frequency domain representation of $f(t)$, with $f(t)$ being the time domain representation.

$$\mathcal{F}\left(f(x)\right) = \hat{f}(x) = \frac{1}{\sqrt{2\pi}} \int_{-\infty}^{\infty} f(x)\, e^{-i\omega x}\, dx \tag{1-25}$$

$$\mathcal{F}^{-1}\left(\hat{f}(x)\right) = f(x) = \frac{1}{\sqrt{2\pi}} \int_{-\infty}^{\infty} \hat{f}(\omega)\, e^{-i\omega x}\, d\omega \tag{1-26}$$

When the waveform is sampled, the discrete Fourier transform (DFT) must be utilized, as stated by Cochran et al. (1967) [511]. The DFT and its inverse are defined by Eq. 1-27 and Eq. 1-28, respectively, according to Kreyszig (2007, p. 525) [510] . In these equations, $f(x_r)$ represents the value of sample $r$, and $N$ denotes the total number of sample points. The Fourier transform is a function of $k$, which is associated with frequency as $f = kfs/N$. Consequently, the frequency resolution from the FFT is expressed as $f_s$ . $\frac{1}{N}$ .

$$\hat{f}(k) = \sum_{r=0}^{N-1} f(x_r)\, e^{-i\left(\frac{2\pi kr}{N}\right)} \qquad k = 0, \ldots\ldots, N-1 \tag{1-27}$$

$$f(x_r) = \sum_{k=0}^{N-1} \hat{f}(k)\, e^{-i\left(\frac{2\pi kr}{N}\right)} \qquad r = 0, \ldots\ldots, N-1 \tag{1-28}$$

The FFT is an algorithm used to compute the discrete Fourier transform (DFT) at a significantly faster rate than the direct method (Newland, 2012, p. 150) [512]. Cooley and Tukey (1965) [513] first introduced the FFT as an efficient algorithm for computing the DFT of a series of data samples. This method has greatly enhanced signal analysis

and filter simulation capabilities on digital computers, substantially reducing the computational burden associated with DFT calculations compared to previous algorithms (Cochran et al., 1967) [511] . It can be demonstrated that the discrete Fourier transform can analyse frequencies up to half of the sampling rate, $f_s/2$ (Newland, 2012, p. 120) [512].

# Appendix B

# 1. Hydrodynamics Loads on FOWTs

The hydrodynamic assessment of an offshore structure typically involves the identification of sea conditions at the specific site depth, the selection of relevant wave theory, the choice of suitable methods for computing hydrodynamic loads, and the calculation of structural response. A typical procedure for evaluating the hydrodynamic loads on large marine structures is to find excitation forces and radiation forces from linear potential flow theory and subsequently add nonlinear excitation forces such as drag forces from the Morison equation if these are of importance. The hydrodynamic loads from linear potential flow theory is covered in detail by Chakrabarti (1987) [514]. When finding the hydrodynamic loads given from linear potential flow theory, the diffraction and radiation velocity potentials are first found with panel methods, as described in Section 2.4. The hydrodynamic loads are then found by integrating the fluid pressure over the mean wetted body surface. The fluid pressure is given by Bernoulli's equation.

The total pressure forces on a submerged body can be found by integrating the pressure given by Bernoulli over the instantaneous wetted body surface, SB. Total pressure consists of three terms. These are: the dynamic fluid pressure, quadratic pressure that contributes to second-order forces, hydrostatic pressure, providing hydrostatic buoyancy and restoring forces. When integrating the hydrodynamic pressure given by Bernoulli in linear wave theory, the second order term in Bernoulli is neglected and pressure is integrated over the mean wetted surface of the submerged body in order to be consistent with the linearisation used in the BVP.

## 1.1. Wave Loads on Slender Structures

The wave-induced loads on offshore structures are influenced by both potential flow effects and viscous effects. Typically, potential flow theory is utilized for large

structures, while Morison's equation is commonly employed for slender structures experiencing viscous forces, particularly in long wave conditions (λ>5D).

## 1.2. Morison's Equation

Fig. 1-1 shows that in small and moderate waves, mass forces are predominant, whereas in extreme waves, viscous forces take precedence. Morison's equation for a fixed structure is represented by Eq. (1-1) [220] where the force direction $F$ is positive in the wave propagation direction, $\rho$ denotes the density of sea water, $A$ represents the wetted surface area, $u$ and $a$ stand for the horizontal undisturbed fluid velocity and acceleration at the midpoint of the strip, respectively. Additionally, $C_A$ and $C_D$ are the non-dimensional added mass coefficient and non-dimensional drag coefficient, respectively, while $(1 + C_A)$ defines the mass coefficient $C_M$.

$$F = \rho A(1 + C_A)a + \frac{1}{2}\rho C_D D|u|u \tag{1-1}$$

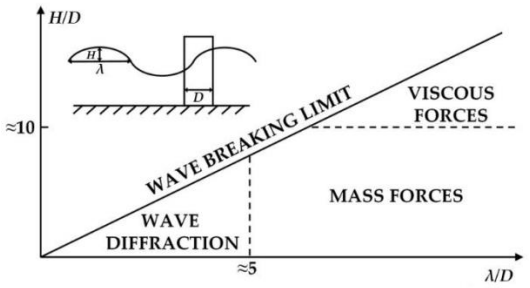


**Fig. 1-1** Relative importance of mass, viscous drag and diffraction forces on marine structures [220]

In the case of a moving structure, where the horizontal rigid body motion is represented by $\eta_1$, the Morison equation can be adjusted as shown in Eq. (1-2), where $u - \dot{\eta}_1$ denotes the relative velocity between the moving structure and the fluid velocity.

$$F = -\rho A C_A \ddot{\eta}_1 + \rho A(1 + C_A)a + \frac{1}{2}\rho C_D D|u - \dot{\eta}_1|(u - \dot{\eta}_1) \tag{1-2}$$

The drag force component in Eq. (1-1) and Eq. (1-2) is identified as the primary contributor to viscous damping, which serves to diminish the amplitude of movements in platforms. It is evident from Eq. (1-1) and Eq. (1-2) that the drag force is

characterized as a quadratic expression of the relative velocity, necessitating linearization for the incorporation of drag force in frequency domain assessments.

If the structure's response is harmonic, the wave velocity can be determined from Eq. (1-3).

$$\eta = \eta_1 \cos(\omega t) + \eta_2 \sin(\omega t) \tag{1-3}$$

The linearized drag force can be expressed as follows.

$$dF_{drag,L} = \frac{4\rho C_D DA}{3\pi}(u - \dot{\eta}_1) \tag{1-4}$$

The viscous damping coefficient resulting from the linearized drag force is

$$B_{viscous} = \frac{4\rho C_D DA}{3\pi} \tag{1-5}$$

The value of A is determined by the following equation:

$$A = \sqrt{(u - \omega\eta_2)^2 + (\omega\eta_1)^2} \tag{1-6}$$

It is evident that the variable A is influenced by the movements of the structure, indicating that the viscous damping is likewise contingent upon the motions of the platform.

## 1.3. Hydrodynamic Coefficients

The drag coefficient $C_D$ represents a dimensionless drag force, as expressed in Eq. (1-7) [482] where $f_{drag}$ denotes the sectional drag force (N/m), $D$ stands for the diameter, and $v$ represents the velocity. Typically, the drag force acts in the direction of the fluid velocity and can be resolved into a normal force $f_N$ a tangential force $f_T$, as illustrated in Fig. 1-2. The added mass coefficient $C_A$ is a dimensionless added mass parameter defined in Eq. (1-8), where $m_a$ denotes the added mass per unit length (kg/m), and $A$ represents the cross-sectional area.

$$C_D = \frac{f_{drag}}{\frac{1}{2}\rho D v^2} \tag{1-7}$$

$$C_A = \frac{m_a}{\rho A} \tag{1-8}$$

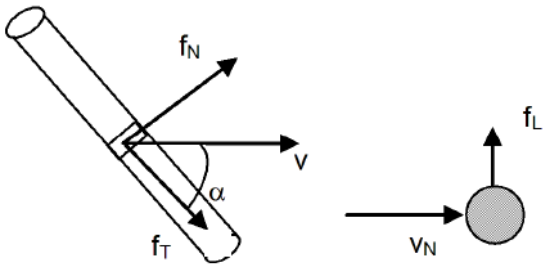


**Fig. 1-2** Definition of normal force, tangential force and lift force on slender structure [482]

## 1.4. Added Mass and Moments

Newman provided the added mass coefficients for 2D bodies by using conformal mapping techniques [515], see Fig. 1-3. $m_{11}$ corresponds to longitudinal acceleration; $m_{22}$ to lateral acceleration in equatorial plane; $m_{66}$ denotes the rotational added moment of inertia.

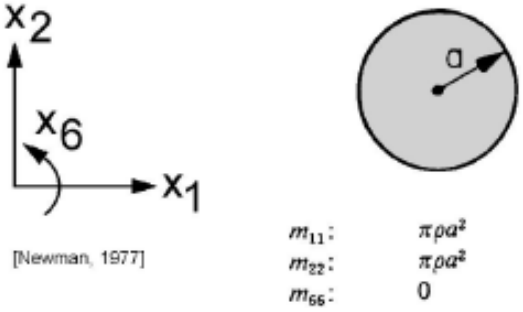


**Fig. 1-3** Added Mass Coefficients of 2D Bodies [515]

## 1.5. Mooring System Stiffness

The stiffness properties of an individual mooring line are regarded as a constituent of the overall stiffness of a mooring system. When examining a single mooring line suspended at point $P$, as shown in Fig. 1-4, the horizontal and vertical tension components at the upper attachment point are denoted as $H$ and $V$, respectively. Eq. (1-11) presents the formulation of the stiffness matrix of the cable within the plane of the cable profile [516, 517].

$$K^P = \begin{bmatrix} K_{11}^P & K_{12}^P \\ K_{21}^P & K_{22}^P \end{bmatrix} = \begin{bmatrix} \frac{\partial H}{\partial l} & \frac{\partial H}{\partial h} \\ \frac{\partial V}{\partial l} & \frac{\partial V}{\partial h} \end{bmatrix} \tag{1-11}$$

When the tension in the mooring line is sufficient to lift it off the seabed, as depicted in Fig. 1-4(a) where $V > W$, the line forms a non-zero angle with the seabed. This scenario can be analysed statically using the equation of an elastic catenary, which can be solved numerically based on the unstretched cable length $L_o$, weight $W$, extensional stiffness ($EA$) and cable end coordinates, as illustrated in Fig. 1-4 (a) [518]. In contrast, in slack mooring systems like those utilized in the ITI barge and the OC3 Spar platforms for offshore floating wind turbines [488], the mooring line forms a zero angle with the seabed. In such cases, where part of the line rests on the seabed and the anchor point experiences only horizontal tension as shown in Fig. 1-4(b) the catenary equation can be modified accordingly, as proposed by Pascoal (2005) [279]. Furthermore, when the mooring line is taut and free of sag, i.e., $\frac{H}{V} \approx \frac{l}{h}$, it can be accurately modelled as a massless linear spring to simplify computations. The stiffness of the tether along its chord, $L$, can be assumed to be equal to $K_I = \frac{EA}{L_o}$, as shown in Fig. 1-4 (c).

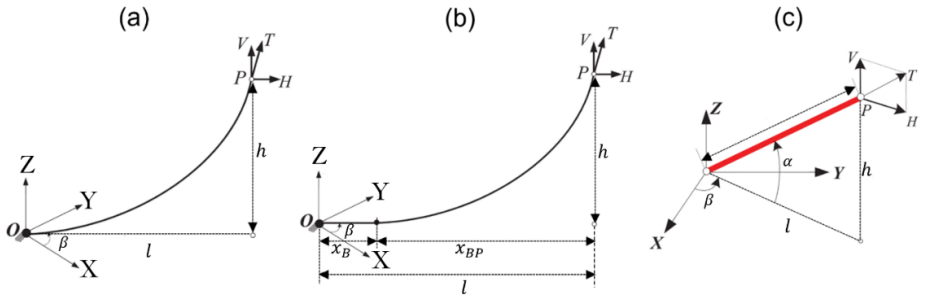


**Fig. 1-4** (a) Suspended line, (b) slack line resting on the seabed and (c) taut line

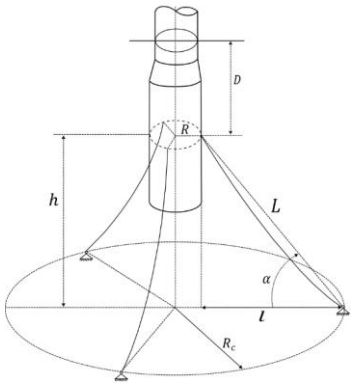


**Fig. 1-5** Symmetric $n$ -tethered system (sketched for $n$ = 3 for clarity) referred to as 'slack catenary' and 'taut-leg' mooring system for slack and taut lines, respectively.

Al-Solihat [287] utilized the massless spring assumption to simplify the analysis, while still maintaining an accurate approximation of the stiffness for the taut mooring system. In the equilibrium configuration of a catenary mooring system consisting of $n$ lines ($n$ ≥3), it is assumed that the anchors are evenly distributed in a circular pattern with a radius of $R_C$ and spaced $\frac{2\pi}{n}$ radians apart. The fairlead distance to the waterline is denoted as $D$, and the fairlead distance to the seabed is denoted as $h$. $T$ represents the tension per mooring line, $L$ is the length of the mooring line, and $K_I = \frac{EA}{L}$ represents the stiffness of the tether along its chord. The upper attachment point has a radius of $R$, and the circumferential distribution of the attachment points is similar to that of their corresponding anchors, as illustrated in Fig. 1-5.

The stiffness matrix of the complete mooring system at its equilibrium state is symmetrical and can be represented as show in Eq. (1-12).

$$K_m = \begin{bmatrix} \mathrm{K}_{11} & 0 & 0 & 0 & \mathrm{K}_{15} & 0 \\ 0 & \mathrm{K}_{22} & 0 & \mathrm{K}_{24} & 0 & 0 \\ 0 & 0 & \mathrm{K}_{33} & 0 & 0 & 0 \\ 0 & \mathrm{K}_{42} & 0 & \mathrm{K}_{44} & 0 & 0 \\ \mathrm{K}_{51} & 0 & 0 & 0 & \mathrm{K}_{55} & 0 \\ 0 & 0 & 0 & 0 & 0 & \mathrm{K}_{66} \end{bmatrix} \quad (1\text{-}12)$$

For catenary mooring system stiffness matrix can be obtained by Eq. (1-13) to Eq. (1-22)

$$K_{11} = \frac{n}{2}\left[K_{11}^{P} + \frac{H}{l}\right] \quad (1\text{-}13)$$

$$K_{15} = -n\left[\frac{R}{2}K_{12}^{P} + \frac{D}{2}K_{11}^{P} + \frac{DH}{l}\right] \quad (1\text{-}14)$$

$$K_{22} = K_{11} \quad (1\text{-}15)$$

$$K_{24} = -K_{15} \quad (1\text{-}16)$$

$$K_{33} = n\,K_{22}^{P} \quad (1\text{-}17)$$

$$K_{42} = K_{24} \quad (1\text{-}18)$$

$$K_{44} = n\left[-DR\,K_{12}^{P} + \frac{D^2}{2}K_{11}^{P} + \frac{R^2}{2}K_{22}^{P} + DV + \frac{HR}{2} + \frac{D^2H}{2l}\right] \quad (1\text{-}19)$$

$$K_{51} = K_{15} \quad (1\text{-}20)$$

$$K_{55} = K_{44} \quad (1\text{-}21)$$

$$K_{66} = n\left[\frac{HR^2}{l} + HR\right] \quad (1\text{-}22)$$

The stiffness matrix of a symmetric taut mooring system can be obtained by Eq. (1-23) to (1-32). $\alpha$ is the angle at which the mooring line is attached to the fairlead.

$$K_{11} = \frac{n}{2}\left[\frac{T}{L}(1 + sin^2\,\alpha) + K_I\,cos^2\,\alpha\right] \quad (1\text{-}23)$$

$$K_{15} = -n\left[\frac{T}{2L}(D + D\,sin^2\,\alpha) + R\,sin\,\alpha\,cos\,\alpha) + \frac{K_I}{2}(Dcos^2\alpha - R\,sin\,\alpha\,cos\,\alpha\right] \quad (1\text{-}24)$$

$$K_{22} = K_{11} \quad (1\text{-}25)$$

$$K_{24} = -K_{15} \quad (1\text{-}26)$$

$$K_{33} = n\left[\frac{T}{L}cos^2\,\alpha + K_I\,sin^2\,\alpha\right] \quad (1\text{-}27)$$

$$K_{42} = K_{24} \quad (1\text{-}28)$$

$$K_{44} = n\left\{T\,(D\,sin\,\alpha + \frac{R}{2}\,cos\,\alpha) + \frac{T}{2L}[(R\,cos\,\alpha + D\,sin\,\alpha)^2 + D^2] + \frac{K_I}{2}(D\,cos\,\alpha - R\,sin\,\alpha)^2\right\} \quad (1\text{-}29)$$

$$K_{51} = K_{15} \tag{1-30}$$

$$K_{55} = K_{44} \tag{1-31}$$

$$K_{66} = n\frac{TR}{L}(R + L\,cos\,\alpha) \tag{1-32}$$

### 1.5.1. Natural Periods Estimation

The natural periods in surge, sway and heave motion can be estimated by Eq. (1-33) to Eq. (1-35) respectively if the surge, sway or heave motion is assumed as uncoupled from other rigid-body motions. And the natural periods in pitch, roll and yaw are given by Eq. (1-36) and Eq. (1-37).

$$T_{11} = 2\pi\sqrt{\frac{M_{11}+A_{11}}{K_{11}}} \tag{1-33}$$

$$T_{22} = T_{11} \tag{1-34}$$

$$T_{33} = 2\pi\sqrt{\frac{M_{33}+A_{33}}{C_{33}+K_{33}}} \tag{1-35}$$

$$T_{44} = T_{55} = 2\pi\sqrt{\frac{M_{55}+A_{55}}{C_{55}+K_{55}}} \tag{1-36}$$

$$T_{66} = 2\pi\sqrt{\frac{M_{66}+A_{66}}{K_{66}}} \tag{1-37}$$

## 1.6. Potential Flow Theory

This section provides an overview of the fundamental principles of linear potential flow theory, a topic extensively discussed in various scholarly works, including Chakrabarti (1987) [514]. In potential flow theory, the flow velocity is characterized as the derivative of a scalar quantity known as the velocity potential $\emptyset$. The flow velocity field can be expressed as per Eq. (1-38), with $u$, $v$, and $w$ denoting the velocity components in the $x-$, $y-$, and $z-$directions, respectively.

$$V = i\frac{\partial\emptyset}{\partial x} + j\frac{\partial\emptyset}{\partial y} + k\frac{\partial\emptyset}{\partial z} = iu + jv + kw \tag{1-38}$$

The overall pressure within the fluid in relation to the atmospheric pressure, denoted as pa, can be mathematically represented using Bernoulli's equation as shown in Eq. (1-39). Here, $\rho$ represents the density of the fluid, commonly around 1025 kg/m$^3$ for seawater, $g$ denotes the acceleration due to gravity, typically assumed as 9.81 m/s$^2$, $\nabla$ signifies the vector differential operator, and $z$ represents the $z$-coordinate.

$$p - p_a = -\rho\left(\frac{\partial \emptyset}{\partial t} + \frac{1}{2}|\nabla \emptyset|^2 + gz\right) \quad (1\text{-}39)$$

According to Bernoulli's equation, the fluid pressure, denoted as $p$, can be represented as a function of the velocity potential. This implies that the four unknowns $u, v, w$, and $p$ can effectively be reduced to a single unknown, the velocity potential $\phi$, when potential flow theory is employed. Several key assumptions are necessary to fully characterize the velocity field using a velocity potential $\phi$, including irrotational flow and an inviscid fluid. In practical applications, the assumption of incompressible fluid is commonly utilized, despite the potential for potential flow theory to describe compressible fluids. Potential flow theory can exhibit both linear and non-linear behaviour. When determining the velocity potential, a boundary value problem (BVP) is solved using the perturbation method, where the unknowns are expanded in powers of the wave steepness, defined as $\epsilon = k\zeta a$. Here, $k$ represents the wave number and is given by $k = 2\pi/\lambda$, with λ denoting the wavelength. The boundary conditions in the BVP are Taylor expanded, and the power series is inserted into the boundary conditions. In the context of linear potential flow theory, only the first-order terms are retained, corresponding to terms proportional to $\epsilon$. The superposition principle is applicable to the unknown potential in this case, as all the governing equations in the BVP are linear. Further detailed explanations of this BVP linearization can be found in various hydrodynamics texts, such as Chakrabarti (1987, p. 244) [514]. The Linear Airy Wave Theory (LAWT) is a mathematical model that describes the behaviour of waves in various media, such as water, soil, and air. It is particularly useful in understanding the propagation of waves in the ocean and their interaction with the seafloor. The response amplitude operator can be found under the assumption of linear wave theory [325]. Extensive details regarding the linear airy wave theory can be found in the specified reference [519].

## 1.7. Panel methods - solution of the potential flow problem

Panel method, also known as boundary element methods (BEM), are numerical techniques utilized to compute the radiation and diffraction potential flow produced in the vicinity of bodies with arbitrary shapes (Chakrabarti 2005, p. 160) [219]. These methods are commonly employed for analysing the linear steady state response of large-volume structures in regular waves (Faltinsen 1993, p. 102) [220], as well as for addressing the second-order potential flow problem (Chakrabarti 2005, p. 161) [219]. The initial numerical solution for potential flow around an arbitrary body moving in an infinite fluid using panel methods was developed by Hess and Smith in 1964 [520]. Panel methods are also commonly called boundary element methods (BEM) and there exist multiple different types of panel methods (Faltinsen 1993, p. 102) [220]. Panel methods involve transforming the three-dimensional Laplace equation over the entire fluid volume into a surface integral equation over the boundaries of the solution domain using Green's theorem. This integral is then solved numerically by dividing the boundary into small elements, each of which must satisfy the Laplace equation with appropriate boundary conditions. The resulting set of integral equations allows for the determination of individual velocity potentials, with the total velocity potential being the superposition of these potentials (Journee and Massie 2000) [521]. It is important to note that panel methods are based on potential flow theory and are therefore limited by the assumptions and simplifications inherent in this theory. Consequently, they may not yield accurate results in cases where viscous effects are significant, such as in structures like risers or tethers, or in situations with substantial viscous damping, such as the rolling motions of a ship (Faltinsen 1993, p. 102) [220].

## 1.8. Coordinate System

In the presence of specific sea conditions such as waves, currents, and wind, floating platforms experience induced loads and motions. Consequently, it is necessary to establish a clear definition of these motions, as different structures may be affected by different types of motion. In a linear system, the oscillatory translational and rotational

motions are categorized as surge, sway, heave, roll, pitch, and yaw (refer to Fig. 1-6). Additionally, the degrees of freedom for floating wind turbines are outlined in Table 1-1.

**Table 1-1** Definition of Degrees of Freedom

| DOF | Description |
|---|---|
| **Surge** | Translation along the longitudinal axis |
| **Sway** | Translation along the lateral axis |
| **Heave** | Translation along the vertical axis |
| **Roll** | Rotation about the longitudinal axis |
| **Pitch** | Rotation about the lateral axis |
| **Yaw** | Rotation about the vertical axis |

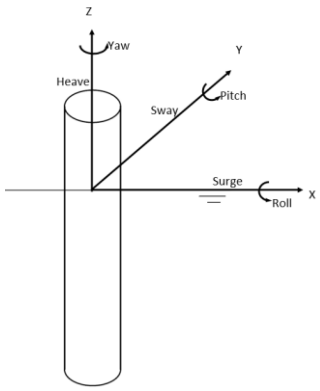


**Fig. 1-6** Coordinate System and Rigid-Body Motions

## 1.9. Wave Loads on Large Volume Structures

The Airy wave theory, also known as linear wave theory, is widely utilized in the offshore industry for medium and large water depths [522]. In potential flow theory [220, 311, 312], the fluid is considered inviscid, irrotational, and incompressible. By incorporating these assumptions into linear theory, the problem of linear wave-body interaction can be simplified to determine the velocity potential, $\phi$, which satisfies the Laplace equation, $\nabla^2\phi = 0 \ in \ \Omega_0$. The boundary condition equations are depicted in Fig. 1-7, where $\Omega_0$ represents the fluid domain (mean fluid volume), $n$ denotes the normal vector pointing into the fluid, $S_{FS}$ signifies the water level free surface, $S_{SB}$ represents the seabed surface, $S_B$denotes the mean body wetted surface, and $V_B$ signifies the body velocity. The unit vector, $\vec{n}$, represents the normal vector to the body boundary, and it is assumed to be pointing towards the body surface, while $(x, y, z)$ denotes the position vector on the body surface.

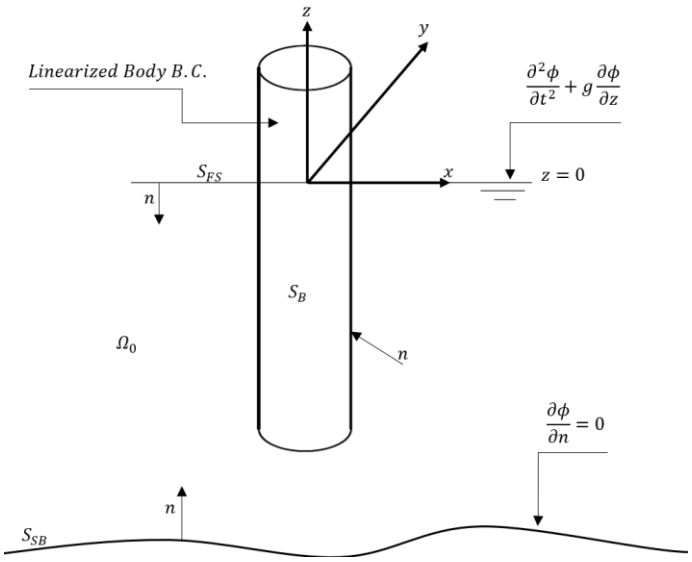


**Fig. 1-7** Linear Wave Body Interaction Problem [101]

The fluid depth can be considered as either infinite, with negligible motion at significant depths, or constant with no vertical velocity on the bottom boundary surface $z = -h$. Within the fluid domain, one or more bodies are positioned, either floating on the free surface or submerged. The part of these bodies below the plane $z = 0$ is collectively referred to as the submerged surface $S_B$ of the body or structure. This surface is assumed to be impermeable, with its normal velocity being equal to the normal component of the fluid velocity. At considerable horizontal distances from the structure, the wave field comprises a prescribed incident wave system along with outgoing waves related to radiation and scattering. The influence of surface tension is disregarded [493].

According to the potential flow theory Faltinsen (1993) [220], the equation of a platform motion is given in Eq. (1-40), where $M_{jk}$ is one of components in the mass matrix $M$ which contain the structural mass and mass moment of inertia; $A_{jk}$ are the components of the added mass matrix; $B_{jk}$ are the components of the damping matrix; $C_{jk}$ are the components of the restoring matrix. the restoring matrix can be split into hydrostatic and the mooring system stiffness. Moreover $\eta, \dot{\eta}, \ddot{\eta}$ are the response displacement, velocity and acceleration respectively. $F_j$ are the complex amplitudes of the exiting forces and moments. The force and moment components are given by the real part of $F_j e^{-i\omega_0 t}$.

$$\sum_{n=1}^{6}\left[(M_{jk}+A_{jk})\ddot{\eta}_k(t)+B_{jk}\dot{\eta}_k(t)+(C_{jk}+K_{jk})\eta_k(t)\right]=F_j e^{-i\omega_0 t} \qquad j=1,\ldots.6 \tag{1-40}$$

## 1.10. Hydrodynamic Loads in Linear potential Flow Theory

The total velocity potential, $\Phi(x,y,z,t)$ at time $t$, satisfies the Laplace equation, $\nabla^2\Phi = 0 \ in \ \Omega_0$, and is subject to different boundary conditions. The boundary value problems (BVPs) will be addressed in the subsequent section, both in first-order and second-order, to examine the hydrodynamic characteristics of a FOWT system. Assuming small unsteady motions relative to the wavelength and relevant length scales of the body, the free-surface boundary condition can be linearized around z = 0. This perturbation method allows the hydrodynamics problem to be divided into three distinct problems: radiation, diffraction, and hydrostatics [318, 341]. By assuming a small wave slope of the incident wave using a perturbation solution, the velocity potential can be expanded in a specific form, as indicated in Eq. (1-41) [523].

$$\Phi(x,y,z,t)=\Phi^{(1)}(x,y,z,t)+\Phi^{(2)}(x,y,z,t)+\cdots \tag{1-41}$$

First-order and second-order boundary value problems are considered separately due to the perturbation of the total velocity potential [524]. The incident wave potential is perturbed to second-order. The nonlinearities of the second-order potential and quadratic first-order quantities are taken into account in the calculation. Furthermore, the nonlinear incremental equation of motion is utilized in the time domain coupled analysis, implying that the stiffness of the platform is updated at each time step [339].

### 1.10.1. The First-Order

The overall first-order velocity potential, denoted as $\Phi^{(1)}(x,y,z,t)$, in the context of wave-body interaction can be formulated as the aggregate of components delineated in Eq. (1-42). Here, $\omega$ denotes the wave frequency, $\Phi^{(1)}(x,y,z)$ represents the complex

first-order velocity potential that is temporally independent, $\xi_j^{(1)}$ signifies the first-order complex amplitude of the oscillatory motion of the body, and $\Phi_j^{(1)}$ denotes the first-order unit-amplitude radiation potential for the body. The harmonic time dependence necessitates the application of the exponential factor $e^{i\omega t}$ to the product of all complex quantities [525].

$$\Phi^{(1)}(x,y,z,t) = Re\{\phi^{(1)}(x,y,z).e^{-i\omega t}\} \\ = Re\left\{\left[\phi_I^{(1)} + \phi_D^{(1)} - i\omega \sum_{j=1}^{6}\left(\xi_j^{(1)} + \phi_j^{(1)}\right)\right]e^{-i\omega t}\right\} \quad (1\text{-}42)$$

In the field of linear hydrodynamics, the hydrodynamic problem can be categorized into two distinct types of problems: diffraction, which occurs when a body is stationary and interacts with incoming waves, and radiation, which occurs when a body is compelled to oscillate in its six degrees of freedom (DOF) without the presence of incoming waves [220, 310, 526]. Consequently, the function $\phi^{(1)}(x,y,z)$ can be expressed as the sum of the incident wave potential, $\phi_I^{(1)}$, diffraction potential, $\phi_D^{(1)}$, and radiation potential, $\phi_R^{(1)}$. The first-order incident wave potential can be defined by Eq. (1-43), where $A$ represents the complex wave amplitude and $k$ is wave number denotes the wave number [335].

$$\phi_I^{(1)} = \frac{-igA\cosh(k(z+h))}{\omega\, Cosh(kh)} e^{ikx} \quad (1\text{-}43)$$

The radiation potential is a combination of the components of motion modes, which can be mathematically represented as shown in Eq. (1-44) [325]. $\xi_j^{(1)}$ represents the first-order complex amplitude of the oscillatory motion of the body platform system in the $j-th$ DOF, whilst $\phi_j^{(1)}$ denotes the first-order unit-amplitude radiation potential. These modes correspond to surge, sway, heave, roll, pitch, and yaw, in increasing order of $j$.

$$\phi_R^{(1)} = -i\omega \sum_j \xi_j^{(1)} \phi_j^{(1)} \quad (1\text{-}44)$$

The primary diffracted and radiated potentials of a structure can be determined through the resolution of BVPs [527]. It is important to account for the far-field condition, as the diffracted waves are expected to propagate away from the body. However, it is noteworthy that the direction of the diffracted waves becomes singular.

## 1.10.2. The second-order

When a floating object is not fixed, the primary motion will impact the secondary solution; this section will present the solution to the secondary boundary value problem, taking into account the quadratic interaction of the two linear wave components with frequencies $\omega_i$ and $\omega_j$ [528]. The second-order velocity potential, denoted as $\Phi^{(2)}(x, y, z, t)$, is expressed in Eq. (1-45), and is decomposed into the sum $(\omega_i + \omega_j)$ and difference $(\omega_i - \omega_j)$ frequency terms, where $\phi_{ij}^{+}$ and $\phi_{ij}^{-}$ represent the sum and difference frequency, respectively [529].

$$\Phi^{(2)}(x, y, z, t) = Re \sum_i \sum_j \phi_{ij}^{+}(x, y, z) e^{-i(\omega_i + \omega_j)t} + \phi_{ij}^{-}(x, y, z) e^{-i(\omega_i - \omega_j)t} \quad (1\text{-}45)$$

The velocity potential of second order, which considers the interaction between two harmonically oscillating components such as two incident linear waves or a wave and body oscillating at first order frequency, is defined in Eq. (1-45) [341].

Similar to the first-order problem, the second-order velocity potential can be divided into three sub-components: the second-order incident wave potential, $\phi_I^{\pm}$, the second-order diffracting wave potential, $\phi_D^{\pm}$ and the second-order radiation potential, $\phi_R^{\pm}$ [339, 341]. The second-order radiation potential $\phi_I^{\pm}$, which includes sum and difference frequency components, is presented in Eq. (1-46) and (1-47), where $A$ represents the amplitude, $k^{\pm} = k_i \pm k_j$ is the vector wave number with Cartesian components, and $\nu^{\pm} = \frac{(\omega_i \pm \omega_j)^2}{g}$. he complex conjugate is denoted by $(*)$ [530].

$$\begin{aligned} \phi_I^{+}(x) &= \frac{1}{2}\left(q_{ij}^{+} + q_{ji}^{+}\right) \frac{\cosh k^{+}(z+h)}{\cosh k^{+}h} e^{ik^{+}x} \\ \phi_I^{-}(x) &= \frac{1}{2}\left(q_{ij}^{-} + q_{ji}^{-*}\right) \frac{\cosh k^{-}(z+h)}{\cosh k^{-}h} e^{ik^{-}x} \end{aligned} \quad (1\text{-}46)$$

$$q_{ij}^{+} = -\frac{igA_iA_j}{2\omega_i} \cdot \frac{k_i^2 - \nu_i^2 + 2k_ik_j - 2\nu_i\nu_j}{\nu^{+} - k^{+}\tan(k^{+}h)}$$
$$q_{ij}^{-} = -\frac{igA_iA_j^{*}}{2\omega_i} \cdot \frac{k_i^2 - \nu_i^2 + 2k_ik_j - 2\nu_i\nu_j}{\nu^{-} - k^{-}\tan(k^{-}h)} \quad (1\text{-}47)$$

The second-order radiation potential, denoted as $\phi_R^{\pm}$, characterizes the perturbation of the second-order body motion as presented in Eq. (1-48) [316, 531]. This potential is directly related to the amplitude of motion, with $\xi_j^{(2)}$ representing the second-order complex amplitude of the oscillatory motion of the platform system, and $\phi_j^{(2)}$ denoting the second-order unit-amplitude radiation potential. Notably, the term "unit amplitude" refers to the linear or angular velocity of the rigid body motion at unit amplitude.

$$\phi_R^{\pm} = -i(\omega_i \pm \omega_j)\sum_j \xi_j^{(2)}\phi_j^{(2)} \quad (1\text{-}48)$$

The second-order wave potential resulting from radiation and diffraction of the platform must adhere to the Laplace equation while taking into account the specified boundary conditions. It is important to emphasize that the equations should incorporate a forcing term at both the free surface and the mean wet surface of the platform [532]. These terms are denoted as $Q_F^{\pm}$ in the equation for the free surface condition, while the body boundary condition, $Q_B^{\pm}$, defines the quadratic forcing functions [523, 533].

The time-dependent forcing terms, $Q_F$ and $Q_B$, can be represented in Eq. (1-49), in a similar manner to the presentation of the definition of the second-order potential in Eq. (1-45) [534].

$$Q_{F,B}(x,y,z,t) = Re\sum\sum\left[\phi_{F,B\,ij}^{+}(x,y,z)e^{i(\omega_i+\omega_j)t} + \phi_{F,B\,ij}^{-}(x,y,z)e^{i(\omega_i-\omega_j)t}\right] \quad (1\text{-}49)$$

By assuming the symmetry conditions $\phi_{F,B\,ij}^{+} = \phi_{F,B\,ji}^{+}$ & $\phi_{F,B\,ij}^{-} = \phi_{F,B\,ji}^{-*}$, the complex amplitudes of the free-surface forcing functions can be expressed as shown in Eq. (1-50) and (1-51). Here, $\phi_i$ and $\phi_j$ represent the first-order potential containing the incident wave potential, diffraction potential, and radiation potential. Eq. (1-52) and (1-53) illustrate the sum and difference frequencies forcing on the body boundary, denoted as $Q_B^{\pm}$, where $H^{\pm}$ represents the quadratic components of the coordinate transformation matrix resulting from the body rotation. This transformation transfers the body fixed coordinate to the inertial reference frame $\boldsymbol{\delta}\,(\delta_1, \delta_2, \delta_3)$ and $\boldsymbol{\alpha}\,(\alpha_1, \alpha_2, \alpha_3)$

respectively, representing the translational and rotational displacements of the body fixed coordinates with respect to the inertial reference frame at its original position. It is important to note that the complex conjugate is indicated by$(*)$ [535, 536].

$$Q_F^+ = \frac{i}{4g}\omega_i\phi_i\left(-\omega_j^2\frac{\partial\phi_j}{\partial z}+g\frac{\partial^2\phi_j}{\partial z^2}\right)+\frac{i}{4g}\omega_j\phi_j\left(-\omega_j^2\frac{\partial\phi_i}{\partial z}+g\frac{\partial^2\phi_i}{\partial z^2}\right)-\frac{1}{2}i(\omega_i+\omega_j)\nabla\phi_i\nabla\phi_j \tag{1-50}$$

$$Q_F^- = \frac{i}{4g}\omega_i\phi_i\left(-\omega_j^2\frac{\partial\phi_j^*}{\partial z}+g\frac{\partial^2\phi_j^*}{\partial z^2}\right)+\frac{i}{4g}\omega_j\phi_j^*\left(-\omega_j^2\frac{\partial\phi_i}{\partial z}+g\frac{\partial^2\phi_i}{\partial z^2}\right)-\frac{1}{2}i(\omega_i+\omega_j)\nabla\phi_i\nabla\phi_j^* \tag{1-51}$$

$$Q_B^+ = \frac{\partial\phi_I^+}{\partial n}+\frac{1}{2}i(\omega_i+\omega_j)\vec{n}\cdot H^+\mathbf{x}+\frac{1}{4}\Big[(\boldsymbol{\alpha}_i\times\vec{n})\cdot\left(i\omega_j(\boldsymbol{\delta}_j+\boldsymbol{\alpha}_j\times\mathbf{x})-\nabla\phi_j\right)+(\boldsymbol{\alpha}_j\times\vec{n})\cdot$$
$$(i\omega_i(\boldsymbol{\delta}_i+\boldsymbol{\alpha}_i\times\mathbf{x})-\nabla\phi_i)\Big]-\frac{1}{4}\vec{n}\Big[\left((\boldsymbol{\delta}_i+\boldsymbol{\alpha}_i\times\mathbf{x})\cdot\nabla\right)\nabla\phi_j+\left(\left(\boldsymbol{\delta}_j+\boldsymbol{\alpha}_j\times\mathbf{x}\right)\cdot\nabla\right)\nabla\phi_i\Big] \tag{1-52}$$

$$Q_B^- = \frac{\partial\phi_I^-}{\partial n}+\frac{1}{2}i(\omega_i+\omega_j)\vec{n}\cdot H^-\mathbf{x}+\frac{1}{4}\Big[(\boldsymbol{\alpha}_i\times\vec{n})\cdot\left(i\omega_j(\boldsymbol{\delta}_j^*+\boldsymbol{\alpha}_j^*\times\mathbf{x})-\nabla\phi_j^*\right)+(\boldsymbol{\alpha}_j^*\times\vec{n})\cdot$$
$$(i\omega_i(\boldsymbol{\delta}_i+\boldsymbol{\alpha}_i\times\mathbf{x})-\nabla\phi_i)\Big]-\frac{1}{4}\vec{n}\Big[\left((\boldsymbol{\delta}_i+\boldsymbol{\alpha}_i\times\mathbf{x})\cdot\nabla\right)\nabla\phi_j^*+\left(\left(\boldsymbol{\delta}_j^*+\boldsymbol{\alpha}_j^*\times\mathbf{x}\right)\cdot\nabla\right)\nabla\phi_i\Big] \tag{1-53}$$

## 1.10.3. Integral Equation Method and Green Function

The numerical solution of the integral equation involves the combination of a boundary element method for the numerical integration of the free surface Green function or free surface sources distributed on the wetted body surface. This approach has been extensively studied in the literature, including works by Frank [537], Lee and Sclavounos [538], Lee and Newman [318] for the case of infinite water depth. The evaluation of the free surface Green function has been the subject of successful investigations by Chakrabarti [539], Liang et al. [540], Newman [541], Noblesse [542], Ponizy et al. [543] , Telste and Noblesse [544] for the case of finite depth.

In order to address the boundary value problem, the integral equation method can be utilized [544, 545]. This allows for the determination of the first-order diffraction

potential and radiation potential using Eq. (1-54) and (1-55), where $\sigma_D$ and $\sigma_j$ denote the source strength of diffraction and radiation potentials, respectively. The Green Function, $G(\boldsymbol{\zeta};\mathbf{x})$, represents the wave source potential, which characterizes the velocity potential at point $\mathbf{x}$ due to a point source of strength of $-4\pi$ at the point $\boldsymbol{\zeta}$ [546]. Consequently, the integral equation for the source strength of diffraction and radiation can be expressed as in Eq. (1-56) and (1-57), and the fluid velocity resulting from the diffraction and radiation potential can be derived from Eq. (1-18).

$$2\pi\phi_D(\mathbf{x}) + \iint_{S_B} d\boldsymbol{\zeta}\,\phi_D(\boldsymbol{\zeta})\frac{\partial G(\boldsymbol{\zeta};\mathbf{x})}{\partial n_{\boldsymbol{\zeta}}} = \iint_{S_B} d\boldsymbol{\zeta}\,(-\frac{\partial \phi_I}{\partial n})G(\boldsymbol{\zeta};\mathbf{x}) \tag{1-54}$$

$$2\pi\phi_j(\mathbf{x}) + \iint_{S_B} d\boldsymbol{\zeta}\,\phi_j(\boldsymbol{\zeta})\frac{\partial G(\boldsymbol{\zeta};\mathbf{x})}{\partial n_{\boldsymbol{\zeta}}} = \iint_{S_B} d\boldsymbol{\zeta}\,n_j G(\boldsymbol{\zeta};\mathbf{x}) \tag{1-55}$$

$$2\pi\sigma_D(\mathbf{x}) + \iint_{S_B} d\boldsymbol{\zeta}\,\sigma_D(\boldsymbol{\zeta})\frac{\partial G(\boldsymbol{\zeta};\mathbf{x})}{\partial n_{\mathbf{x}}} = -\frac{\partial \phi_I}{\partial n} \tag{1-56}$$

$$2\pi\sigma_j(\mathbf{x}) + \iint_{S_B} d\boldsymbol{\zeta}\,\sigma_j(\boldsymbol{\zeta})\frac{\partial G(\boldsymbol{\zeta};\mathbf{x})}{\partial n_{\mathbf{x}}} = n_j \tag{1-57}$$

$$\nabla\phi\,(\mathbf{x}) = \nabla \iint_{S_B} d\boldsymbol{\zeta}\sigma(\boldsymbol{\zeta})\,G(\boldsymbol{\zeta};\mathbf{x}) \tag{1-58}$$

The panel method offers a solution for the integral equations of diffraction and radiation by assuming that the unknown quantities remain constant across each panel, and enforcing the integral at the centre of each panel. Consequently, the discrete representation of Eq. (1-59) to (1-62) can be expressed as follows:

$$2\pi\phi_D(\mathbf{x}_p) + \sum_{n=1}^{Num}\phi_D(\mathbf{x}_n)\int_{S_n} d\boldsymbol{\zeta}\frac{\partial G(\boldsymbol{\zeta};\mathbf{x}_p)}{\partial n_{\boldsymbol{\zeta}}} = \sum_{n=1}^{Num} -\frac{\partial \phi_I(\mathbf{x}_n)}{\partial n}\int_{S_n} d\boldsymbol{\zeta}\,G(\boldsymbol{\zeta};\mathbf{x}_p) \tag{1-59}$$

$$2\pi\phi_j(\mathbf{x}_p) + \sum_{n=1}^{Num}\phi_j(\mathbf{x}_n)\int_{S_n} d\boldsymbol{\zeta}\frac{\partial G(\boldsymbol{\zeta};\mathbf{x}_p)}{\partial n_{\boldsymbol{\zeta}}} = \sum_{n=1}^{Num} n_j\,(\mathbf{x}_n)\int_{S_n} d\boldsymbol{\zeta}\,G(\boldsymbol{\zeta};\mathbf{x}_p) \tag{1-60}$$

$$2\pi\sigma_D(\mathbf{x}_p) + \sum_{n=1}^{Num}\sigma_D(\mathbf{x}_n)\int_{S_n} d\boldsymbol{\zeta}\frac{\partial G(\boldsymbol{\zeta};\mathbf{x}_p)}{\partial n_{\boldsymbol{\zeta}}} = -\frac{\partial \phi_I(\mathbf{x}_n)}{\partial n} \tag{1-61}$$

$$2\pi\sigma_j(\mathbf{x}_p) + \sum_{n=1}^{Num}\sigma_j(\mathbf{x}_n)\int_{S_n} d\boldsymbol{\zeta}\frac{\partial G(\boldsymbol{\zeta};\mathbf{x}_p)}{\partial n_{\boldsymbol{\zeta}}} = n_j(\mathbf{x}_n) \tag{1-62}$$

The total number of panels, denoted as $Num$ and the coordinate of the centre of the $p$-th panel, denoted as $\mathbf{x}_p$, are used to evaluate the influence of the continuous distribution of the Rankine part of the wave source potential on a quadrilateral panel

[547]. This evaluation is based on the methodologies outlined in Newman [541]. Each quadrilateral panel is defined by four vertices. The centre $\mathrm{x}_p$ can be calculated as the average of the vertices' coordinates. The Rankine source potential represents the potential flow due to a point source. For continuous distribution, this potential needs to be integrated over the surface of each panel. Utilize Green's function [543] and the boundary element method (BEM) as discussed in Newman's work to transform the boundary integral equation into a discrete form [527]. The influence coefficient $\mathrm{I}_{pq}$ quantifies the effect of the $q$-th panel's source distribution on the $p$-th panel. Evaluating the influence of the continuous distribution of the Rankine part of the wave source potential on a quadrilateral panel using Newman's methodologies. The key steps involve defining panel geometry, calculating the potential function, numerically integrating to find influence coefficients, and constructing the influence matrix for the entire panel system [548].

The Green function in finite depth, as defined by Wehausen and Laitone (1960) [549], and expressed in Eq. (1-63), involves the terms $r^2 = (x-a)^2 + (y-b)^2 + (z-c)^2$, $\ddot{r}^2 = (x-a)^2 + (y-b)^2 + (z+c+2h)^2$, where $(a, b, c)$ represent the coordinates of $\boldsymbol{\zeta}$, $J_0(x)$ denotes the Bessel function of zero order, $R = \sqrt{(x-a)^2 + (y-b)^2}$, and $\nu$ is equal to $\frac{\omega^2}{g}$.

$$G(\boldsymbol{\zeta}; \mathbf{x}) = \frac{1}{r} + \frac{1}{\ddot{r}} + 2\int_0^\infty dk \frac{(k+\nu)\cosh(z+h)\cosh(c+h)}{k\sinh(kh) - \nu\cosh(kh)} e^{-kh} J_0(kR) \qquad (1\text{-}63)$$

The Fourier k-integration is positioned above the pole on the real axis to enforce the radiation condition. The wave component of the Green function is computed using the methodologies outlined in Newman [550]. The integration across a panel is executed utilizing Gauss quadrature [523].

However, the resolution of the diffraction potential differs from that of the first-order problem due to the inhomogeneous free surface condition and body boundary condition with forcing terms. The second-order solution of the radiation potential is equivalent to that of a first-order radiation problem at the sum and difference

frequencies. Consequently, the solution of the second-order diffraction potential, $\phi_D^{\pm}$, can be derived from Green's integral equation, as presented in Eq. (1-64), where the terms on the right-hand side encompass the integral over the body, $S_B$, and the free surface integral term, $S_{FS}$.

$$2\pi\phi_D^{\pm} + \iint_{S_B} \phi_D^{\pm}(\boldsymbol{\zeta}) \frac{\partial G(\boldsymbol{\zeta};\mathbf{x})}{\partial n_{\boldsymbol{\zeta}}} ds = \iint_{S_B} \phi_B^{\pm}\boldsymbol{\zeta}\, G(\boldsymbol{\zeta};\mathbf{x}) ds + \frac{1}{g}\iint_{S_{FS}} \phi_F^{\pm}\boldsymbol{\zeta}\, G(\boldsymbol{\zeta};\mathbf{x}) ds \tag{1-64}$$

The panel method is capable of solving second-order integral equations in a manner analogous to that of first-order equations. While the left side of Eq. (1-64) resembles the first-order potential equation, its discrete form remains consistent with the expression in Eq. (1-49). However, the right side of the integral equation differs. When considering the integral over the mean wetted surface, $S_B$, of the fixed body, the evaluation of $\phi_B^{\pm}(\mathbf{x})$ only encompasses the normal velocity induced by the incident wave potential, $\phi_I^{\pm}$. Additionally, Stokes's theorem is utilized to modify the double special derivative of the first-order velocity potential for the floating body [551].

$$\begin{aligned}
&\iint_{S_B} ds\, G\{\vec{n}\cdot[(\boldsymbol{\delta}+\boldsymbol{\alpha}\times\mathbf{x})\cdot\nabla]\nabla\phi\} \\
&\quad = \iint_{S_B} ds\,[\vec{n}\cdot(\boldsymbol{\delta}+\boldsymbol{\alpha}\times\mathbf{x})](\nabla\phi\cdot\nabla\mathrm{G}) \\
&\quad + \iint_{S_B} ds\, G\{\vec{n}\cdot[(\nabla\phi\cdot\nabla)(\boldsymbol{\delta}+\boldsymbol{\alpha}\times\mathbf{x})]\} \\
&\quad - \iint_{S_B} ds\, \frac{\partial\phi}{\partial n}[(\boldsymbol{\delta}+\boldsymbol{\alpha}\times\mathbf{x})\cdot\nabla\mathrm{G}] \\
&\quad + \iint_{WL} dl\cdot G[\nabla\phi\times(\boldsymbol{\delta}+\boldsymbol{\alpha}\times\mathbf{x})]
\end{aligned} \tag{1-65}$$

By assuming that $Q_B^{\pm}$ remains constant on each panel and evaluating it at the centroids of the panels, Eq. (1-65) is utilized to replace $Q_B^{\pm}$ in Eq. (1-64). The integral over $S_B$ is then substituted by a summation of integrals over each panel. The waterline is approximated by linear segments formed by the sides of the panels that are adjacent to the free surface. $Q_F^{\pm}$ is then substituted into the integral of the free surface, and the integral is computed in two separate domains, which are divided by a partition circle with a radius of $\rho = b$. Here, $b$ chosen to be sufficiently large to disregard the influence of the evanescent waves outside the circle, and where $\rho = \sqrt{x^2+y^2}$ [523, 536].

The numerical integration is utilized for the inner domain, while in the outer domain, both the Green function and the asymptotic of the first-order potentials are expanded in Fourier-Bessel series [552]. The free-surface integrals are simplified to the sum of line integrals with respect to the radial coordinate, $\rho$, after integrating the trigonometric functions with respect to the angular coordinate [523, 553]. Consequently, within the inner domain, the second-order derivatives of the first-order potential in the surface integral can be converted into first-order derivatives and line integrals around the waterline $(WL)$ and the partition circle $(PC)$ using Gauss theorem [523], as presented in Eq. (1-66).

$$\iint_{S_F} \phi_i \frac{\partial^2 \phi_j}{\partial z^2} G ds - \iint_{WL+PC} \phi_i \left(\nabla \phi_j \cdot \vec{n}\right) G dl + \iint_{S_F} \left[\left(\nabla \phi_i \cdot \nabla \phi_j\right) G + \phi_i (\nabla \phi_j \cdot \nabla G)\right] ds \tag{1-66}$$

It is important to acknowledge that the divergence $\nabla$ and the normal vector $\vec{n}$, are interpreted in the context of two dimensions on the $z = 0$ plane, with $S_F$ representing the inner domain of the free surface. Further details on the discrete method for boundary value problems can be found in the WADAM Theory Manual and Kim & Yue (1989) [523, 553]. In the outer domain, the far-field behaviour of the general-ordering source $G$ for $R/h \gg 1$, can be expressed in Eq. (1-67) as described by John (1950) [554, 555], where $k$ represents the incident wave number, $H_0$ is the zeroth-order first-kind Hankel function, and $K_0$ is the zeroth-order second-kind modified Bessel function. The real roots of Eq. (1-68) are denoted as $k_m$ with $m = 1,2, \ldots$.

$$G = -2\pi i C_0 \cosh\left(k(z+h)\right) \cosh\left(k(c+h)\right) H_0(kR) + 4 \sum_{m=1}^{\infty} C_m \cos\left(k_m(z+h)\right) \cos\left(k_m(c+h)\right) K_0(k_m R) \tag{1-67}$$

$$C_0 = \frac{\nu^2 - k^2}{k^2 h - \nu^2 h + \nu} \quad \& \quad C_m = \frac{k_m^2 + \nu^2}{k_m^2 h + \nu^2 h - \nu} \tag{1-68}$$

$$\omega^2 = -k_m \, g \, tan(k_m h) \quad for \quad (m - \tfrac{1}{2})\pi \leq k_m h \leq m\pi \tag{1-69}$$

Eq. (1-70) demonstrates that the second component of Eq. (1-61) diminishes as the radial distance increases in the context of finite water depth. The far-field behaviour of $G$ is characterized by the initial term, which signifies the propagation of waves away from the source. The far-field behaviour of the ring sources is determined through the application of the addition theorem as outlined by Kim and Yue [556], and is articulated in Eq. (1-71).

$$G = -2\pi i C_0 \cosh\big(k(z+h)\big)\cosh\big(k(c+h)\big)\,H_0(kR) + O(e^{-k_1 R}) \tag{1-70}$$

$$G_n = -4\pi^2 i C_0 \cosh\big(k(z+h)\big)\cosh\big(k(c+h)\big)\,J_n(k\rho)H_n(k\rho) + O(e^{-k_1 R}) \tag{1-71}$$

### 1.10.4. First-order Forces and Moments

The equations for the forces of first and second order can be obtained by directly integrating the fluid pressure across the boundary of a body. A portion of these forces can be determined without solving the scattering potential by applying Green's theorem [365]. Given that the diffraction potential and radiation potential have been previously resolved, the first-order hydrodynamic pressure can subsequently be computed from the velocity potential, as demonstrated in Eq. (1-72), where $\rho$ represents the fluid density.

$$p(x,y,z,t) = -\rho\frac{\partial \Phi^{(1)}(x,y,z,t)}{\partial t} = Re\left\{\left[\phi_I^{(1)} + \phi_D^{(1)} - i\omega\sum_{j=1}^{6}\left(\xi_j^{(1)} + \phi_j^{(1)}\right)\right]e^{-i\omega t}\right\} \tag{1-72}$$

Subsequently, the hydrodynamic force acting on the object due to radiation potential can be deduced and represented as shown in Eq. (1-73), with $\mu$ denoting the added mass and $\lambda$ representing the damping. Additionally, the forces exerted by the incident wave and diffracted wave can be determined using Eq. (1-74), where $p_I$ and $p_D$, as defined in Eq. (1-75) and (1-76), correspond to the hydrodynamic pressures computed based on the incident wave and diffracted wave in accordance with the Bernoulli equation.

$$F_R^{(1)} = Re\left\{\left[\sum_{j=1}^{j=6}\left(\omega^2\mu_j + i\omega\lambda_j\right)\xi_j^{(1)}\right]e^{-i\omega t}\right\} \quad (1\text{-}73)$$

$$F_{I+D}^{(1)} = \iint_{S_B}(p_I + p_D)n_j ds \quad (1\text{-}74)$$

$$p_I = -\rho\frac{\partial\Phi_I}{\partial t} = \rho Re\left\{i\omega\phi_I^{(1)}e^{-i\omega t}\right\} \quad (1\text{-}75)$$

$$p_D = -\rho\frac{\partial\Phi_D}{\partial t} = \rho Re\left\{i\omega\phi_D^{(1)}e^{-i\omega t}\right\} \quad (1\text{-}76)$$

The overall primary force can be represented by the Eq. (1-77), in which $F_{HS}^{(1)}$ denotes the primary hydrostatic restoring force, and $F_I^{(1)} + F_D^{(1)}$ can be combined as $F_{Ex}^{(1)}$, representing the primary wave exciting force.

$$F^{(1)} = F_I^{(1)} + F_D^{(1)} + F_R^{(1)} + F_{HS}^{(1)} \quad (1\text{-}77)$$

Similar to the fist-order velocity potential, the first-order time-dependent surface elevation, $\varsigma^{(1)}$, can be represented by Eq. (1-78) and Eq. (1-79), and is indicative of the initial time-independent surface elevation, denoted as $\eta^{(1)}$.

$$\varsigma^{(1)} = -\frac{1}{g}\frac{\partial\Phi^{(1)}}{\partial t}\Big|_{z=0} = Re\left\{\eta^{(1)}e^{-i\omega t}\right\} \quad (1\text{-}78)$$

$$\eta^{(1)} = \frac{i\omega}{g}\phi^{(1)} = \frac{i\omega}{g}\left(\phi_I^{(1)} + \phi_D^{(1)} - i\omega\sum_{j=1}^{6}\left(\xi_j^{(1)} + \phi_j^{(1)}\right)\right) \quad (1\text{-}79)$$

## 1.10.5. Second-order Force and Moment

The problem of second-order radiation for $\Phi_R^{(2)}$ is identical to that for first-order radiation potential. Therefore, the second-order motions can be determined in a similar manner, accounting for changes in wave frequencies, added mass, and hydrodynamic damping coefficients. The second-order exciting force is defined in Eq. (1-80), encompassing all second-order nonlinear aspects and considering only incident wave

and diffraction wave forces, while radiation is treated separately. Consequently, the quadratic transfer function (QTF), $f_{ij}^{\pm}$ of the second-order exciting force is presented in Eq. (1-81), with $f_{qij}^{\pm}$ and $f_{pij}^{\pm}$ derived in Eq. (1-82) and (1-83), respectively, and caused by quadratic first-order and second potentials. The rotation amplitude in roll, pitch, and yaw of the body with respect to the coordinate system is denoted as $\theta_{1,2,3} = \xi_{3,4,5}$. The vector $\vec{n}_c$ is defined as$\frac{\vec{n}}{|cos\gamma|}$, where $\gamma$ represents the angle between the normal vector, $\vec{n}$, and the horizontal plane; for wall-sided bodies at the waterline, this is equivalent to $\vec{n}$. $A_i$ and $A_j$ denote the amplitude of the incident wave with frequencies $\omega_i$ and $\omega_j$. The centre of the water plane is denoted by $(x_f, y_f)$. Furthermore, as the expressions for the difference-frequency problem are similar to the sum frequency problem, Eq. (1-82) and (1-83) exclusively express the sum frequency problem.

$$F_{Ex}^{(2)}(x,y,z,t) = Re\left[A_i A_j f_{ij}^{+} e^{-i\omega^{+}t} + A_i^{*} A_j f_{ij}^{-} e^{-i\omega^{+}t}\right] \tag{1-80}$$

$$f_{ij}^{\pm} = f_{qij}^{\pm} + f_{pij}^{\pm} \tag{1-81}$$

$$f_{qij}^{+} = \left[\rho i(\omega_i + \omega_j) \iint_{S_B} (\phi_I^{+} + \phi_D^{+})\vec{n}\, ds\right] / A_i A_j \tag{1-82}$$

$$\begin{aligned} f_{pij}^{+} = \Bigg\{ & \left[-\frac{\rho}{4}\iint_{S_B} ((\nabla\phi_i^{(1)} \cdot \nabla\phi_j^{(1)}) - (i\omega_i \xi_j^{(1)} \cdot \nabla\phi_i^{(1)}) - (i\omega_j \xi_i^{(1)} \cdot \nabla\phi_j^{(1)})\vec{n} ds\right] \\ & + \left[\frac{\rho}{4}\iint_{S_B} \left(\left(i\omega_i \phi_i^{(1)} \theta_j^{(1)} \times \vec{n}\right) + \left((i\omega_j \phi_j^{(1)} \theta_i^{(1)} \times \vec{n}\right)\right) ds\right] \\ & + \left[\frac{\rho g}{4}\oint_{WL} \left(\eta_i^{(1)}\eta_j^{(1)} - \xi_{3,i}^{(1)}\eta_j^{(1)} - \xi_{3,j}^{(1)}\eta_i^{(1)}\right)\vec{n} dl\right] \\ & - \left\{\frac{\rho g A_w}{4}\begin{bmatrix} \left(\left(\theta_{1,i}^{(1)}\theta_{3,j}^{(1)} + \theta_{1,j}^{(1)}\theta_{3,i}^{(1)}\right)(x_f - x_c')\right) \\ + \left(\left(\theta_{2,i}^{(1)}\theta_{3,j}^{(1)} + \theta_{2,j}^{(1)}\theta_{3,i}^{(1)}\right)(y_f - y_c')\right) \\ + \left(\theta_{1,i}^{(1)}\theta_{1,j}^{(1)} + \theta_{2,j}^{(1)}\theta_{2,i}^{(1)}\right) z_c' \end{bmatrix} \vec{k}\right\} \Bigg\} / A_i A_j \end{aligned} \tag{1-83}$$

The cumulative second-order force can be represented by the incident wave $(I)$, diffracted wave $(D)$, wave radiation $(R)$, hydrostatic restoring force $(HS)$, with $F_q^{(2)}$ denoting the second-order force resulting from quadratic first-order quantities. Additionally, the sum of $F_I^{(2)} + F_D^{(2)} + F_q^{(2)}$ can be denoted as $F_{Ex}^{(2)}$, which signifies the second-order wave exciting force. The comprehensive second-order force can also be depicted as indicated in Eq. (1-84).

$$F^{(2)} = F_R^{(2)} + F_{HS}^{(2)} + F_{Ex}^{(2)} \tag{1-84}$$

The expression for the second-order surface elevation, denoted as $\varsigma^{(2)}$, is given by Eq. (1-85), in which $\eta_{ij}^{+}$ represents the QTF of the second-order surface elevation. This can be further decomposed into $\eta_{qij}^{\pm}$ and $\eta_{pij}^{\pm}$, as demonstrated in Eq. (1-86), and the components of the sum and difference frequencies can be computed using Eq. (1-87) and (1-48). It is important to note that in the case of a monochromatic wave, where $\omega_i = \omega_j$, the difference-frequency component $\eta_{ij}^{\pm}$ becomes a constant component, denoted as $\bar{\eta}$, while the sum-frequency component, $\eta_{ij}^{+}$, becomes the double frequency component, denoted as, $\eta^{(2)}$.

$$\varsigma^{(2)} = Re\left\{\sum_{i=1}^{2}\sum_{j=1}^{2}\left[\eta_{ij}^{+}e^{-i\omega^{+}t} + \eta_{ij}^{-}e^{-i\omega^{-}t}\right]\right\} \tag{1-85}$$

$$\eta_{ij}^{\pm} = \eta_{qij}^{\pm} + \eta_{pij}^{\pm} \tag{1-86}$$

$$\eta_{qij}^{\pm} = \mp\frac{1}{4g}\nabla\phi_i^{(1)}\nabla\phi_j^{(1)} \mp \frac{\omega_i\omega_j(\nu_i+\nu_j)}{4g^2}\phi_i^{(1)}\phi_j^{(1)} \tag{1-87}$$

$$\eta_{pij}^{\pm} = \frac{i\omega^{\pm}}{g}\phi^{\pm} \tag{1-88}$$

## 1.11. Motion Equation

The equations of motion for a cylinder structure, based on Newton's second law, can be expressed in Eq. (1-89), where $M_{jk}$ is one of components in the mass matrix $M$, $\ddot{x}_k$ is one of components in the body acceleration vector $\ddot{x}$, $F_j$ is one of components in the force vector $F$, and $j$ is indicating the degree of freedom. The equation of motion for the linear wave structure interaction problem can then be written as in Eq. (1-90), where $\mu_{jk}$ is the added mass coefficient, $\lambda_{jk}$ is the damping coefficient, and $C_{jk}$ is the linear restoring coefficient. The equations of motion can be written using matrix form as expressed in Eq. (1-91).

$$\sum_{n=1}^{6} M_{jk}\ddot{x}_k(t) = F_j\,(t) \tag{1-89}$$

$$\sum_{n=1}^{6}\left[(M_{jk} + \mu_{jk})\ddot{x}_k(t) + \lambda_{jk}\dot{x}_k(t) + C_{jk}x_k(t)\right] = F_j e^{-i\omega t} \qquad j = 1, \ldots 6 \tag{1-90}$$

$$\big(M + \mu(\omega)\big)\ddot{x} + \lambda\dot{x} + Cx = F \tag{1-91}$$

By considering a linear system in a state of equilibrium, the resulting response exhibits oscillations at the same frequency as the applied force, with the magnitude of the response being directly related to the force. Therefore, it is reasonable to posit that the force loads, denoted as $F$, are directly proportional to the amplitude of the incident wave, represented as ξ, and oscillate at a frequency denoted as $\omega$, for a general angle between the body and the direction of wave propagation. Given that the platform's motion can be determined using hydrodynamic coefficients and wave loads, the equations of motion in the frequency domain for the linear interaction problem between the wave and structure can be expressed as demonstrated in Eq. (1-92).

$$(-\omega^2(M + \mu) + i\omega\lambda + C)\xi(\omega) = F_{Ex}(\omega) \tag{1-92}$$

In the given equation, $M$ represents the mass, $\mu$ denotes the added mass, $C$ signifies the hydrostatic restoring moment, and $\lambda$ stands for the damping coefficient. These

parameters are represented as 6x6 matrices. The frequency-domain motion amplitude $\xi(\omega)$ is presented as a 6x1 vector. The equations also encompass the sum-and difference frequency responses, which are same to those of a first-order response, with the exception of alterations in frequencies. The mass matrix is expressed in Eq. (1-53), where $m$ denotes the body mass and $(x_G, y_G, z_G)$ denotes the centre of gravity. The mass moments of inertia, denoted as I, are expressed as $I = \frac{\pi D^4}{64}$, and are uniform across all axes. The roll, pitch, and yaw moments of inertia are represented as $I_{44}, I_{55}, I_{66}$, respectively, with the roll-yaw moment of inertia adhering to the symmetry relation $I_{46} = I_{64}$.

$$M = \begin{bmatrix} m & 0 & 0 & 0 & mz_G & 0 \\ 0 & m & 0 & -mz_G & 0 & mx_G \\ 0 & 0 & m & 0 & -mx_G & 0 \\ 0 & -mz_G & 0 & I_{44} & 0 & I_{46} \\ mz_G & 0 & -mx_G & 0 & I_{55} & 0 \\ 0 & mx_G & 0 & I_{64} & 0 & I_{66} \end{bmatrix} \quad (1\text{-}93)$$

## 1.12. Hydrostatic

One of the significant forces influencing the substructure of an offshore wind turbine is buoyancy. This force is primarily due to the pressure distribution in a fluid, specifically the pressure exerted by the fluid on an immersed body. The pressure is determined by the depth of the object in an incompressible fluid with density and acceleration due to gravity [557]. The average loading on the hull of the structure is a crucial factor in detailed design, as hydrostatic pressure can impact the stability of free-floating structures [220, 558]. These hydrostatic loads can affect the platform laterally or vertically and are related to both buoyancy forces and moments. However, they have a lesser impact on the overall rotational or translational motion of the platform. The equation of hydrostatic equilibrium is presented in Eq. (1-94), where the first term represents the buoyancy force and the second term represents the change in the hydrostatic force and moment resulting from the effects of the water-plane area and the centre of buoyancy as the support platform is displaced [308].

$$F_i(q) = \rho g V_w \delta_{i3} - C_{ij} q_j \quad (1\text{-}94)$$

The given equation includes various parameters such as water density, $\rho$, gravitational acceleration constant, $g$, displaced volume of fluid, $V_w$, the $(i,3)$ component of the Kronecker-Delta function, $\delta_{i3}$ [308, 559, 560] and the $(i,j)$ component of the linear hydrostatic-restoring matrix, $C_{ij}$, $q$ represents the set of platform DOFs. It is important to note that the hydrostatic loads are not influenced by the incident wave or any outgoing waves from diffraction and radiation. The first term, $\rho g V_w \delta_{i3}$, represents the buoyancy force [561], which acts vertically upward and is equivalent to the weight of the fluid displaced by the platform. For floating wind turbines, it is crucial to separately consider the contributions of gravity due to the changing metacentric height (GM) caused by wind turbine flexibility. These contributions encompass the weight of the wind turbine and support platform, the mooring system weight in water, and buoyancy forces. The hydrostatic stiffness of a cylinder-shaped platform as a rigid body relies on the waterplane geometry, the overall centre of buoyancy ($z_B$), and the overall centre of gravity ($z_G$). It is assumed that the body-fixed xz-plane of the submerged portion of the support platform and the body-fixed yz-plane of the submerged platform are planes of symmetry [220]. The non-zero coefficients, $C_{ij}$, in the hydrostatic restoring matrix are determined using Eq. (1-95).

$$C_{ij} = \begin{bmatrix} 0 & 0 & 0 & 0 & 0 & 0 \\ 0 & 0 & 0 & 0 & 0 & 0 \\ 0 & 0 & \rho g A_w & 0 & -\rho g \int_{A_w} x dS & 0 \\ 0 & 0 & 0 & \rho g V_w \left( \int_{A_w} y^2 dS + z_B + z_G \right) = \rho g V_w \overline{GM}_T & 0 & 0 \\ 0 & 0 & -\rho g \int_{A_w} x dS & 0 & \rho g V_w \left( \int_{A_w} x^2 dS + z_B + z_G \right) = \rho g V_w \overline{GM}_L & 0 \\ 0 & 0 & 0 & 0 & 0 & 0 \end{bmatrix}$$

(1-95)

The hydrostatic matrix offers restoring forces for roll, pitch, and heave movements, while restoring forces for other modes of motion are dependent on the mooring system. The motion equations in the time domain are described using the impulse response theory. The platform's motion equation can be represented as shown in Eq. (2-96):

$$[M+\mu(\infty)]\ddot{x}(t)+\left[\int_{-\infty}^{t}k(t-\tau)d\tau\right]\dot{x}(\tau)+Cx(t)=F_{Ex}+F_W+F_C+F_M \quad (1\text{-}96)$$

The expression $\int_{-\infty}^{t}k(t-\tau)d\tau$ describes radiation loads, where $k(t)$ referred to as the wave radiation retardation kernel, and the term $k(t-\tau)$ represents the convolution term of velocity, signifying the memory effect of the reaction force of fluid dynamics. The variable $\tau$ is a dummy variable with the same units as the simulation time, $t$. The coefficients for added mass and damping in Eq. (1-96) are frequency dependent and are expressed in Eq. (1-97) and (1-98) respectively. The radiation loads are determined in the time domain using hydrodynamic added mass and damping matrices. In this investigation, WADAM [320] is employed to compute hydrodynamic added mass and damping matrices, as well as the excitation forces.

$$\mu(\omega)=\mu(\infty)+\int_0^{\infty}k(\tau)\cos(\omega\tau)d\tau \quad (1\text{-}97)$$

$$\lambda(\omega)=\omega\int_0^{\infty}k(\tau)\sin(\omega\tau)d\tau \quad (1\text{-}98)$$

The relationship between the retardation function and frequency-dependent damping is established by utilizing the Fast Fourier transform (FFT) on Eq. (1-97), leading to the formulation as presented in Eq. (1-99).

$$k(t)=\frac{2}{\pi}\int_0^{\infty}\lambda(\omega)\frac{\sin(\omega\tau)}{\omega}d\omega \quad (1\text{-}99)$$

In accordance with the impulse theory [562], Eq. (1-100) demonstrates the conversion of the wave excitation force in the frequency domain, denoted as $F_{Ex}(\omega)$, to the time domain excitation force, $F_{Ex}(t)$, as expressed in Eq. (1-101). Here, the term $\varsigma(\tau)$ represents the wave coordinate of a wave at time $\tau$. The impulse response of the wave excitation force in the frequency domain can be derived through the diffraction theory in the frequency domain, and by multiplying the wave amplitude time history $\varsigma(\tau)$, the wave excitation force in the time domain can be obtained as specified in Eq. (1-101). Furthermore, $h(t)$ is related to the Fourier relationship with the frequency response, which can be computed using Eq. (1-102).

$$F_{Ex}(\omega) = \int_0^{\infty} h(t-\tau)\varsigma(\tau)\, d\tau \quad (1\text{-}100)$$

$$F_{Ex}(t) = \int_{-\infty}^{+\infty} h(t)\, e^{-i\omega t}\, dt \quad (1\text{-}101)$$

$$h(t) = \frac{1}{2\pi}\int_{-\infty}^{+\infty} F_{Ex}(\omega)\, e^{-i\omega t}\, d\omega \quad (1\text{-}102)$$

In accordance with the DNV-RP-C205 guideline [482], the wind and current forces are determined using wind and current coefficients. The wind and current forces are represented by Eq. (1-103) and (1-104) respectively, where $C_W$ denotes the wind coefficient, $\rho_\alpha$ represents the air density, $A_W$ signifies the shadow area, $U$ denotes the relative wind speed on the platform, $C_C$ stands for the current coefficient, $\rho_w$ denotes the fluid density, $A_C$ represents the shadow area in the current direction, and and $V$ signifies the current speed.

$$F_{Wind} = \frac{1}{2} C_W \rho_\alpha A_W U^2 \quad (1\text{-}103)$$

$$F_{Current} = \frac{1}{2} C_C \rho_w A_C V^2 \quad (1\text{-}104)$$

The determination of the velocity profile of the current is challenging in the absence of measurements and is often assumed to be uniform. However, in reality, the profile varies with depth, resulting in different velocities along the z-axis.

The mooring system plays a crucial role in maintaining the stability of the floating platform against the influence of wind, waves, and currents. It comprises cables connected to the floating platform and an anchor linked to the seabed. These mooring system cables are constructed from various materials such as chain, steel, or composites. The tension on the cables is a critical factor in ensuring the stability of the platform under environmental conditions and is influenced by cable elasticity, water location, cable weight in water, extensional stiffness of the cable, and the number of cables. The total load on the platform from all mooring lines is defined in Eq. (1-105), where $F_M$ represents the total mooring system component and $F_{Pre-tension}$ denotes the pre-tension of lines resulting from the weight of the cable not resting on the seafloor; if the lines are buoyant, then $F_{Pre-tension}$ should be zero. $C_{Elastic\ Stiffness}$ signifies the elastic stiffness of the mooring lines, and the effective geometric stiffness of the weight of the cables in water also depends on the layout of the mooring system.

$$F_M = F_{Pre-tension} - C_{Elastic\ Stiffness} \quad (1\text{-}105)$$

## 1.13. Wave-Induced Response of Floating Structures

### 1.13.1. Frequency Domain Analysis

The frequency domain refers to the analysis of mathematical functions in relation to frequency. The calculation of wave-induced forces in a non-uniform sea involves combining forces generated by regular wave components in a linear manner [482]. When a consistent amplitude harmonic input, as outlined by Newland (1993) (Eq. (1-106)) [563], is applied to a linear system, the corresponding output $y(t)$ can be determined using a complex frequency response function $H(\omega)$ evaluated at the angular frequency ω. The function $H(\omega)$ is defined as the ratio between response and excitation, denoted as $|H(\omega)|$, and the phase angle between response and excitation is represented by $\emptyset = arctan(\frac{B}{A})$.

$$x(t) = x_0 e^{i\omega t} \quad (2\text{-}106)$$

$$y(t) = H(\omega) x_0 e^{i\omega t} \quad (2\text{-}107)$$

$$H(\omega) = A(\omega) - iB(\omega) = \sqrt{A^2 + B^2}\, e^{-iarctan\left(\frac{B}{A}\right)} \quad (2\text{-}108)$$

The frequency-domain approach is particularly suitable for analysing systems subjected to random wave conditions, as it allows for the direct calculation of the random response spectrum using the transfer function and wave spectrum as outlined in Eq. (2-109) [564], where $\omega$ represents the angular frequency, $H(\omega)$ denotes the response transfer function, $S_{xx}(\omega)$ signifies the wave spectrum, and $S_{yy}(\omega)$ corresponds to the response spectrum.

$$S_{yy}(\omega) = |H(\omega)|^2 S_{xx}(\omega) \quad (2\text{-}109)$$

## 1.14. Time Domain Coupled Analysis

A time-domain coupled analysis was utilized to compute the motion equations of the platform system in all six degrees of freedom, considering the fully coupled effects of the attached mooring lines and wind turbine. This analysis involves two primary steps. Firstly, the static analysis determines the static equilibrium position based on the kinetic parameters derived from the frequency domain analysis, such as added mass, damping matrix, and hydrostatic matrix. Subsequently, the dynamic analysis is conducted, which performs the coupled dynamic analysis in the time domain. The equilibrium position obtained in the static analysis serves as the initial position in the dynamic analysis. To account for the influence of the mooring system on each platform, each platform is integrated as a rigid body point component in the 3D finite element method (FEM), with the mooring lines represented as a line of finite elements for slender structures [565].

As outlined in the Riflex Theory Manual [506], the dynamic equilibrium of a spatially discretized finite element system model can generally be expressed as shown in Eq. (1-110), where $R^I$, $R^D$, $R^S$, and $R^E$ represent the inertia, damping, internal structural reaction, and external force vectors respectively. $r$, $\dot{r}$, and $\ddot{r}$ denote the structural displacement, velocity, and acceleration vectors, respectively. The external force vector is constructed from all elements and encompasses all specified external forces, including rigid body forces (e.g., buoys, clump weights) and contributions from distributed loading, such as weight, buoyancy, and wave forces on the rigid body point. All force vectors are established through the assembly of element contributions and specified discrete nodal forces.

$$R^I(r,\ddot{r},t) + R^D(r,\dot{r},t) + R^S(r,t) = R^E(r,\dot{r},t) \tag{1-110}$$

$$R^I(r,\ddot{r},t) = [M^S + M^F(r) + M^H(r)]\ddot{r} \tag{1-111}$$

$$R^D(r,\dot{r},t) = [C^S(r) + C^H(r)]\dot{r} \tag{1-112}$$

The inertia force vector can be determined using the Eq. (1-111), while the damping force vector is represented in Eq. (1-112). $M^S$ denotes the structural mass matrix; $M^F(r)$ represents the mass matrix accounting for internal fluid flow, which is set to zero as internal fluid is not considered. $M^H(r)$ is the displacement-dependent hydrodynamic mass matrix, which accounts for the structural acceleration terms in the Morison equation as added mass contributions in local directions. $C^S(r)$ denotes the internal structural damping, and $C^H(r)$ is the hydrodynamic damping matrix, which accounts for diffraction effects for floating, partly submerged elements.

The internal reaction force vector, $R^S(r,t)$, is computed based on the instantaneous state of stress in each of the various elements of the entire system. The external load vector, $R^E(r,\dot{r},t)$, takes into account the weight and buoyancy for each element, forced displacements, environmental forces, and other specific forces. The distinctive characteristic of this analysis module lies in its treatment of nonlinearity in the analysis, involving a step-by-step numerical integration of the incremental dynamic equilibrium equations, with a Newton-Raphson type equilibrium iteration at each time step. This approach enables the proper treatment of all the described nonlinearities. However, nonlinear dynamic analysis is time-consuming due to the repeated assembly of system matrices (mass, damping, and stiffness) and triangularization during the iteration process at each time step. Eq. (1-113) asserts that the increment in external loading is balanced by increments in inertia, damping, and structural reaction forces over the time interval $\Delta t$.

$$(R^I_{t+\Delta t} + R^I_t) + (R^D_{t+\Delta t} + R^D_t) + \left(R^S_{t+\Delta t} + R^S_t\right) = (R^E_{t+\Delta t} + R^E_t) \tag{1-113}$$

In order to obtain a numerical solution, the nonlinear incremental equation of motion is linearized by incorporating the tangential mass, damping, and stiffness matrices at the onset of the increment. The resulting linearized incremental equation of motion is denoted as Eq. (1-114). Subsequently, by introducing the tangential mass, damping, and stiffness matrices at the commencement of the subsequent time increment, and integrating the residual force vector from the preceding time step, the linearized incremental equation of motion is expressed as Eq. (1-115).

$$M_t\Delta\ddot{r}_t + C_t\Delta\dot{r}_t + K_t\Delta r_t = \Delta R_t^E \quad (1\text{-}114)$$

$$M_t\Delta\ddot{r}_t + C_t\Delta\dot{r}_t + K_t\Delta r_t = \Delta R_t^E - (R_t^I + R_t^D + R_t^S) \quad (1\text{-}115)$$

In the given equation, $M_t$, $C_t$, and $K_t$ represent the tangential mass, damping, and stiffness matrices at time $t$. The incremental displacement, velocity, acceleration, and external force vectors are denoted as $\Delta r_t$, $\Delta\dot{r}_t$, $\Delta\ddot{r}_t$, and $\Delta R_t^E$, respectively. The numerical solution is obtained through the application of a dynamic time integration scheme, specifically the Newmark β-family methods. Subsequently, a Newton-Raphson type of equilibrium iteration is utilized to achieve dynamic equilibrium at the conclusion of the time step [565]. By employing the Newmark β-family method, Eq. (1-114) can be modified to address dynamic equilibrium at time $t + \Delta t$, with the incremental equation being computed for the incremental displacement vector over the time interval $\Delta t + \theta\Delta\tau$. Eq. (1-117) is a reformulated version of Eq. (1-116), where $\widehat{K}_t$ denotes the effective stiffness. The effective incremental load vector, $\Delta\widehat{R}_t$, is then defined in accordance with the Newmark β-family method through Eq. (1-117) and Eq. (1-118).

$$\widehat{K}_t\Delta r_t = \Delta\widehat{R}_t \quad (1\text{-}116)$$

$$\widehat{K}_t\Delta r_t = \frac{1}{\beta(\Delta t)^2}M_t + \frac{1}{\beta\Delta t}C_t + K_t \quad (1\text{-}117)$$

$$\Delta\widehat{R}_t = R_{t+\Delta t}^E - (R_t^I + R_t^D + R_t^S) + \left(\frac{1}{\beta\Delta t}\dot{r}_t + \frac{1}{2\beta}\ddot{r}_t\right) + C_t\left[\frac{\gamma}{\beta}\dot{r}_t + (\frac{\gamma}{2\beta} - 1)\Delta t\ddot{r}_t\right] \quad (1\text{-}118)$$

The parameters $\beta$ and $\gamma$ represent the time integration parameters derived from the Newmark β-family methods, and they govern the functional changes in displacement, velocity, and acceleration within the integration method. The level of numerical damping in the method is determined by the parameter $\gamma$. The integration method remains stable without condition when $\gamma > 1/2$ and $\beta \geq \frac{1}{4}(\gamma + 1/2)^2$. In this study, the constant average acceleration method has been employed, with $\gamma = 0.256$ and $\beta = 0.505$, to introduce a minimal amount of numerical damping into the simulation. This

numerical damping does not significantly affect the system's damping during the analyses but serves to prevent numerical instability in the calculations. A time step of 0.005s has been utilized, as recommended in SIMA for FOWTs. The constant acceleration method is based on maintaining constant acceleration within the time step [566], as illustrated in Fig. 1-8. Further information on the numerical time integration methods can be found in the Riflex Theory Manual [506], the study by Langen and Sigbjørnsson [567], and the study by Clough and Penzien [568].

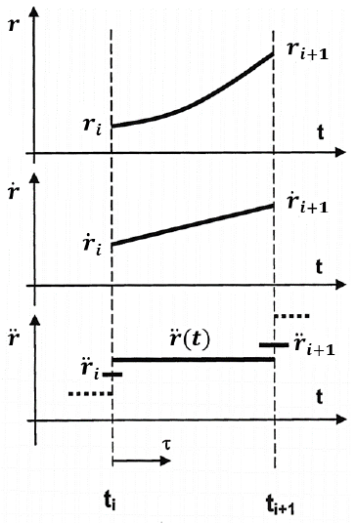


**Fig. 1-8** Constant Average Acceleration [101]

The steps involved in the nonlinear integration procedure, including equilibrium iteration, are as follows:

- Establish integration constants based on the integration parameters.
- Set initial conditions and calculate the effective stiffness matrix.
- Calculate the effective stiffness matrix.
- Calculate the effective load vector.
- Compute the incremental displacement.
- Calculate velocity and acceleration.
- Perform the equilibrium iteration.
- Establish the effective stiffness matrix based on the tangential mass, damping, and stiffness matrices at iteration i.
- Calculate the effective residual load vector.

- Compute the additional displacement increments.
- Calculate the improved displacement increment.
- Calculate velocity, acceleration, and displacement vector.
- Test for convergence.

### 1.14.1. SIMO-RIFLEX

SIMO is a software application designed to replicate the movements and actions of intricate floating vessels. It operates as a time-domain physics engine simulation and incorporates a mooring line model based on the one utilized in the mooring analysis program MIMOSA, which was developed by MARINTEK [381]. The quasi-static analysis involves the calculation of a two-dimensional line characteristics table using the upper end's position relative to the anchor. Subsequently, the line forces acting on the structure at a later stage are determined through a series of steps, including the transformation of the fairlead coordinate into the line plane, interpolation from the line characteristics table to find the total tension and direction, and the transformation of the resulting force back into the body coordinate system. Additionally, a simplified dynamic model developed by Larsen and Sandvik [354] can be employed alongside the quasi-static analysis in SIMO. This model assumes that only the tangential component of the top end motion of the line affects the dynamic tension, and that the shape of the dynamic motion resulting from this top-end motion is equivalent to the alteration in static line geometry.

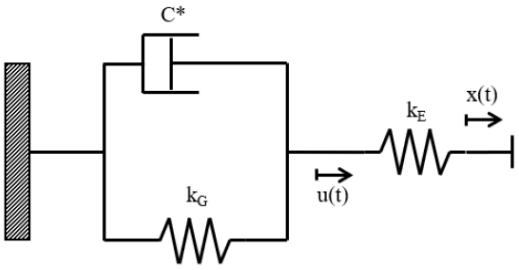


**Fig. 1-9** Equivalent Geometric Model for Dynamic Mooring Line Effects in SIMO [381].

The model can be depicted using an equivalent geometric representation, as illustrated in Fig. 1-9. In this representation, $x(t)$ denotes the applied tangential motion

of the upper line end, while $u(t)$ represents the portion of this upper-end motion that is counteracted by the geometric alteration of the line. The diSparity between $x$ and $u$ consequently signifies the axial stretching of the line. The parameters $k_G$ and $k_E$ denote the geometric catenary stiffness and the axial line stiffness of the line, respectively, and $C^*$ represents the generalized line damping. However, this approach necessitates the calculation of the wave frequency motion of the FOWT in the frequency domain, thereby excluding contributions from nonlinear effects in vessel motions. Nonlinear effects are particularly pertinent for load cases involving severe sea states and substantial vessel motions. Consequently, this dynamic model has not been employed in the simulations conducted in this study [381].

The RIFLEX model is constructed using supernodes and lines, with the supernodes serving as the system connections. The coordinates determine the position of the supernodes, and they can be subjected to constraints in any of the six degrees of freedom, as well as prescribed offsets for static analysis in RIFLEX. The supernodes are linked to each other through lines, which are composed of one or more segments. Each segment can incorporate a distinct set of cross-sectional properties, and the division of a line into multiple segments allows for the inclusion of different cross-sectional properties. Furthermore, each segment can be subdivided into multiple elements for the finite element method (FEM) formulation. The relationship between lines, segments, and elements is illustrated in Fig. 1-10 [487].

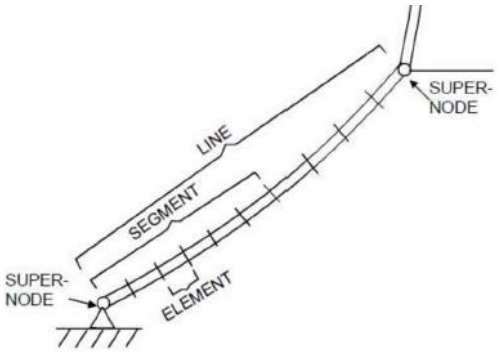


**Fig. 1-10** Definition of Line, Segment, and Element in RIFLEX [487]

# Appendix C

Two external control systems based on the DTU 10MW references turbine are integrated to RIFLEX for modelling of operational and survival conditions (rotating blades in operational event and no rotating blades in survival condition). The Cut-out time (s) is set to 10800s for operational condition while it is 0 for survival event.

```
' Input file for DTU 10MW controller
' November 7, 2019
'
'
' Rated power [kW]
10000.0
'
' Minimum rotor speed [rad/s]
0.628
' Rated rotor speed [rad/s]
1.005
' Maximum allowable generator torque [Nm]
15.6e6
' Minimum pitch angle, theta_min [deg],
100.0
' if |theta_min|>90, then a table of <wsp,theta_min> is read '
' from a file named 'wptable.n', where n=int(theta_min)
' Maximum pitch angle [deg]
90.0
' Maximum pitch velocity operation [deg/s]
10.0
' Frequency of generator speed filter [Hz]
0.8
' Damping ratio of speed filter [-]
0.7
' Frequency of free-free DT torsion mode [Hz], if zero no notch filter used
1.65
' Partial load control parameters
' Optimal Cp tracking K factor [kNm/(rad/s)^2],
' Qg=K*Omega^2, K=eta*0.5*rho*A*Cp_opt*R^3/lambda_opt^3
0.100131E+08
' Proportional gain of torque controller [Nm/(rad/s)]
0.683456E+08
' Integral gain of torque controller [Nm/rad]
0.153367E+08
' Differential gain of torque controller [Nm/(rad/s^2)]
0.0
'
' Full load control parameters
' Generator control switch [1=constant power, 2=constant torque]
1
' Proportional gain of pitch controller [rad/(rad/s)]
0.00524485
' Integral gain of pitch controller [rad/rad]
0.000141233
' Differential gain of pitch controller [rad/(rad/s^2)]
0.0
' Proportional power error gain [rad/W]
0.4e-8
' Integral power error gain [rad/(Ws)]
0.4e-8
' Coefficient of linear term in aerodynamic gain scheduling, KK1 [deg]
198.32888
' Coefficient of quadratic term in aerodynamic gain scheduling, KK2 [deg^2] &
' (if zero, KK1 = pitch angle at double gain)
693.22213
' Relative speed for double nonlinear gain [-]
1.3
'     Cut-in simulation parameters
' Cut-in time [s]
0.1
' Time delay for soft start of torque [1/1P]
4.0
'     Cut-out simulation parameters
' Cut-out time [s]
10800
' Time constant for 1st order filter lag of torque cut-out [s]
5
' Stop type [1=linear two pitch speed stop, 2=exponential pitch speed stop]
1
' Time delay for pitch stop 1 [s]
1
' Maximum pitch velocity during stop 1 [deg/s]
```

# Appendix D

The hydrostatic calculation of 6M-12.5d-52 D Model.

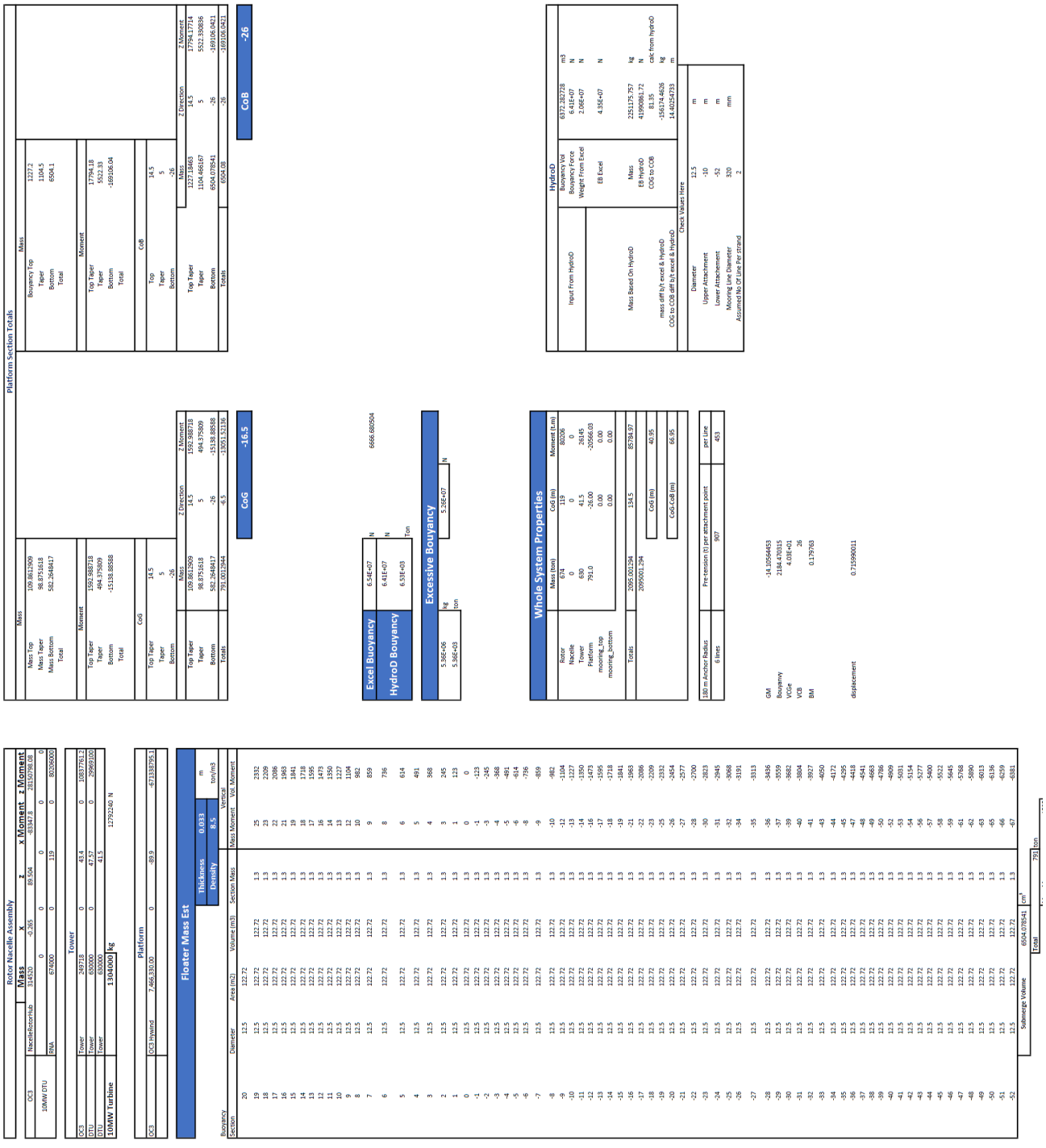

# The pretension and mooring stiffness matrix calculation

## 6Mooring

| Platform | | | |
|---|---|---|---|
| at | Depth | | Diameter |
| | -10 | (m) | 12.5 |
| | -52 | (m) | 12.5 |

| | | |
|---|---|---|
| Lines | (no) | 6 |
| Angle | (deg) | 60 |
| Anchor Radius | (m) | 180 |
| Water Depth | (m) | 110 |
| Weight in Air | (kg/m) | 142.286 |
| Weight in Water | (kg/m) | 59.85060877 |
| MBF | (t) | 3097.1312 |
| Pre-Tension (t) | Top | 906.7663371 |
| | Bottom | 906.7663371 |
| Line Diameter | (mm) | 320 |

30382.85707

0.080424772

| Material | | poly | N |
|---|---|---|---|
| Axial Stiffness | (kN) | 1.21E+06 | 1.21E+09 |

| Reduction Lengh | | Top | 1.47583 | m |
|---|---|---|---|---|
| | | Bottom | 1.34849 | m |
| 10 | 3.04E+08 | 3.04E+05 | 1.82E+09 | 1822971.424 60 |
| 20 | 6.08E+08 | 6.08E+05 | 2.10E+09 | 2096417.138 69 |
| 30 | 9.11E+08 | 9.11E+05 | 2.16E+09 | 2157182.852 71 |
| 40 | 1.22E+09 | 1.22E+06 | 2.25E+09 | 2248331.423 74 |

0.736177318

## Output

### Fairleads

| Point 1 | Point 2 | Point 3 | Point 4 |
|---|---|---|---|
| 6.25 m, 0 m, -10 m | 3.125 m, 5.41265877365274 m, -10 m | -3.125 m , 5.41265877365274 m, -10 m | -6.25 m, 0 m, -10 m |
| 6.25 m, 0 m, -52 m | 3.125 m, 5.41265877365274 m, -52 m | 3.125 m , -5.41265877365274 m, -52 m | -6.25 m, 0 m, -52 m |

### Anchors

| Point 1 | Point 2 | Point 3 | Point 4 |
|---|---|---|---|
| 180 m , 0 m , -110 m | 90m , 155.884572681199 m , -110 m | -90 m , 155.884572681199 m, -110 m | -180 m , 0 m , -110 m |

### Mooring Line Length

| Segment | Distance | Section1 | Section2 |
|---|---|---|---|
| Top | 200.4720991 | 20 | 180.4720991 |
| Reduced | | | 178.9962689 |
| Lower | 183.1749505 | 20 | 163.1749505 |
| Reduced | | | 161.8264581 |

| 6 Lines | |
|---|---|
| MooringWeight | 2401305 N |

| Compensation Force | 4.59E+07 | 45924238.47 | 45393903.86 |
|---|---|---|---|

| Define Anchor Section | | | |
|---|---|---|---|
| K_B | 1.14E+06 | vertical | 3.60E+05 |
| | | Horizontal | 1.08E+06 |
| K_T | 1.04E+06 | vertical | 5.18E+05 |
| | | Horizontal | 9.00E+05 |

## 12.5 Diameter & 52 Draft

| | | |
|---|---|---|
| Fv (N) | 43,522,933.20 | |
| $T_{Total}$ (N) | 1.69E+07 | |
| β (degree) | 18.4597 | |
| β (rad) | 0.322182147 | |
| $Sin^2(β)$ | 0.100259105 | |
| $Cos^2(β)$ | 0.899740895 | |
| $T_{per\ NO.\ of\ n}$ (N) | 8.90E+06 | 906.7663371 |
| E (N/mm²) | 2588 | |
| r (mm) | 160 | |
| A (mm²) | 80424.77193 | 2.08E+08 |
| $D_{submerged}$ (mm) | 52000 | |
| Depth (mm) | 110000 | |
| L (mm) | 183174.9505 | 173750 small L |
| D (mm) | 52000 | Radius |
| R (mm) | 6250 | |
| $K_r$ (N/m) | 1.14E+06 | 1.29E+06 |
| n | 6 | |
| Sin(β)/Sin(α) | 0.634769204 | |
| X_α | 0.611707144 | |
| X_β | 0.388292856 | |

### 6 Mooring Line Pairs

### System Stiffness Matrix

$K_m$

| | | | | | |
|---|---|---|---|---|---|
| *3.07E+09* | 0 | 0 | 0 | -153098402397.92 | 0 |
| 0 | 3067251864.38 | 0 | 153098402397.92 | 0 | 0 |
| 0 | 0 | *6.84E+08* | 0 | 0 | 0 |
| 0 | 153098402397.92 | 0 | 801835987909382.00 | 0 | 0 |
| -153098402397.92 | 0 | | 0 | 801835987909382.00 | 0 |
| 0 | 0 | | 0 | 0 | 327794819.94 |

Anchor Radius (mm) 180000

E

vertical 7.07E+08

Horiz 5.13E+09

| Yaw Factor | 1.8 |
|---|---|

| Stiffness Matrix | | | |
|---|---|---|---|
| $K_{11}$ | 3067251.864 | 3067251864 | N/m |
| $K_{15}$ | -1.53098E+11 | -1.53098E+11 | N |
| $K_{22}$ | 3067251.864 | 3067251864 | N/m |
| $K_{24}$ | 1.53098E+11 | 1.53098E+11 | N |
| $K_{33}$ | 683800.8457 | 683800845.7 | N/m |
| $K_{42}$ | 1.53098E+11 | 1.53098E+11 | N |
| $K_{44}$ | 8.01836E+17 | 8.01836E+14 | N.m |
| $K_{51}$ | -1.53098E+11 | -1.53098E+11 | N |
| $K_{55}$ | 8.01836E+17 | 8.01836E+14 | N.m |
| $K_{66}$ | 3.27795E+11 | 3.28E+08 | N.m |

| | | | | | |
|---|---|---|---|---|---|
| *5.41E+09* | 0.00 | 0.00 | 0.00 | -1.68E+11 | 0.00 |
| 0.00 | 5.41E+09 | 0.00 | 1.68E+11 | 0.00 | 0.00 |
| 0.00 | 0.00 | *2.23E+09* | 0.00 | 0.00 | 0.00 |
| 0.00 | 1.68E+11 | 0.00 | 9.35E+14 | 0.00 | 0.00 |
| -1.68E+11 | 0.00 | 0.00 | 0.00 | 9.35E+14 | 0.00 |
| 0.00 | 0.00 | 0.00 | 0.00 | 0.00 | 1.13E+09 |

2.78E+04

| | | |
|---|---|---|
| T (N) | 26,623,289.15 | |
| α (degree) | 29.9221 | |
| α (rad) | 0.522239685 | |
| $Sin^2(α)$ | 0.248823918 | |
| $Cos^2(α)$ | 0.751176082 | |
| $T_{per\ NO.\ of\ n}$ (N) | 8.90E+06 | 906.7663371 |
| E (N/mm²) | 2.59E+03 | |
| r (mm) | 160 | |
| A (mm²) | 80424.77193 | |
| $D_{submerged}$ (mm) | 10000 | |
| Depth (mm) | 110000 | |
| L (mm) | 200472.0991 | 173750 small L |
| D (mm) | 10000 | Radius |
| R (mm) | 6250 | |
| $K_r$ (N/m) | 1.04E+06 | |
| n | 6 | |

### System Stiffness Matrix

$K_m$

| | | | | | |
|---|---|---|---|---|---|
| *2.34E+09* | 0 | 0 | 0 | -14982938619.58 | 0 |
| 0 | 2339882418 | 0 | 14982938619.58 | 0 | 0 |
| 0 | 0 | *1.55E+09* | 0 | 0 | 0 |
| 0 | 14982938619.58 | 0 | 133634382749053.00 | 0 | 0 |
| -14982938619.58 | 0 | | 0 | 133634382749053.00 | 0 |
| 0 | 0 | | 0 | 0 | 299512002.96 |

Anchor Radius (mm) 180000

Vertical 7.73E+08

Horizontal 2.03E+09

| Stiffness Matrix | | | |
|---|---|---|---|
| stiffness | (N &N/mm) | (N&N/m) | |
| $K_{11}$ | 2339882.418 | 2339882418 | N/m |
| $K_{15}$ | -14982938620 | -14982938620 | N |
| $K_{22}$ | 2339882.418 | 2339882418 | N/m |
| $K_{24}$ | 14982938620 | 14982938620 | N |
| $K_{33}$ | 1550242.278 | 1550242278 | N/m |
| $K_{42}$ | 14982938620 | 14982938620 | N |
| $K_{44}$ | 1.33634E+17 | 1.33634E+14 | N.m |
| $K_{51}$ | -14982938620 | -14982938620 | N |
| $K_{55}$ | 1.33634E+17 | 1.33634E+14 | N.m |
| $K_{66}$ | 2.99512E+11 | 299512003 | N.m |